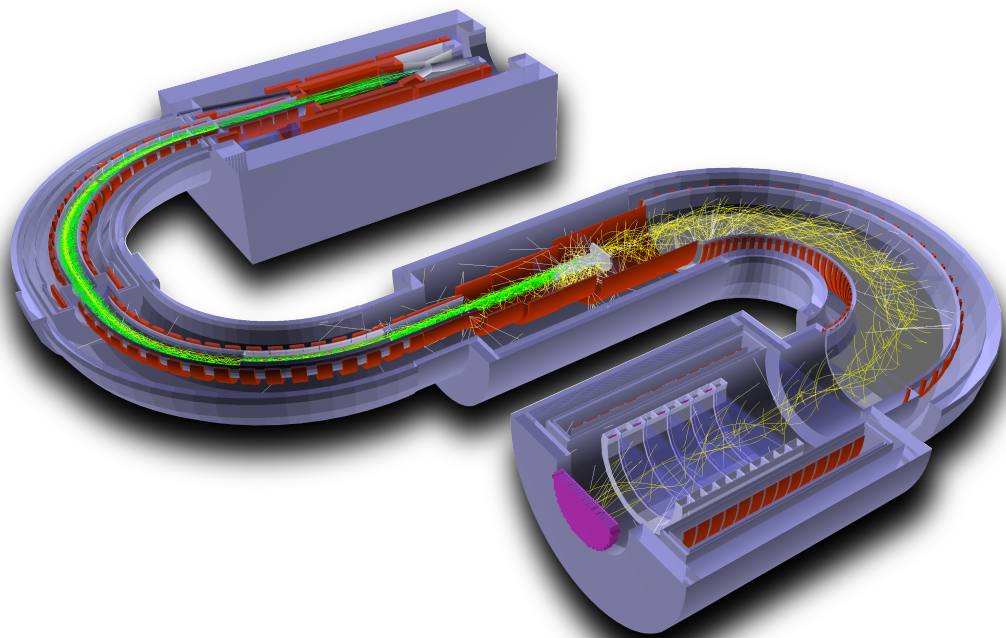


Sensitivity and Background Estimates for Phase-II of the COMET Experiment

Benjamin Edward Krikler

High Energy Physics Group, Department of Physics
Imperial College London



A dissertation submitted to Imperial College London
for the degree of Doctor of Philosophy

Abstract

Conservation of Lepton Flavour in the Standard Model (SM) requires that neutrino emission accompanies muon decay. COMET is one experiment looking for Charged Lepton Flavour Violation. It searches for COherent Muon to Electron Transitions, where a muon converts to a 105 MeV electron in the presence of an atomic nucleus, without emitting neutrinos. The current limit on this process is 7×10^{-13} at 90% C.L., which COMET intends to improve by four orders of magnitude.

To realise such an improvement, COMET will use several novel techniques to produce a very intense, low-energy muon beam, with very high signal acceptance and strong background suppression. Given the challenge this presents, COMET will run in a staged approach. Phase-I is currently under construction with first data-taking due in JFY 2018, and the goal of measuring μ - e conversion with a Single-Event Sensitivity (SES) of 3×10^{-15} . Phase-II should follow at the start of the next decade and achieve a SES of 3×10^{-17} .

This thesis provides an overview of CLFV, μ - e conversion, and the COMET experiment itself. It sets out the software and simulation that has been developed to help understand and analyse the experiment, and then uses this to perform a comprehensive optimisation of the Phase-II set-up, providing a new baseline configuration. The expected performance of this baseline is assessed, with studies on the signal sensitivity demonstrating that an SES of 2.6×10^{-17} can be achieved in 1.57×10^7 s of beam. Background rates are also estimated and, although subject to large uncertainties, predict 0.662 background events can be expected during Phase-II. Suggestions for future performance studies and experiment improvements are also discussed, with a possible improvement in the SES of a factor of 2.5 likely achievable.

Declaration

This dissertation is the result of my own work, except where explicit reference is made to the work of others, and has not been submitted for another qualification to this or any other university. This dissertation does not exceed the word limit for the respective Degree Committee.

Benjamin Edward Krikler

The copyright of this thesis rests with the author and is made available under a Creative Commons Attribution Non-Commercial No Derivatives licence. Researchers are free to copy, distribute or transmit the thesis on the condition that they attribute it, that they do not use it for commercial purposes and that they do not alter, transform or build upon it. For any reuse or redistribution, researchers must make clear to others the licence terms of this work

Acknowledgements

Sir Isaac Newton is supposed to have said, “If I have seen further than others it is by standing upon the shoulders of giants.” Exactly how tall these giants were, why they do not seem to be around any more, and how they managed to co-exist with humans, are all open questions. One thing is certain however: if it had not been for friends, family, and colleagues, Sir Isaac would have had a much harder time getting on to the giants’ shoulders.

The same has been true for my PhD, although only in the figurative sense. Getting through the last four years would not have been possible if it were not for the people around me (none of whom are giants, sadly).

To Lorena, my brilliant fiancée, thank you for all your support, your caring, and your patience, though I suppose I now need a new excuse beyond ‘PhD stress’ to get out of the house work. English may not be her first language, but that has certainly not stopped her from correcting mine.

Mum and dad, thank you for everything that you have given me. From the food and the chauffeuring, to the curiosity and confidence to pursue what I love, I can honestly say that without you, I would be less existent. Will, Sophie, Chris, and Marie-Claire, you are all much more recent additions to my life, but it is a far better life for it; I love you all. To my brother Dan who, ever since he was born, has been my brother—I would struggle to find a better alternative. And to my grand-parents, my aunts, my uncles, and my cousins, and my cousins, and my cousins: I hope I can make you all as proud of me, as I am of you.

I owe a deep gratitude to my collaborators on the COMET and AlCap experiments, who have not only endured my pedantry in code reviews, questions at collaboration meetings, and mistakes at beam tests, but they have always made me feel very welcome whilst doing it. Specifically to Yoshi Kuno and Satoshi Mihara, thank you both for

supporting me during my times in Japan: I imagine few students can claim to have been personally driven to the airport by the spokesperson of their experiment!

To my COMET colleagues at Imperial, thank you too. To my supervisor, Yoshi Uchida, not only have you pushed me to improve as a physicist, but you have also taught me the difference between an en-dash and an em—dash, and helped me to master the dark-art of that highly-complicated grammatical—construct that is the compound-adjective (I think). Phill, Ewen, Per, Ajit, Peter, Jordan, Paul, Andy E. (previously at UCL, now at USA)—thank you all for the feedback and support you have given me over the last few years, and thank you for putting up with my daft ideas and naive questions during our meetings; I am sure one day I will find a use for a reverse Monte Carlo, and I promise that you will be the first to hear! To the rest of the Imperial HEP group, thank you too for creating such a fertile environment for a young physicist to work and grow. Perhaps it is time to clean some of those coffee cups out now, though.

Finally, to all my friends: from home, from my undergraduate studies, from my Erasmus year, from these post-graduate studies, from Uberlandia and my trips to other places, and to all the other friends that cannot be put in a group (though I suppose that sort of defines a group): thank you for all the laughter, the stories, and the distractions. It would take up too much space to write you all out in full, so I shall just put your initials here: A, B, C, D, E, F, G, H, I, J, K, L, M, N, O, P, Q, R, S, T, U, V, W, X, Y, Z; my apologies if I have missed anyone out!

Oh, and there is one more thank-you to make: thank you to the muon, for without you this PhD would absolutely not have been possible or else would certainly have been a lot smaller: “The COMET experiment is searching for muon-to-electron conversion. Since there is no such thing as a muon, however, the predicted sensitivity and background rates are, respectively, zero and zero. The end.”

Contents

| | |
|--|-----------|
| List of figures | 11 |
| List of tables | 19 |
| 1 The History and Theory of Charged Lepton Flavour Violation (CLFV) | 22 |
| 1.1 The Muon and the Birth of the Standard Model | 22 |
| 1.2 Neutrino Oscillations Break Lepton Flavour Conservation | 26 |
| 1.3 In Search of Charged Lepton Flavour Violation (CLFV) | 28 |
| 1.3.1 Motivations and Status | 28 |
| 1.3.2 Muon CLFV Channels | 31 |
| 2 Muon-to-Electron Conversion and the Muonic Atom | 34 |
| 2.1 Muon Decay in Orbit | 37 |
| 2.2 Muon Nuclear Capture | 39 |
| 2.3 Experimental Searches for μ - e conversion | 40 |
| 2.3.1 SINDRUM-II: Present Limits | 40 |
| 2.3.2 Experiments Beyond SINDRUM-II | 41 |
| 3 The COMET Experiment | 43 |
| 3.1 The COMET Signal | 44 |
| 3.2 Overview of Background Processes | 44 |
| 3.3 General Experimental Techniques | 47 |
| 3.3.1 Proton Beam Energy and Production Target | 47 |
| 3.3.2 Particle Transport through Bent Solenoids | 49 |
| 3.3.3 Stopping Target Material and Beam Pulsing | 51 |
| 3.4 COMET Phase-I | 54 |
| 3.5 COMET Phase-II | 56 |
| 3.6 Key Sub-component Descriptions | 58 |
| 3.7 Schedule and Status | 61 |

| | |
|--|-----------|
| 4 Offline Software and The COMET Simulation | 65 |
| 4.1 Developing the COMET Offline Framework | 65 |
| 4.2 Overview of ICEDUST | 68 |
| 4.3 The COMET Simulation | 70 |
| 4.3.1 Handling Geometry | 72 |
| 4.3.2 Field Calculation | 75 |
| 4.3.3 Production Target Simulations | 79 |
| 4.3.4 Extending the Geant4 Physics Modelling | 80 |
| 4.4 Analysis Using the Beamline Coordinate System | 86 |
| 4.4.1 Distributions as a Function of Distance Along the Beamline | 87 |
| 5 COMET Phase-II: Optimisation | 89 |
| 5.1 Optimisation Strategy | 89 |
| 5.2 Production Target Optimisation | 91 |
| 5.2.1 Production Target Simulations | 91 |
| 5.2.2 Length Scan | 92 |
| 5.2.3 Radius scan | 96 |
| 5.2.4 Final Result | 96 |
| 5.3 Dipole Strengths of the Muon Beamline | 98 |
| 5.3.1 Large-sample Production Target Simulation | 98 |
| 5.3.2 The Optimised Dipole Field Strengths | 99 |
| 5.4 Electron Spectrometer's Dipole | 101 |
| 5.4.1 Method and Potential Short-comings | 102 |
| 5.4.2 Results | 102 |
| 5.5 Stopping Target Position | 105 |
| 5.5.1 Muon Stopping Rate | 106 |
| 5.5.2 Signal Acceptance | 108 |
| 5.5.3 Impact of the Beam Blocker | 109 |
| 5.5.4 Stability of Electron Spectrometer Dipole Tune | 111 |
| 5.5.5 Results | 111 |
| 5.6 Collimators in the Muon Beamline | 112 |
| 5.6.1 Collimator Placement | 113 |
| 5.6.2 Collimator Height Optimisation | 116 |
| 5.7 The Beam and Decay-in-Orbit Blockers | 120 |
| 5.8 Summary of optimised parameters | 124 |
| 5.9 Future optimisations | 124 |

| | |
|---|------------|
| 6 COMET Phase-II: Signal Sensitivity | 126 |
| 6.1 Muon Stopping Rate | 126 |
| 6.2 Acceptance of Stopping Target Electrons | 129 |
| 6.2.1 Geometric Acceptance | 129 |
| 6.2.2 Timing Window Efficiency | 130 |
| 6.2.3 Momentum Cut Efficiency | 131 |
| 6.2.4 Total Signal Acceptance | 134 |
| 6.3 Single Signal Event Sensitivity (SES) and Run Time | 135 |
| 6.3.1 Fraction of Conversion Events That Excite the Nucleus | 136 |
| 7 COMET Phase-II: Backgrounds | 137 |
| 7.1 Muon Decay in Orbit (DIO) | 137 |
| 7.2 Radiative Muon Capture (RMC) | 139 |
| 7.2.1 Calculation and Simulation of RMC | 142 |
| 7.2.2 Aluminium-26 and RMC | 143 |
| 7.3 Radiative Pion Capture (RPC) | 145 |
| 7.3.1 Photons from Radiative Pion Capture (RPC) | 146 |
| 7.3.2 Pion Stopping Rate | 146 |
| 7.3.3 Simulating RPC | 148 |
| 7.4 Antiprotons in the Beam | 150 |
| 7.4.1 Antiproton Production Rate and Spectrum | 151 |
| 7.4.2 Modelling Antiproton Production | 153 |
| 7.4.3 Simulating Antiproton Backgrounds | 159 |
| 7.4.4 Reducing Antiproton Backgrounds Further | 166 |
| 7.5 Direct Beam-Related Backgrounds | 167 |
| 7.6 Cosmic Ray Background | 172 |
| 7.6.1 Simulating Cosmic Muons | 173 |
| 7.6.2 Results of the Simulated Cosmic Background Rate | 174 |
| 7.7 Summary of Background Rates | 176 |
| 7.7.1 Backgrounds Not Considered | 178 |
| 7.7.2 Impact of Momentum Resolution | 179 |
| 7.7.3 Principal Uncertainties | 180 |
| 7.8 Further Studies and Improvements | 183 |
| 8 Revisiting the Phase-II Stopping Target Region | 184 |
| 8.1 Understanding the Stopping Target Region | 184 |

| | | |
|-------------------------|--|------------|
| 8.2 | Improving the Target Design | 189 |
| 8.2.1 | Muon Stopping Rate | 190 |
| 8.2.2 | Signal Acceptance | 193 |
| 8.2.3 | Summary and Future Improvements | 193 |
| 9 | Summary | 194 |
| List of Acronyms | | 197 |
| Bibliography | | 199 |
| A | Figure Permissions | 208 |
| B | Kinematic End-point for Antiproton Production | 210 |
| B.1 | Derivation | 211 |
| C | Summary of the AlCap Experiment | 214 |
| C.1 | Introduction | 215 |
| C.2 | Run 2013: Charged Particles | 217 |
| C.2.1 | Datasets | 218 |
| C.2.2 | Preliminary Analysis | 219 |
| C.3 | Run 2015a: Neutral Particles | 222 |
| C.3.1 | Setup | 222 |
| C.3.2 | Activation Study | 223 |
| C.3.3 | Analysis | 224 |
| C.4 | Run 2015b: Charged Particles | 225 |
| C.5 | Summary | 225 |

List of figures

| | | |
|-----|---|----|
| 1.1 | One of the earliest cloud chamber photographs of a muon, taken in 1940 [2]. | 23 |
| 1.2 | The setup of the first experiment to look for photons produced during muon decay taken from [7]. | 24 |
| 1.3 | Feynman diagrams for Standard Model muon decay and neutrino oscillation-mediated μ - e gamma | 27 |
| 1.4 | Feynman diagram for the neutrinoless muon decay in the presence of an atomic nucleus— μ - e conversion—caused by neutrino oscillations. | 28 |
| 1.5 | The historic evolution of experimental upper limits on CLFV in muon channels | 29 |
| 1.6 | Feynman diagrams that produce μ - e conversion through New Physics models. | 31 |
| 1.7 | Comparison of μ - e conversion and $\mu^+ \rightarrow e^+\gamma$ | 32 |
| 2.1 | Schematic summary of the experimental and theoretical basis for a μ - e conversion search | 35 |
| 2.2 | The most intense line of the muonic atom atomic cascade, the $2p - 1s$ transition, surrounded by the peaks of the muonic-magnesium Lyman series. | 36 |
| 2.3 | The spectrum of electrons produced by muon decay-in-orbit, according to Czarnecki et al. [34]. | 38 |
| 2.4 | Selected experimental measurements of charged particle emission following muon capture, from the late 1960s to 1970s. | 40 |
| 2.5 | The SINDRUM-II experiment, which holds the current limit on μ - e conversion. | 41 |

| | | |
|------|--|----|
| 2.6 | The muon beamline and detector planned for the MECO experiment [41]. | 42 |
| 3.1 | Double differential cross section of pion production on a tantalum target from protons with 10 GeV kinetic energy. | 48 |
| 3.2 | Angular dependence of the magnitude of vertical drift in a bent solenoid field. | 50 |
| 3.3 | The effect of changing the atomic number on the lifetime, conversion energy (shown as $M_\mu - E_e$), and branching ratio | 52 |
| 3.4 | Schematic for the timing structure used in the COMET experiment. | 53 |
| 3.5 | Schematic layout of COMET Phase-I including the two detector systems that will run separately, being swapped in and out of the detector solenoid depending on the study. | 56 |
| 3.6 | The COMET Phase-II layout, schematically and from the simulation. | 57 |
| 3.7 | A summarised timeline for the COMET experiment including Phase-I and Phase-II based on the 2016 TDR [44]. | 62 |
| 3.8 | Photographs of the experiment hall being constructed and first sections of beamline being installed. | 63 |
| 3.9 | Research and development for the Straw-tube tracker and Electromagnetic Calorimeter (StrECAL) showing both the individual straws or crystal and a prototype set-up used at test beams to characterise the sub-detectors. | 64 |
| 3.10 | The CDC being assembled and strung. | 64 |
| 4.1 | Overview diagram for the ND280 framework. | 66 |
| 4.2 | Overview diagram for the ICEDUST framework. | 69 |
| 4.3 | Diagram showing the stages used to simulate COMET. | 71 |
| 4.4 | How parameters are shared amongst different components of the geometry within ICEDUST. | 73 |
| 4.5 | An example set of parameter definitions which control the geometry for the Torus2. | 74 |

| | | |
|------|---|----|
| 4.6 | Two of the possible simulation ‘worlds’ that can be selected at run-time | 75 |
| 4.7 | Fieldmap produced by Opera and G4Beamline. | 76 |
| 4.8 | The ratio of the Opera and G4Beamline fieldmap calculations shown in Fig. 4.7. | 77 |
| 4.9 | The dipole field calculations used in ICEDUST for Phase-II. | 78 |
| 4.10 | Comparison of various hadron production codes with experimental data from the HARP experiment, taken from the thesis of A. Edmonds [67]. | 79 |
| 4.11 | Comparison of the realistic spectra for decay-in-orbit (DIO) electrons, and protons coming from muon nuclear capture. | 82 |
| 4.12 | The classes involved in simulating the various processes of stopped negative muons. | 84 |
| 4.13 | The longitudinal (a) and horizontal (b) components of the beamline coordinate system for different points in the global X-Z plane. | 87 |
| 4.14 | Different flux plots that make use of the beamline coordinate system. | 88 |
| 5.1 | Change to momentum distributions at the entrance to the first 90 degrees of the bent muon beam solenoid for different target lengths. | 93 |
| 5.2 | Integrated muon and pion yields up to a certain momentum at the entrance to the first 90 degrees of the bent muon beam solenoid as a function of target length. | 94 |
| 5.3 | Change in the momentum distribution of muons and pions at the entrance to the first 90 degrees of the bent muon beam solenoid as a function of target length. | 94 |
| 5.4 | Change to momentum distributions at the entrance to the first 90 degrees of the bent muon beam solenoid for different target radii. | 95 |
| 5.5 | Integrated muon and pion yields up to a certain momentum at the entrance to the first 90 degrees of the bent muon beam solenoid as a function of target radius. | 95 |

| | |
|---|-----|
| 5.6 Change in the momentum distribution of muons and pions at the entrance to the first 90 degrees of the bent muon beam solenoid as a function of target radius. | 96 |
| 5.7 Variation in muon and pion yields as a function of target radius when the total target length is set to the optimised value of 32 cm. | 97 |
| 5.8 Comparison of the muon and pion yields per POT for Phase-I and Phase-II. | 97 |
| 5.9 Muon stopping rate as a function of the two dipole field strengths. | 99 |
| 5.10 Pion stopping rate as a function of the two dipole field strengths. | 100 |
| 5.11 The heights of electrons along the electron spectrometer that originate in the target with 105 MeV for different dipole field values. | 103 |
| 5.12 Mean height of signal electrons for different values of the dipole field strength. | 104 |
| 5.13 Survival probability for signal electrons as a function of the distance along the beamline for different values of the electron spectrometer's dipole field strengths. | 105 |
| 5.14 Geometric acceptance into the StrECAL detector as a function of the dipole field strength over the electron spectrometer. | 105 |
| 5.15 Muon stopping rate per Proton-on-Target (POT) for different target positions. | 107 |
| 5.16 The momentum dependence of the electron acceptance into the detector for different target positions. | 107 |
| 5.17 Electron acceptance into detector for different stopping target positions and with different momenta. | 108 |
| 5.18 The momentum dependence of the electron acceptance into the detector for different target positions when the beam blocker is removed. | 109 |
| 5.19 The effect of stopping target position on the height of electrons with a fixed momentum as they pass through the Electron Spectrometer. | 110 |
| 5.20 Dispersive effect of the 180° bent transport solenoid and dipole field on muons. | 112 |

| | | |
|------|---|-----|
| 5.21 | The heights of muons as they pass along the beamline. | 114 |
| 5.22 | The separation between muons that stopping and those with high enough momentum to produce background. | 115 |
| 5.23 | The effect of changing the height of the collimator in Torus1 on the particle distributions. | 116 |
| 5.24 | The number of particles reaching the end of the Torus2 solenoid relative to the number that enter the Torus1 solenoid (i.e. the survival probability) for different heights of both collimators in Torus1 and Torus2. | 117 |
| 5.25 | Contours showing 2.5 percentage point changes to the stopping and dangerous muon flux, as a function of the collimator heights. | 118 |
| 5.26 | The heights of muons as they pass along the beamline. | 119 |
| 5.27 | Location of the beam blocker and one possible geometry for the DIO blockers, both highlighted in dark green, shown here before optimisation. . | 120 |
| 5.28 | Momentum-dependent dispersion of electrons passing through the spectrometer. | 121 |
| 5.29 | Acceptance into the straw tracker for electrons with different momentum at the stopping target as a function of the beam and DIO blocker dimensions. | 122 |
| 5.30 | The impact of the beam and DIO blockers on the StrECAL hit rate and signal acceptance. | 123 |
| 6.1 | The momentum and rates of muons reaching the final beam collimator, the stopping target, and actually stopping in the target. | 127 |
| 6.2 | Projections of the final position of stopped muons in the stopping target. . | 128 |
| 6.3 | Geometric acceptance of signal events as a function of distance along the beamline. | 129 |
| 6.4 | Timing of signal electrons. | 130 |
| 6.5 | The transfer matrix for electrons originating at the target, including the geometric acceptance and energy loss. | 131 |

| | | |
|------|--|-----|
| 6.6 | The spectrum of electrons coming from DIO and μ - e conversion assuming a conversion rate of $\mathcal{R} = 3 \times 10^{-16}$ | 132 |
| 6.7 | Relative signal versus DIO background as a function of the low-momentum cut value assuming a conversion rate of $\mathcal{R} = 3 \times 10^{-16}$ and with a fixed upper threshold of 105.5 MeV/c. | 133 |
| 7.1 | The DIO background rate as a function of momentum threshold for different total running times. | 138 |
| 7.2 | Comparison of the various available DIO end-point expansions. | 139 |
| 7.3 | Observed background electrons from a simulation of 6×10^7 Radiative Muon Capture (RMC) photons. | 143 |
| 7.4 | Spectrum of photons coming from Radiative Pion Capture (RPC) [89]. . | 146 |
| 7.5 | Stopping distributions of pions in the muon stopping target. | 147 |
| 7.6 | The momentum of muons and pions for those that reach the target area and those that actually stop in the target | 147 |
| 7.7 | Digitised and smoothed spectrum of RPC from magnesium (see Fig. 7.4b) used as input to the Monte Carlo simulation. | 148 |
| 7.8 | Observation of secondary electrons coming from RPC photons in the stopping target. | 149 |
| 7.9 | Variation in the antiproton production rate as a function of incident proton energy | 152 |
| 7.10 | Experimental data for antiproton production rates for 10 GeV protons [96, 97]. | 153 |
| 7.11 | The kinematic end-point for antiproton production as a function of the outgoing antiproton direction with respect to the incoming proton in the frame of the target nucleus (the lab frame). | 155 |
| 7.12 | Piecewise fitting to experimental data and kinematic end-points for antiproton production. | 156 |
| 7.13 | The angular dependence of the rate of antiproton emission, integrated over all momenta. | 157 |

| | | |
|------|--|-----|
| 7.14 | The survival probability of antiprotons and secondaries pions per antiproton produced in the target as a function of distance along the beamline. . . | 159 |
| 7.15 | The heights of antiprotons passing along the beamline for the four different angular regions of productions. | 161 |
| 7.16 | The heights of secondary pions passing along the beamline produced from antiprotons in each of the four different angular regions of productions. . . | 162 |
| 7.17 | The arrival time of antiprotons and secondary pions at various points along the beamline | 164 |
| 7.18 | The timing and momentum of beam electrons detected at the straw tracker, and passing a plane immediately after the beam blocker. | 168 |
| 7.19 | Projections of the momentum and arrival time of beam electrons after the target and at the detector | 170 |
| 7.20 | Distributions of momenta and the transverse direction for the cosmic muon and antimuon fluxes provided by the ND280 collaboration. | 173 |
| 7.21 | Projection onto beamline coordinate system of electrons from cosmic rays with momenta greater than 100 MeV/c, from a simulation of about 170 million cosmic muons. | 174 |
| 7.22 | Momentum of electrons that hit one and two layers (planes) of the straw tracker. | 175 |
| 7.23 | Dependence of the intrinsic background rates on σ_2 , the width of the high/low momentum tail in the reconstruction distribution. | 180 |
| 8.1 | The magnitude of the magnetic field around the stopping target. | 185 |
| 8.2 | The ability for a particle to be mirrored downstream, if it is initially heading upstream at this point. | 186 |
| 8.3 | Growth in the beam envelope as a function of the distance along the beamline. | 187 |
| 8.4 | The effective signal sensitivity achieved by placing a disk of fixed radius at a given location along the beamline. | 188 |
| 8.5 | The new geometry of the stopping target, with the beam blocker removed. | 189 |

| | | |
|-----|--|-----|
| 8.6 | Projections of the muon stopping distribution with the improved target design, to be compared to Fig. 6.2. | 191 |
| 8.7 | The momentum of muons that reach the stopping target and eventually stop. | 191 |
| 8.8 | The observed momentum distribution and acceptance for signal electrons. | 192 |
| C.1 | Experimental set-up and acquired datasets from Run 2013. | 217 |
| C.2 | A close up of the $2p-1s$ transition line at around 347 keV used for the normalisation of stopped muons for the Al100 dataset. | 219 |
| C.3 | Charged particle analysis and preliminary results. | 220 |
| C.4 | Progress on analysis of the Neutron detectors. | 224 |

List of tables

| | | |
|-----|--|-----|
| 3.1 | Backgrounds for COMET Phase-I (from the 2016 TDR [44]) and Phase-II (from the 2009 CDR [45]). | 45 |
| 5.1 | Aspects of the experiment that can be optimised and estimates for the number of parameters that define each aspect. | 90 |
| 5.2 | Optimised values for the parameters studied in this chapter. Many more parameters remain to be optimised that were considered beyond the scope of the present work. | 124 |
| 6.1 | Numbers that go into estimating the total signal acceptance from this study compared to the previous evaluation in the 2009 CDR. | 134 |
| 6.2 | Parameters that determine the run time and single event sensitivity for COMET Phase-II based on this study. | 135 |
| 6.3 | Comparison between the run time and single-event sensitivity from this study and from the 2009 CDR, the Phase-I TDR, and the Mu2e experi- ment’s TDR. | 136 |
| 7.1 | The RMC end-points for several potential daughter nuclei of nuclear muon capture in ^{27}Al | 140 |
| 7.2 | Summary of experimental values of the rate of RMC producing photons with energy greater than 57 MeV, R_γ , and the observed end-point, k_{\max} , redacted from [80]. | 141 |
| 7.3 | Parameters and their values in the determination of the RPC background rate. | 150 |

| | | |
|------|--|-----|
| 7.4 | Angular regions and the source of the data used to build the momentum spectrum for that region of antiproton production phase-space. | 158 |
| 7.5 | Antiproton stopping rates and fluxes at key points along the muon beamline | 163 |
| 7.6 | Secondary pion fluxes from antiprotons observed at key points along the beamline. | 163 |
| 7.7 | Final estimated antiproton-induced background rates. | 165 |
| 7.8 | Parameters and their values in the determination of the background rate due to high-energy particles in the beam. | 171 |
| 7.9 | Parameters and their values for the determination of the cosmic ray background rate. | 175 |
| 7.10 | Overall predicted background rates and events | 177 |
| 8.1 | Parameters of the target disks used in the proof of principle simulation. . | 190 |
| C.1 | Datasets acquired during R2015a | 223 |

“I find it so pretentious when a thesis starts with a quote.”
— Yoshi Uchida

Chapter 1

The History and Theory of Charged Lepton Flavour Violation (CLFV)

“Who ordered that?”

— The author, upon presentation of ‘ika-no-ikizukuri’ (live squid sashimi) at a collaboration meeting in Fukuoka, Kyushu Island

1.1 The Muon and the Birth of the Standard Model

In 1897, the British physicist Thomson discovered the first sub-atomic particle: the electron. Over the next 30 years or so, the supposedly indivisible object of the atom was further divided multiple times, giving way to the neutron, and the proton. Far from the simple, solid sphere previously assumed, the atom had become a dynamic object, with a cloud of negative electrons bound to a positive nucleus consisting of neutrons and protons.

That the electrons were bound to the nucleus was readily understood due to their opposite electric charges, but the nucleus itself posed two bigger problems. Firstly, some nuclei had been observed to emit ‘beta-rays’ and change a proton to a neutron in the process (beta-rays are now known to be electrons or their antiparticle, positrons). Secondly, the nucleus consisting of only neutral and positive particles posed a problem, since the positive charges should repel one another. In both cases, something new was needed.

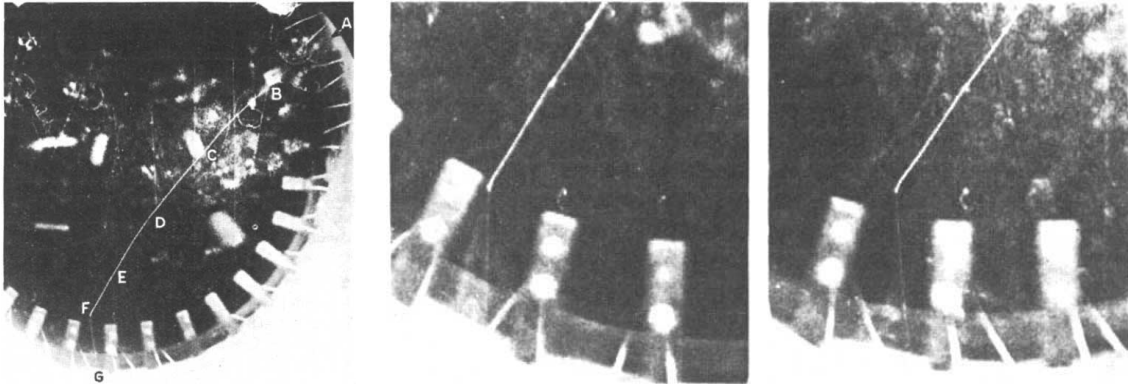


Figure 1.1: One of the earliest cloud chamber photographs of a muon, taken in 1940 [2]. In the left-most image the muon enters the chamber at point A and travels to point F, where it eventually decays to an electron which can be seen faintly leaving the image at point G. The images to the right are a stereoscopic zoom in on point F, showing the relatively slow and more ionising muon and the faster, less ionising electron.

In 1935, Yukawa—a physicist from Japan, where this thesis will often return—proposed a solution to the second challenge. He suggested that, as for the electromagnetic force binding electrons to the nucleus via the exchange of some carrier particle (the photon), an exchanged particle could explain the very strong force that helped to glue the protons and neutrons together. Unlike the photon, though, this particle would have to be massive and readily absorbed by the protons and neutrons. Yukawa was even able to predict the mass of this particle via the uncertainty principle, finding it to be around 100 MeV [1].

Then, in 1937, a particle with a mass very close to this prediction was observed in cosmic ray events by several physicists in Japan [3] and the US [4, 5]. But the initial hopes that this was indeed the Yukawa particle faded quickly as it easily penetrated through the matter of the detectors, whilst Yukawa’s particle should be rapidly absorbed. So unexpected was this new particle with its mass in between that of an electron and a proton and its relatively long lifetime, that Rabi was forced to ask, “Who ordered that?”. It took some time, but eventually this particle became known as the muon.

The muon was interesting because it seemed to interact very weakly with matter, and because it seemed only to decay to an electron, as first observed in 1940 [2] and shown in Fig. 1.1. For this to happen, something else has to be emitted in order to conserve momentum and energy, given that the electron is about 207 times lighter than the muon. There were two obvious possibilities for the ‘something else’ [6]: a photon, or a pair of particles that were known as neutrinos.

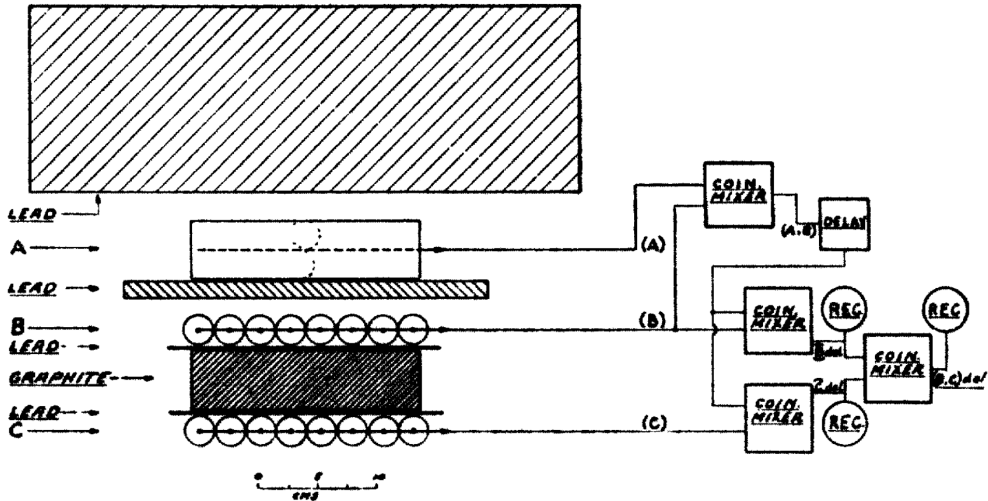


Figure 1.2: The setup of the first experiment to look for photons produced during muon decay taken from [7]. Cosmic muons arrived from the top, slowing down in the big block of lead, triggering two Geiger-Muller counters (A and B) as they passed and eventually coming to stop in the graphite. From there, electrons and any potential photons would be detected in the counters above and below the graphite (B and C). No photons were seen in coincidence with an electron from muon decay, which lead theorists to hypothesise two distinct neutrino flavours.

Neutrinos were originally proposed to solve the first issue of nuclear beta-decay. When a proton inside a nucleus becomes a neutron (or vice versa), an electron (or positron) is emitted. The difference in the mass between the original and final nuclei has a fixed value, and yet electrons were observed with a range of energies all less than the value of this difference. The neutrino was proposed as a solution: a massless particle was carrying away the missing energy and had the additional property of interacting only very weakly making it nearly impossible to detect. By studying the spin of the parent and daughter nuclei it was also realised that the neutrino had spin of $\hbar/2$.

Muon decay was similar to this, in that the electron appeared with less energy than was available to it. On the other hand, it was clear from the spectrum of emitted electrons that not one, but two neutrinos were being emitted. Being spin-half particles, either the neutrino was its own anti-particle, or one would be a neutrino and the other an anti-neutrino. Either way, having two neutrinos emitted posed its own challenge since the two neutrinos would be able to annihilate with one another, and muon decay to a photon and electron would become comparably large. Searches for a muon decaying to a photon and electron were performed starting with the experiment of Hincks and Pontecorvo [7], shown in Fig. 1.2. Since these experiments came back empty-handed, it

was concluded that something else, something new, had to be introduced to distinguish one neutrino from the other, such that they were unable to annihilate.

This something became known as ‘lepton flavour’. One neutrino carried away the ‘flavour’ of the muon, the other cancelled out the ‘flavour’ of the electron, so that if one started with a muon, one finished with either a muon or a muon-neutrino. Similarly, since muon decay starts with no electrons one must finish with no electron flavour, achieved by having an electron and electron-antineutrino simultaneously produced. Nowadays, this is known as Lepton Flavour Conservation and was cemented into theory when muon-neutrinos were identified in an experiment at Brookhaven in 1962 [8]. This experiment produced a beam of neutrinos by the decay of pions (the modern name for Yukawa’s particle) to a muon. If Lepton Flavour Conservation was correct, the neutrinos produced in this decay would all have muon flavour, and would only produce muons when detected. If the concept was incorrect, however, both electrons and muons would be observed. Since no electrons were seen, Lepton Flavour had to be conserved.

Thus, not only had the discovery of the muon been the discovery of a new charged particle, but it was also responsible for a new type of neutrino, and a new law of conservation!

Yet this conservation law is tough to motivate theoretically. Noether’s theorem tells us that for every system with a continuous symmetry, some quantity will remain conserved. This is the rule that gives us conservation of momentum, energy, and angular momentum (the conserved properties) in systems that are the same regardless of their place, time, or direction (the continuous symmetries). An extension of this theorem applies for local transformations of the system’s ‘gauge’, which is any property that when changed has no impact on the physics outcome, such as the absolute value of the ground in an electric circuit. In particle physics, this extension gives rise to the various particle charges, such as the electromagnetic charge caused by the $U(1)$, or simple phase, of a particle’s wavefunction, and the hypercharges of the $SU(2)$ and $SU(3)$ symmetry groups of the weak and strong (colour) forces. In the case of the conservation of lepton flavour however, no such symmetry exists. Instead, this conservation is embedded into the Standard Model (SM) of particle physics through the electroweak theory and lepton universality.

In addition to the leptons and their interactions via the electroweak forces, the SM describes the quark sector and their interactions via Quantum Chromodynamics (QCD). Quarks are the particles that make up the neutrons and protons (not only have we divided the atom, but also its constituents) and even the pion, Yukawa’s predicted particle that

was discovered in 1947. Built around the frameworks of local gauge invariance, quantum field theory, and spontaneous symmetry breaking, the SM has been one of the most rigorously tested theories, and with only a few exceptions has held up incredibly well to measurements so far.

1.2 Neutrino Oscillations Break Lepton Flavour Conservation

Around the same time that the muon neutrino was discovered, work was already underway that would start to put holes in Lepton Flavour Conservation. In 1968, Raymond Davis Jr. and his group at Brookhaven measured the number of electron neutrinos coming from the Sun and found there to be about one third of what was expected [9]. This puzzle remained until it was solved by experiments in Canada and Japan in the early 2000s: the neutrinos were being produced in the expected quantity, but as they propagated through the mass of the Sun and the distance from there to Earth, they changed their flavour! Nowadays, experiments in Japan and the US, such as the T2K [10] and NO ν A [11] experiments, produce beams of muon neutrinos, yet see most disappear, having changed to tau neutrinos, and a tiny fraction that appear with electron flavour.

Explaining this requires that neutrinos have mass, although far less than any other of the particles in the SM. Not only that, but the neutrino states with definite mass are not the same as the flavour states in which neutrinos are created. A particle's propagation depends on its energy and its mass. Since a neutrino is created in a flavour eigenstate, which is an admixture of the three mass eigenstates and, since each mass eigenstate propagates differently, the overlap with a given flavour eigenstate changes as a neutrino propagates. The effect is an oscillation, where the probability of detecting a neutrino in a given flavour state depends periodically on how far it has travelled and its energy.

As it was for the discovery of the muon, the discovery of the non-zero value of the neutrino mass and the oscillation between neutrino flavour states has opened a whole host of new questions. How does the neutrino acquire its mass? Why is the mass scale so much smaller than any other known particle? As the only chargeless, massive fermions in the SM, what is the nature of this mass? Is it produced via an interaction with the Higgs or via a Majorana mechanism, in turn making the neutrino into its own antiparticle? Is it a combination of these mechanisms?

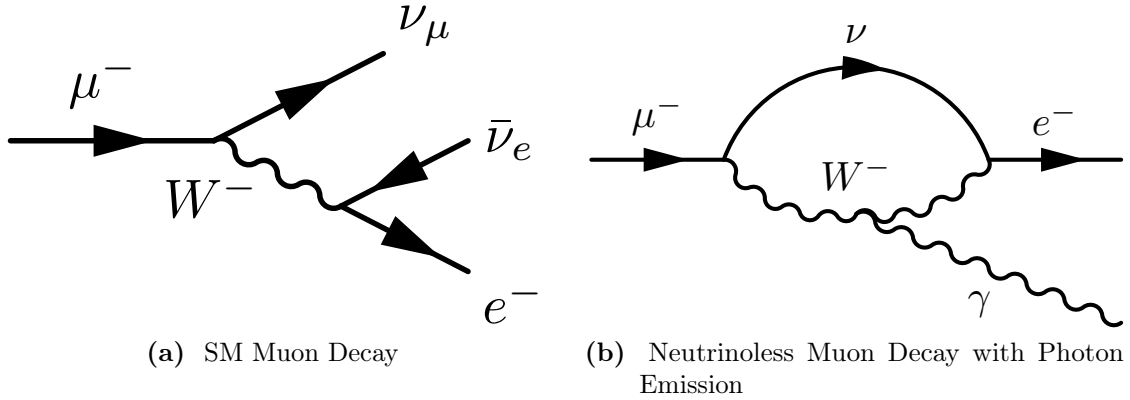


Figure 1.3: The outgoing neutrinos produced in the SM decay (a) can be made into an internal neutrino propagator (b) via neutrino oscillations, whilst the addition of a photon ensures conservation the 4-momentum. Although allowed in the SM with neutrino oscillations, the actual rate from such a diagram is well below present experiment sensitivities. A similar diagram was envisaged to show that the lack of observation of $\mu^\pm \rightarrow e^\pm \gamma$ implied distinct neutrino flavours.

Either way, it is clear that the neutrinos themselves do not conserve lepton flavour, and this immediately makes it possible that the charged leptons—the electron, the muon, and the tau—also break Lepton Flavour Conservation. How neutrinos can cause this is demonstrated in Fig. 1.3b, where the muon neutrino annihilates with the electron neutrino whilst energy and momentum are conserved by the emitted photon. We can nowadays calculate the rate for such a diagram and find it to be heavily suppressed:

$$\mathcal{BR}(\mu \rightarrow e\gamma) \propto \left| \sum_i U_{\mu i}^* U_{ei} \frac{M_{\nu_i}^2}{M_W^2} \right|^2 < 10^{-54}, \quad (1.1)$$

where $U_{\alpha i}$ is an element of the mass-mixing matrix transforming the α flavour state to the i -th mass state with mass M_{ν_i} (the Pontecorvo-Maki-Nakagawa-Sakata (PMNS) matrix), and M_W is the mass of the W -boson. This rate can be considered doubly suppressed: the summation over the different mass eigenstates produces a GIM suppression, whilst the mass imbalance between the neutrinos and the W -boson suppresses this further.

Emission of a photon is not the only additional muon decay process made possible by neutrino oscillations. A negative muon that has become bound to the nucleus of an atom (discussed further in chapter 2) will also be able to convert to an electron without emitting neutrinos, via the diagrams shown in Fig. 1.4. In this case, however, the rate calculation is complicated by the quark and gluon contents of the nucleus, form factors of

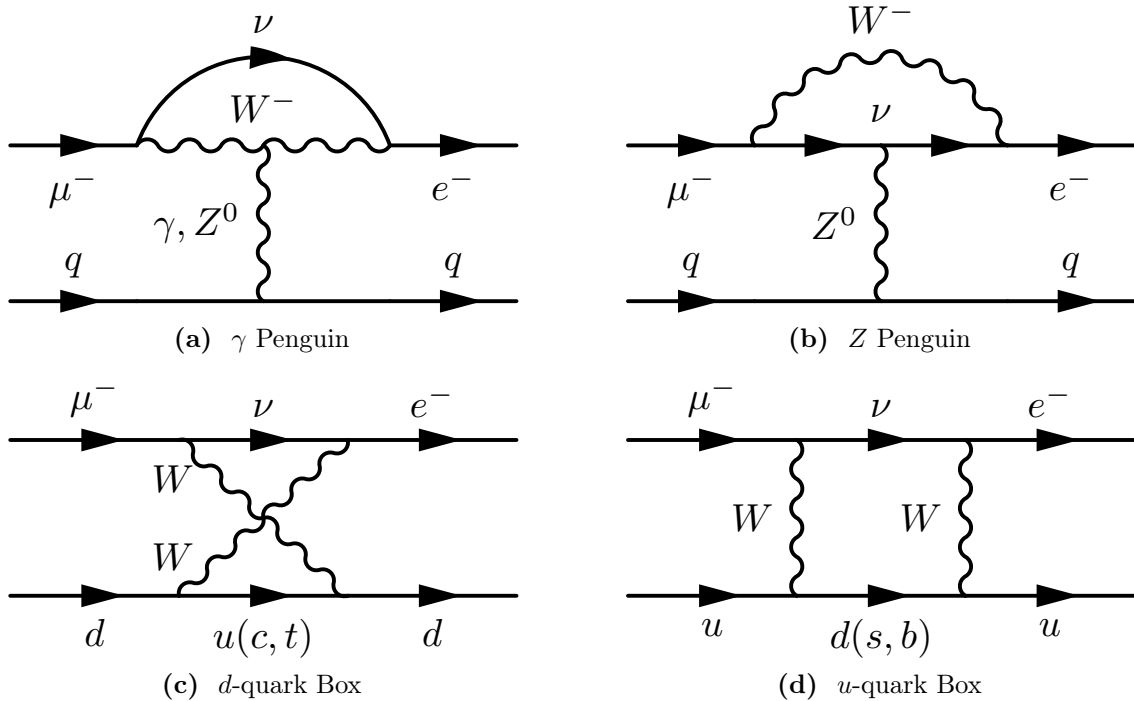


Figure 1.4: Feynman diagram for the neutrinoless muon decay in the presence of an atomic nucleus— μ - e conversion—caused by neutrino oscillations. Compared to $\mu^\pm \rightarrow e^\pm \gamma$ there are now four possible diagrams, so that the rate depends on the nucleus and picks up interference terms.

the quarks and gluons in the nucleons and nucleons in the nucleus, and the interference that can occur between each diagram.

1.3 In Search of Charged Lepton Flavour Violation (CLFV)

1.3.1 Motivations and Status

Searches for Lepton Flavour Violation (LFV) go back right to the discovery of the muon, but that is not to say that they ended there. Over the past eighty years or so, experiments have continued to push the limits on such processes down through around 13 orders of magnitude, as shown in Fig. 1.5. Whilst the original experiments relied on cosmic muons, modern experiments use accelerators to produce intense beams of muons and can even produce large quantities of tau leptons at the large colliders.

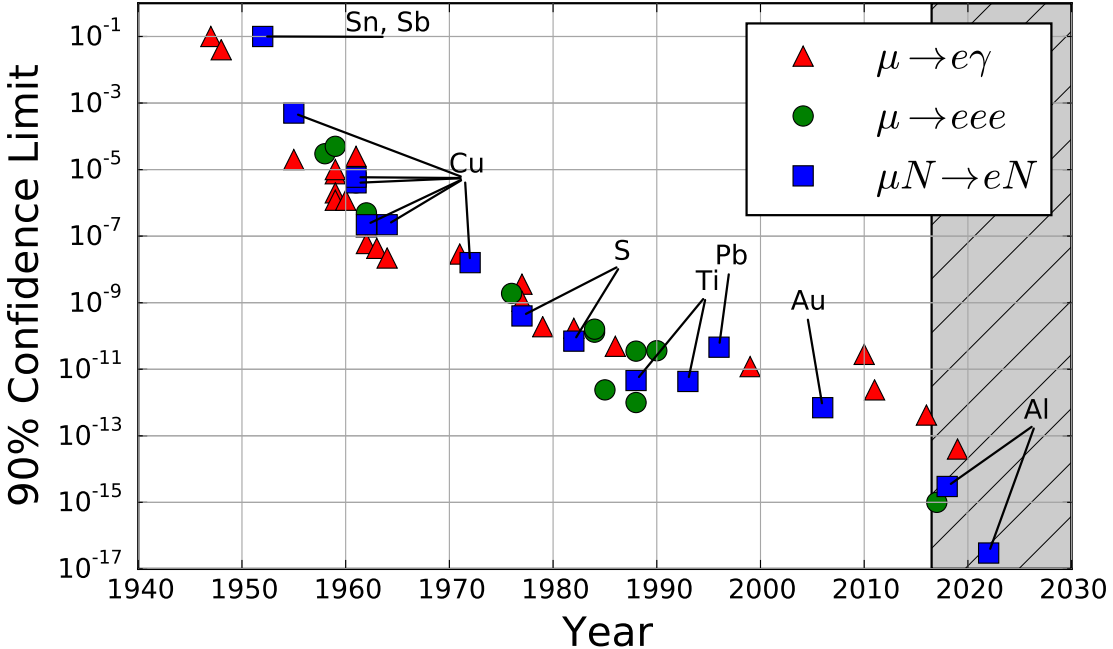


Figure 1.5: The experimental limits on CLFV in muon channels has been reduced by some 13 orders of magnitude since the first search in 1947. Each improvement in the limit is primarily due to the increasing intensity of the muon source: cosmic muons were used around 1950; accelerator-produced muons followed; surface muon sources further increased the intensity; and nowadays superconducting solenoids will capture and focus the resulting muon beam. The shaded grey region shows measurements that are currently under preparation. Data until 2015 is taken from the summary tables from [12].

Of the searches involving muon decays the three most searched for modes have been $\mu^\pm \rightarrow e^\pm \gamma$ ('mu to e gamma'), $\mu^- N \rightarrow e^- N$ ('mu e conversion'), and $\mu^+ \rightarrow e^+ e^- e^+$ ('mu to three e'). From an experimental perspective these modes are attractive since the Lepton Flavour Conserving-counterparts all have neutrinos in the final state, and since these neutrinos are massless they typically carry away around half the available energy. By removing the neutrinos from the final state, then, a clear separation between the signal and the Standard Model version appears.

The SM nowadays faces many other difficulties beyond neutrino masses such as dark matter and energy, the stability of the vacuum, and the unification of gravity, the electroweak force, and QCD. A vast number of extensions to the SM try to address these issues. The assumption that New Physics introduces no additional flavour changing is often referred to as Minimal Flavour Violation, and used to reduce the number of parameters contained in Beyond the Standard Model (BSM) theories, but just how valid

is such an assumption? As an accidental symmetry in the SM, whether or not these extensions produce CLFV is very difficult to constrain by some theoretical reasoning, and must instead be directly measured.

Whilst neutrino oscillations can, themselves, directly produce CLFV, searches for CLFV processes are important in constraining many of the New Physics models proposed to answer the questions raised by the small, non-zero neutrino masses. Models such as type-I and type-II see-saw mechanisms provide significant enhancement to CLFV rates [13]. If heavy neutrinos exist they can remove both the GIM suppression and the mass imbalance that cause the rates from the SM with neutrino oscillation to be so small.

A number of recent anomalies, in particular with muon measurements, hint at CLFV. The experimentally measured value of $g - 2$ of the muon has disagreed with the theoretical prediction by around 3σ for one and a half decades, even widening as the theoretical prediction has been improved [14, 15]. At the same time, measurements of the proton radius using the hyperfine structure of muonic hydrogen has shown a 7σ discrepancy [16] compared to other methods. Both of these could be explained by interactions of the muon with some new physics, typically a new vector boson [17, 18], and can be invoked to directly produce CLFV [19].

In addition, a number of collider-based measurements have turned up anomalies. The LHCb experiment, studying the branching fraction ratio, R_K , of $B^+ \rightarrow K^+ l^+ l^-$ with $l = \mu, e$, have found a deviation of about 2.6σ favouring the di-electron decay [20]. At the same time, the ratio for the decay $B^0 \rightarrow D^{*+} l^- \bar{\nu}_l$ where $l = \mu, \tau$, $R(D^*)$, has been found to disagree with the SM, at each of the LHCb [21], Belle [22] and Babar [23] experiments, with a combined discrepancy of around 3.9σ [24]. At CMS an excess in $h \rightarrow \tau\mu$ decays during Run-1 of the LHC [25] was observed with a significance of 2.4σ , although analysis of Run-II has not seen this [26]. Although many of these discrepancies directly only require lepton non-universality, this can be shown to imply CLFV in many cases [27].

Finally, for cosmological purposes CLFV has an importance for the Baryon Asymmetry of the Universe that we observe. Many models generate this asymmetry in the early universe via leptonic CP-violation. However, it has been shown that if CLFV processes occur at the present limits, the Baryon Asymmetry generated by these means can be washed out [28].

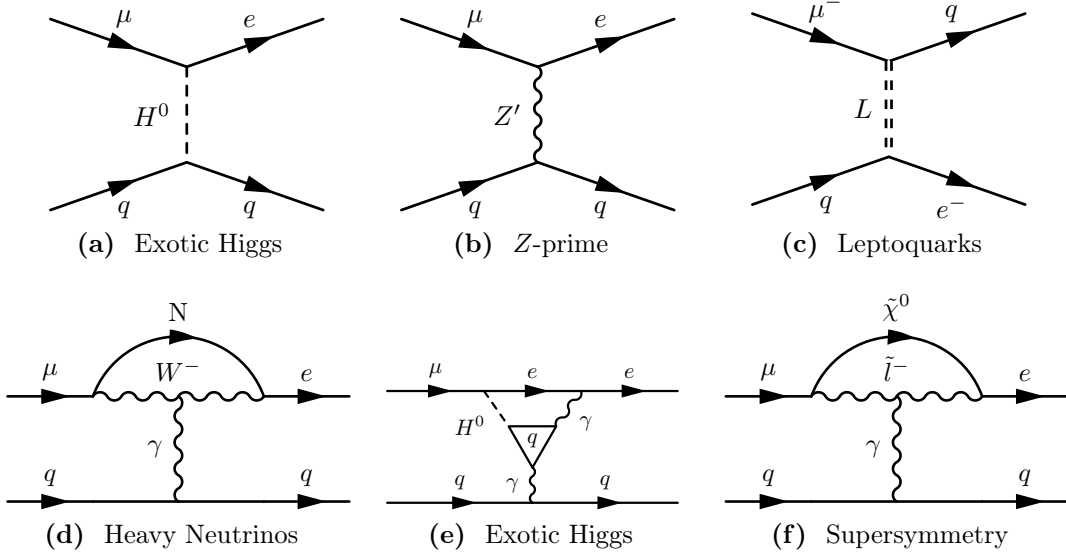


Figure 1.6: Feynman diagrams that produce μ - e conversion through New Physics models. The upper three diagrams ((a) to (c)) all connect to the nucleus via some massive exchange particle, whereas the lower three diagrams ((d) to (f)) all connect via an exchanged photon. In addition to interactions with the quarks, since μ - e conversion interacts with the whole nucleus, there are also models where the interaction involves external gluon lines.

1.3.2 Muon CLFV Channels

Fig. 1.6 shows a variety of Feynman diagrams for μ - e conversion involving new particles and couplings predicted by many BSM theories. The large variety of models to which μ - e conversion would be sensitive makes this a particularly attractive search channel for New Physics [29].

It can also be seen how complementary the different muon CLFV channels will be. In the case of leptoquarks for example, shown in Fig. 1.6c, one can expect μ - e conversion to take place at tree level, whilst generating a signal in a $\mu^+ \rightarrow e^+ e^- e^+$ experiment can only occur via loop diagrams. Similarly, the relative sensitivities between $\mu^+ \rightarrow e^+ \gamma$ searches and μ - e conversion searches can be used to pin down what the New Physics is in the case of a positive observation, or heavily constrain numerous different models in the case of a null measurement. This is apparent from the fact that New Physics can be classed as photonic (such as the lower three diagrams in Fig. 1.6) or as a four-Fermi contact interaction (as in the upper three diagrams in Fig. 1.6). The new physics, which ‘switches on’ at some new mass scale, is integrated away to leave an effective, low-energy field theory.

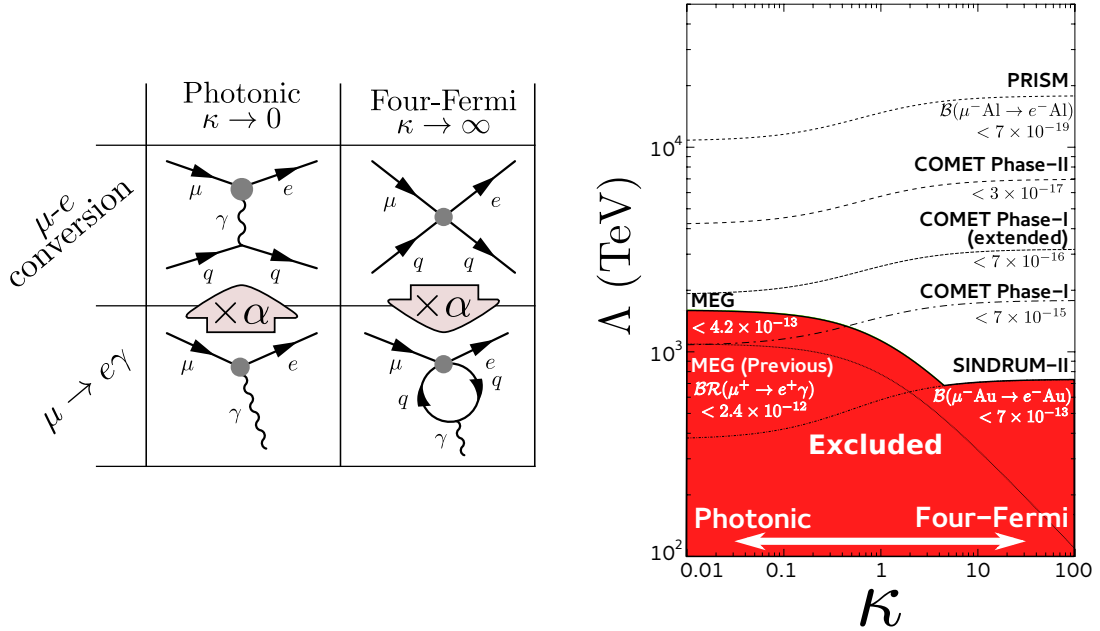


Figure 1.7: Searches for μ - e conversion and $\mu^+ \rightarrow e^+ \gamma$ have relative sensitivities that depend on the underlying physics, making the two channels highly complementary. As shown on the left, New Physics can produce a signal in both channels, but one channel or the other can be comparatively suppressed due to the need to include extra vertices and loops. The plot on the right is adapted from [30], based on [31], and shows the relative sensitivity for the toy lagrangian of equation (1.2) as a function of κ , how non-photonic the New Physics is, and Λ , the mass scale assuming coupling strengths of unity.

By constructing a toy Lagrangian consisting of two new interaction terms, one being photonic and the other a contact term, it is possible to study the relative sensitivities of μ - e conversion and μ - e gamma searches. The interaction terms in such a Lagrangian would look like:

$$L = \frac{1}{\kappa + 1} \frac{m_\mu}{\Lambda^2} (\bar{\mu}_R \sigma^{\mu\nu} e_L F_{\mu\nu}) + \frac{\kappa}{\kappa + 1} \frac{1}{\Lambda^2} (\bar{\mu}_L \gamma^\mu e_L) (\bar{q}_L \gamma_\mu q_L) \quad (1.2)$$

where κ is a dimensionless parameter that determines to what degree the new physics appears photonic ($\kappa \rightarrow 0$) or four-Fermi-like ($\kappa \rightarrow \infty$).

If the underlying new physics is photonic in nature, then one can expect a direct search for μ - e gamma to be more sensitive: coupling the photon to the nucleus of an atom will pick up an extra factor of α , reducing the μ - e conversion rate by about two orders of magnitude. On the other hand, if the new physics favours interacting directly with the nucleus, as a four-Fermi contact term, then μ - e conversion would be more sensitive. In

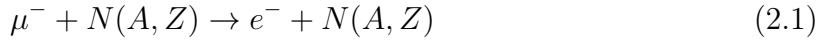
this case, producing an outgoing photon would still be possible, but would require the quark lines to reconnect, suppressing this by a factor of α and various loop factors. All of this is pulled together in Fig. 1.7, where the relative sensitivities of the most recent $\mu^+ \rightarrow e^+\gamma$ search and several $\mu\text{-}e$ conversion experiments is shown. From this it can also be seen that the mass scales that can be probed are several orders of magnitude greater than can be reached in direct searches, such as at the LHC or B-factories.

Experiments that search for CLFV with intense muon beams, therefore, make for highly sensitive tests of New Physics, which together can provide answers to some of the fundamental challenges facing the Standard Model of particle physics. Of the three most searched-for exotic muon decay modes, $\mu\text{-}e$ conversion maintains high sensitivity in nearly all generic extensions to the Standard Model.

Chapter 2

Muon-to-Electron Conversion and the Muonic Atom

Muon-to-electron conversion is the spontaneous decay of a muon to an electron within the Coulomb potential of an atomic nucleus and without the emission of neutrinos. It proceeds according to the formula:



In general, the nucleus involved can be excited under μ - e conversion, although all experimental searches to date have required that the nucleus be left unchanged. This constraint has two effects: firstly, coherent terms in the μ - e conversion cross section dominate, since the interaction will largely take place with the whole nucleus. Being coherent, the rate of μ - e conversion will, in general, grow more quickly as a function of the atomic mass or number (though exactly which of these determines the rate is itself model dependent). Secondly, the constraint of an unchanged nucleus means that all the free energy of the initial muon has to go into the kinetic energy of the electron and the recoil of the nucleus. Since the initial system is at rest, and as a two body decay, the energy of the outgoing electron is fixed:

$$E_e = M_\mu - E_{\mu, \text{binding}} - E_{\text{recoil}} \quad (2.2)$$

where $M_\mu = 105.66 \text{ MeV}/c^2$ is the muon mass, $E_{\mu, \text{binding}}$ the binding energy of the muon in the ground state of the muonic atom, and E_{recoil} is the kinetic energy of the recoiling nucleus. In the aluminium target used for COMET (see section 3.3.3) the electron energy

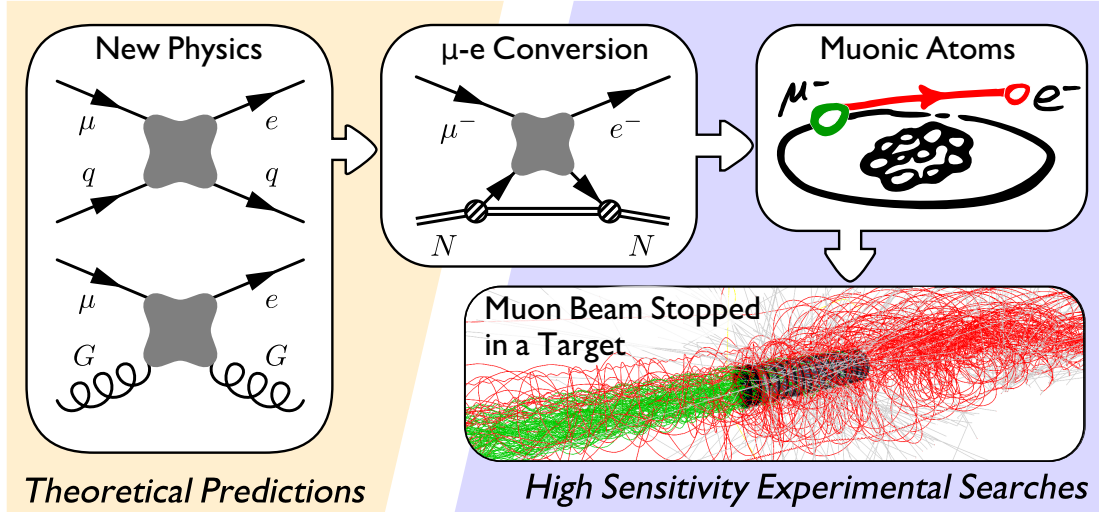


Figure 2.1: A New Physics model, introducing CLFV, generates μ - e conversion when connected to a nucleus. Observing this requires many muonic atoms be formed and so μ - e conversion experiments progress by stopping an intense muon beam in a target and looking for electrons leaving with a specific energy.

is $E_e = 104.97$ MeV. The simplicity and model independence of the signal—a single, monoenergetic electron—makes the process experimentally very attractive.

Fig. 2.1 illustrates how μ - e conversion is searched for. A New Physics model, which is capable of generating CLFV against a quark or gluon, makes a prediction for coherent μ - e conversion against a nucleus. To observe this, muonic atoms are formed with the muon in the ground state. An interaction between the muon and the nucleus causes Lepton Flavour Violation, producing an electron. In order to form many muonic atoms, an intense beam of negative muons is stopped in a target and any resulting electrons then detected.

When muons in the beam enter the target—typically a series of thin disks—they initially lose energy predominantly through ionisation. Once negative muons reach energies of a few keV they become atomically bound to the Coulomb potential of the nucleus. From here, on the order of 100 fs, these muons will undergo Auger and radiative transitions to the ground state. The X-rays emitted during this electromagnetic cascade have well defined energies and intensities and can therefore be detected as a means to evaluate the number of muons stopped in the target. Fig. 2.2 shows the most intense transition peak, $2p-1s$ in the X-ray spectrum for muonic aluminium, and the muonic magnesium lines that occur with similar energies.

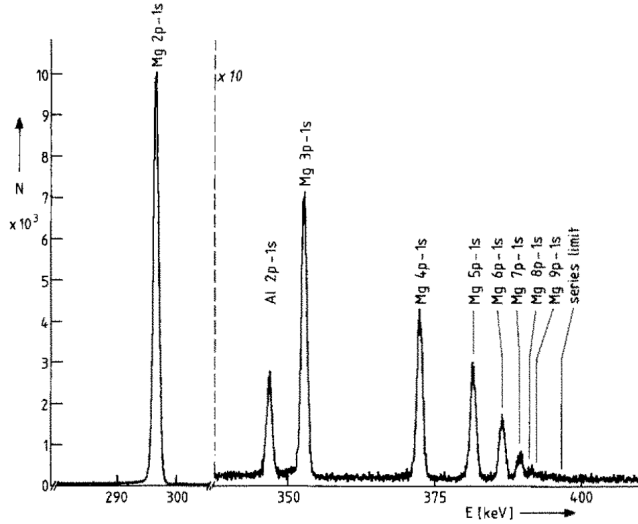


Figure 2.2: The most intense line of the muonic atom atomic cascade, the $2p - 1s$ transition, surrounded by the peaks of the muonic-magnesium Lyman series. Reproduced from [32].

From the ground state there are two processes that can occur to the bound muon in the Standard Model (SM): decay-in-orbit (DIO) and nuclear capture. DIO is the normal decay of a muon with neutrino emission, although the spectrum of the emitted electron is modified compared to the free muon decay due to the presence of the nucleus, as is discussed in more depth below. On the other hand, nuclear capture of the muon occurs when the muon is absorbed into the nucleus, decreasing the atomic number by a single unit in analogue to nuclear electron capture or inverse beta decay. A single muon-neutrino is emitted as well as various possible gamma-rays and hadrons, since the daughter nucleus is often unstable.

Both of these are important in μ - e conversion searches, since they impose various experimental constraints. Furthermore, these two processes determine the lifetime of the bound muon, which is not the same as the free muon. In the case of decay, being bound to the nucleus reduces the available energy, therefore reducing the available phase-space for the resultant electron and neutrinos. In addition, a time-dilation effect occurs since the bound muon is never truly at rest. As a result, the partial lifetime of muon decay increases in the bound muon system compared to the free muon, and this increase grows with the atomic number as the muon binds more tightly to the nucleus. However, whilst the rate of decay decreases with atomic number, the rate of muon capture increases. This occurs, firstly, because there are more protons against which to capture and, secondly, because the overlap between the muon wavefunction and the nucleus increases. For atomic

numbers larger than $Z = 30$ this effect begins to saturate since the muon wavefunction becomes contained almost completely within the nucleus. Whilst for light elements, up to around $Z = 12$, the decay process is more frequent, for the rest of the periodic table the capture process dominates. For an aluminium target, the two processes are comparatively similar, with branching ratios of 61 and 39% for capture and decay respectively, giving the muon a lifetime of 864 ns¹ [33].

Since the muon is more than 200 times heavier than the electron, the muon wavefunction feels the effect of the nucleus a lot more, creating some theoretical uncertainty on the initial muon wavefunction. Rather than the full branching ratio, typically μ - e conversion experiments discuss the conversion rate, which is given by:

$$\mathcal{C.R.} = \frac{\Gamma(\mu\text{-}e \text{ conversion})}{\Gamma(\text{nuclear capture})} \quad (2.3)$$

which reduces the theoretical uncertainty introduced from the initial wavefunction.

Based on this, one defines the Single-Event Sensitivity (SES) to be:

$$\text{S.E.S}(\mu^- N \rightarrow e^- N) = \frac{1}{N_\mu \mathcal{B}_{\text{capture}} A_{\mu \rightarrow e}} \quad (2.4)$$

where N_μ is the number of muons stopped, $\mathcal{B}_{\text{capture}}$ is the branching ratio for muon nuclear capture, and $A_{\mu \rightarrow e}$ is the total acceptance of electrons coming from μ - e conversion.

2.1 Muon Decay in Orbit

In free muon decay the maximum energy for the outgoing electron occurs when the neutrinos recoil back-to-back with the electron. In this configuration, exactly half the energy released in the decay is available to the electron, so that the maximum energy of an electron coming from the decay of a free and stationary muon is: $\max(E_e^{\text{free}}) = m_\mu/2 = 52.83 \text{ MeV}$.

The end-point configuration is altered significantly once the muon becomes bound to the nucleus of an atom. Once bound, the neutrinos can be arranged back-to-back with one another, and thus carry away a negligible amount of energy. Four-momentum can still be conserved however, since the nucleus of the atom recoils against the electron.

¹ This is very important to the COMET experiment and so we revisit this aspect in the next chapter.

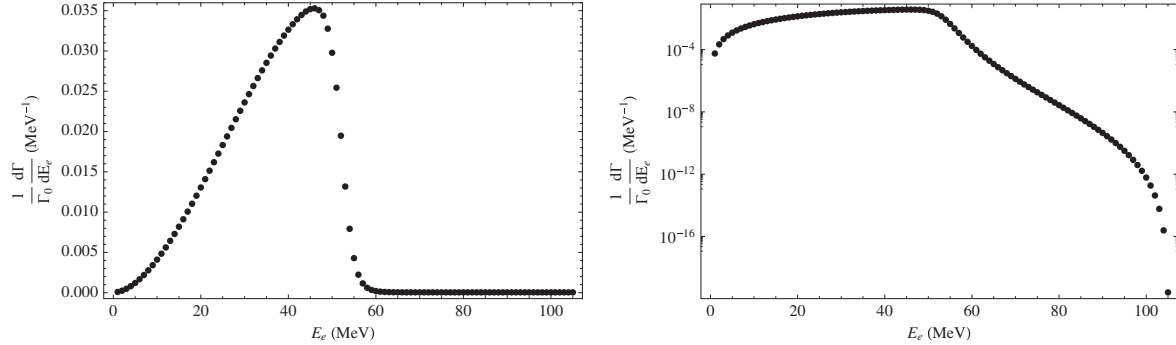


Figure 2.3: The spectrum of electrons produced by muon decay-in-orbit, according to Czarnecki et al. [34]. The two plots show the same data, but left is on a linear-linear scale whilst the right plot is on a log-lin scale which shows clearly the high-energy tail reaching up to the μ - e conversion signal energy of 104.97 MeV.

Given the enormous mass of any nucleus compared to the electron, conservation of momentum is possible for small kinetic energies of the nucleus and thus the maximum electron energy is hugely increased compared to the free decay. In fact, in the limit where the neutrinos carry away no energy, the kinematic configuration of this decay becomes identical to that of μ - e conversion, but for the mass of the neutrinos², and accordingly: $\max(E_e^{\text{DIO}}) \simeq E_e^{\text{conversion}}$.

The spectrum of electrons from DIO in aluminium is shown in Fig. 2.3. It can be seen how the peak electron energy is close to the free muon decay end-point, and in reality about 99% of DIO electrons will be emitted below 58 MeV. Whilst the end-point for the spectrum is indeed around 104.97 MeV, it is clear how suppressed this part of the spectrum is—being some twenty orders of magnitude less likely than at the peak energy. Achieving the end-point energy requires radiative connections between the nucleus and either the incoming muon, intermediate W -boson, or the outgoing electron; the low value of the neutrino momenta brings about a helicity suppression; and the specific energies of all particles implies a small phase-space volume for the decay products.

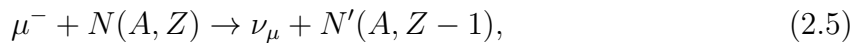
Given the enormous suppression at the end-point, μ - e conversion searches historically described themselves as ‘background free’. However, at the projected sensitivities of modern experiments, the DIO rate close to the end-point of the spectrum is now at an appreciable level. Indeed, the next generation of searches (and COMET Phase-I

² It would be interesting whether precise observations at the DIO end-point would be sensitive to the effective neutrino masses, $\langle M_{\bar{\nu}_e} \rangle + \langle M_{\nu_\mu} \rangle$. The current limits of less than 1 eV mean a direct measurement of the end-point is not realistic, but if the shape of the spectrum contained information then this might be exploitable. Certainly, massive sterile neutrinos could be searched for as a kink or shoulder at the DIO end-point with sensitivity to masses down to a few MeV.

in particular) will be the first to measure the DIO spectrum above 90 MeV, itself an important cross-check for the theoretical prediction of muon DIO³.

2.2 Muon Nuclear Capture

The nuclear capture of negative muons proceeds by the equation:



and as an incoherent process, one would expect direct capture of the muon against a proton to result in a prompt neutron being emitted. However, prompt protons can also be produced if the capture takes place between a nucleon cluster and the muon. The typical nuclear excitation from such a process is around 50 MeV, with the remainder of the total incoming energy lost to the outgoing neutrino and nuclear recoil. Even if prompt neutrons and protons are produced, the remnant nucleus is often left in an excited, unstable state, such that during de-excitation other particles can also be emitted. These include gamma-rays, deuterons, triton, and alpha particles as well as additional neutrons and protons.

From the perspective of a sensitive μ - e conversion experiment, the emission products following nuclear capture can be dangerous since, in the case of charged particles, they can swamp the detector if left unchecked. Similarly, neutrons and gamma rays produced by nuclear capture can damage electronics systems. As such it is important to understand the rates at which these particles are emitted following nuclear capture of the muon.

However, due to the nuclear environment theoretical predictions of the rates and energy distributions of capture products are extremely complex, and experimental measurements are necessary. Furthermore, in the case of aluminium—the target choice for COMET—the existing experimental data is not extensive. Fig. 2.4 shows a summary of the available

³In addition to neutrino mass and sterile neutrino searches, the precision measurement of the end-point of the DIO spectrum would seem (to the author) an interesting aspect for theoretical physicists given its connection to the anomalies of the muon g-2 and the proton radius puzzle. The end-point calculation requires radiative corrections, which would likely be sensitive to vacuum corrections in a similar way to these other measurements. If, at COMET Phase-I, we observe any deviation in this region, even if it does not look like μ - e conversion, this could provide additional evidence for lepton non-universality. In contrast, if we observe no deviation, might this be translated into limits on New Physics models that explain the other anomalies?

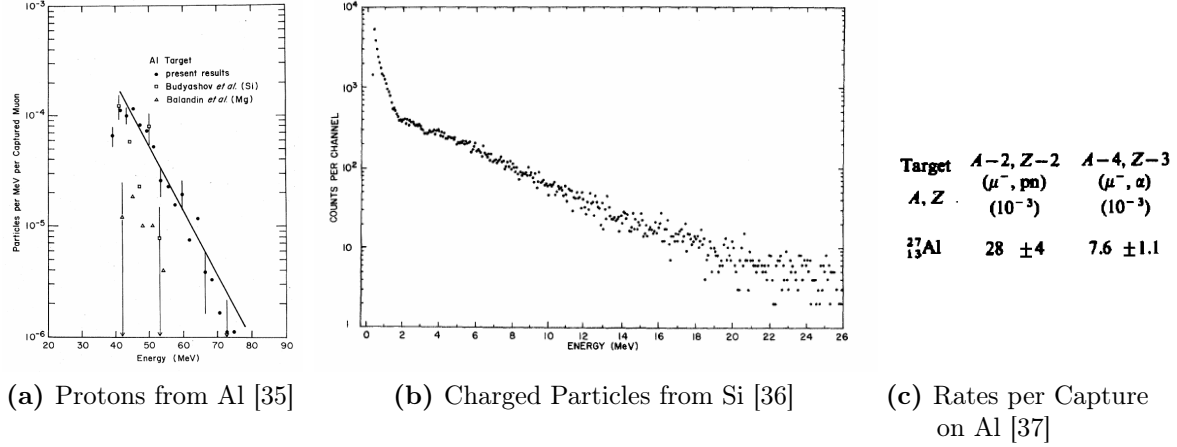


Figure 2.4: Selected experimental measurements of charged particle emission following muon capture, from the late 1960s to 1970s. (a) Protons produced with 40 MeV energy or greater following μ^- capture on aluminium [35]. (b) Inclusive charged particle emission at low energies from silicon [36]. (c) Branching Ratio per μ^- capture on aluminium of two specific modes, detected by gamma-emission lifetime analysis [37].

literature, where one can see how incomplete the current available data is. Accordingly, it has been necessary to measure this directly.

The AlCap experiment [38] is a joint effort between COMET and Mu2e tasked with measuring the rate and spectra of particles emitted following muon capture in aluminium. Three data-taking runs have been held at The Paul Scherrer Institute (PSI) from 2013 to 2015, and analysis is ongoing, although preliminary neutron and proton spectra and rates have been achieved. The measured proton rate is low enough that COMET does not expect to have to take any precautionary measures to reduce it further. For more information on AlCap, see appendix C and the PhD thesis by Nam Hoai Tran [39].

2.3 Experimental Searches for μ - e conversion

2.3.1 SINDRUM-II: Present Limits

The SINDRUM-II experiment operated at PSI, last taking data in 2000 [40]. As well as searching for $\mu^+ \rightarrow e^+ e^- e^+$, they set the current limit on μ - e conversion, published in 2006 to be $\mathcal{C.R} < 7 \times 10^{-13}$ at 90% confidence level. The experiment, shown in Fig. 2.5,

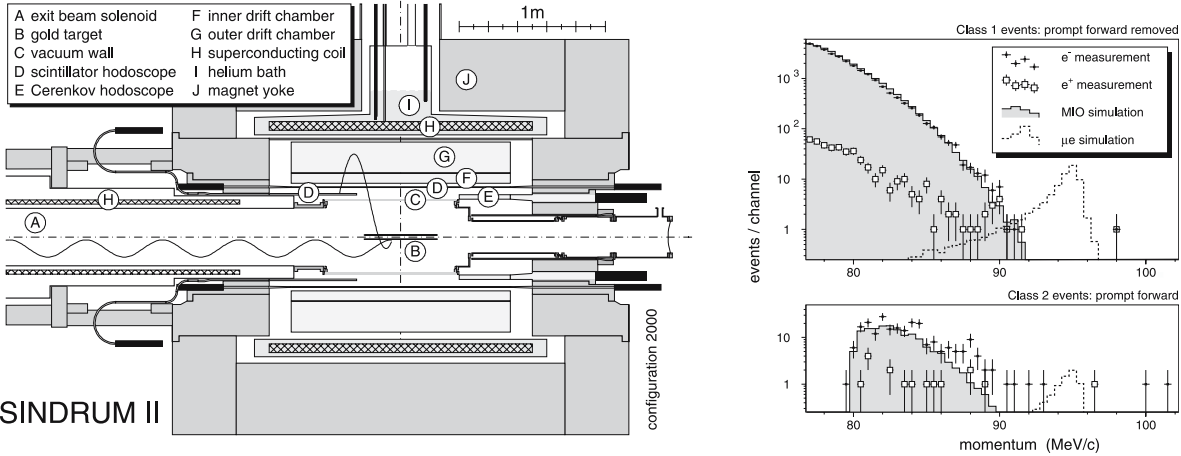


Figure 2.5: The SINDRUM-II experiment, which holds the current limit on μ - e conversion. Left: the detector and target, with the muon beam produced from decay of a pion beam created by protons striking a target. Right: the observed electron and positron energies and expected background and signal spectra. Reproduced from [40].

used a gold target positioned in the centre of a cylindrical detector. Both of these were placed coaxially with a solenoidal field allowing for momentum measurements by reconstructing the helical trajectories of the detected electrons.

The dominant backgrounds at SINDRUM-II were cosmic events and pions in the beam. The observed energy distribution (from the main event category) is shown to the right of Fig. 2.5. The single Class 1 event that was observed above the expected μ - e conversion energy in gold was attributed to a pion in the beam.

2.3.2 Experiments Beyond SINDRUM-II

Towards the end of SINDRUM-II's operation, preparation for experiments that would reach to sensitivities around 10^{-16} were made. The first, MELC [43], was intended to be built at the Moscow Meson Factory. The stopping target was to be either aluminium or titanium and, for the first time, the muon beam would be produced from pions captured in a solenoidal magnetic field around the production target. Partly due to the need to adapt the primary beam at the host facility, MELC was never completed, although some aspects of the experiment had been constructed.

With its cancellation, proponents of the experiment shifted their plans to the United States of America. The new proposal, known as MECO, was planned to run at the

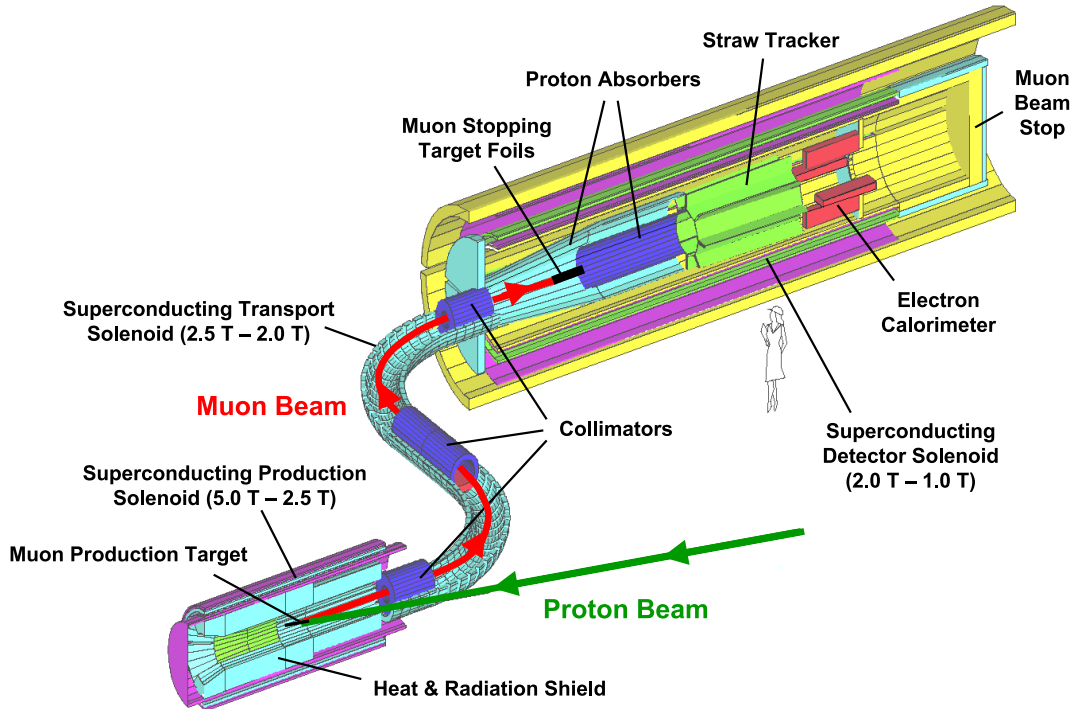


Figure 2.6: The muon beamline and detector planned for the MECO experiment [41]. The Mu2e experiment [42] looks very similar to this design, and although it looks rather different COMET also has a lot in common with the MECO design.

Berkeley National Lab (BNL), and largely kept the design of the MELC experiment. With the goal SES of 2×10^{-17} it was planned that MECO would run in 2004 having been built and commissioned in the preceding few years [41]. Fig. 2.6 shows the MECO experiment's beamline.

Sadly, MECO was never built. Plans again shifted, with Fermilab deciding to take on the experiment, now known as Mu2e. The Mu2e experiment has kept close to the design of MECO [42], and is now scheduled to begin data-taking around the same time as the COMET experiment's Phase-II. Mu2e and COMET have similar target sensitivities and similar schedules, and use some of the same experimental techniques. With that said, they do differ in some crucial aspects, and it is to COMET that we now turn.

Chapter 3

The COMET Experiment

The COMET experiment will search for COherent Muon to Electron Transitions with a single-event sensitivity of 3×10^{-17} or better. This amounts to an improvement of four orders of magnitude compared to the current limit by SINDRUM-II [40], made possible by significant changes to the way the experiment operates compared to its predecessor.

Reaching such a sensitivity requires that COMET stops many muons in the target, whilst maintaining a high-signal acceptance but suppressing potential background sources to well below a single event during the lifetime of the experiment. This tension between simultaneously high-signal sensitivity and background suppression can be translated into the more specific requirements of:

- a very high-intensity, low-energy, and high-purity muon beam,
- a thin stopping target and low-material budget detector,
- the use of timing information of signal process with respect to backgrounds.

The design of COMET realises these goals by employing several novel experimental techniques and, as such, it has been decided to operate in two stages, Phase-I and Phase-II. Phase-I aims both to help understand these techniques, the muon beam, and key backgrounds rates, as well as making an intermediate measurement of μ - e conversion at a sensitivity of 3×10^{-15} —two orders of magnitude better than the SINDRUM-II experiment. Phase-II will follow and should achieve the final objective of 3×10^{-17} .

3.1 The COMET Signal

Muon-to-electron conversion, as described in the previous chapter, is the process where a muon, bound within the Coulomb potential of an atomic nucleus, decays to an electron without emitting neutrinos. If the nucleus is not excited in the process, coherent transitions dominate, and the electron is produced monoenergetically. In addition to the energy, the lifetime of the muon once bound to the nucleus is also characteristic of the signal process.

Thus the signal for COMET is a single electron, with a well-defined energy and an exponential lifetime matching that of the bound muon. In the aluminium target used in COMET, the lifetime of the muon is 864 ns, whilst the energy of the electron will be 104.97 MeV.

3.2 Overview of Background Processes

The Single-Event Sensitivity (SES), defined in the previous chapter, is a statement of the experiment's ability to observe the μ - e conversion signal. It does not, however, account for the background rates. Clearly, for any observation to be confidently labelled as signal or, in the event of a null-observation, in order to set the tightest possible confidence limit, the background rate must be kept comparably low. In order to understand the design of the COMET experiment, a simple appreciation of the key backgrounds is therefore necessary.

Table 3.1 summarizes the results of previous studies for background rates at Phase-I and Phase-II. There are four groups of background source: intrinsic, prompt, delayed, and cosmic.

Intrinsic processes are those that arise from muons stopping in the target and will always be present regardless of the muon beam properties. Muon decay-in-orbit (DIO), which was described in the previous chapter, is one such background. In addition, radiative nuclear capture of a muon is kinematically capable of producing photons very close to the signal energy. If the photon is converted to a high-energy electron this can produce background events.

Prompt and delayed beam-related backgrounds come from impurities in the muon beam, be they pions, antiprotons, or high-energy muons and electrons. The key

| Type | Background | Number of events during run | |
|--|---|-----------------------------|---------------|
| | | Phase-I [44] | Phase-II [45] |
| Intrinsic | Muon Decay-in-Orbit | 0.01 | 0.15 |
| | Radiative Muon Capture | 0.0019 | < 0.001 |
| | μ^- Capture w/ n Emission | < 0.001 | < 0.001 |
| | μ^- Capture w/ Charged Part. Emission | < 0.001 | < 0.001 |
| Prompt | Radiative Pion Capture | 0.00028 | 0.05 |
| | Beam Electrons | ≤ 0.0038 | < 0.1* |
| | Muon Decay in Flight | | < 0.0002 |
| | Pion Decay in Flight | | < 0.0001 |
| | Neutron Induced | $\sim 10^{-9}$ | 0.024 |
| Delayed | Delayed Radiative Pion Capture | ~ 0 | 0.002 |
| | Antiproton Induced | 0.0012 | 0.007 |
| | Other delayed B.G. | ~ 0 | — |
| Cosmic | Cosmic Ray Muons | ≤ 0.01 | 0.002 |
| | Electrons from Cosmic Ray Muons | | 0.002 |
| Total background | | < 0.032 | < 0.34 |
| Signal (Assuming $B = 1 \times 10^{-16}$) | | 0.31 | 3.8 |

Table 3.1: Backgrounds for COMET Phase-I (from the 2016 TDR [44]) and Phase-II (from the 2009 CDR [45]). Prompt backgrounds arise by protons that occur in between bunches and are therefore suppressed by the extinction factor. For Phase-I, the recently measured value of 10^{-12} was used for the extinction factor, but for Phase-II the older expectation of 10^{-9} was used. If this is not taken into account, the Phase-I estimates suggest a greater background to signal sensitivity than for Phase-II. *) Result was statistically limited.

distinction between these two is the timing at which the background is detected with respect to the arrival of the proton beam. For example, pions that reach the stopping target region are dangerous since they can produce high-energy gamma rays which can pair produce to create 105 MeV electrons. Since pion capture against a nucleus is extremely fast, the timing of pion-induced backgrounds is determined predominantly by the arrival time of pions into the target region. In order to survive from the production target to the target region without decaying the pions must be relatively high-momentum: about 60 MeV/c or greater.

As a result, backgrounds from pion capture are typically expected close to the arrival time of protons at the production target. Prompt processes such as this are suppressed by using a pulsed proton beam (discussed in more depth later) and ensuring very few protons in between pulses. Other beam related issues include the decay-in-flight of muons and pions to electrons. An electron of 100 MeV/c can be produced by muons or pions with momentum greater than 70 or 50 MeV/c respectively, and so the flux of higher energy particles in the beam must also be reduced.

Delayed processes are those where the timing of the proton beam cannot be used to improve suppression since the characteristic time between the primary proton striking the target and the detection of the background for these processes is large compared to the time between beam pulses. Possible sources of this delay include the mirroring of particles by the magnetic field, or by some heavy particle from the production target producing pions and high-energy electrons. At a given momentum, antiprotons travel more slowly than muons or pions given their considerably larger mass, washing out any timing information from their production.

Cosmic Backgrounds arise from high-energy muons that pass through the building and enter the detector or beamline. Events where a muon decays to an electron, which is then detected as 105 MeV, are counted as backgrounds. In particular, muons that produce high-energy electrons close to the target are dangerous since cuts on the reconstructed direction and position will be less effective.

All these processes will be discussed and evaluated in more depth in chapter 7.

3.3 General Experimental Techniques

Suppressing background rates while maintaining a high-signal efficiency leads to several novel techniques being used in the COMET experimental set-up. The following techniques are common to both Phase-I and Phase-II.

3.3.1 Proton Beam Energy and Production Target

The muon beam used in COMET is produced from the decay of a secondary pion beam created by protons striking a target. If maximising the muon intensity were the only concern, then both the proton beam power and atomic mass of the target material would similarly be maximised since the pion production cross section grows with these two parameters. However, the need to suppress background rates and maintain the mechanical and operational stability of the target constrains both of these parameters.

In particular, protons striking an individual, stationary (and, in theory, unbound) nucleon with more than about 5.6 GeV have sufficient energy to produce antiprotons, which travel relatively slowly and can produce backgrounds. Since the antiproton yield grows very quickly above this threshold, it has been chosen to use protons with 8 GeV kinetic energy.

As well as the beam energy, the intensity is ideally maximised to increase the number of protons on target per second. For Phase-II running, the main ring will operate at $7 \mu\text{A}$ so that a beam power of 56 kW is achieved. Phase-I on the other hand will use a lower beam intensity of $0.4 \mu\text{A}$ or 3.2 kW.

Whilst a heavy metal target is preferable since it increases the number of nucleons that interact with the proton beam and therefore the pion yield, the target must maintain its mechanical strength. This requires the selection of a high-melting point material and possibly the use of active cooling. To simplify the situation in Phase-I, a graphite target will be used which can be passively cooled by thermal radiation. In Phase-II however, tungsten has been selected due to its high-melting point of 3422 C, although water cooling may be additionally employed.

Finally, only those pions and muons emitted in the backwards direction with respect to the proton beam are captured and transported to the muon beamline. This is a strong way to reduce the high-energy components of the muon and pion distributions since

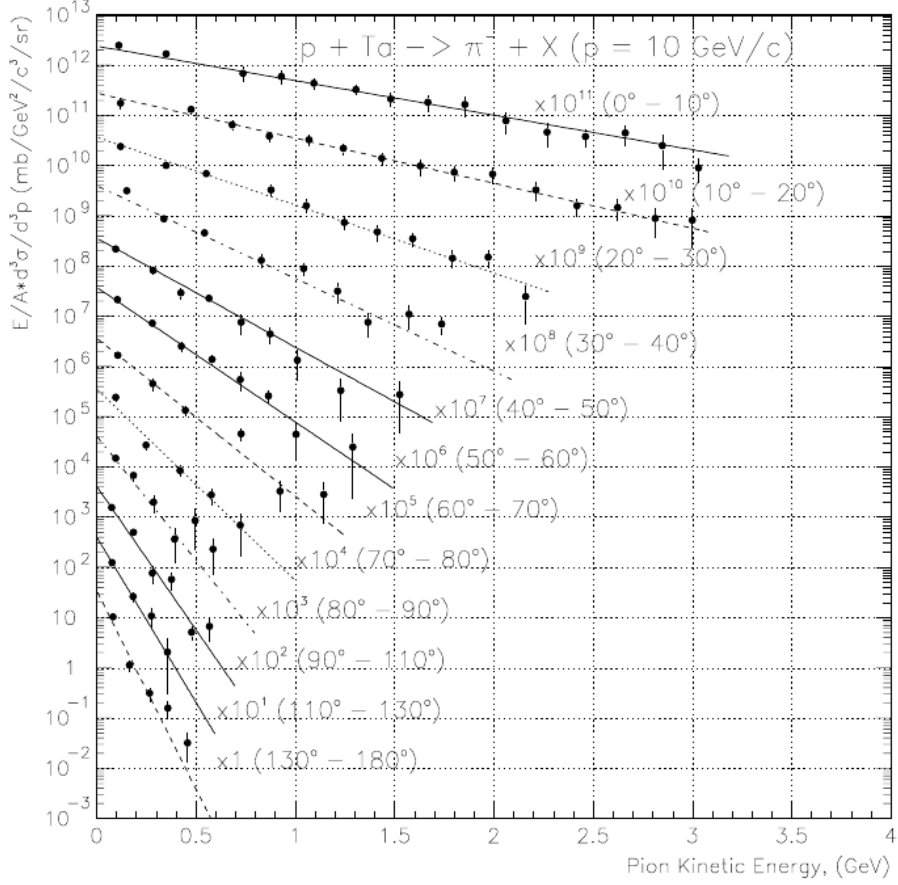


Figure 3.1: Double differential cross section of pion production on a tantalum target from protons with 10 GeV kinetic energy (reproduced from Meco note 23 [46] which itself used [47]). It is clear that the high-energy component of the spectrum is suppressed as you move to higher production angles which is important for reducing background rates. Note that each line is scaled an order of magnitude compared to the line below.

the high-energy tail is greatly suppressed in the backwards direction, whilst the yields for low-momentum pions in both directions are similar. Presently, however, there is a dearth of experimental measurements for pion production in the backwards direction with 8 GeV protons on a graphite or tungsten target. Fig. 3.1 shows a measurement of the cross section for pion production with 10 GeV protons on tantalum (which is adjacent to tungsten on the periodic table).

3.3.2 Particle Transport through Bent Solenoids

Both Phase-I and II make use of bent solenoids to help select particles of a particular momentum. When transported through a bent solenoid, charged particles are dispersed proportionally to their momentum and charge. This creates a separation between the high and low-momentum components of the beam, such that collimators can selectively remove the high-momentum particles.

Charged particles moving through a straight solenoid follow a helical trajectory, orbiting a point that moves parallel to the solenoidal axis with a constant velocity fixed by the longitudinal momentum of the particle. The transverse momentum, on the other hand, determines the frequency with which the particle rotates about this point (the cyclotron frequency or frequency of gyration).

By comparison, if a charged particle moves through a bent solenoid channel, the particle can still be considered to orbit a point, only now the motion of that point can be shown to drift vertically, out of the plane of bending. This drift arises partially due to the gradient introduced to the field by bending the solenoid but also from the non-rectilinear coordinate system of the field lines. The total drift, D , of a particle with mass and charge, m and q respectively, through a solenoid bent with a fixed radius of curvature, R , is given by:

$$D = \frac{1}{qB} \left(\frac{s}{R} \right) \frac{p_L^2 + 0.5p_T^2}{p_L} \quad (3.1)$$

$$= \frac{1}{qB} \left(\frac{s}{R} \right) \frac{p}{2} \left(\cos \theta + \frac{1}{\cos \theta} \right) \quad (3.2)$$

where B is the magnetic field strength¹, s is the distance travelled through the solenoid, p the momentum of the particle, with p_L and p_T its longitudinal and transverse components with respect to the solenoid axis. The pitch angle, θ , is a property of the helical trajectory taken by the particle and defined as:

$$\theta = \tan^{-1} \left(\frac{p_T}{p_L} \right) \quad (3.3)$$

¹Strictly speaking, B is the field strength along the path of the centre of gyration, which is constant for a fixed transverse distance from the focus of the bent solenoid.

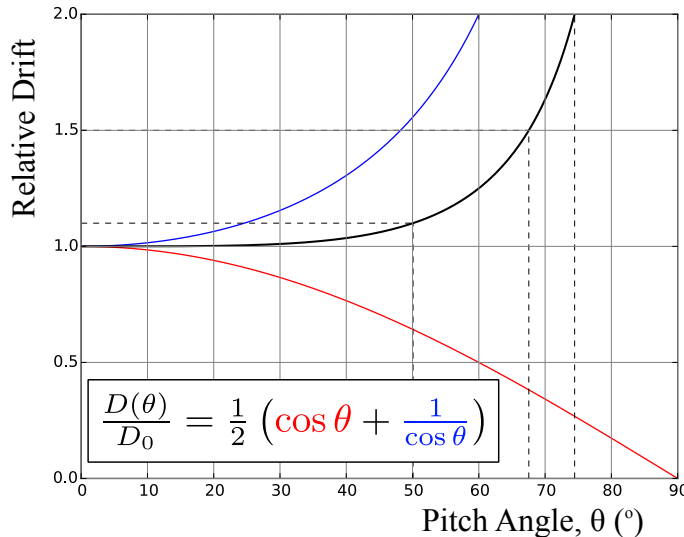


Figure 3.2: Angular dependence of the magnitude of vertical drift in a bent solenoid field. The total variation (black) remains below 10% for pitch angles below 50°.

The angular dependence of equation (3.2) is shown in Fig. 3.2 where it can be seen that for angles below 50 degrees the variation in the drift is less than 10%, such that the drift is determined almost completely by the momentum for particles below these angles.

Since the drift is proportional to the momentum of the particle, particles with zero momentum would remain on axis, whilst higher momentum particles, including those of interest (105 MeV electrons in the Phase-II electron spectrometer and around 40 MeV/c muons in the muon beam line), drift to the sides. However, an additional vertical component is introduced to the magnetic field. If the solenoid were straight the axis of a particle's helical trajectory would follow the field line. A vertical component would, therefore, cause the trajectories to move upwards with the field line itself, irrespective of the particle's momentum. The same result is true in a bent solenoid such that a vertical component can be used to counter the drift from the bent solenoid field for particles of a specific momentum, which will then remain on-axis.

Two techniques have been considered to introduce this vertical component: tilting the solenoid coils themselves, or adding additional dipole coils around the solenoids. COMET has chosen to pursue the latter, using a special, proprietary winding technique developed by Toshiba to introduce a vertical component by placing additional conductor around the solenoid coils. Since the current through these dipole coils can be altered separately to the solenoid coils, this approach has the advantage that the two components can be tuned individually. This allows for the optimal dipole field to be found during operation

running, or for the on-axis momentum and charge to be shifted for background and acceptance studies or searches for other physical observables.

Particles that drift by large amounts will come into contact with the beampipe and are thereby removed from the beam. Additional collimating material (typically tungsten or copper) can be introduced to more precisely remove particles with undesirable momenta.

Bent solenoids are used in COMET for both Phase-I and II to disperse high-energy muons and pions in the muon beam, and as a spectrometer system for electrons coming from the stopping target in Phase-II, which will both be described in more detail below.

3.3.3 Stopping Target Material and Beam Pulsing

The combination of using backwards-going pions and the long, bent-solenoid transport channel is already effective at reducing potential background issues. In addition to these however, there is one further method which helps both to reduce beam-related backgrounds and improve the detector occupancy and reconstruction requirements: the use of a pulsed proton beam with a relatively light stopping target.

Since the signal process is coherent, its cross section grows roughly as the square of the number of nucleons (or protons, depending on the model)² until the muon is contained almost completely within the nucleus, at which point the rate levels off. It is therefore desirable to use a high-Z target in order to increase the probability of conversion and indeed SINDRUM-II used both lead and gold targets, with its most stringent limit set on a gold target [40].

However, as the nucleus gets larger, the lifetime of the muonic atom falls steeply due to the increase in the nuclear capture rate. This is illustrated in Fig. 3.3 where it can be seen that for elements heavier than iron ($Z > 26$) the muon lifetime is less than 200 ns. The COMET production target and beamline produces a beam flash that lasts for about 200 ns after the arrival of a proton. This means that, for targets heavier than iron, timing information is not a useful parameter to distinguish particles in the beam from electrons coming from stopped muons.

Whilst these are the two dominant factors in deciding the target material, other factors like the mechanical stability, cost, isotopic purity and the stability of the daughter nuclei

²Although this growth is offset by the normalisation to the capture rate which is typically treated as incoherent so that it grows linearly with the number of nucleons. The overall conversion rate for lighter elements is roughly proportional to the atomic number.

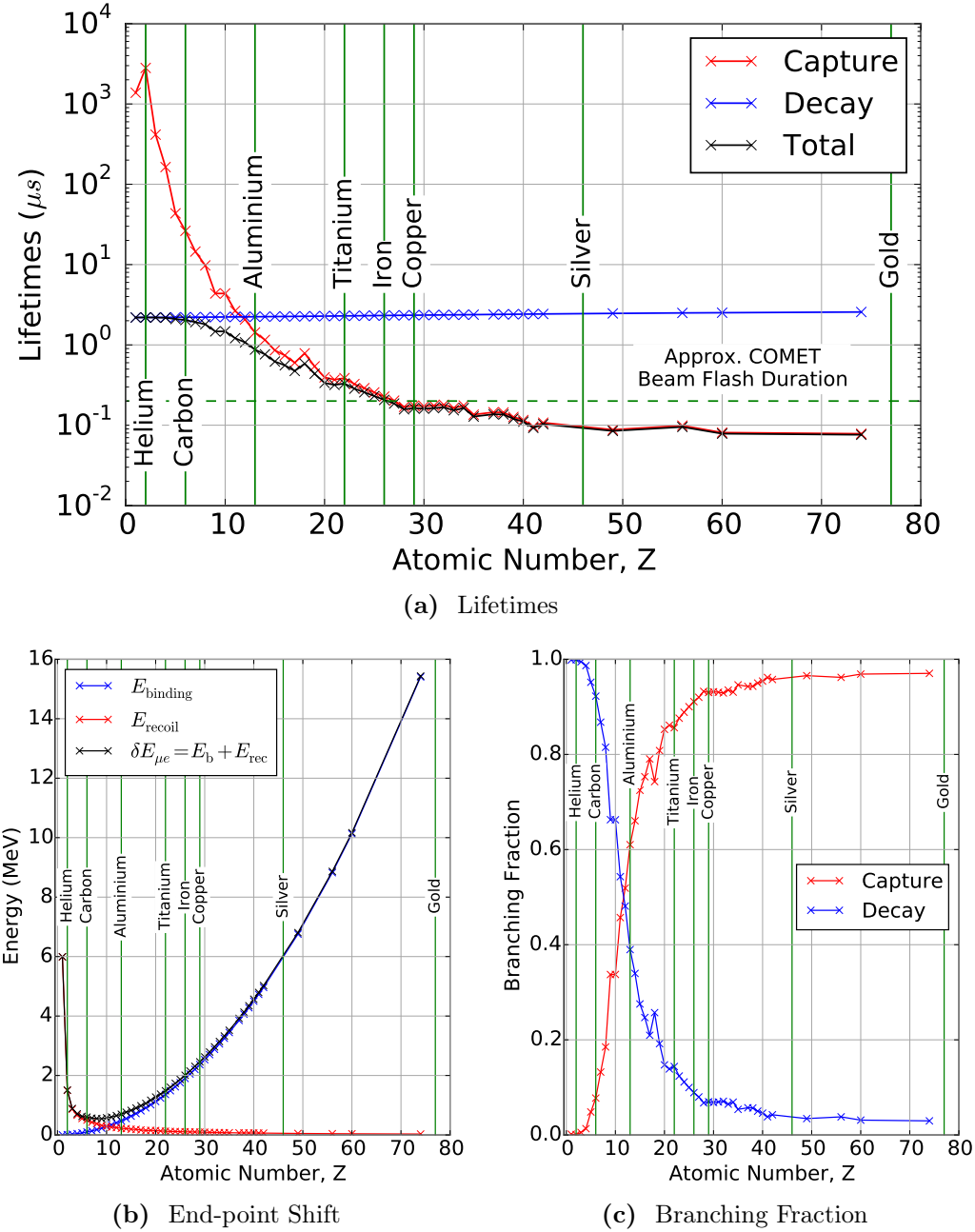


Figure 3.3: The effect of changing the atomic number on the lifetime (a), conversion energy (shown as $M_\mu - E_e$) (b), and branching ratio (c). For the branching ratio and lifetime plots, the partial rate for muon nuclear capture and decay-in-orbit are shown separately. The capture and decay rates are taken from the Geant4 [48] parametrisation for stopped negative muons. Only elements for which at least 1 isotope uses a measured value are plotted. The values for the end-point energy level are calculated using the Bohr model for the muon ground-state binding energy.

following muon capture on the target must also be considered. Accordingly, titanium and aluminium are considered the two most viable target materials. Titanium, in which the muon lifetime is about 330 ns, would be considerably harder to measure μ -e conversion so at this stage the COMET experiment is focussed on using aluminium where the muon lifetime is about 864 ns [49].

The J-PARC accelerator has buckets separated by 550 ns, although separations of multiples of this number can, in principle, be achieved. For COMET running the intention is to fill every second bucket so that pulses are separated by 1.17 μ s. Fig. 3.4 shows the beam timing schematically. A window from about 700 to 1100 ns after the proton beam arrival is then used to look for signal events, by which time most of the beam flash should have passed whilst signal events remain probable.

Having a well-defined bunch structure is crucial for this scheme to work. Protons arriving in between bunches would produce (a fragment of) beam flash that could include high-energy muons or pions. If these produce signal-like electrons that would a background source that the timing window would be unable to remove. The extinction

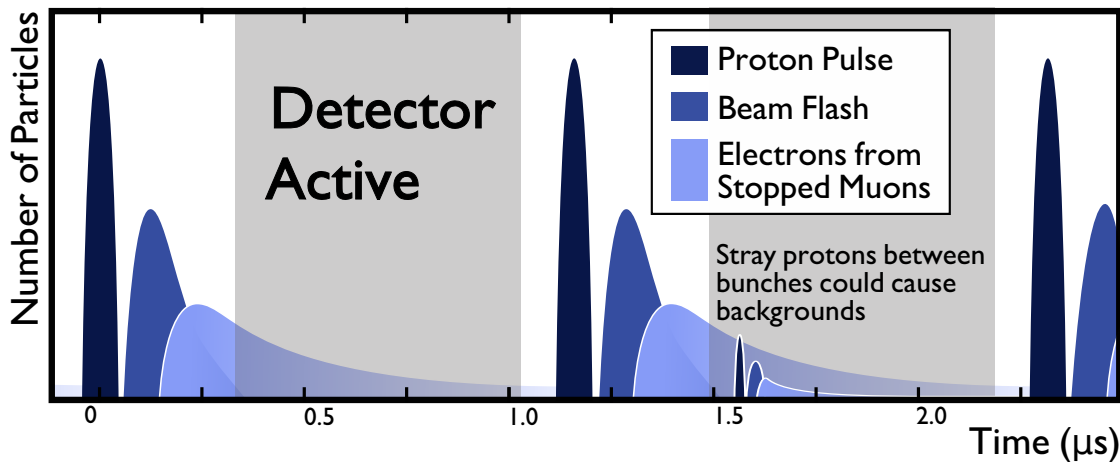


Figure 3.4: Schematic for the timing structure used in the COMET experiment. Protons arrive at the production target in 100 ns bunches separated by about 1.17 μ s. These pulses create a flash of particles in the detector which lasts for about 300 ns. Muons that stop in the aluminium target have a lifetime of 864 ns, such that signal electrons should be detected with this timing and be well removed from the beam flash. In between bunches there should be very few protons, or else the resultant secondaries could be detected as backgrounds.

factor is used to quantify the probability of protons arriving out of time, and is given by:

$$R_{\text{Extinction}} = \frac{N(p \text{ between bunches})}{N(p \text{ per bunch})}. \quad (3.4)$$

Original background predictions were made assuming $R_{\text{Extinction}}$ was around 10^{-9} [45] (about 1 out-of-time proton for every 7 Phase-I bunches) although recent measurements have been able to demonstrate extinction at a level of 10^{-12} [44] (about 1 out-of-time proton for every 7100 Phase-I bunches).

The bunch structure is initially defined by the linear accelerator (linac) at J-PARC which accelerates protons up to 600 MeV. The J-PARC Rapid Cycling Synchrotron (RCS) then takes these protons up to 3 GeV where up to two buckets can be stored, although for COMET only one bunch at a time will be filled. The protons are then injected into the J-PARC Main Ring (MR) which accelerates them up the final energy of 8 GeV and is capable of storing up to 9 buckets at once. Using the linac chopper alone would not be sufficient to produce the desired extinction factor since stray protons tend to drift into the unfilled buckets. Achieving the high-extinction factor then is possible only by using the injection kicker from the RCS to the MR in a ‘double-kick’ mode. The kicker excitation length is set to two buckets (so that the RCS is completely emptied into the MR). The kicker is then activated again immediately after the first filled bunch has performed a complete rotation of the MR such that protons that had diffused into the second bunch of the RCS are now kicked away. Thus only every second bucket in the MR is filled and all other buckets are kept empty.

3.4 COMET Phase-I

Phase-I will see the construction of the COMET hall, the production target capture solenoids, the first 90 degrees of the bent muon transport solenoid, and the detector solenoid. The beamline is shown schematically in Fig. 3.5 where the two interchangeable detector systems can also be seen.

There are two key goals to Phase-I:

1. measure μ - e conversion at a Single-Event Sensitivity (SES) of 3×10^{-15} , and
2. prepare for Phase-II by measuring the beam profile, particle yields and background rates, and prototype the detector technology.

Since the dynamics of bent solenoids are complicated, it is important to study the beam as close to the production target as possible. However, due to the high-radiation environment around the production target, the detector and electronics cannot be placed too close and must be well shielded. Phase-I will therefore measure the beam after the first 90 degrees of bent solenoid with the same detector system to be used in Phase-II, namely the Straw-tube tracker and Electromagnetic Calorimeter (StrECAL) detector—a series of Straw Tracker stations followed by an ECAL all sitting in the beam.

However, since the StrECAL detector will be hit by the full force of the muon beam, it would not be feasible to conduct a μ - e conversion search using this detector. As such, for Phase-I, a second detector called the Cylindrical Detector (CyDet) will be used for this purpose. The CyDet uses a Cylindrical Drift Chamber (CDC) to reconstruct the trajectories of charged particles and a pair of Cherenkov and Scintillation counters (one upstream and one down) to trigger the read-out of the system. The CyDet escapes the issue of the beam flash that the StrECAL would face in Phase-I since only the outer region is instrumented. Because the detector sits in a 1 T solenoid field (and both the detector and solenoid are co-axial), particles follow helical trajectories with the radius of gyration determined by the transverse momentum of the particle. The beam is introduced in the centre and typically remains in an envelope of 15 cm whilst the stopping target sits in the centre of the detector with a radius of 10 cm. As such the detector itself is geometrically blind to charged particles in the beam and electrons coming from muon DIO in the target with momentum less than 60 MeV/c which make up the majority of the DIO spectrum. To reconstruct the longitudinal position of the particle’s trajectory an all-sereo configuration is used in the Cylindrical Drift Chamber, where each layer of wires is rotated in the opposite direction to the previous layer by an angle of 4° with respect to the solenoid axis.

Because the Phase-I detector sits much closer to the stopping target than at Phase-II, there is greater exposure to hadrons emitted following nuclear capture of the stopped negative muons, such as protons, deuterons, alpha particles and so on. Despite being emitted with kinetic energies of a few tens of MeV, momenta above 60 MeV/c are readily achieved given the large mass of these particles. For similar reasons these particles are typically very heavily ionising so, if left unchecked, could easily dominate the occupancy of the CDC. The AlCap experiment has shown that for muon capture on Al-27 nuclei, the emission of a proton occurs for about 3% of every muon capture [39]. At this level, it is believed that no specific shielding is required beyond the carbon inner wall of the CDC needed to contain the gas mixture.

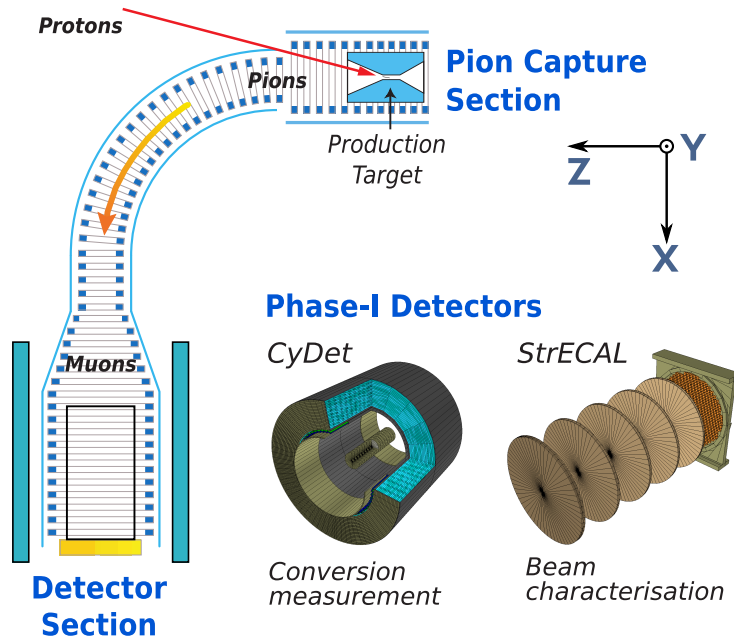
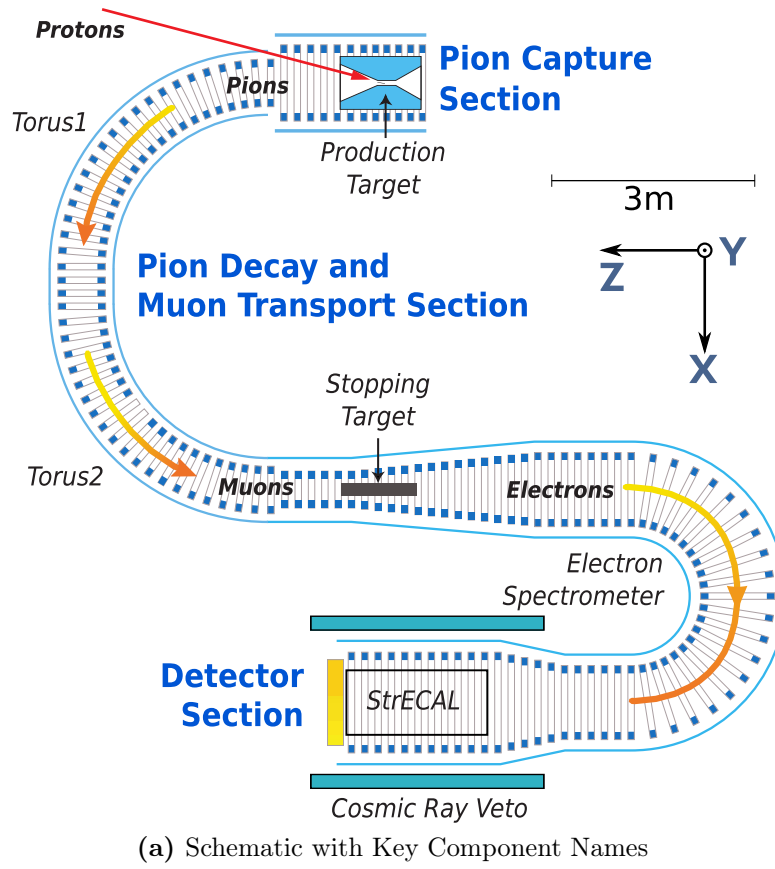


Figure 3.5: Schematic layout of COMET Phase-I including the two detector systems that will run separately, being swapped in and out of the detector solenoid depending on the study.

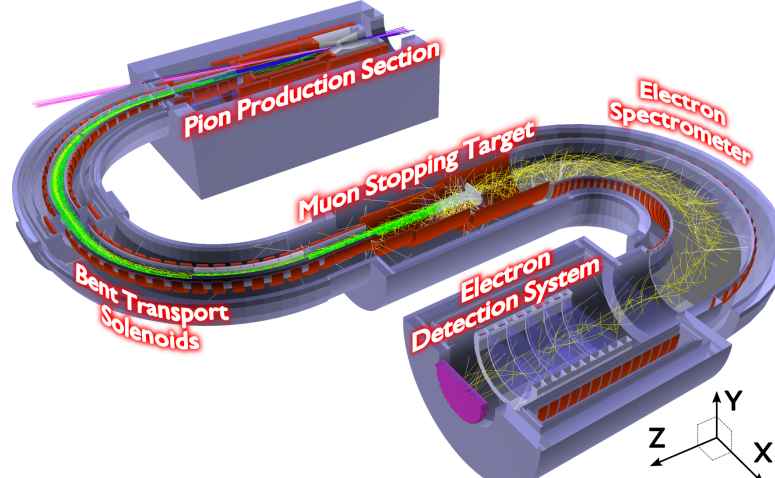
Four layers of scintillation bars will surround the outside of the detector to provide a veto for cosmic ray events. The most dangerous event would be a high-energy muon reaching the target and decaying to a 105 MeV electron which is then detected. Dedicated cosmic runs will be performed prior to operation with a beam in order to understand the flux of cosmic muons.

3.5 COMET Phase-II

COMET Phase-II will be the final stage of the experiment and should achieve the overall goal of measuring μ - e conversion with an SES of 3×10^{-17} . It will extend the muon beamline built for Phase-I by an extra 90° , and add two extra solenoid sections: one to hold the stopping target, and a second 180° bent solenoid with a large aperture of 60 cm radius. This layout is shown in Fig. 3.6. The bent solenoid after the stopping target is primarily there to remove the low-energy DIO electrons which otherwise could significantly increase the hit rate in the detector. The final detector system for Phase-II will use the StrECAL from Phase-I but probably with thinner diameter straw tubes,



(a) Schematic with Key Component Names



(b) Event Display with Particle beams

Figure 3.6: The COMET Phase-II layout, schematically (a) and in the simulation (b). The 8 GeV proton beam (magenta in (b)) enters from the top-left, producing (amongst other things) pions (dark blue). Pions travelling backwards with respect to the proton beam are then transported through the Torus1 and Torus2 bent solenoids, during which time most of the pions decay, producing an intense muon beam (green). About 40% of these muons then stop in the stopping target (centre of image). Any electrons (yellow) coming from $\mu-e$ conversion are then transported through another 180 degrees of bent solenoid into the detector system. Also shown in this image is the global COMET coordinate system, with the Z-direction parallel to the beam axis at the production target and the Y-direction vertical.

thinner straw material, and more tracking stations in order to improve the energy resolution.

As for Phase-I, an active cosmic ray veto will prevent triggering on events caused by cosmic muons. At least the detector solenoid will be covered, but it is likely that both the spectrometer and the stopping target area are also contained in the veto. In Phase-I, with the target surrounded by the detector, there is a degree of self-shielding against cosmic events. In Phase-II, however, this will not be the case since the target and detector are widely separated.

3.6 Key Sub-component Descriptions

The following sections describe the sub-components and beamline sections for both Phase-I and Phase-II in more detail. For Phase-I, parameters come from the latest geometry which is close to that of the TDR [44] but with some improvements. For Phase-II, the description is largely based on the design as laid out in the 2009 CDR [45].

Production Target Section (`ProdTgtSec`)

Magnet names: *CS, MS, TS1*. Constructed by: *Phase-I, but target changed for Phase-II* Super-conducting solenoid containing the pion production target. The proton beam strikes the production target, which produces a range of particles, principally pions. The solenoidal fields captures the backwards-going pions and delivers them into the transport solenoids. The target itself consists of a single, solid, cylindrical rod. In Phase-I the target will be made of graphite, whilst in Phase-II it will be tungsten. Since graphite has a larger interaction length, the target in Phase-I will likely be longer than in Phase-II. Contains a significant amount of shielding to protect the magnet coils from overheating in the high-radiation environment. In the forward proton direction sits a large iron beam dump, which will absorb the protons that miss the target and forward-produced pions and other particles.

- Min. shielding radius = 12 cm
- Target solenoid aperture = 44 cm
- Matching sole. aperture = 18 cm
- Target length (Phase-I) = 60 cm
- Target length (Phase-II) = 16 cm
(2009 optimisation)
- Field strengths = 5 T at the target,
3 T along matching solenoids

Torus1 (Tor1)

Magnet names: *TS2*. Constructed by: *Phase-I*

Bent solenoid section containing antiproton absorber foils and muon beam collimators. Special dipole coils are placed around the normal solenoid coils to add a tunable vertical component to the field. During Phase-I, the detector solenoid will sit immediately after the Torus1, although with a small additional matching coil. In Phase-II this will be replaced with the small TS3 coil to connect it to Torus2.

- Aperture size = 18.5 cm
- Solenoid field strength = 3 T
- Bending radius = 3 m

Torus2 (Tor2)

Magnet names: *TS4*. Constructed by: *Phase-II*

Very similar in design to Torus1, although possibly with different collimator placement and designs. The dipole field along this half of the bent muon transport solenoids might well be different to the dipole along the first half (Torus1).

- Aperture size = 18.5 cm
- Solenoid field strength = 3 T
- Bending radius = 3 m

Stopping Target Section (StopTgtSec)

Magnet names: *TS5, ST*. Constructed by: *Phase-II*

The straight section of solenoid housing the muon stopping target for Phase-II. The electromagnetic field reduces dramatically around the mid-point of the StopTgtSec to improve signal acceptance. The stopping target itself will consist of 200 um disks made of pure aluminium, then followed by a tungsten or aluminium beam blocker. There should be no line of site between the exit of the Torus2 and the entrance to the downstream solenoid, the Electron Spectrometer to remove high-energy particles in the muon beam. The reduction in the field strength in this region is used to improve the signal acceptance by magnetically mirroring back signal electrons that initially head upstream from the target.

- Aperture size = 18.5 cm at the entrance, increasing to 61 cm by the exit
- Solenoidal field strength = 3 T at the entrance, tapering to about 1 T at the exit

Electron Spectrometer (ElSpec)

Magnet names: *ES*. Constructed by: *Phase-II*

The 180° bent solenoid used to prevent very low energy particles reaching the detector. Also useful for removing backgrounds due to gammas and neutrons coming from the

stopping target. The magnetic field in the Electron Spectrometer is much weaker than the preceding beamline, at close to 1 T.

- Aperture size = 60 cm
- Solenoidal field strength = 1 T along beam-axis
- Bending radius = 2 m

Detector Solenoid (DetSol)

Magnet names: *DS*. Constructed by: *Phase-I, but possibly extended for Phase-II*

The final straight solenoid section that houses the actual detector. This will be re-used in Phase-II after Phase-I finishes, although additional coils may be added to extend the solenoid to house additional straw tracker stations. The Stopping Target in Phase-I will be located in this solenoid, within the CyDet.

- Aperture size = 96 cm
- Field strength = 1 T

StrawTracker + ECAL Detector (StrECAL)

Constructed by: *Phase-I, upgraded for Phase-II.*

Detector system used in Phase-II to measure conversion electrons. In Phase-I will be used to measure beam properties. Consists of 5 Straw Tracker stations (in Phase-I, with possibly more in Phase-II), each transverse to the beam. Each station consists of 4 perpendicular layers of straw tubes. The LYSO-based ECAL will measure particle energies with 5% resolution and serve primarily as a trigger and to support PID.

- Straws per layer = 120
- layers per station = 4 (2 X, 2 Y)
- Number of stations = 5
- Straw length = 69.2 to 130 cm
- Wire radius = 10 micron
- Straw outer radius = 4.9 mm
- Straw material = Aluminised mylar
- No. of ECAL crystals = 1920 Crystal
- Crystal dimensions = $2 \times 2 \times 12$ cm
- Crystal material = LYSO

Cylindrical Detector (CyDet)

Constructed by: *Only used in Phase-I.*

The primary detector for Phase-I to measure conversion electrons at 200 keV resolution. Consists of a cylindrical drift chamber arranged coaxially with the beam and stopping target. Wires in the drift chamber are angled in opposite directions on alternating layers to allow for all-stereoscopic reconstruction of the longitudinal component of a particle's trajectory. In addition to the drift chamber, triggering hodoscopes and scintillation bars at the upstream and downstream ends of the detector provide a timestamp and trigger decision, although this will likely be supplemented by a track trigger using Drift Chamber information.

- No. of Layers = 20 (including 2 guard layers)
- No. of Field wires = 14562
- No. of Sense wires = 4986
- Field wire = 126 micron Al
- Sense wire = 25 micron Au plated W

Cosmic Ray Veto (CRV)

Constructed by: *Phase-I and upgraded and extended for Phase-II.*

An active veto against cosmic muons that enter the detector. Formed from four layers of scintillating strips, read-out via wavelength shifting fibres. The CRV surrounds the detector solenoid on all sides and above. Layers of concrete and iron are contained between the detector solenoid and the CRV in order to protect the CRV from the high neutron fluxes from the beam and stopping target.

- Number of layers = 4 per side
- Total number of strips = 3816
- Strip material = Polystyrene scintillator
- Shielding between detector = layers of concrete, iron, polyethylene, and lead

Concrete and Iron shielding

Constructed by: *Phase-I.*

Experiment hall shielding to capture and constrain the neutron and gamma radiation from the beam, principally around the production target section and proton beam dump. Air-tight interlocking concrete and iron blocks will surround the production target region and experiment hall. The detectors themselves will be isolated from the production target by concrete and iron blocks, with the only connection being the hole through which the muon transport solenoids pass.

3.7 Schedule and Status

The overall schedule for the COMET experiment is shown in Fig. 3.7. Phase-I is due to start data taking in Japanese Fiscal Year (JFY) 2018 and construction and development is well underway.

With regards to the facility, the building that will house the experiment is now finished, sitting to the side of the existing Hadron Hall at the Japanese Proton Accelerator Research Complex (J-PARC). Cooling and power supplies are being installed and the shielding for the concrete hatch area is being produced. In the mean time the development of the new beamline to extract protons from the MR and deliver them to the COMET area is being installed. In particular, the Lambertson magnet which directs the protons

towards COMET rather than the existing Hadron Hall has been built. For the muon beamline, the Phase-I section of the bent muon transport solenoids has been fabricated and installed, and is now under commissioning studies. Construction of the detector solenoid has also begun with the capture solenoids around the production target soon to begin. A selection of photographs that show the construction of the facility and installation of the bent transport solenoid are shown in Fig. 3.8.

Much of the recent activity for the collaboration has been on the design and construction of the detector systems. Beam tests to understand the performance and resolution of prototype ECAL crystals, straw tubes, and the CDC have taken place. For the StrECAL, production of all 2500 Phase-I straws has been completed and procurement of the Cerium-doped Lutetium Yttrium Oxyorthosilicate (LYSO) crystals for the ECAL is under way with some 200 or so crystals already purchased. Ageing tests of the straw tubes are on-going with straws being held for an extended duration under pressure and tension at KEK. Beam-test data is being analysed to understand the position resolution for a given straw and the energy resolution of the ECAL. In the case of the ECAL, an energy resolution better than 5% has already been shown for 105 MeV electrons. Fig. 3.9 shows photographs of the prototypes and beam test set-ups of the Straw Tube Tracker and the ECAL.

In the meantime the full CDC has been strung, with some 20,000 wires—about 15,000 field wires of $125\text{ }\mu\text{m}$ thickness, and about 5,000 sense wires of $25\text{ }\mu\text{m}$ diameter—being inserted. Every wire has had its tension checked using a vibrational resonance method,

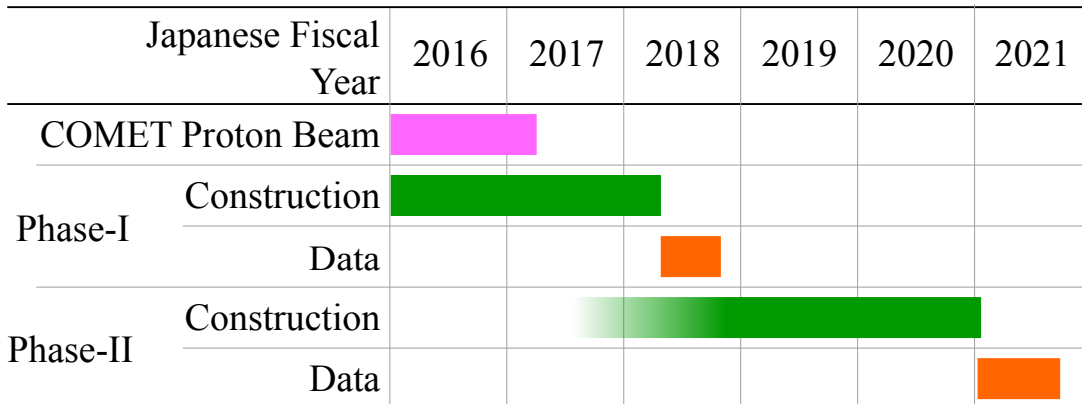


Figure 3.7: A summarised timeline for the COMET experiment including Phase-I and Phase-II based on the 2016 TDR [44]. At the time of writing, construction of the detector solenoid is underway as well as the final stages of the facility.

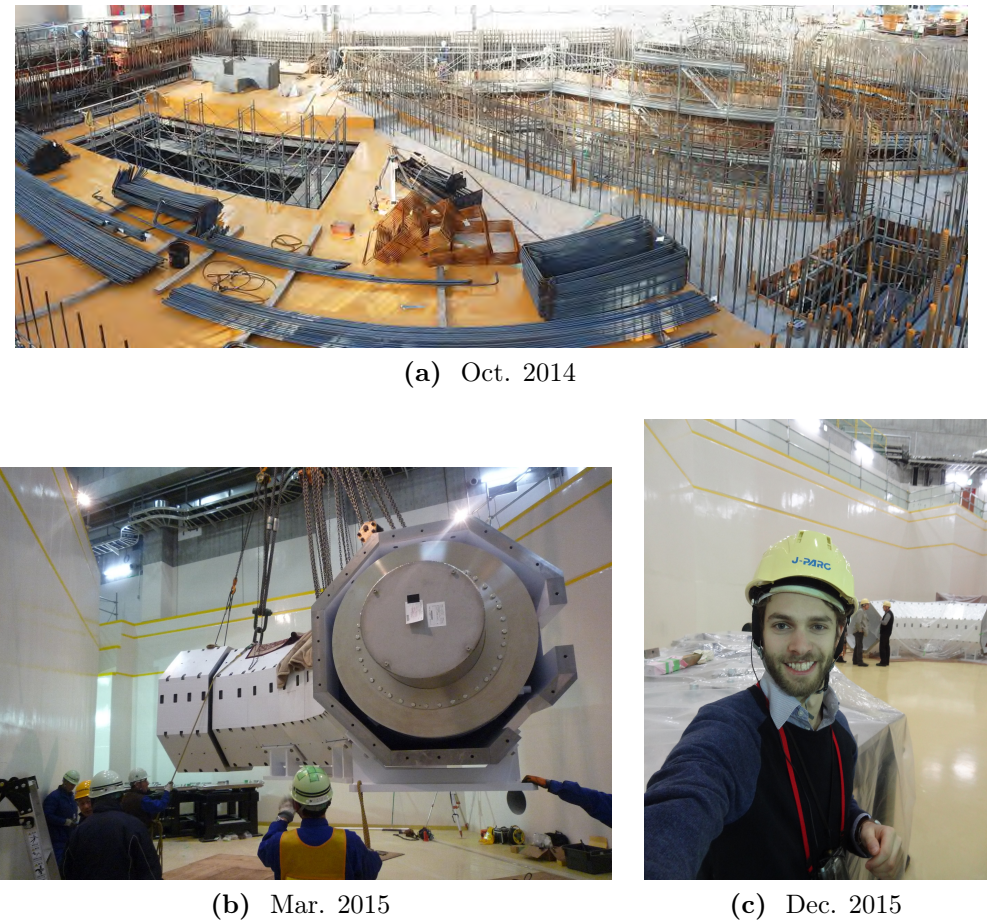
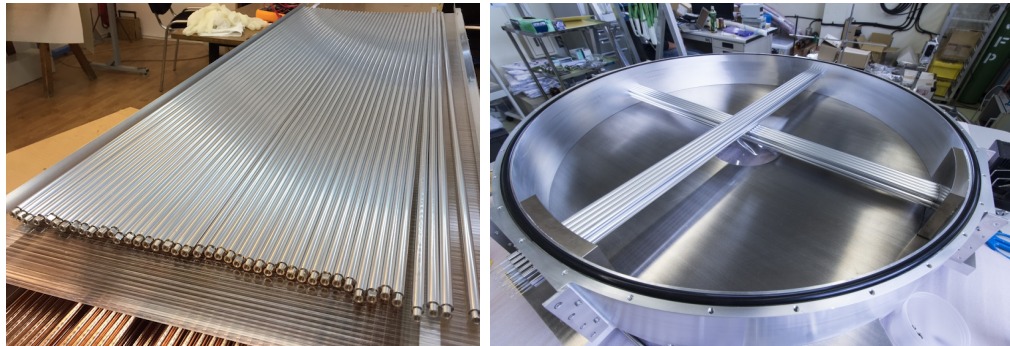


Figure 3.8: Photographs of the experiment hall being constructed and first sections of beamline being installed.

which showed some 90 wires were outside of design tolerances. These have since been replaced. In June 2016, the inner wall of the CDC was successfully inserted, completing the CDC construction, so that leak tests can begin shortly. Fig. 3.10 shows photographs from the stringing of the CDC. In parallel, cosmic ray tests have been used to study the performance of CDC prototypes and analysis of the data is under way to deduce the X-T curve for the CDC cells.

In the less-tangible realm that is software and simulation, in April 2015 the offline software reached its first stable release, and has since been used to perform three large-scale Monte Carlo productions of Phase-I. Reconstruction algorithms, including track finding and fitting in the CDC are under development and techniques to perform Particle Identification (PID) using the StrECAL in the Phase-I beam are also under development. More discussion on the software and simulation can be found in the next chapter.



(a) Straw Tube Construction and Prototype Tracker



(b) Crystal Wrapping and Test Beam

Figure 3.9: Research and development for the StrECAL showing both the individual straws or crystal and a prototype set-up used at test beams to characterise the sub-detectors.



Figure 3.10: The CDC being assembled and strung.

Chapter 4

Offline Software and The COMET Simulation

In 2013, when I first worked on the COMET experiment, many disparate and stand-alone simulations were being used without a common approach in the data structures and analysis. Since then, a single unified software framework has been prepared and is now being used throughout the collaboration. Developing this framework has been a large part of my work over the last four years, so this chapter presents both a summary of the framework and its development, as well as an explanation of the techniques used.

4.1 Developing the COMET Offline Framework

Work to produce a common, standardised software framework for COMET began when funding was awarded for Phase-I. With some four years to go before the switch on, it was clear that the support structure to handle and analyse the data needed to be in place soon. Given the scale of the project and the available resources, the decision was taken to base the COMET offline framework on an existing one, which would reduce the amount of work needed and improve the reliability of the software since it would have been tested elsewhere. A requirements document was drawn up [50] with a list of functionality that the software should provide. A survey of existing experiments was then undertaken to build a list of candidate frameworks. The list contained:

art A framework being developed primarily at Fermilab [51] which is also being used by Mu2e amongst other experiments.

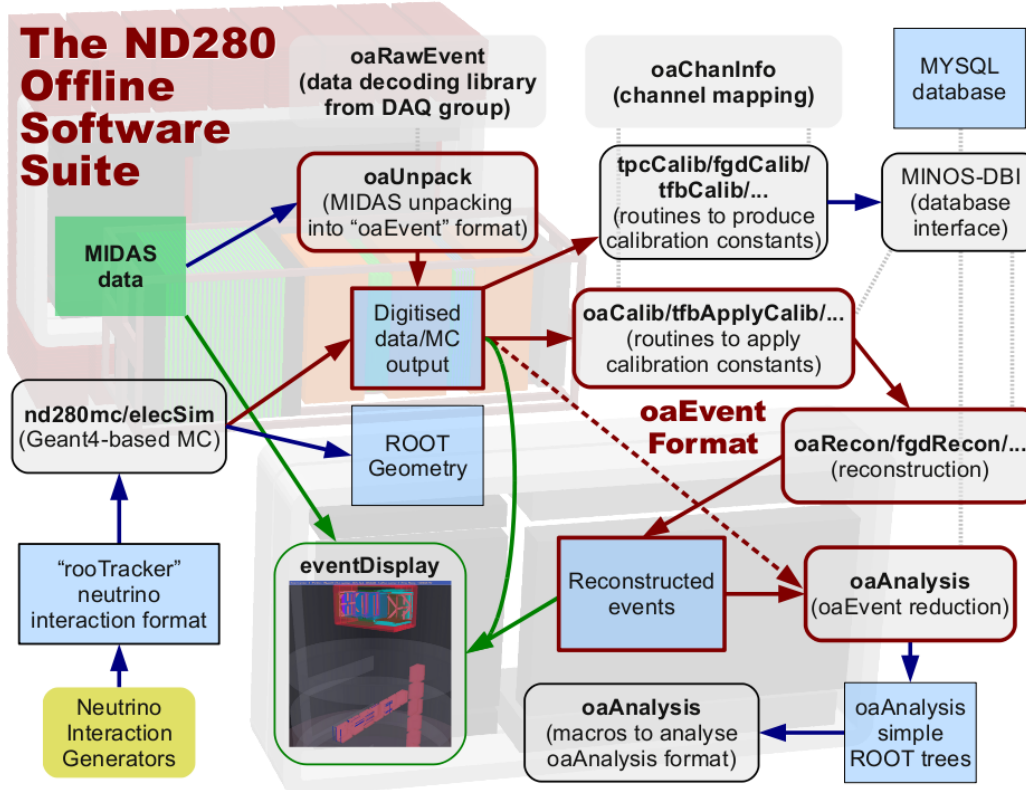


Figure 4.1: Overview diagram for the ND280 framework.

ND280 The framework [10] used by the near detectors of the T2K experiment, which are also based at J-PARC.

GAUDI which is used by LHCb amongst other experiments [52].

MARLIN The software being developed for the International Linear Collider (ILC) [53].

The final decision was to use the ND280 framework¹ since GAUDI and MARLIN would have required too much effort to adapt to the COMET requirements; since art is a relatively new framework and will be used by Mu2e (keeping the software distinct is important for the two experiments to co-exist as cross-checks); and because the ND280 software was already known to a large part of the COMET collaboration and had been tested, debugged, and used on real data at J-PARC.

¹The term ‘ND280’ can refer to one of either the ND280 detector itself, the site at J-PARC that houses both the ND280 and INGRID detectors, or the software used to analyse and simulate the T2K near-detectors. For the purposes of this chapter, unless specified explicitly, the term ‘ND280’ should be taken as referring to the software.

Fig. 4.1 shows an overview of the ND280 framework, including its package structure and the various interactions between packages.

With the decision to base the COMET experiment on the ND280 framework—and with the selection of the new name: ‘ICEDUST’—the process of forking the software was begun. As the ND280 framework had evolved somewhat organically, a review of the coding conventions was performed. For example, whilst the ND280 software prefixes all classes with a capital ‘T’, the ICEDUST conventions [54] agreed to swap this to a capital ‘I’ to reduce clashes with ROOT which also uses ‘T’. The package renaming scheme [55] was developed so that the purpose of a package and its role with the other packages could be more clearly identified.

Whilst fundamental, low-level packages have been left relatively unchanged, higher-level packages which include more detector-specific details had to be developed. Additionally, some aspects of COMET needed considerably more support than had been present in the ND280 software. Some of the key changes that have been introduced between ICEDUST and ND280 are:

Simulation Although the fundamental data types have not been changed, the simulation has been almost completely rewritten. In particular, support for hadron production codes have been added to model the production target; both the Geant4-based package (renamed to SimG4) and the detector response simulation (renamed as SimDetectorResponse) were given near-total makeovers; a new package (SimHitMerger) for resampling the G4Hits (simulated charge or energy deposits) was added. Custom physics models have been added to SimG4 to improve the modelling of the COMET-specific physics processes.

Magnetic Field handling Whilst the ND280 detector has a fairly straight-forward magnetic field, the COMET experiment has anything but this. Accordingly, significant work has been made to replace the way the magnetic field was handled, from essentially a few constants to the ability to use complete fieldmap descriptions made with external field calculation software.

Geometry handling The unusual shape of the COMET experiment, the level of detail needed for background estimations in a high-precision experiment, and the changing nature of a staged experiment meant a more elaborate scheme for handling the geometry was necessary than had existed in ND280.

Reconstruction and Calibration packages The interdependence of the calibration and reconstruction packages has been refined, with the data flow and user interface being better defined and standardised. Additionally, support for track fitting using Genfit2 [56] has been added as well as new track finding algorithms developed.

In addition to the above changes to the way the software runs, the distribution of the software has changed from using CMT [57] with CVS version control to being based on git with a GitLab [58] web-based user interface for the official repository. The switch to GitLab also brought a new ‘merge request’ workflow, which has allowed development of ICEDUST to progress rapidly with only a small number of developers. Although initially the intention was also to switch the build system from CMT to CMake [59], this decision has since been reversed due to improvements in CMT.

In the 3 years since the summer of 2013 and the initial work to fork ND280 to ICEDUST, some 3,200 commits have edited about two million lines of code in the official version of the framework. This has been the work of some 25 collaborators whilst about 15 other users have GitLab accounts and use the software. ICEDUST has been used to run three large Monte Carlo productions, most recently simulating about 10^{11} Proton-on-Target (POT) events—equivalent to 18,000 Phase-I bunches—and producing some 100 TB of simulated data.

4.2 Overview of ICEDUST

ICEDUST Can Efficiently Do Useful Software Things and stands for the Integrated COMET Experiment Data User Software Toolkit. Fig. 4.2 shows the flow of data through the different packages of the framework and the data formats used.

Inside the framework, nearly all processing is done using a ROOT file-based format known as oaEvent. Files of this type contain header information providing run identification numbers as well as a description of the geometry and magnetic field. The data payload contained in oaEvent files is stored in a ROOT TTree with a single branch containing a single COMET event per entry. Each COMET event has a dynamic structure and can contain any number of objects that derive from the IDatum base class.

Data from the detector systems is recorded in MIDAS [60] format, which also contains data from the slow control monitors such as temperature sensors and high-voltage power supplies. The task of converting the MIDAS files into the oaEvent format is handled by

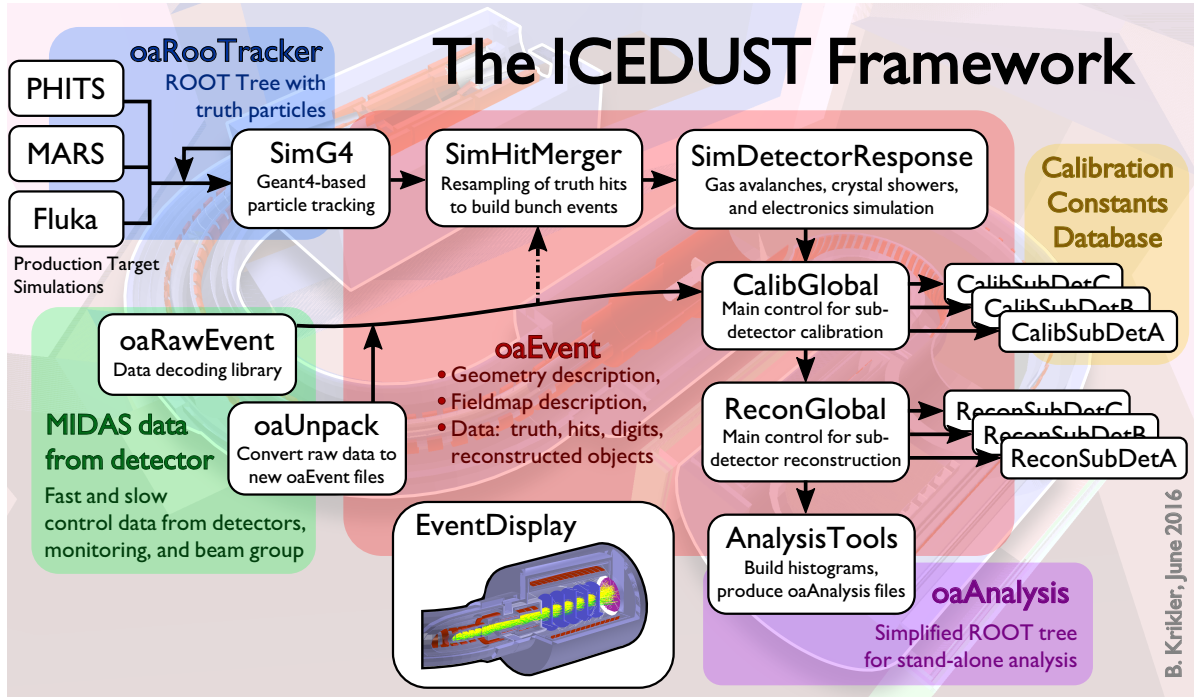


Figure 4.2: Overview diagram for the ICEDUST framework. Data produced from simulation or taken in the real experiment are treated identically through the calibration and onwards up to analysis.

the package `oaUnpack`, which writes out new, converted files, and `oaRawEvent`, which can convert the MIDAS files to `oaEvent` format on the fly.

Simulated data is also produced in the `oaEvent` format and involves some 4 to 6 packages being called, described in more depth in the next section.

Once either simulated data has been produced or real data has been converted, calibration routines can then be applied. Each sub-detector's routine is capable of pulling previously-generated constants from an SQL database and applying these to the detected (or simulated) energy deposits.

These calibrated hits are then passed into the reconstruction stage. Here each sub-detector system is first allowed to handle the data, which is then passed to a global reconstruction routine until a fully reconstructed event is produced. For the tracking detectors this stage typically involves an initial track finding stage, where noise hits are removed and track candidates consisting of a list of hits are collected and, secondly, a track fitting stage where the actual path of the underlying particle is reconstructed and key values like momentum and helical pitch-angle deduced.

Nearly all of the processing of data up to this stage has used the oaEvent format. The final analysis stage, however, moves into a simpler, flatter format, known as oaAnalysis, which produces a data summary tree (as opposed to tape) that can be accessed without a dependence on the full ICEDUST software.

Around all of this there are several utility packages such as the event display, which can visualise any oaEvent file, and IcedustControl, which can run a single set of data through the data chain and is the main steering mechanism used for production running.

4.3 The COMET Simulation

During Phase-I and Phase-II some 10^{19} and 10^{21} protons will strike the production target. Of these, fewer than 1 background events should be observed, whilst the signal efficiency should be demonstrably as high as possible.

Simulation plays a crucial role in making such a demonstration. Before the experiment is built and operated it allows one to optimise crucial aspects of the geometry and parameters, such as the magnetic field strengths or timing cuts. In addition, using Monte Carlo techniques in an accurate simulation allows an estimation of the background rate by sampling the parameter space corresponding to each stage of the experiment. Clearly, then, the simulation itself must be as faithful a reproduction of the true experiment as possible.

The COMET simulation therefore needs to be both highly accurate and highly efficient. As well as custom physics modelling, and special handling for the magnetic field, several resampling techniques have been introduced to increase the statistical power. The steps needed to build up the COMET simulation are shown in Fig. 4.3.

To reduce the uncertainties associated with the production target and the muon and pion yield, various different hadron-production models can be used, including PHITS [61], MARS [62], Fluka [63] and Geant4 [48]. The SimG4 package, which is based on Geant4, then takes over the muon beam simulation and tracking of particles to the detectors. These energy deposits, referred to as G4Hits, can then be converted to realistic electronic detector-readouts by the SimDetectorResponse package. On most occasions, though, the G4Hits are first reshuffled with G4Hits from other Proton-on-Target (POT) events so that a realistic bunch structure is built up and processed, since it is this structure that the true detector will see. SimG4 produces one output event for every primary

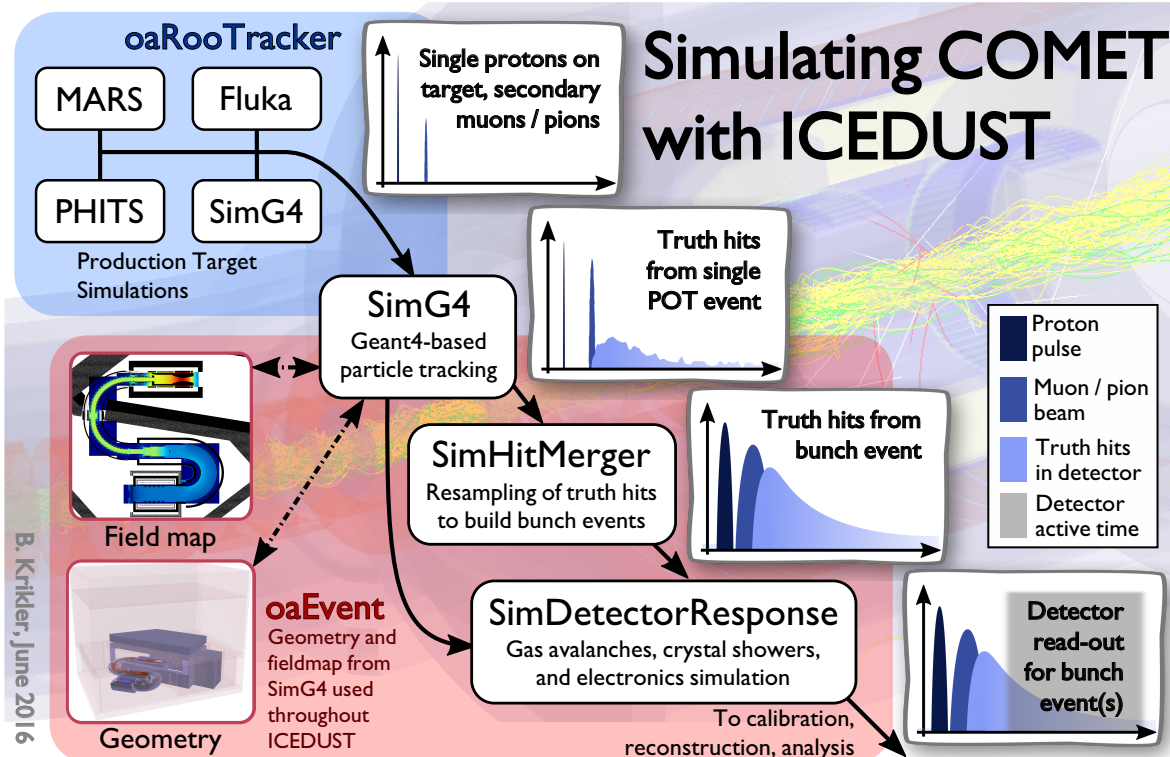


Figure 4.3: Diagram showing the stages used to simulate COMET. The timing schematics on the right show how a simulated event is built up, firstly by producing many individual proton interactions with the production target, then by transporting the secondary particles to produce energy deposits in the detector, which are then combined with the truth hits from other proton events to produce a realistic bunch structure. Finally, these bunch events are processed through the detector response simulation to produce fake waveforms and other detector read-outs.

vertex introduced², whereas SimDetectorResponse needs to produce the same sort of data structure as will be seen in the real experiment, which is one event per proton bunch.

This requires some intermediate step, known as the SimHitMerger, to shuffle the events from SimG4 together and build up realistic bunch events. This is one point where a degree of resampling is introduced, since there are virtually no correlations between proton events. Within a SimG4 output event all timing is given with respect to the original primary vertex. Since protons on target are introduced at $t = 0$, all G4Hits have their timing given with respect to the proton arriving at the production target. In the process of building bunch events, a realistic timing structure for the proton beam is

²This typically means one output event per proton-on-target, but in principle could be something else, such as one output event per signal electron in a dedicated trigger simulation

introduced by shifting the time of all hits for a given proton event by a fixed amount, as if the proton had arrived slightly earlier or later.

A bunch event in Phase-I will consist of about 8×10^6 POT so, without resampling, a simulation of 8×10^8 POT events, for example, could only produce 100 bunches. Since the proton events are uncorrelated, by picking different proton events and applying different time shifts to each one it is possible, in principle, to build a much larger number of bunch events.

An additional form of resampling can also be used during the Geant4 simulation, by dividing up the experiment into different stages and restarting the simulation multiple times at a later stage, reusing the output from the earlier section. For example, a simulation of the production target region is used to track particles up to the boundary of the muon beam line. The muon beam simulation is then repeated multiple times using the particles that left the production target section as an input and changing the initial random seed for each restart. This technique was used in the most recent large scale mass production twice—once at the production target section and again at the entrance to the detector solenoid region—restarting the simulation five times for each section, so that for each initial proton on target, 25 times this number of events were tracked through the detector solenoid.

Both of these resampling techniques must be handled with care since this can produce correlations between the events produced from resampled inputs. Reconstruction methods often employ machine learning techniques which are particularly sensitive to correlations within a dataset. To reduce any potential impact due to resampling, the resampled data is handled in distinct sets so that within a set no proton on target event is repeated in more than one output bunch event.

4.3.1 Handling Geometry

During the change from ND280 to ICEDUST, a new geometry handling scheme was introduced to the SimG4 package. This change was motivated by: the fact that COMET has a large number of components with a large variety of complexities, shapes, and sizes; the COMET geometry will change dramatically throughout the lifetime of the experiment; all pieces of material close to the beam could potentially contribute to background rates if, for example, they scatter high energy particles into a high-acceptance region of phase space.

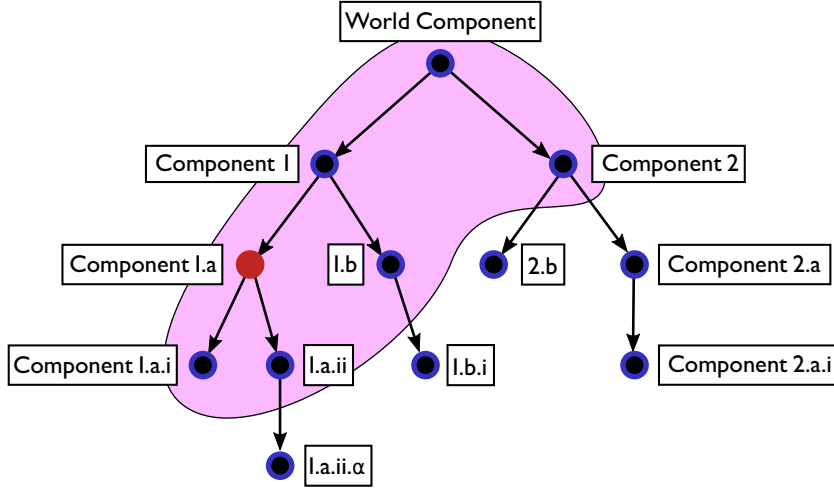


Figure 4.4: How parameters are shared amongst different components. Parameters of component 1.a (in red) can access the value of parameters owned by components contained in the larger violet region.

The aim of the new geometry handling scheme tries to address these issues. The goals in developing the new approach were to:

- define a clear mechanism for how the geometry is implemented and controlled;
- decouple the code for physically isolated parts of the experiment;
- provide the flexibility to add and remove parts of the experiment;
- maximise the maintainability of the code related to geometry;
- allow for easy inspection of both the geometry and the various parameters that control it.

The final scheme uses a nested component structure, which is built up using compiled c++ to define the volume hierarchy in a modular way, with parameters provided at run-time to define the actual shapes and locations of the volumes. The run-time parameters are ‘owned’ by the component they are attributed to and can be assigned values based on that of other parameters and inspected easily by various print commands. Access to the values of other parameters is possible if and only if they are owned by an accessible component. Whether or not another component is accessible depends on its relative position in the component hierarchy: the target component must either be an ancestor, immediate child, or share the same parent component, as demonstrated in Fig. 4.4.

To provide the value of a parameter, standard, human-readable, infix notation allows arithmetic between integers, floating point numbers, three-vectors, and rotation matrices. In addition, parameters can be easily repeated or indexed, such as for the positions of

```

/comet/Torus2/TS4_First/Dimension InnerR = 23*cm
/comet/Torus2/TS4_First/Dimension OuterR = [InnerR]+22*mm
/comet/Torus2/TS4_First/Dimension Length = 10*cm
/comet/Torus2/TS4_First/Material Material = Copper

/comet/Torus2/TS4_Middle/Dimension InnerR = 23*cm
/comet/Torus2/TS4_Middle/Dimension OuterR = [InnerR]+43*mm
/comet/Torus2/TS4_Middle/Dimension Length = 10*cm
/comet/Torus2/TS4_Middle/Material Material = Copper

/comet/Torus2/TS4_Last/Dimension InnerR = 23*cm
/comet/Torus2/TS4_Last/Dimension OuterR = [InnerR]+43*mm
/comet/Torus2/TS4_Last/Dimension Length = 10*cm
/comet/Torus2/TS4_Last/Material Material = Copper

/comet/Torus2/Count Coils:Count = 16
/comet/Torus2/Angle Coils:PositionPhiStart = 0*degree
/comet/Torus2/Angle Coils:PositionDeltaPhi \
    = ([PhiTotal]-2*[Coils:PositionPhiStart])/([Coils:Count]-1)
/comet/Torus2/Position (i<[Coils:Count]) Coils:Position \
    = ( r=[LargeRadius], theta=90*degree, \
        phi=[Coils:PositionPhiStart]+[i]*[Coils:PositionDeltaPhi])
/comet/Torus2/Rotation (i<[Coils:Count]) Coils:Rotation \
    = (axis=(1,0,0),angle=90*degree) \
    *( axis=(0,1,0), \
        angle=[Coils:PositionPhiStart]+[i]*[Coils:PositionDeltaPhi])

```

Figure 4.5: An example set of parameter definitions which control the geometry for the Torus2. Parameter specifications use natural arithmetic notation and can reference other parameters and use standard units. They can also be formed as sets where each element has a different value, such as the Coils:Position parameter.

crystals in the ECAL or straws in a straw tracker plane, where the i^{th} position depends on the value of i . A demonstration of valid parameter assignments is shown in Fig. 4.5.

Using this scheme, multiple ‘worlds’ have been developed corresponding to different stages and run-configurations of COMET, between which a user can easily change. Each world is able to re-use much of the code for another, such as the experiment hall building, which appears in every world. In addition, it has been straight forward to build up significant complexity in key areas such as the production target. Fig. 4.6 shows two of the available worlds that have been created using this scheme.

A more thorough description of the geometry scheme in SimG4, as well as a users guide and walk-through, can be found at www.hep.ph.ic.ac.uk/~bek07/comet/SimG4/documentation/index.shtml.

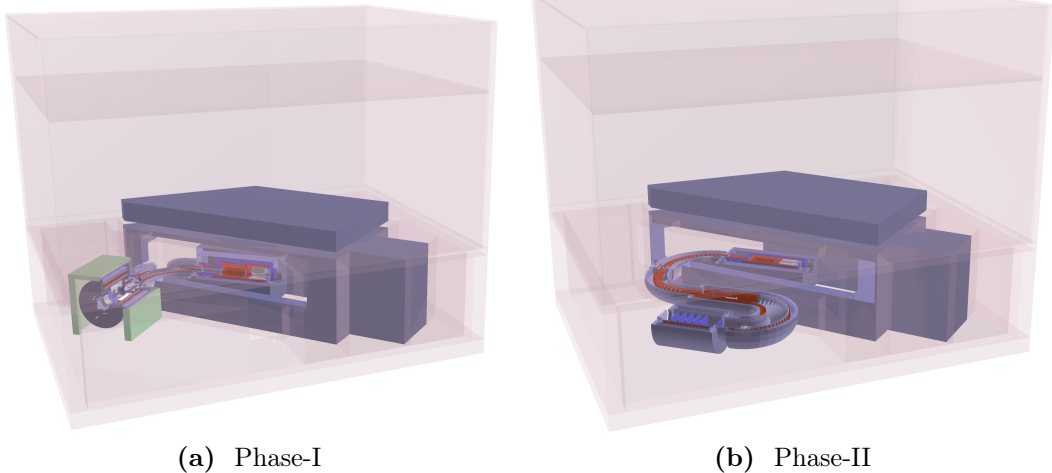


Figure 4.6: Two of the possible simulation ‘worlds’ that can be selected at run-time: (a) Phase-I with the CyDet detector installed, and (b) Phase-II. Multiple Phase-I worlds exist, one for each potential running configuration.

Once SimG4 has created the geometry, it writes it out to a ROOT-based format alongside the data, using ROOT’s TGeo classes [64]. This is then used by the other packages, such as calibration and analysis. The event display also uses this to show the various hits and tracks overlaid on the geometry.

4.3.2 Field Calculation

An essential aspect of the COMET experiment is the static magnetic field that is used along the beam line to capture, focus, or disperse charged particles. Modelling this field accurately is important to ensure any outcomes of the simulation are reliable. In particular, local reductions in the field strength risk mirroring particles backwards or even trapping particles for extended periods. This could be especially dangerous for COMET since, in the process, the timing information of the particle is lost, reducing the effectiveness of the timing cut to suppress backgrounds.

Magnetic field calculations can become quite computationally expensive. As a result, approximations and assumptions are often made to simplify the process, such as the assumption of symmetry about an axis or plane to reduce the effective number of dimensions to the problem. As well as modelling the current in the coils, material effects should also be accounted for, particularly in the yoke and surrounding material of the beamline. Often these material effects are linear, but in regions of high magnetic field this

linearity can be lost via processes such as saturation, further increasing the computational complexity.

There are two distinct types of magnetic field used in COMET: a solenoidal field produced by a winding of superconducting cable in a spiral, and that of the dipole fields, which are produced by a novel winding technique that is proprietary to Toshiba. Although there are several areas of ‘bent’ solenoid, these are actually formed by a series of smaller straight solenoid sections and so do not need special treatment in the field calculation. Straight solenoids are used in many other applications such that existing coil calculation methods are reliable. Calculating the dipole field, however, is not so straightforward since the exact configuration is owned by Toshiba.

The COMET collaboration have used several different methods to perform field map calculations. G4Beamline [65] is a simulation toolkit that makes numerous extensions to Geant4 and is able to perform simple solenoid calculations directly. Whilst it cannot model material effects, its speed and simplicity allows quick and simple studies. The methods for solenoid calculations of this open-source project have been incorporated into SimG4, so that the package can directly produce the field for solenoid coils contained in its geometry. The resultant fieldmap is shown in Fig. 4.7b.

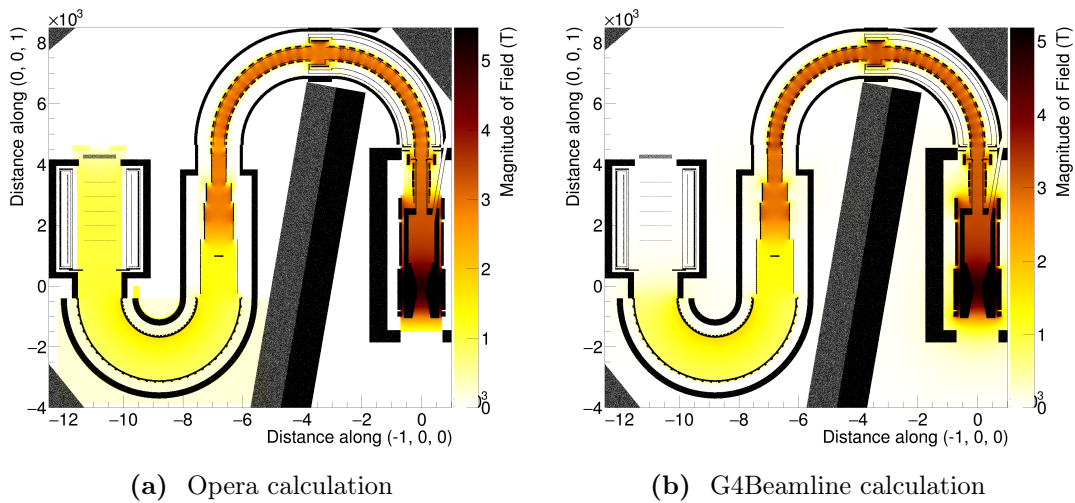


Figure 4.7: Fieldmap produced by (a) Opera and (b) G4Beamline. Although the fringe field is larger with the G4Beamline calculation, the lack of material effects make this calculation less reliable. Note that the G4Beamline calculation does not include the detector solenoid.

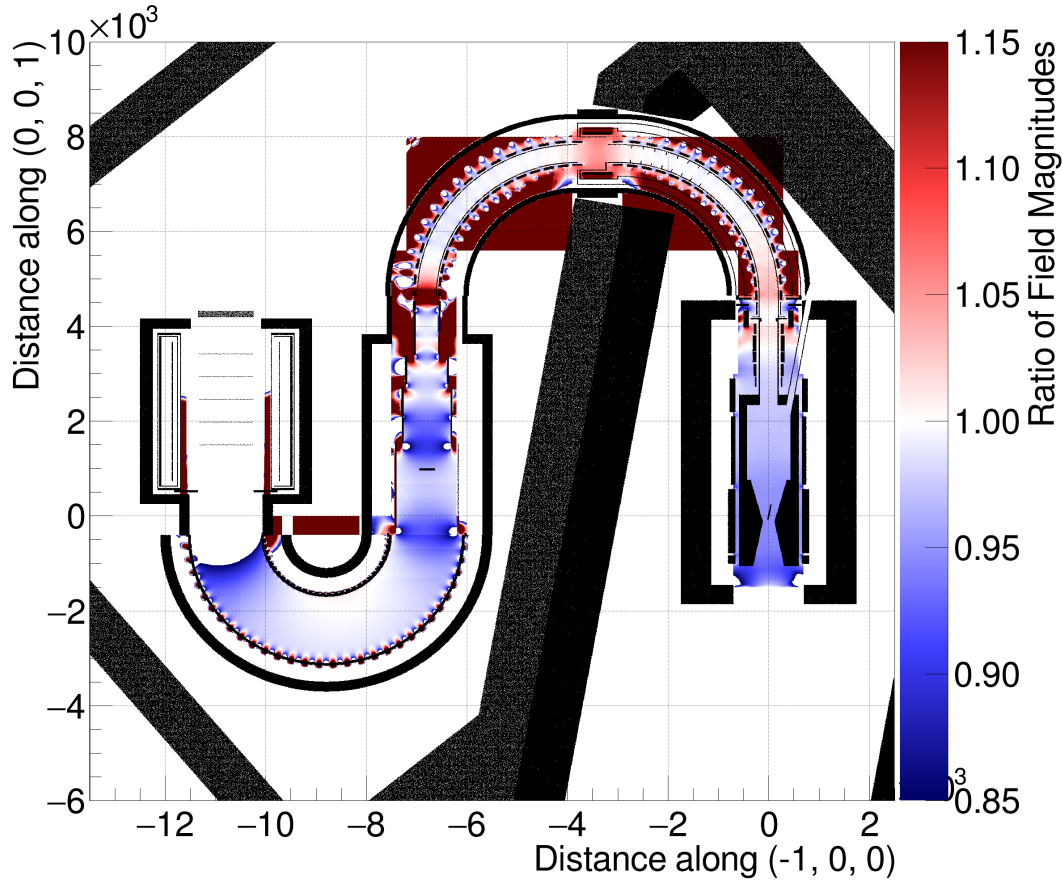


Figure 4.8: The ratio of the Opera and G4Beamline calculations shown in Fig. 4.7. For most of the field within the beamline the calculations agree within 10%, although around the ends of the solenoids the agreement is poorer.

For more elaborate calculations, Opera 3D finite-element-analysis software was used with the TOSCA sub-module [66] for static electromagnetic fields. This calculation includes non-linear material effects in the yoke and shielding so that the final fieldmap should be much more accurate. Fig. 4.7a shows the fieldmap calculated by Opera in the plane of the beam line axis. The ratio between the G4Beamline and Opera calculations is given in Fig. 4.8, where it can be seen how the two models disagree most at the exit of the solenoids.

Whilst the above two methods have been used for the solenoid fields, calculating the dipole field structure is a different story, given that the winding is proprietary information belonging to Toshiba. For the dipoles in the muon beamline Toshiba have provided a calculation for one octant of one winding, which is then mirrored and placed multiple

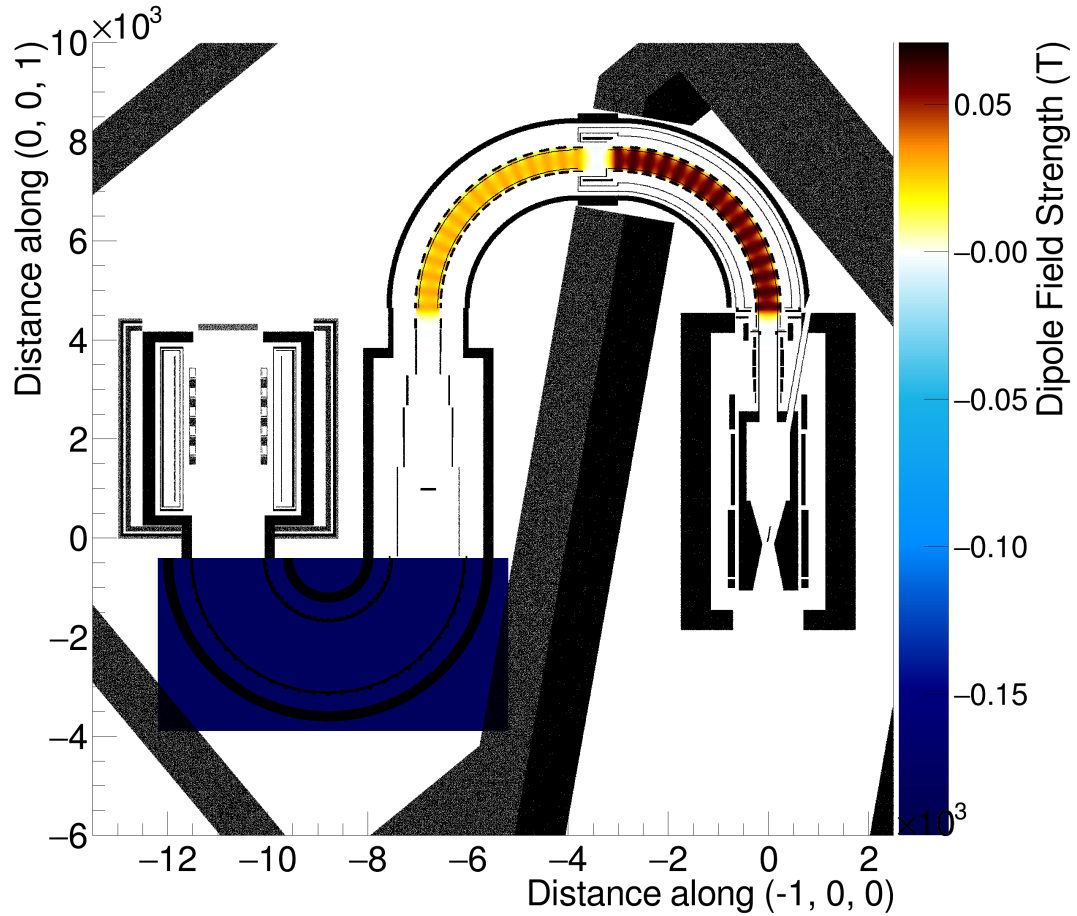


Figure 4.9: The dipole field calculations used in ICEDUST for Phase-II. Three dipoles are applied in COMET, one over each of the Torus1, Torus2 and the Electron Spectrometer. The dipoles over the bent muon transport beamline point in the opposite direction to that over the electron spectrometer. It can also be seen that the calculation for the dipole along the muon transport beamline contains realistic features (fringe fields, non-uniformities, etc) whilst the dipole field for the electron spectrometer is artificially uniform.

times along the beamline. For the dipoles along the electron spectrometer of Phase-II there is no accurate calculation at this time. The dipole field is shown in Fig. 4.9.

Whilst only magnetic fields have been used in the simulation up to now, ICEDUST is able to handle electric fields in exactly the same way. For instance future work might see the electric fields for the straw tracker and CDC included to account for the impact that these fields might have on particle scattering in the detector.

Field map files are treated as a single data file which are loaded in and placed with a given rotation and translation as well as an overall field scale factor. It is important that subsequent processing of data files be able to reproduce the same field as used to

generate the data. Since many individual field map files are often loaded in to assemble an overall representation of the field to facilitate such book-keeping, a description of each of the used fieldmap files is stored alongside the data, in a similar way to the geometry. This information contains the name and a check-sum for the original fieldmap file as well as the rotation, translation, and scale factor. Given a data file and the location of a directory containing the fieldmap files, all ICEDUST programs are, therefore, able to re-instantiate the field. Other types of field component, such as the solenoid fields produced with the incorporated G4Beamline code, are also persisted and re-instantiated in this manner.

4.3.3 Production Target Simulations

There is currently a lack of experimental data for interactions of protons with 8 GeV kinetic energy with a tungsten target, especially for production of negative pions in the backwards direction. Fig. 3.1 seems to be the best source of experimental data, but even this is problematic in that it represents 10.1 GeV protons striking a tantalum target and that the actual data points are not tabulated anywhere in the literature.

The HARP experiment [68] has also measured pion yields in the context of future neutrino beam facilities and have used an 8 GeV proton beam with a tungsten target

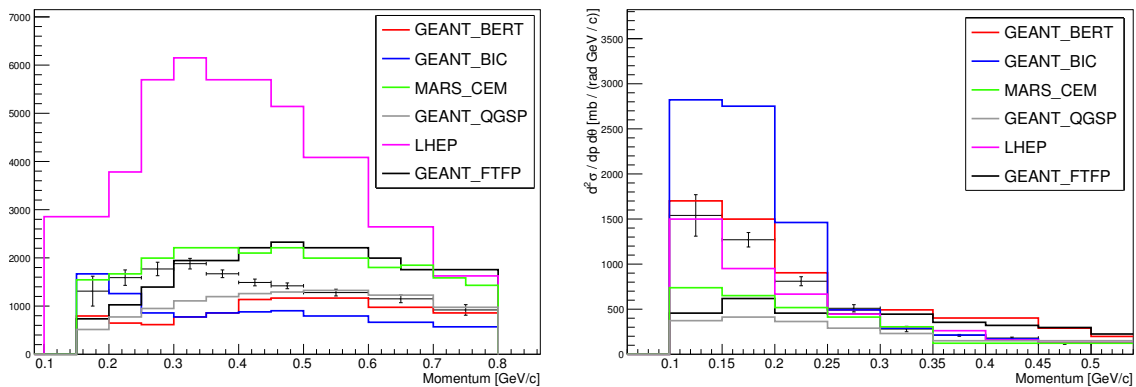


Figure 4.10: Comparison of various hadron production codes with experimental data from the HARP experiment, taken from the thesis of A. Edmonds [67]. Points with error bars are the experimental data. Left: double differential-production cross-section for pion production from 20 to 32° with respect to the incoming proton direction; right: from 100 to 112°. The hadron production code that best reproduces the data depends strongly on the angular region under consideration.

Unfortunately they only observed pion yields at angles of less than around 2 radians for such a combination of target and proton energy.

As a result of this shortage of measured values, it is important to use as many hadron models as possible to pin down the uncertainty on the predicted pion and muon yield. Previous studies have compared the HARP data to predictions from several hadron codes [67, 69] some of which are reproduced in Fig. 4.10. From these it is clear that no one model can reproduce the experimental data accurately for all angular regions and all materials.

Currently, PHITS [61], MARS [62], Fluka [63], and Geant4 [48] can all be used to run production target simulations and feed results into the rest of the experiment. The level of integration of these packages varies, however. SimG4 (which is based on Geant4) and SimMARS (which interfaces MARS into ICEDUST) are able to read directly the standard ICEDUST geometry and fieldmap formats and they are able to output directly to a format known as oaRooTracker, which the SimG4 package is able to read back in. On the other hand, both Fluka and PHITS (interfaced via SimFluka and SimPHITS, respectively) are written in Fortran and have proved harder to integrate. At this point in time, each must separately produce the geometry and fieldmap and have their outputs post-converted to the oaRooTracker format. Fluka also lacks a primitive Torus volume implementation, so that other studies such as neutron rates are further limited in Fluka at this stage.

4.3.4 Extending the Geant4 Physics Modelling

Geant4 physics modelling

Aside from the production target region, most of the tracking of particles and creation of secondaries takes place in the SimG4 package, which is built against the Geant4 library. In Geant4, the trajectory of a particle is built up in steps, each of which terminates either by a physics process (which might change the particle's direction or energy, or produce secondary tracks) or by the boundary of a volume in the simulated geometry. To decide what actually limits the step taken by a given particle (a positron, for example), Geant4 calls the list of possible processes this particle can undergo (for example Bremsstrahlung, annihilation, inverse Compton scattering, etc.) and asks each process for a proposed step length. In the case of a geometry limit, the step length is the distance until the boundary of the geometry, including deflections to the trajectory due to any electromagnetic field.

On the other hand, for a physics process the proposed step length is typically selected randomly using a relevant probability distribution for this process. Often this involves a characteristic length or time of the process, for example the half-life of a particle that will decay. Out of all possible step limits, the process proposing the shortest limit (or, if the particle is at rest, the soonest limit) is chosen. The current position and momentum of the particle is updated accordingly and any secondary particles produced are prepared for tracking.

Determining which processes are applied to which particles and how each process is modelled is an important part of building a Geant4 simulation; the library provides a list of standard physics lists to help the process. Choosing the right physics list depends on the goal of the simulation, for example which particles are involved; what energy ranges are interesting; and which background effects must be included. To simulate COMET the QGSP_BERT_HP physics list [71] was chosen as a starting point. This model is expected to perform well for low energy dosimetry, shielding, and neutron calculations [72].

On top of this physics list, custom changes have been made to the way negative muons are treated once stopped in material. COMET is somewhat unusual in the field of modern particle physics for dealing with muons at very low energy, unlike at the Organisation européenne pour la recherche nucléaire (CERN) experiments, for example, where they are normally treated as minimally-ionising particles (MIPs). As a result, the modelling of low-energy negative muons is relatively simplistic in the default physics processes of Geant4. In addition to this, for the COMET experiment it is important to add the process of coherent μ - e conversion, which, as a currently unobserved process, is not included in Geant4.

In the Standard Model (SM), a stopped negative muon that has been captured to an atomic orbital can either undergo decay or nuclear capture. As previously discussed, the end-point for electrons coming from muon DIO reaches up to the μ - e conversion limit, or around 105 MeV/c. Vanilla Geant4, however, is unable to produce this tail, and on aluminium is only able to produce electrons up to around 60 MeV/c. This is because the bound muon decay model in Geant4 uses the free muon decay spectrum and applies a boost in a random direction, with the boost factor set by the muon binding energy. A comparison of the electron spectrum from this model and that proposed by Czarnecki et al. [34] is shown in Fig. 4.11a, where it can be seen how the high energy tail falls far more rapidly in the Geant4 spectrum.

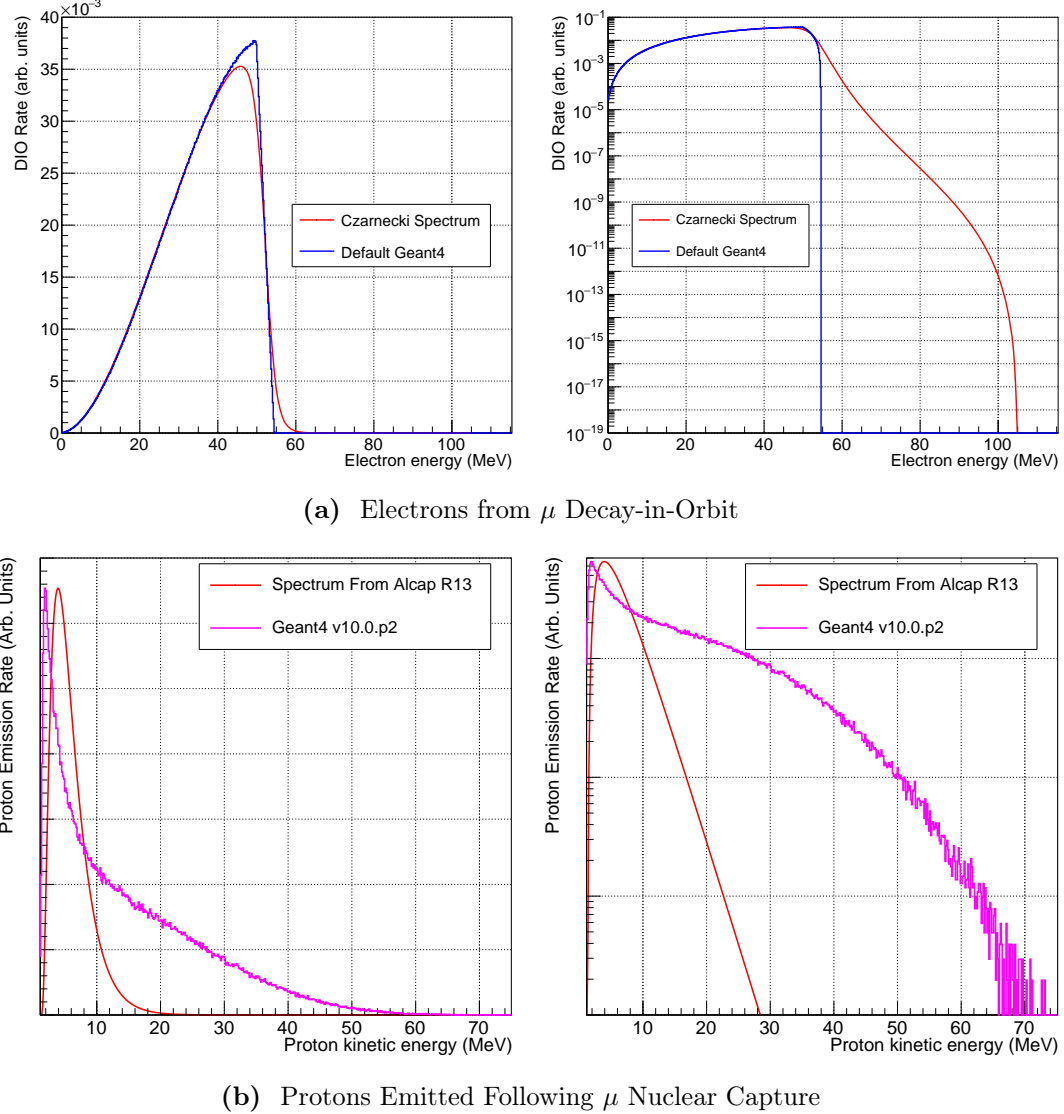


Figure 4.11: Comparison of the realistic spectra for DIO electrons, (a) (normalised to agree at 35 MeV), and protons coming from muon nuclear capture, (b) (normalised to have the same maximum value), each on a linear scale (left) and a logarithmic scale (right). The DIO spectrum used in default Geant4 has a sharp cut-off slightly above the free muon decay end-point, to be compared with the long but steeply falling tail of the Czarnecki et al. theoretical calculation [34]. Comparison of protons coming from muon capture between the preliminary result from AlCap [70, 38] and default Geant4 shows that the true proton spectrum is much softer than the Geant4 model.

Similarly, for the nuclear capture of the muon, there are sizeable disagreements between the available (but limited) data and the default Geant4 model. For example, the AlCap experiment [38] has improved the knowledge of proton emission following muon nuclear capture in aluminium. This showed that proton emission occurs for around 3 % of all nuclear captured muons; Geant4 produces around 7 to 8 times more than this. The overall shapes of the proton spectra also disagree. Although the AlCap result is still only preliminary, the spectrum that has been observed is much softer than that produced by standard Geant4, as shown in Fig. 4.11b.

Standard Geant4 models nuclear capture of negative muons using a Bertini cascade which was developed using incident hadrons [73]. Muon nuclear capture is thought to occur via a combination of direct capture on a proton, producing a neutron, or via an interaction with a set of clustered nucleons. The latter is typically invoked to explain proton emission. The Bertini cascade model handles negative muon capture by first handling the prompt process of muon capture on the nucleons, then cascading the resultant nucleons through the nucleus. A point within the nucleus is chosen homogeneously and then the muon interacted with either a single proton or a nucleon pair. It is not clear, at this stage, what causes the discrepancy between this model and the experimentally observed result for proton emissions.

Extending the physics processes

To resolve these issues, custom physics classes have been added to the COMET simulation. The key design goal of these classes was to allow future improvements in the experimental and theoretical inputs to be added, yet decouple the implementation from the normal Geant4 implementation so that future updates to Geant4 could easily be absorbed.

Fig. 4.12 shows the class interaction diagram for the extended physics modelling for stopped negative muons. The standard Geant4 model sets up these processes using the ‘G4MuonMinusCapture’ class, which passes concrete implementations for decay and nuclear capture into its base-class ‘G4HadronStoppingProcess’. This base-class contains three instances of a ‘G4HadronicInteraction’: one to perform the electromagnetic cascade between the atomic orbitals; another to perform DIO; and a third to perform the nuclear capture. The ‘G4HadronStoppingProcess’ class is also used to simulate stopped negative pions, kaons, and so on, and bound decay is only considered if a valid instance of such a process has been provided. When a stopped particle is processed through this class, the electromagnetic cascade is always run first, producing X-rays and Auger electrons.

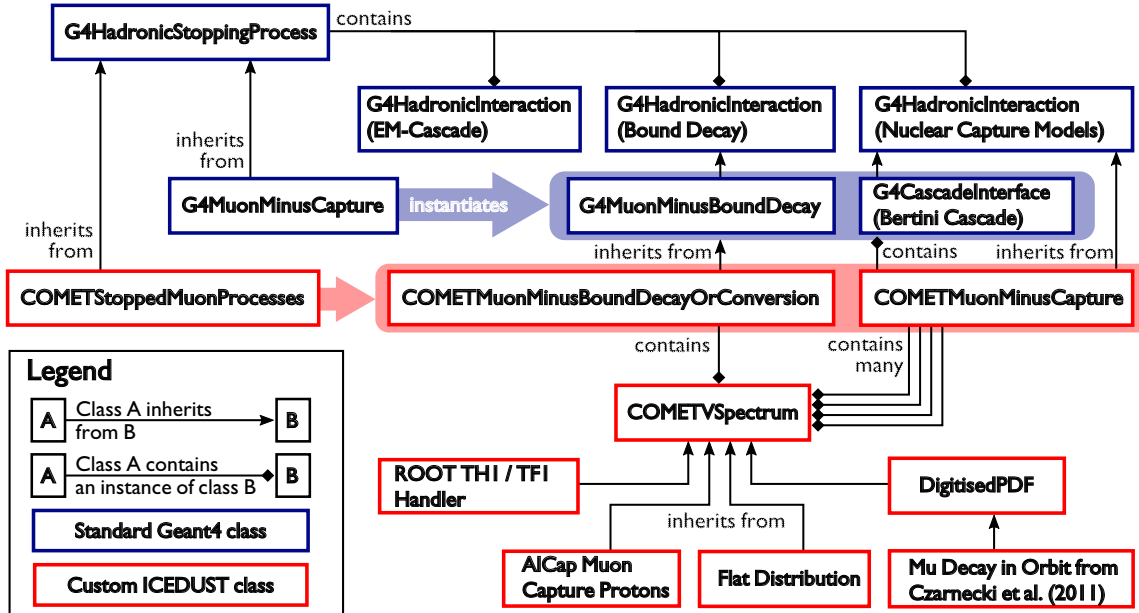


Figure 4.12: The various classes involved in simulating the various processes of stopped negative muons. The standard Geant4 model is activated by registering ‘G4MuonMinusCapture’, which instantiates ‘G4MuonMinusBoundDecay’ and ‘G4CascadeInterface’ to run the DIO and nuclear capture respectively. To use the custom COMET muon physics, an instance of ‘COMETStoppedMuonProcess’ should be registered, which sets up ‘COMETMuonMinusBoundDecayOrConversion’ to produce the electron (and possibly neutrinos) from DIO or conversion, and ‘COMETMuonMinusCapture’ to do the nuclear capture.

Then one of either bound decay or nuclear capture is chosen by asking the bound decay process whether or not it will kill the particle; if so, bound decay is considered to have taken place and the nuclear capture is not run. Default Geant4 uses nuclear capture rates based on a 1987 paper by Suzuki et al. [49], filling in experimental blanks with a semi-empirical model, and decay rates based on a largely theoretical 1977 model by Mukhopadhyay [74]. Fig. 3.3 was produced by extracting these parameters.

To extend the default Geant4 modelling and include the improved theoretical understanding of the DIO process and measurements of muon nuclear capture, three new classes have been written which mirror the way the default Geant4 model is implemented but add more detail. These new classes are shown in Fig. 4.12 in red. Currently they only play a role if the muon stops in aluminium otherwise they invoke directly the default Geant4 model. ‘COMETMuonMinusBoundDecayOrConversion’ takes over the task of bound decay by first deciding whether to capture, decay, or convert based on rates which can be adjusted at run-time by Geant4 commands. The default rates are

the normal Geant4 rates of capture and decay and a conversion rate of 10^{-15} (which is multiplied by the capture rate to get the total conversion branching ratio). If the conversion process is chosen, an electron with total energy of 104.97 MeV is produced in a random direction. If decay is chosen, a DIO spectrum is used to randomly generate an energy, which at the time of writing defaults to the 2011 Czarnecki spectrum [34], although other spectra can be specified at run-time. If neither of these processes are selected, then the ‘COMETMuonMinusBoundDecayOrConversion’ class returns, leaving the muon status as alive such that the capture process takes place. At this point, control would pass to the ‘COMETMuonMinusCapture’ class, which contains an instance of the default Geant4 Bertini Cascade model to use for materials other than aluminium. Run-time controls allow the default model to be re-enabled for aluminium.

The ‘COMETMuonMinusCapture’ class contains a list of types of secondary particle which it is able to produce. For each possible secondary, both a spectrum and the total production probability per capture must be supplied. When a muon captures in aluminium, firstly the default model is run. Then, for each of the secondaries produced by this, if a custom rate and spectrum have been provided for a particle of this type, the secondary from the Bertini cascade is removed. Next, for each of the particles that do have custom rates and spectra, a particle is produced with the given probability and each of these particles assigned an energy given randomly according to the selected spectrum. By using the default model first, particles for which experimental rates or spectra do not exist can still be produced in the simulation.

There are, however, some downsides to this approach. Although the remnant nucleus is not actually tracked, in principle energy conservation is not guaranteed since the custom models do not work with the default model to ensure this. In addition, the custom models cannot simulate correlations between different particle types. For example, the probability of emitting a neutron or gamma particle might be dependent on whether or not an alpha particle is emitted. Although such details cannot be included in this modelling, the impact to the outputs of the simulation are expected to be small, if not negligible, since the detector will see particles from hundreds of thousands of stopped muons per bunch, and will not look at the correlations between different particle types.

Finally, to handle the various spectra that might be added to the simulation, a special spectrum and spectrum-factory class design was added. The ‘COMETVSpectrum’ base-class was added to represent the abstract idea of a 1-dimensional spectrum. Custom spectra, such as the Czarnecki DIO spectrum or the AlCap protons from muon capture spectrum, can be included by writing a concrete instance of a spectrum, derived from

'COMETVSpectrum'. Custom physics processes can use these spectra as they like, and since the 'COMETSpectrumFactory' class is able to produce concrete spectra when given a string with the name of the desired spectrum, the custom physics models can easily have different spectra selected by run-time commands. In addition, a new primary particle generator has been added which allows the momentum or energy of a particle to be set according to a named spectrum, which will be identical to the spectrum used in the tracking process. This makes it easy to run specific acceptance studies and also reduces the effort needed to add a new physics model since one spectrum can be written and immediately used by both the primary event generators and the tracking physics.

4.4 Analysis Using the Beamline Coordinate System

The geometry of the COMET beamline makes a single natural coordinate system non-trivial to define. The global coordinate system in ICEDUST defines the origin as the pion production target and sets the +Z direction pointing in the direction of the pion and muon transport solenoids at this point. The positive Y direction points vertically upwards, such that the positive X coordinate points from the production target towards the Phase-II detector solenoid (and is therefore parallel to the beamline at the 90° point, at the end of the Torus1, where the Detector solenoid will sit in Phase-I).

The fact that the beamline bends and even doubles back on itself in Phase-II, makes simple projections to a plane in the global Cartesian coordinate system difficult to interpret. For this reason, the concept of a 'beamline' coordinate system has been implemented into ICEDUST to facilitate a allow for more intuitive data visualisation and to ease some common transformations.

A point in the beamline coordinate system is defined by a distance along the beamline axis and a vertical and horizontal translation in the plane perpendicular to the beamline axis. The mapping of a point, \vec{r} , in cartesian coordinates to a point in beamline coordinates is performed by locating the point, \vec{b} , on the beamline axis closest to \vec{r} . The beamline distance is then the distance travelled along the beamline to reach \vec{b} , whilst the transverse plane coordinates are defined by the vertical and horizontal components of $\vec{b} - \vec{r}$. Fig. 4.13 shows the beamline and horizontal coordinate for points in the X-Z plane changes for the Phase-I geometry.

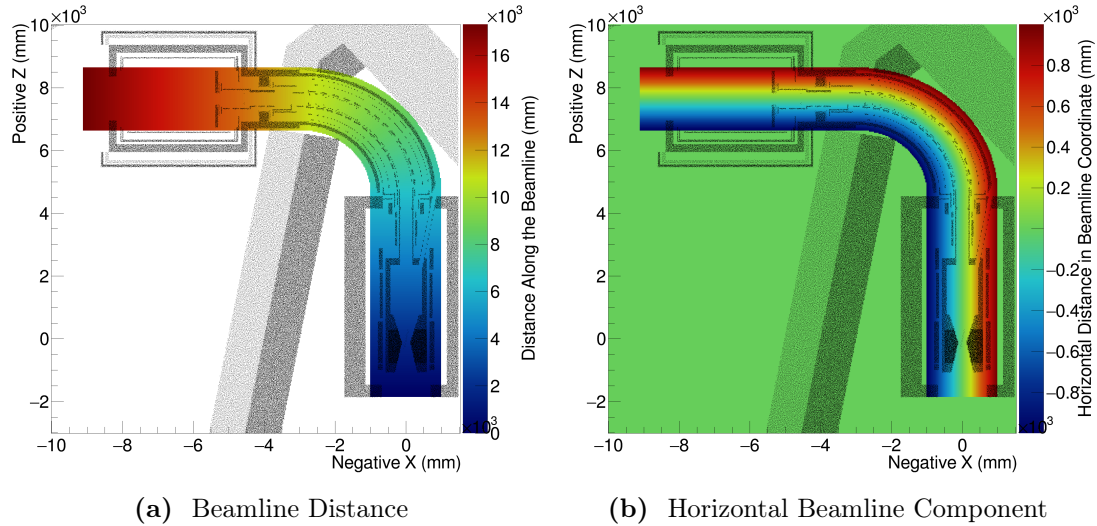


Figure 4.13: The longitudinal (a) and horizontal (b) components of the beamline coordinate system for different points in the global X-Z plane. Although this image shows the Phase-I geometry, the implementation in ICEDUST will semi-automatically adjust to whatever geometry was used.

In order to perform this transformation, one needs to know the shape of the beamline axis itself. Since within ICEDUST this geometry is persisted alongside the data, the beamline shape can be inferred directly from the geometry, using a set of semi-automatic queries to the geometry. This means that the beamline coordinate system should work for both Phase-I and Phase-II geometries or if a component in the beamline is extended.

4.4.1 Distributions as a Function of Distance Along the Beamline

By defining such a beamline coordinate system, studying the evolution of various parameters as a function of the distance along the beamline becomes much easier. This technique is used extensively later in this thesis, to help study and optimise Phase-II.

Fig. 4.14 shows two projections to the beamline coordinate system of simulated data. In Fig. 4.14a, the density of simulated trajectories is shown as a heat-map and as a function of both distance along and the height relative to the beamline is shown. Overlaid on this plot is a slice through the geometry to help interpret where in the experiment each effect occurs. Each trajectory in the simulation is persisted as a list of points along the particle's path. To make such a plot, therefore, one has to force Geant4 to produce

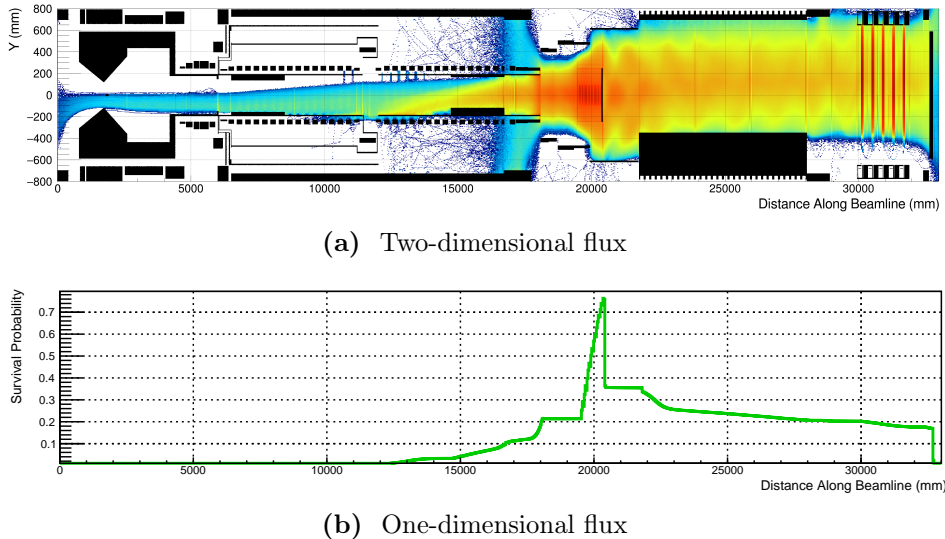


Figure 4.14: Different flux plots that make use of the beamline coordinate system. (a) Projection of trajectories onto the vertical-beamline axis plane. Setting a limit to the maximum step size forces Geant4 to create steps with more regular interval. Each step is then projected to the vertical-beamline surface, such that the density of points represents the flux of particles. (b) A one dimensional flux plot, where every bin between the beginning and end of a particle's track is filled.

a higher-than-normal density of points along each trajectory. However, a step point is always inserted when a particle crosses a boundary in the geometry of the simulation, creating a spike in the density of points at a single surface in the plot, which does not correspond to a physical increase in the particle flux. By taking the profile of this distribution, the mean height of particles at each point along the beamline can be found, which is particularly useful information when studying the bent solenoid dynamics.

Fig. 4.14b shows a one-dimensional flux plot, i.e. the number of particles passing a given point along the beamline. Conceptually this is similar to the above two dimensional plot, however, because of the issue of step points being added when a particle crosses a boundary, the direct projection of the two-dimensional version becomes much harder to read, due to the large spikes produce at these surfaces. Instead, to produce the one-dimensional flux plot, the location of the start and end point of the trajectory is found in the coordinate system and every bin in between these values filled. This works well for trajectories that move at constant longitudinal velocity along the beamline, but introduces an issue when trajectories slow down (which should increase the density of step points) and especially if the particle is mirrored, in which case points will only appear on the same side of the start point as the finish point, and no bins will be filled in the region where the mirroring occurred.

Chapter 5

COMET Phase-II: Optimisation

The last study into the sensitivity of COMET Phase-II was performed in 2009 [45], before the staged approach and Phase-I design had been considered. That study found that a Single-Event Sensitivity (SES) of 2.6×10^{-17} could be achieved in 2×10^7 seconds of running, with a total expected background count of fewer than 0.34 events for the entire run period. Since then, the collaboration’s focus has shifted to research and development for Phase-I and no further studies have been made of the Phase-II design.

The purpose of this chapter is to make use of the updates in the fieldmap calculation, the geometry handling, and physics modelling to revisit the design of Phase-II. In addition to updates in the simulation, some aspects of the actual design have been refined and fixed alongside Phase-I preparation, such as the experiment hall and the superconducting magnet coils and cold-mass of the first stages of the muon beamline. The aspects of the experiment that remain open for optimisation are shown in Table 5.1.

As an initial configuration, much of the design from the 2009 study will be used, with updates included for the areas of the experiment that have since been refined by the Phase-I design.

5.1 Optimisation Strategy

To perform a comprehensive optimisation of Phase-II, there are many parameters to be changed, corresponding to the shapes, positions, field strengths, and so on, of the different regions along the beamline. Table 5.1 lists some 32 parameters, each one of which could be studied. And yet, this number alone does not describe the full challenge of optimising the Phase-II design, since many of these parameters will correlate to one another. For

| Region for optimisation | Approx. No. of parameters |
|---|---------------------------|
| Production target dimensions and location | $3 + 3$ |
| Torus1 dipole field strength | 1 |
| Torus2 dipole field strength | 1 |
| Muon beam collimator shapes, position, and material | $3 + 1 + 1$ |
| Stopping target shape and location | $4 + 3$ |
| Beam blocker position, form, and material | $3 + 3 + 1$ |
| Electron spectrometer dipole field strength | 1 |
| DIO blockers in the spectrometer | 4 |
| Approx. total number of parameters | 32 |

Table 5.1: Aspects of the experiment that can be optimised and estimates for the number of parameters that define each aspect. In the case of the target, beam blocker, and collimator shapes the number of parameters is only approximate; crudely speaking there is at least a width, length and height but in principle one could have a very irregular shape that cannot be parametrised by only three numbers, for example, shapes that change as a function of distance along the beamline.

example, a correlation likely exists between the position and shapes of the muon beam collimator(s), the stopping target, and the beam blocker, since all involve removing or stopping muons and other particles in the beam. Other less intuitive correlations might also exist and a complete optimisation should be able to include the impact of these as well.

A full optimisation study then would involve a scan through a parameter space with at least 32 dimensions. A brute force search of such a space would be nightmarishly slow and require an enormous amount of computing power. Machine learning algorithms or intelligent scanning techniques might be able to tackle such a problem, and perhaps in the future these methods will be used. In the meantime, however, we make use of the technique known as ‘physicist’s intuition’ to approach the problem, whereby some parameters are assumed uncorrelated whilst others are disregarded on the expectation that their impact be small. The goal of this chapter, therefore, is not only to optimise the experiment but also to gain qualitative understanding for the correlations and dependencies between the controlling parameters.

This task is further complicated because it is not just the signal sensitivity that must be maximised, but the background rate that must be kept low. When this work began, no start-to-finish simulation existed to estimate the signal and background rates. As

such, this study will progress by focussing on optimising the signal efficiency in the first instance, and then move to background estimation described in chapter 7.

It is important to note that the outputs of this optimisation should not be considered as final but should instead be treated as a baseline from which more intelligent approaches or physicists can iterate and improve.

5.2 Production Target Optimisation

In the Phase-II Conceptual Design Report (CDR), the production target is given as 16 cm in length and 4 mm in radius [45]. Since then, there have been changes to the magnetic field in this region as well as the lengths and locations of solenoids, shielding and beam-pipe, and the proton beam. Previous studies have looked at comparing the tungsten target proposed for Phase-II to other materials [67], and also drawn a comparison between MARS [62], Geant4 [48] and the limited data available.

5.2.1 Production Target Simulations

The goal of this study is to maximise the total muon and pion yield below 80 MeV at the entrance to the Torus1 bent solenoid, by varying the radius and length of the production target. Whilst it is really the rate at which negative muons stop in the Stopping Target that ought to be optimised, since it is known that muons above about 40 to 50 MeV/c will not stop, and since the bent transport solenoids themselves need optimising, we assume here that maximising the number of muons and pions below 80 MeV/c will also maximise the stopping rate. In addition this has the advantage of increasing the speed of the simulation. The production target is one of the more computationally intensive aspects of the experiment, given the relatively high-energy protons and hadronic nature of their interactions with the target, which together result in a large number of secondaries.

The production target is formed from a solid cylinder of tungsten. To find the optimal target geometry the radius and lengths were both varied individually, and then a combined scan performed where the length was held at the observed optimum. The location and orientation of the target were held fixed, since the axis of the proton beamline is fixed to intercept the muon beam axis at a given point. Once a more realistic proton beam becomes available, the location and direction of the production target would also benefit

from optimisation, however. During the scan over length, the back face of the target was kept fixed, 8 cm away from the point of interception of the proton beamline and muon beamline axes, since the radiation shielding has previously been optimised. Thus only the front face of the target was moved, in order to change the length of the target.

Primary protons were generated according to the description in the 2014 Phase-I TDR [75]. This provides the position profile as a two-dimensional Gaussian ($\sigma_x = 5.8$ mm, $\sigma_y = 2.9$ mm) as well as the spread in energy of the 8 GeV kinetic energy protons ($\sigma_E = 0.135$ MeV). It does not discuss any dispersion or divergence in the beam, however. The proton beam is currently under study, which is why the description at this stage is fairly simplistic. The impact of a more realistic proton beam description will need to be studied in future work.

Protons in the simulation originated from a plane but, since there is some scope to tune the proton beam's position, the input particle plane was moved to remain 1 cm away from the front surface of the target. Since the aim is to maximise the muon and pion yield by varying only the length and radius, shifting the proton beam input plane in this way removes any variation of target acceptance due to divergences of the proton beam in the field before the target. This too will need to be revisited once the proton beam distribution is better understood.

5.2.2 Length Scan

Different length targets were simulated with 3×10^5 Protons-on-Target (POT) for each length. The target length was varied in steps of 8 cm from 8 to 64 cm, whilst the target radius was held fixed at the CDR value of 4 mm. Following a recommendation from the COMET magnet group, the back face of the target was held in a fixed position relative to the rest of the beamline. As a result, the change to the length of the target was produced by moving the front face towards the incoming proton beam, on the basis that the heat-load of the capture solenoid's shielding had been designed with respect to the back face of the target. The back face of the production target is position 8 cm away from the origin of the ICEDUST coordinate system, which is given by the intercept of the proton beamline and capture solenoid's cylindrical axis. Therefore, the production target in these studies becomes asymmetric about the capture solenoid axis for lengths other than 16 cm.

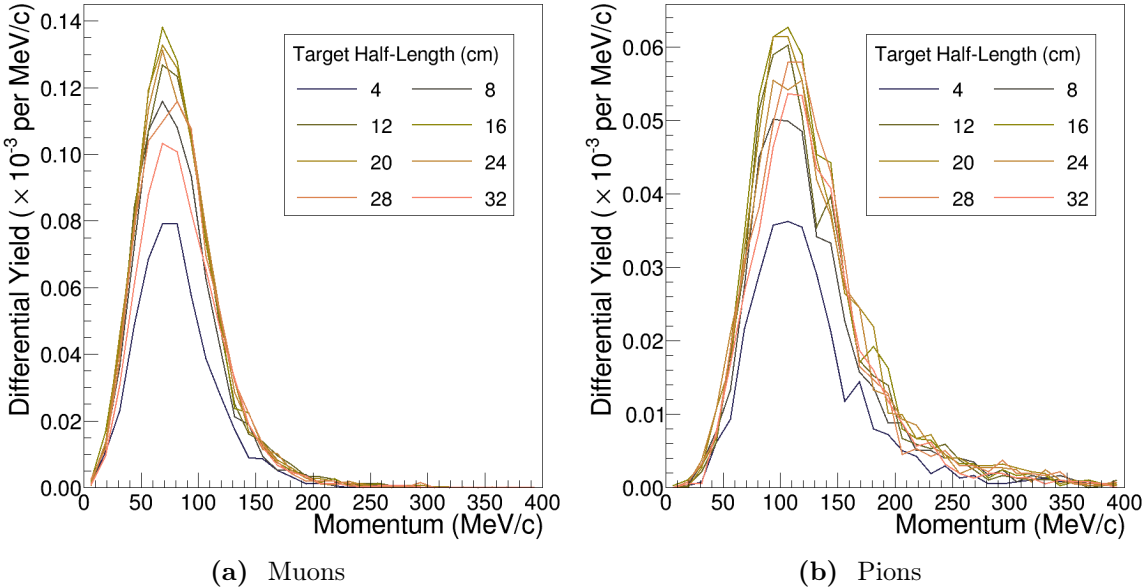


Figure 5.1: Change to momentum distributions at the entrance to the first 90 degrees of the bent muon beam solenoid for different target lengths. Target length is given as half-length which is the Geant4 convention.

Fig. 5.1 shows the momentum distributions of pions and muons for different target lengths (presented as half-lengths following the Geant4 convention). Fig. 5.2 then shows these distributions integrated up to different momenta. From these plots it can be seen that for both muons and pions, the optimum target length occurs around a total length of 32 cm. At lengths greater than this, the pion and muon yields at the entrance to the bent muon transport solenoid begin to reduce. This arises because the front face of the target has moved outside of the acceptance of the capture solenoids, which have an aperture of 18 cm.

Additionally it can be seen from Fig. 5.3 that the shape of the momentum distributions changes only weakly as a function of the target length. These plots were produced by normalising the integrated momentum contours of Fig. 5.2 to the total integral below 400 MeV/c. As a result, it is possible that the actual variation of the shape is even weaker than apparent here, since in the present sample size, the high-momentum tail is not well sampled for small target lengths, such that a skew in the normalisation might occur as events appear above 400 MeV/c.

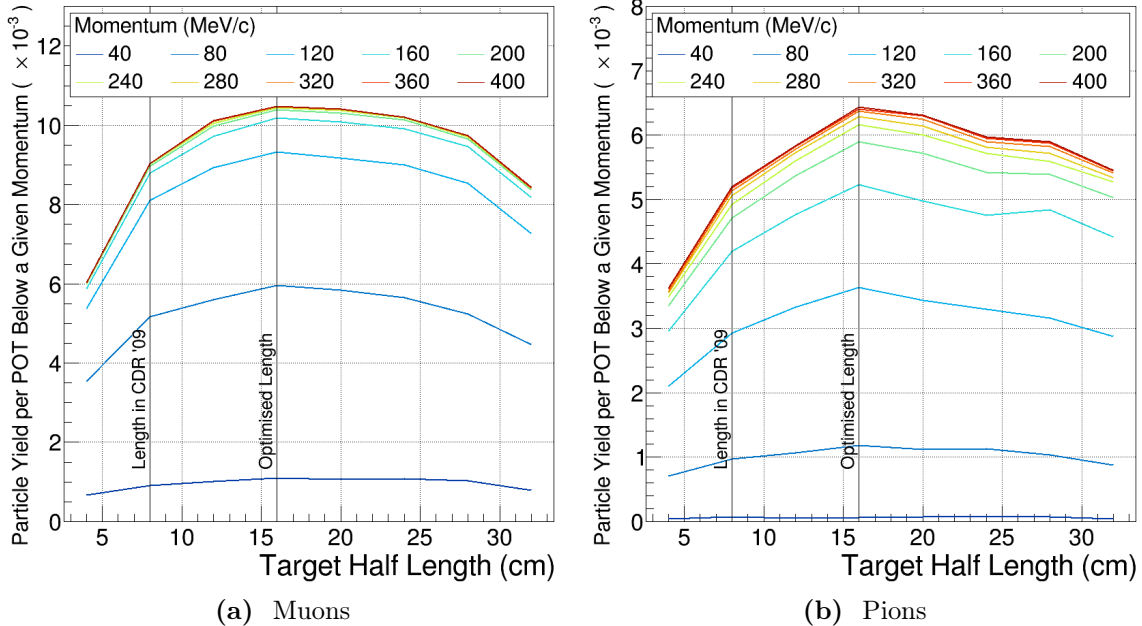


Figure 5.2: Integrated muon and pion yields up to a certain momentum at the entrance to the first 90 degrees of the bent muon beam solenoid as a function of target length.

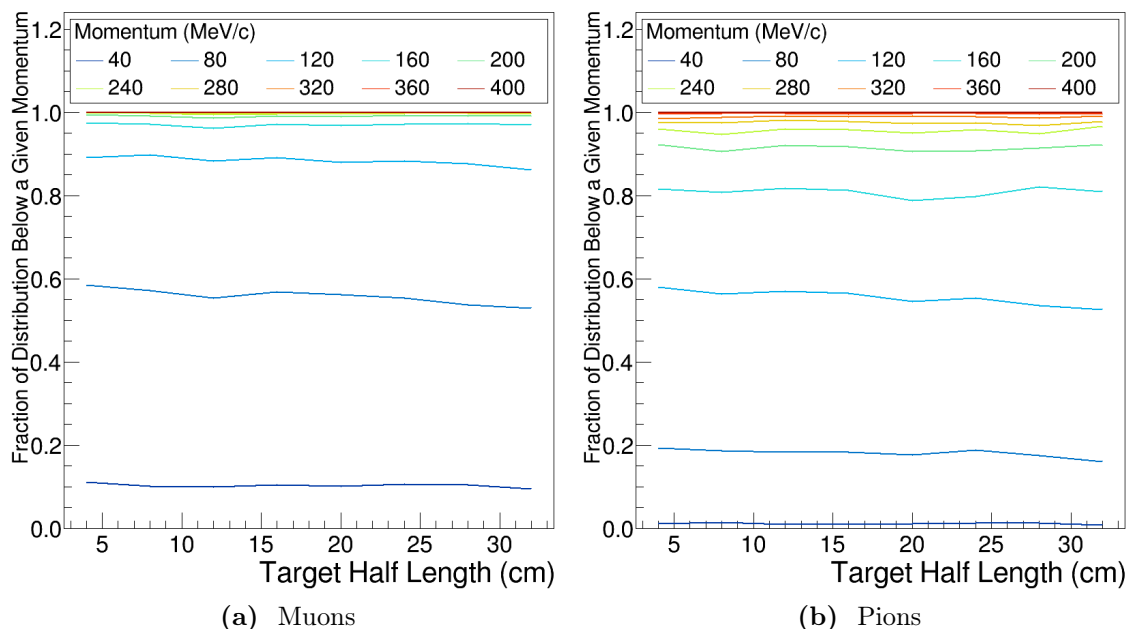


Figure 5.3: Change in the momentum distribution of muons and pions at the entrance to the first 90 degrees of the bent muon beam solenoid as a function of target length.

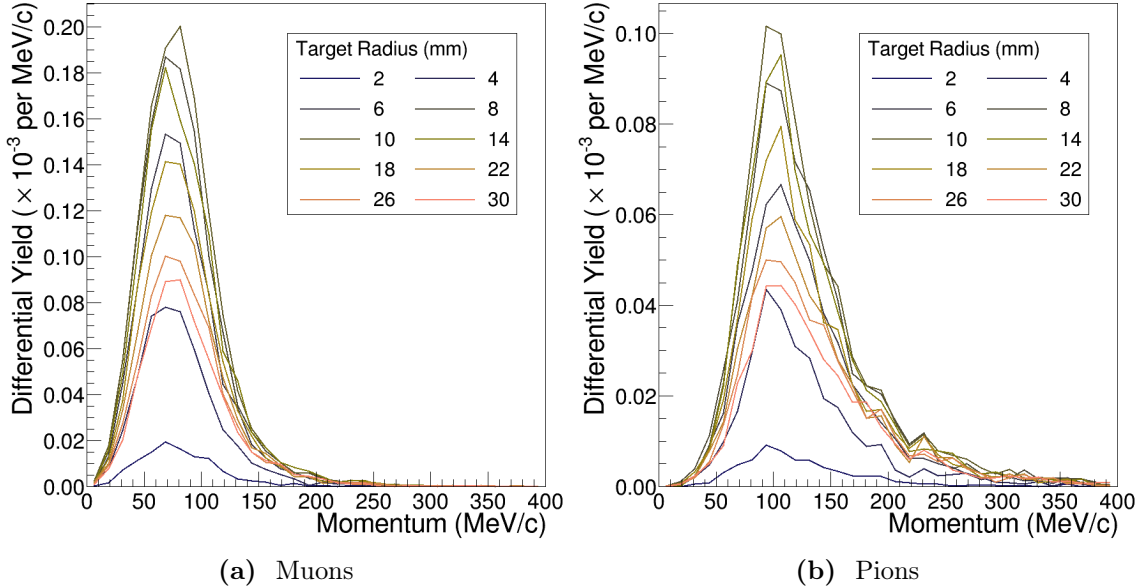


Figure 5.4: Change to momentum distributions at the entrance to the first 90 degrees of the bent muon beam solenoid for different target radii.

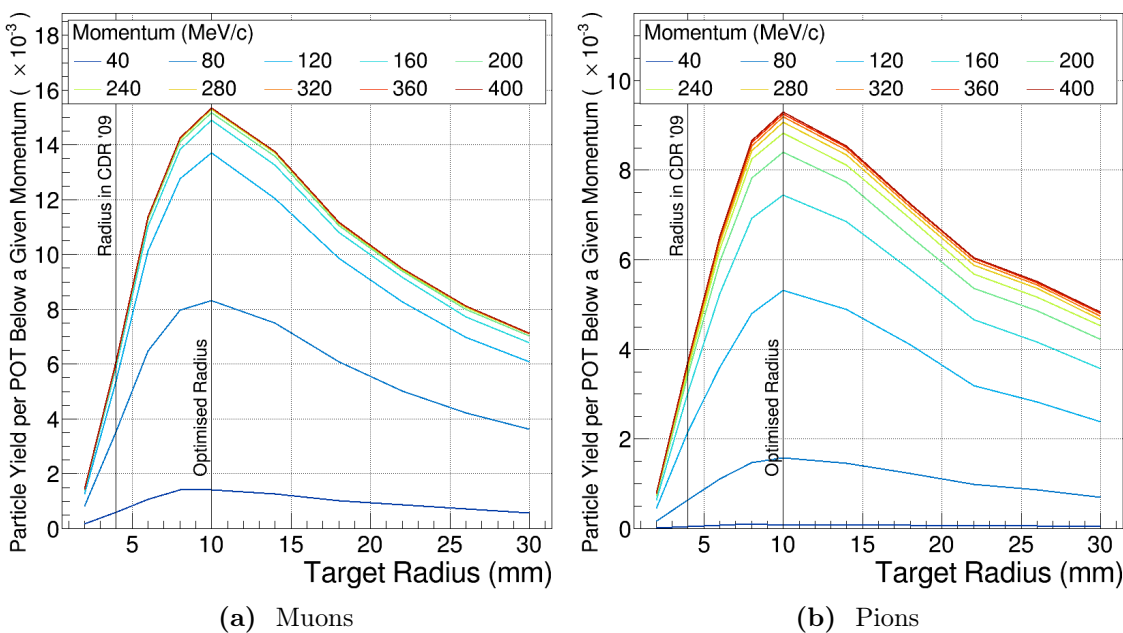


Figure 5.5: Integrated muon and pion yields up to a certain momentum at the entrance to the first 90 degrees of the bent muon beam solenoid as a function of target radius.

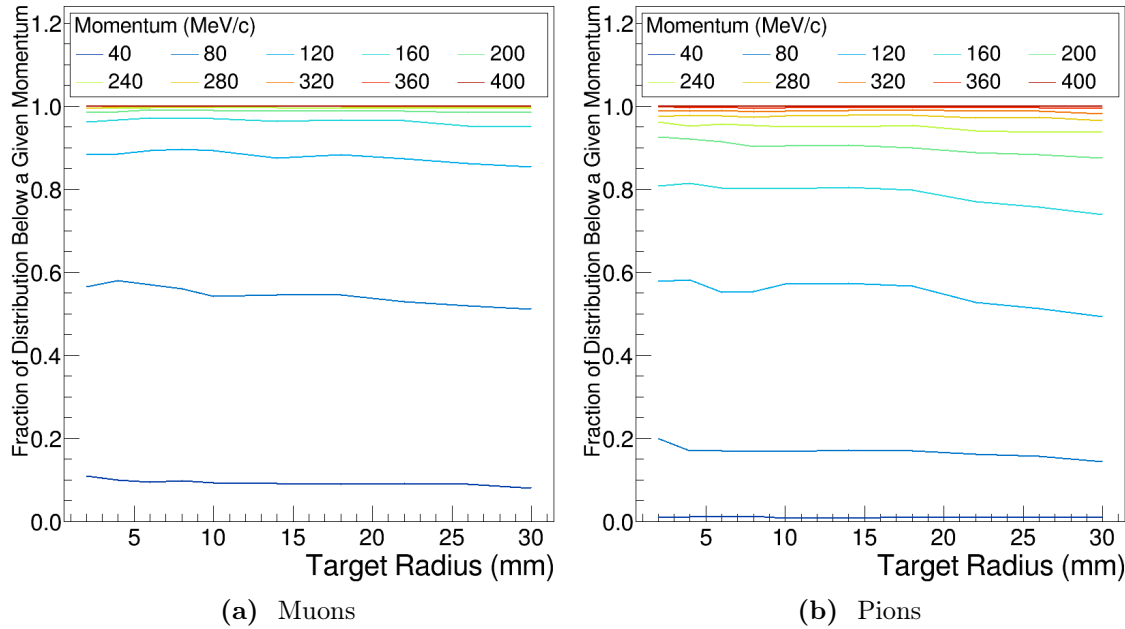


Figure 5.6: Change in the momentum distribution of muons and pions at the entrance to the first 90 degrees of the bent muon beam solenoid as a function of target radius.

5.2.3 Radius scan

In parallel to the length optimisation scan, different radii targets were also simulated. Targets with radii of 2, 4, 6, 8, 10, 14, 18, 22, 26, and 30 mm were tested. The target length was held at the CDR value of 16 cm in total.

The results of these scans are shown in Fig. 5.4 and Fig. 5.5, where it can be seen that a maximum in both the muon and pion yields at the entrance to the Torus1 section is achieved at a radius of about 10 mm. As in the length scan, the variation in the shape of the momentum distributions is rather weak as a function of target radius, as shown by Fig. 5.6

5.2.4 Final Result

Since the length and radius scan were performed in parallel, a final cross check was performed where the optimal radius was confirmed at the optimised target length. The integrated spectrum is shown in Fig. 5.7 where it can be seen that the optimum radius once the target length is increased to 32 cm is still 10 mm. The shape of the dependence

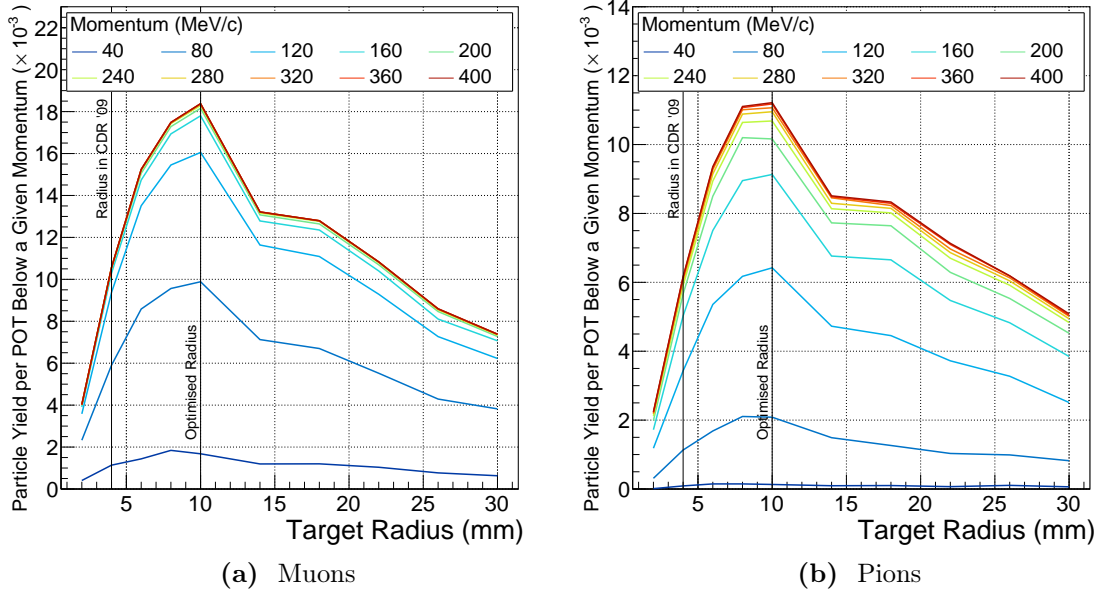


Figure 5.7: Variation in muon and pion yields as a function of target radius when the total target length is set to the optimised value of 32 cm. Despite the longer target length the optimal radius is still 1 cm.

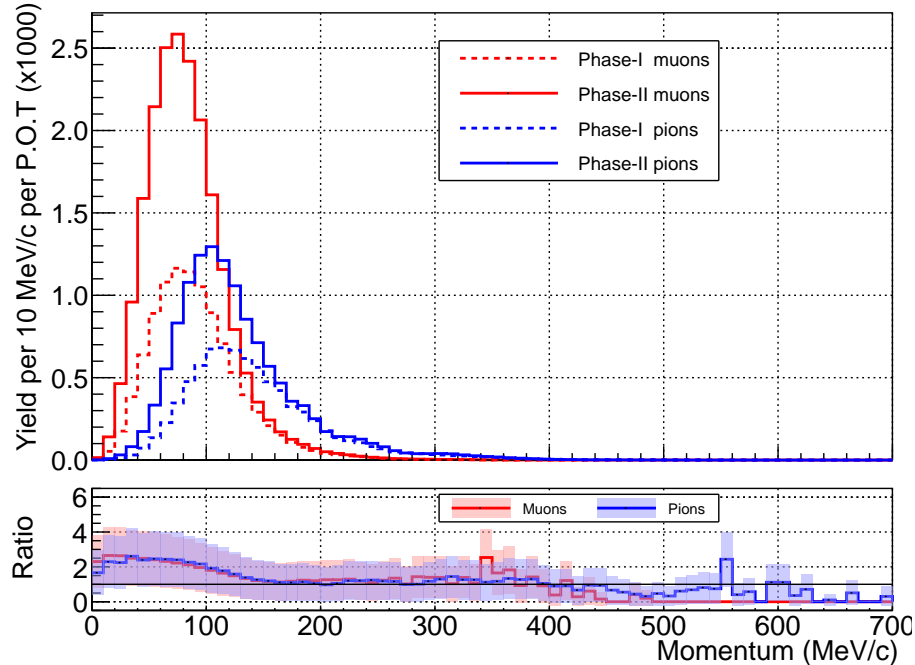


Figure 5.8: Comparison of the muon and pion yields per POT for Phase-I and Phase-II. The difference arises from the change of target material between the phases.

on the radius is however changed, with a more pronounced drop, then slow tail-off towards larger radii, than for the radius scan with the unoptimised length.

Fig. 5.8 shows the total muon and pion yields at the entrance to the Torus1 for the final optimised Phase-II target and compares this to the optimised Phase-I target design. Both sets of distributions were generated with Geant4—it would be informative to study this with other hadron production codes as well. The increased yield in the low-momentum range is due to the heavier target nucleus which produces more low-momentum pions in the backwards direction. Since only muons below around 50 MeV/c tend to stop in the target, this increase in the low-momentum yield amounts to a factor 2 or so gain in the stopping muon rate per POT.

5.3 Dipole Strengths of the Muon Beamline

The full 180° bent solenoid that makes up the bulk of the muon transport beam line is actually broken down into two 90° pieces—Torus1 and Torus2 (also known as TS2 and TS4 by the magnet group). Each of these sections has its own dipole field which need not be the same strength. The Torus1 section has been built already and was previously optimised for both Phase-I [44] and Phase-II [45]. The dipole coils that it contains are designed to produce a dipole field of 0.055 T. By running a lower current through these coils one could reduce the Torus1 dipole field without too much effort. However, if Phase-II should require a greater dipole field strength for this region that might be trickier since it could require additional windings to be inserted—this would not be impossible but might be costly.

5.3.1 Large-sample Production Target Simulation

Before the muon beam section could be optimised, a large set of POT events were produced, transporting all secondary particles from the Production Target up to the entrance of the muon beam section. In total, 2.3×10^8 POT were simulated, equivalent to about 1.5 bunches at Phase-II. The production target used the optimised geometry from the previous section. All particles that hit the surface of the Torus1 container volume were read out for later re-use in a way that ensured double-counting of particles could not occur. In addition, particles entering the proton beam dump were also saved if later simulations wished to study their impacts.

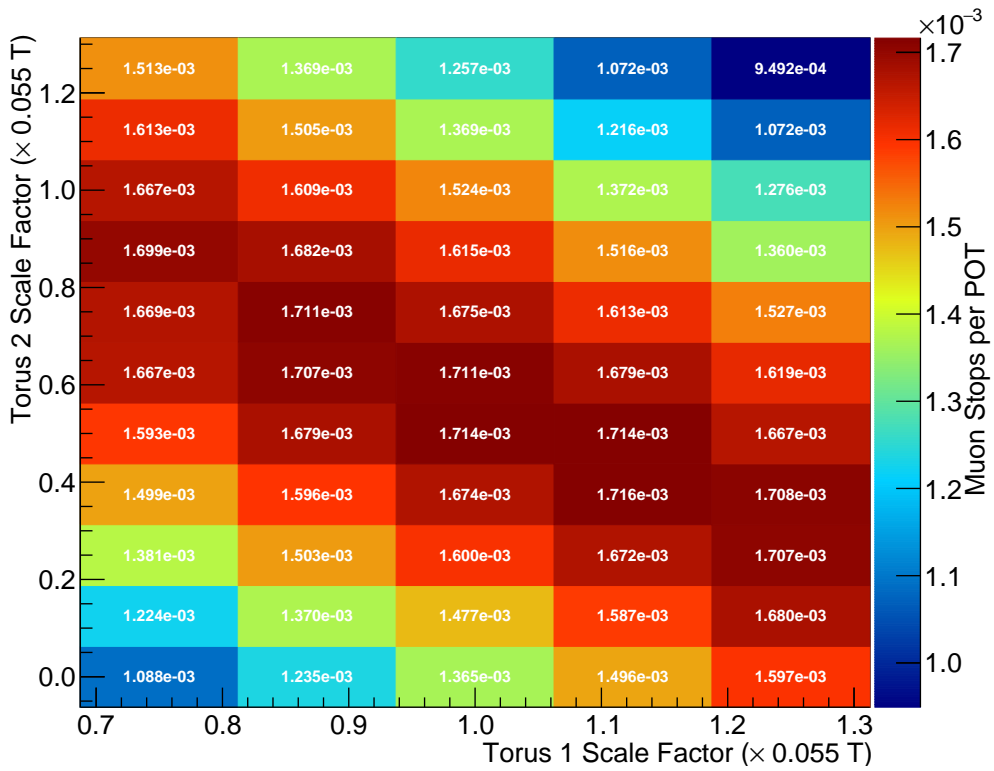


Figure 5.9: Muon stopping rate as a function of the two dipole field strengths (given relative to the Phase-I design specification). A clear anti-correlation is visible which is discussed in the text.

5.3.2 The Optimised Dipole Field Strengths

The figure-of-merit for this optimisation is the muon stopping rate, which will be greatest for the optimal field configuration. To identify such a configuration, a two-dimensional scan over the Torus1 and Torus2 dipole field strengths was performed. To vary the field strength, a scale factor was applied for each of the 90° section to the realistic dipole field description that was provided by Toshiba and described in 4.3.2. These scale factors were varied in steps of 0.125 (equivalent to about 6.875 mT) and for each combination muons and pions from 8×10^6 POT were transported to the stopping target.

The muon stopping rate as a function of the two dipole field strengths is shown in Fig. 5.9. The horizontal axis in that figure shows the scale factor applied to the Torus1, the 90° bent solenoid already built for Phase-I, whilst the vertical axis shows the scale factor for the Torus2. A scale factor of 1.0 means the magnetic field will be same as the current Phase-I design.

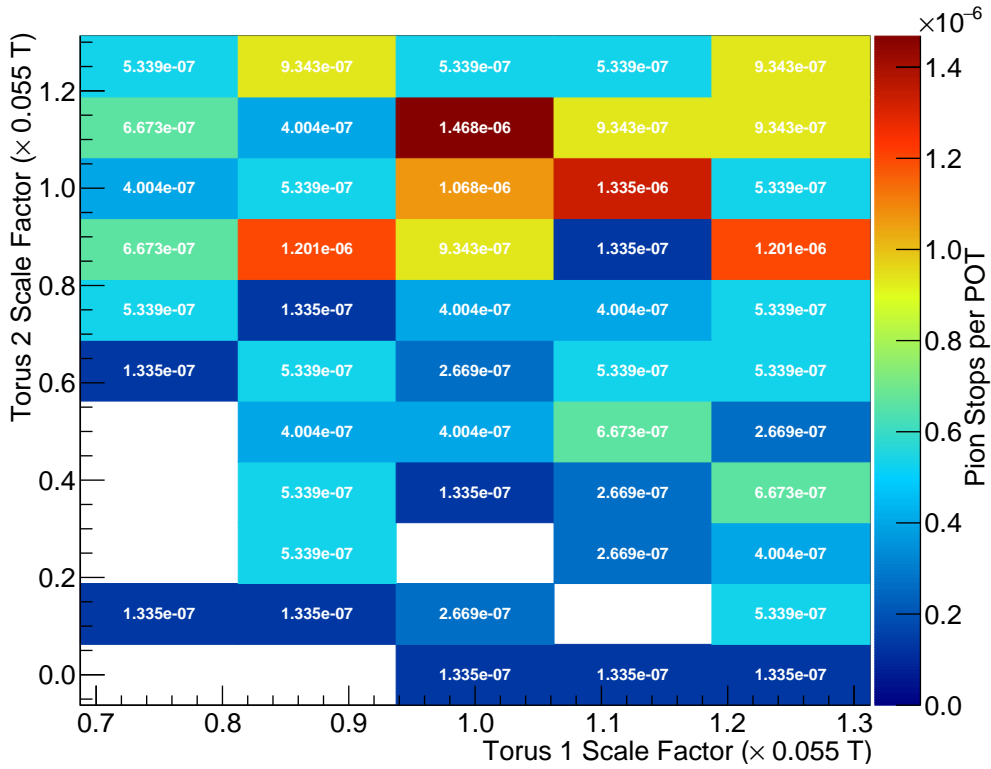


Figure 5.10: Pion stopping rate as a function of the two dipole field strengths (given relative to the Phase-I design specification). At the level of statistics used to generate each point, no clear trend is obvious. Empty squares are those where no pions stopped in the run.

The maximum muon stopping rate occurs when the Torus1 scale factor is about 1.125 and Torus2 is scaled by 0.375. However, achieving this configuration would require additional coil windings in the Torus1 compared to the Phase-I design, which would incur extra costs and risks. With scale factors of 1 and 0.5 for the Torus1 and Torus2 respectively, the difference is about 0.1%, from the absolute optimum, which is about the statistical error one would expect in the present study. As a result, the recommendation is to use dipole field strengths of 0.055 and 0.0275 T, for the Torus1 and Torus2 respectively.

Also striking from Fig. 5.9 is the anti-correlation between the two dipole field strengths. Roughly speaking the sum of the optimal dipole field values is constant, i.e. $B_1^{\text{optimal}} + B_2^{\text{optimal}} = \text{const}$. This correlation had not been seen before, perhaps due to the lack of computing power necessary to scan such a large parameter space. Such a correlation can be understood in the following way. The geometry of the stopping target (and its position) has been kept fixed during the dipole scan, which essentially fixes the upper momentum of muons that can stop in the target to about 40 MeV/c. Given the momentum distribution peaks beyond this limit (see Fig. 5.8), one tends to optimise for momenta close to the

maximum that can stop in the target. The drift of a particle due to the dipole field is proportional only to the distance travelled in that dipole field and the dipole field strength, and does not depend on the particle's momentum. Since each section is the same length, the total drift of a particle will be approximately proportional to the sum of the dipole field strengths. Thus we need to compensate for the drift of particles of a fixed momentum, which means a fixed amount of compensating drift due to the dipoles, such that the sum of the dipole field strengths is constant.

With that said, the Torus1 section has a higher pion flux which causes some asymmetry between the two sections. Keeping more pions on-axis in the Torus1 section means that more muons will enter the Torus2 section from those pions that have decayed. But since the pion momentum distribution is slightly higher than the muon distribution, keeping pions on axis requires a larger dipole field strength. This could explain the slight asymmetry where the muon stopping rate appears slightly larger if Torus1's field is larger than that of Torus2.

It is also interesting to consider the pion stopping rate as a function of the dipole field strengths. However, as can be seen from Fig. 5.10 the stopping rate is close to the level of POT events used in the simulation so that the plot is dominated by statistical fluctuations.

5.4 Electron Spectrometer's Dipole

The next element in the beamline after the muon transport solenoids will be the stopping target. However, in order to study the impact of changing the stopping target parameters one will need to look at the impact on the signal acceptance into the detector. To study that requires the components of the beamline intermediate to the target and the detector be optimised, namely the electron spectrometer. The key free parameter in this section is the dipole field strength along the spectrometer. The solenoidal field and solenoid aperture could also be optimised in principle, but this is considered beyond the scope of the present study. As such we use here the same values for the aperture and solenoidal field strength as for the CDR, which are about 1 T on axis and 60 cm respectively.

The point of this section is to establish the optimal dipole field strength given fixed target parameters. The target parameters will then be studied separately, whilst the stability of this dipole field tune is checked.

5.4.1 Method and Potential Short-comings

To study the effect of the dipole field on signal acceptance, a realistic muon-stopping distribution in the target was produced by transporting muons from the production target simulation through to the stopping target. Signal electrons were then injected at the target with the resulting stopping distribution and propagated through the beamline to the detector with different dipole field strengths.

A non-trivial short-coming of the current study is that the dipole field along the spectrometer is poorly modelled—no realistic coil simulation exists, unlike for the bent muon transport beamlines. As a result, a perfectly uniform dipole field is assumed with a sharp switch on and off at the entrance and exit of the spectrometer. The impact that this has on the final result is not clear: one might expect it to be small given the relative strengths of the dipole and solenoidal fields and overall it is the integrated field that tends to matter. However, the sharp switch-on of the field at the entrance and exit of the spectrometer is clearly not physical. Given that the gradient introduced in the field by bending is present before the actual entrance and after the exit of the spectrometer (as a fringe field), some drift can be anticipated in this region. A realistic dipole field with a realistic fringe field might overcome some of this drift however, such that the uniform field used here cannot capture this compensating effect. Nevertheless, given the absence of a realistic dipole field and scope of this study, the uniform one is the only available option at this point.

5.4.2 Results

Fig. 5.11 shows the projection of electron trajectories to the beam axis coordinate system for three different dipole field values. The potency of this approach is clear from these plots; the tunable dipole fields allow the momentum of electrons which remain on-axis to be accurately controlled (during run-time), which will benefit systematic and calibration studies that wish to observe the decay-in-orbit (DIO) spectrum at a lower energy. Fig. 5.12 then collects these plots with other dipole field strengths, plotting the mean height for all simulated electrons against the distance along the beam axis. From this plot it can be seen how a dipole field of about 0.18 T appears optimal to keep the signal electrons on axis.

The probability for electrons to reach a given point in the beamline is shown in Fig. 5.13, and indeed from this it can be seen that to maximize the probability of an

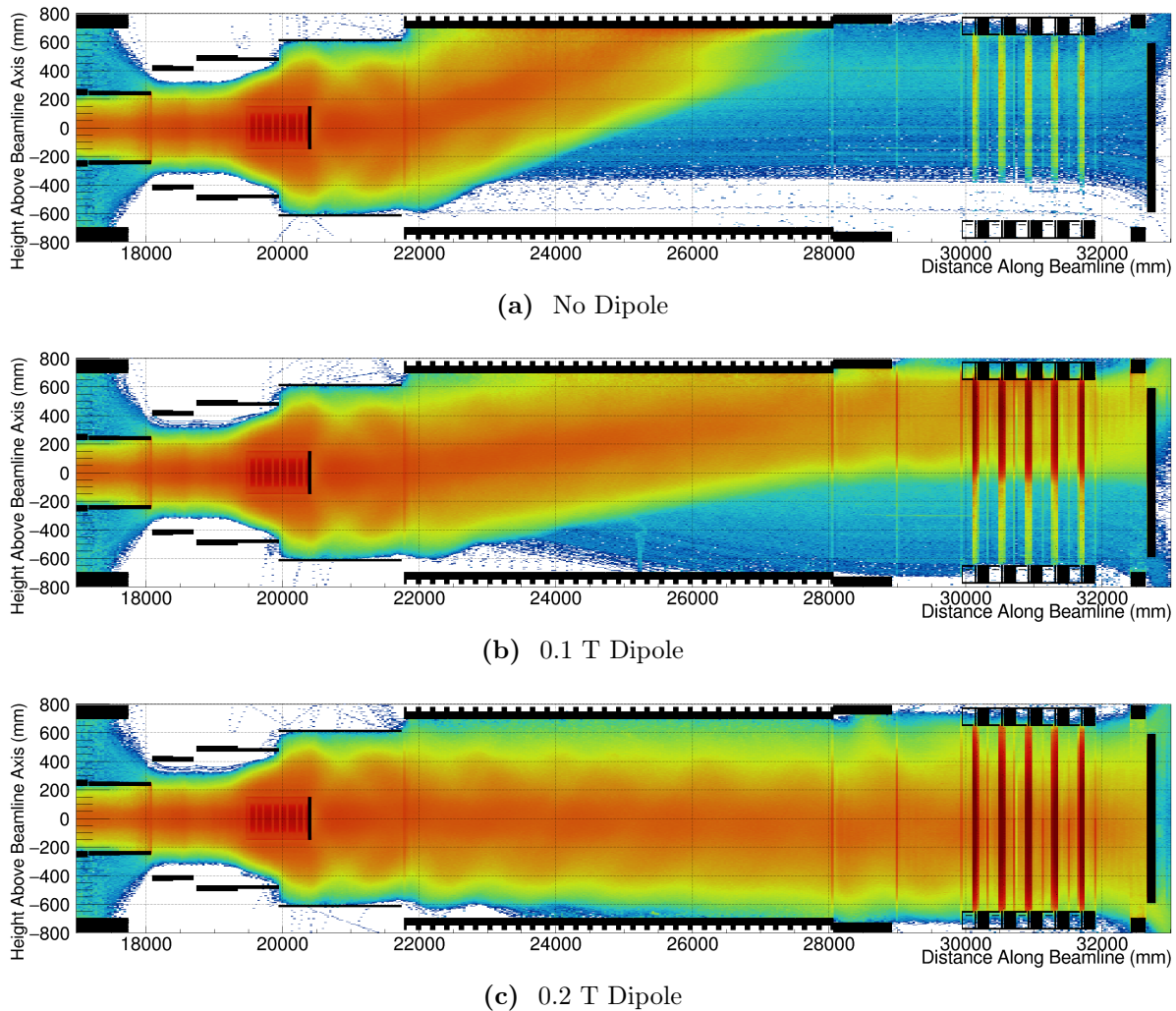


Figure 5.11: The heights of electrons along the electron spectrometer that originate in the target with 105 MeV for different dipole field values. With no dipole field, (a), very low energy electrons remain on-axis (straight, blue lines) whilst the signal all drifts vertically and is removed by the beampipe. At larger dipole fields, such as (c), the reverse is true.

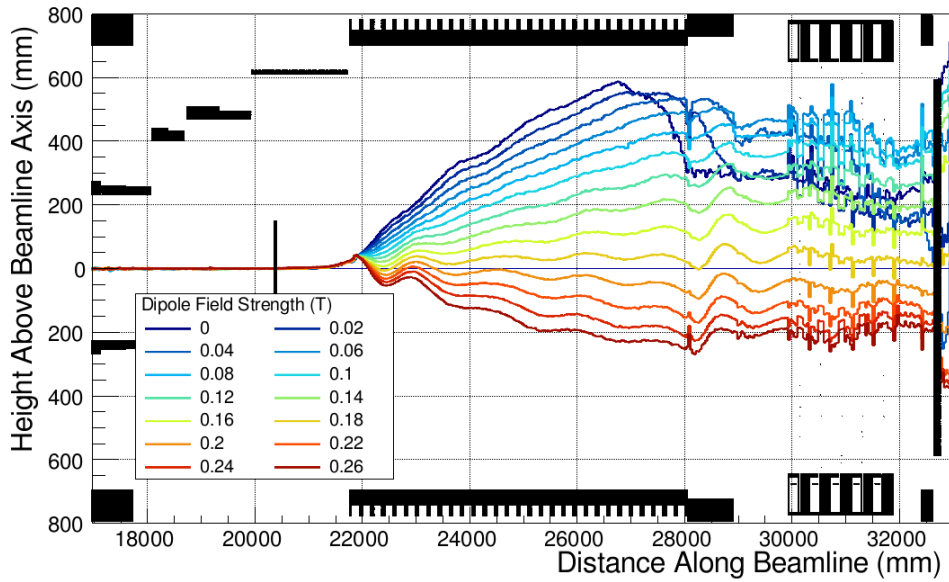


Figure 5.12: Mean height of signal electrons for different values of the dipole field strength.

electron reaching the detector, a dipole of around 0.18 T is desirable. The behaviour of the low dipole field values (0 to 0.08 T) in this plot was not expected, but it is believed this is an artefact of the way this plot is made (see section 4.4.1), coupled with a degree of mirroring at the entrance to the spectrometer which is enhanced as the dipole field strength increases. If correct, a realistic dipole field calculation would be important to quantify and confirm this behaviour.

Finally, to confirm the optimal dipole field strength the true geometric acceptance of the detector system is checked as a function of the dipole field strength, which is shown in Fig. 5.14. An electron is considered to have been geometrically accepted by the detector in this simulation if it produces at least one hit in the detector system. In principle this could be in any straw plane, but in practice this is almost always in the first layer of straws. Since this is a different way to analyse the acceptance compared to the survival probability, it would not suffer from the artefact seen for low dipole field values in Fig. 5.13. Nonetheless, Fig. 5.14 confirms that the optimal dipole field strength is very close to 0.18 T.

A second important conclusion can be drawn from the fact that the dependence on the dipole field strength is relatively weak around the optimal value of 0.18 T. A change of about 10% in the dipole field strength only reduces the signal acceptance by about 3% whilst a change of about 5% would see a reduction of only about 0.7%.

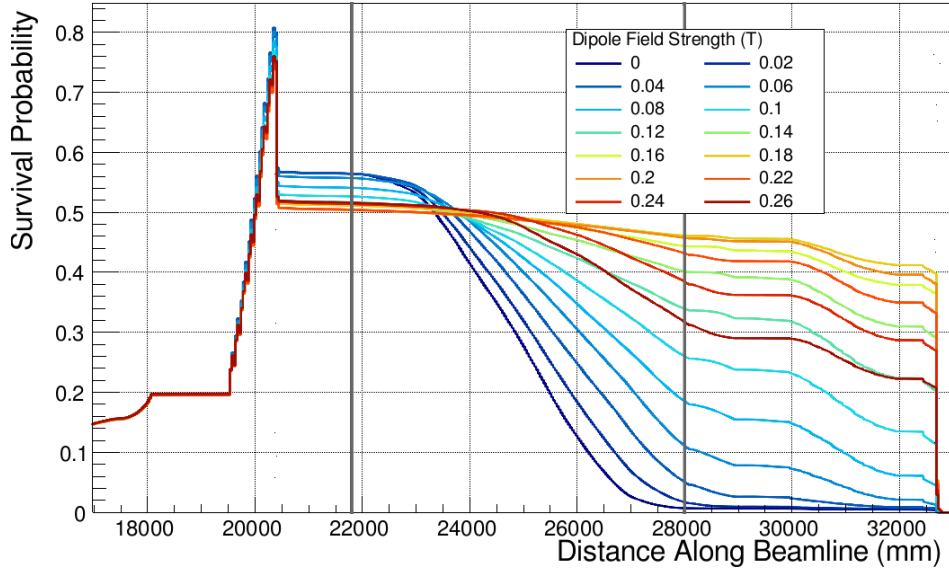


Figure 5.13: Survival probability for signal electrons as a function of the distance along the beamline for different values of the electron spectrometer’s dipole field strengths.

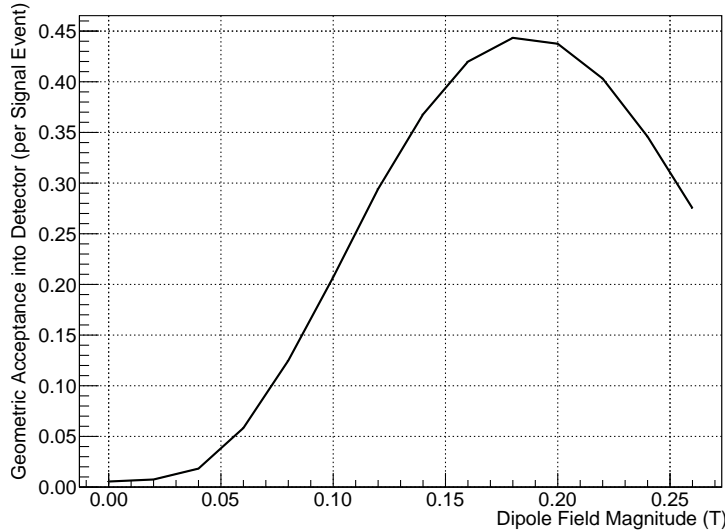


Figure 5.14: Geometric acceptance into the StrECAL detector as a function of the dipole field strength over the electron spectrometer.

5.5 Stopping Target Position

The final aspect to be studied with regards to maximizing the signal sensitivity is the stopping target. In principle there are many parameters related to the stopping target such as the location, disk shape (profile and thickness), and disk spacing. The beam blocker ought to be considered in parallel to this, since it sits so close to the target and

can be expected to have a big impact on the signal acceptance. However, this leaves far too many parameters to be considered all at once.

Since the field around the target tapers sharply, various competing factors must be considered. For example, prior to the stopping target region the muon beam is transported through a 3 T solenoidal field. The magnetic field in the target region, however, reduces to about 1 T, which would cause the envelope of the muon beam to grow. Moving the stopping target downstream would mean that the muon beam arrives with a larger aperture, and would therefore prefer a stopping target with a larger radius to maximize the stopping rate. On the other hand, from the perspective of signal acceptance, the tapered field can be used to mirror signal electrons that are initially produced heading upstream, thereby increasing the signal acceptance. Moving the target further upstream will reduce this effect as the difference between the magnetic field strengths at the exit of the bent muon transport solenoid and at the stopping target is reduced.

Given this and the need to reduce the number of parameters inspected, the target and beam blocker design was held fixed in this study and only the position was changed by moving the target upstream and downstream by ± 50 cm in steps of 10 cm with respect to the nominal target location as given in the CDR [45]. Given that the target disks will in total occupy about 1 m, a shift of 50 cm corresponds to half the target length. In each different position of the stopping target, as for the spectrometer dipole optimisation, a realistic stopping distribution was produced by running muons from the large-scale production target simulation through to the target. This stopping distribution was then re-used to introduce signal electrons accordingly. Additionally, low-momentum electrons were also studied in order to check the impact of target position on the height of both signal and low-energy electrons as they pass through the spectrometer. This is important both to check the correlation of the dipole field tune with the stopping target position, but also how the subsequent DIO blocker height optimisation will correlate to the target's position.

5.5.1 Muon Stopping Rate

Fig. 5.15 shows how the rate of muon stops per POT is affected by changing the position of the stopping target. The relationship is roughly linear, dropping from around 2.2×10^{-3} muon stops per POT when the target is shifted upstream by 50 cm to about 1.3×10^{-3} muon stops per POT if the target is shifted 50 cm in the other direction. This

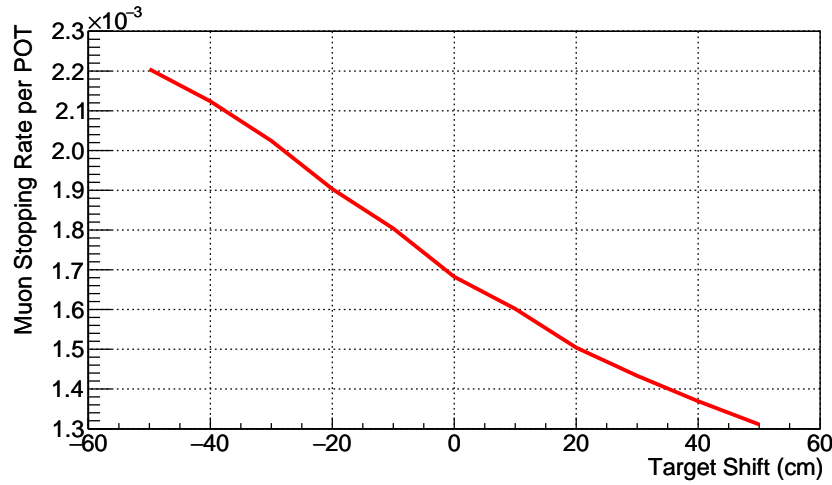


Figure 5.15: Muon stopping rate per POT for different target positions. The linear behaviour arises from the reduced field strength and fixed target radius such that fewer muons impact the target as it is moved downstream.

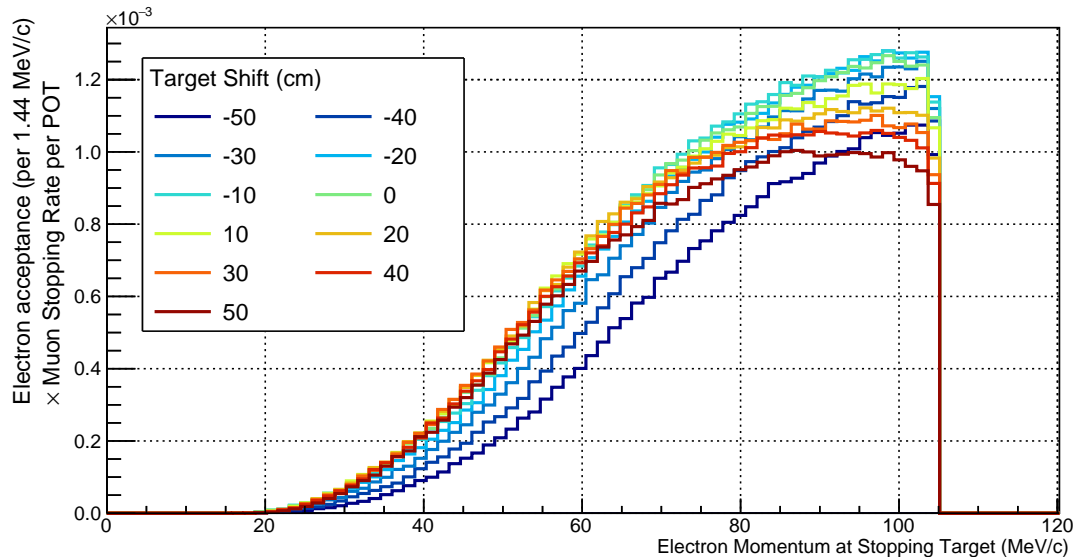


Figure 5.16: The momentum dependence of the electron acceptance into the detector for different target positions. The spectrum for each target position is normalised to the muon stopping rate for that position, such that each curve shows the sensitivity to electrons of that momentum.

relationship is to be expected given the fixed radius of the target and the growth of the muon beam aperture that occurs as the field strength is reduced.

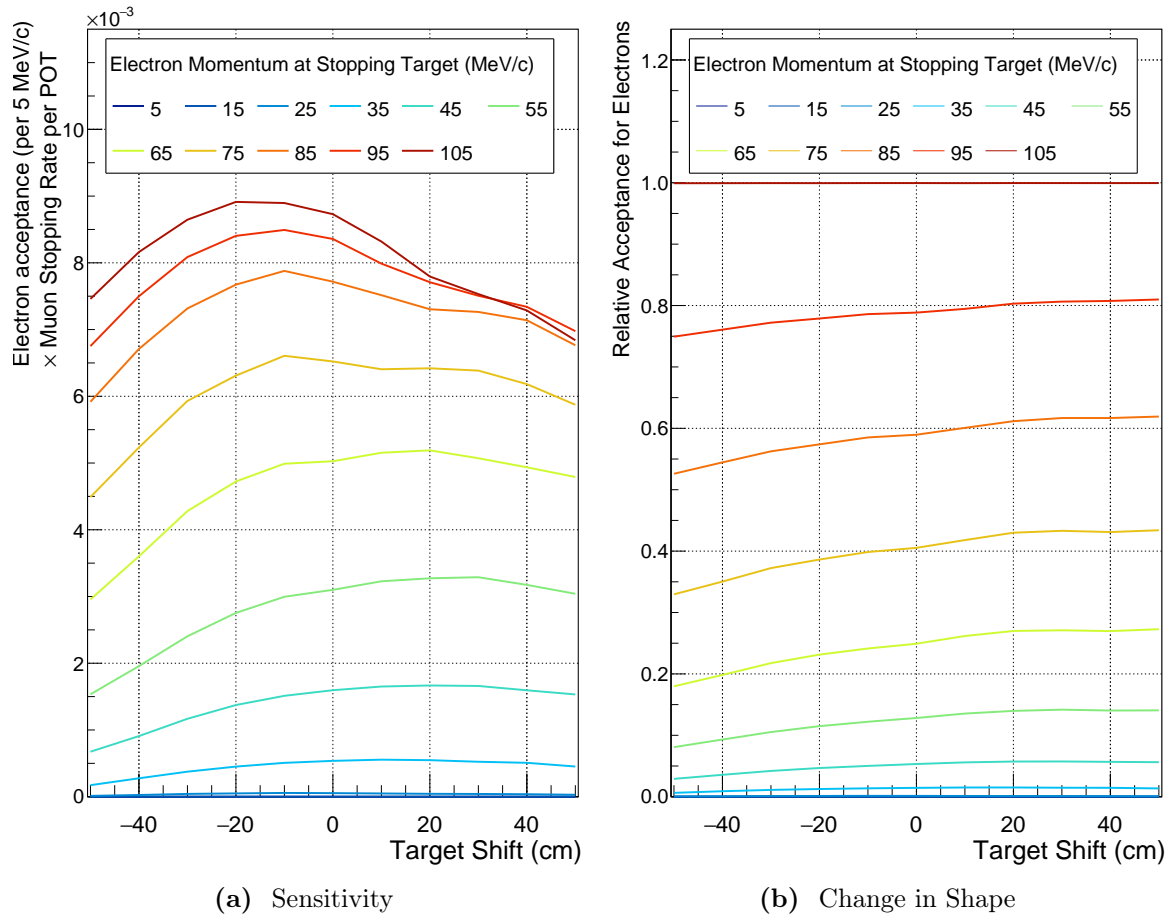


Figure 5.17: (a) The variation in sensitivity (acceptance \times stopping rate) to electrons with different momenta as a function of the target position with respect to the nominal location. The darkest red line towards the top of the plot represents the sensitivity to signal, and it is that line that should therefore be maximised. (b) The change in the shape of the acceptance vs. momentum spectrum as a function of the stopping target location.

5.5.2 Signal Acceptance

In Fig. 5.16 one can see the way the electron acceptance changes for different target positions. Acceptance here is defined as producing at least one hit in the detector and the momentum shown is the momentum at the target, which is not necessarily the same as the momentum at which the electron is observed. Each histogram in Fig. 5.16 is normalised to the number of primary electrons introduced at the target per MeV/c and then scaled to the muon stopping rate. This normalisation makes the value of each curve proportional to the sensitivity of the experiment to different momentum electrons, up to factors such as analysis cuts like timing and reconstruction quality.

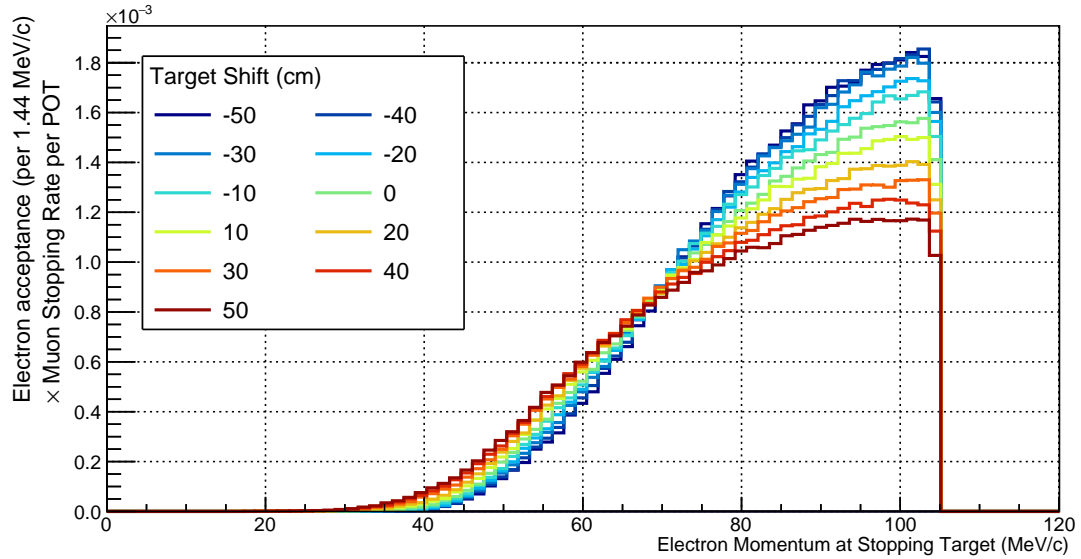


Figure 5.18: The momentum dependence of the electron acceptance into the detector for different target positions when the beam blocker is removed.

Since the parameter we wish to optimise here is the location of the stopping target, Fig. 5.17a represents the same data as in Fig. 5.16 but with each line representing the content of a different 5 MeV/c bin as a function of the target position. For signal, it is the 105 MeV/c line (dark burgundy) that is most important and it can be seen that this is optimised for shifts upstream of the nominal position from between 10 and 20 cm. It is also interesting to note that the acceptance of lower energy electrons is relatively decreased as the target is moved upstream, as can be seen in Fig. 5.17b. This could be useful as a way to suppress hit rate from DIO electrons later.

5.5.3 Impact of the Beam Blocker

Whilst we do not intend to optimise the beam blocker at this point, to check the impact that it has on the optimisation of the target position, simulations were performed where the blocker was completely removed. Fig. 5.18 shows the product of the stopping rate and electron acceptance when the blocker is removed. From this the trend is much cleaner, electrons below 70 MeV/c are suppressed as one moves the target upstream, whereas the high-energy electron acceptance is increased.

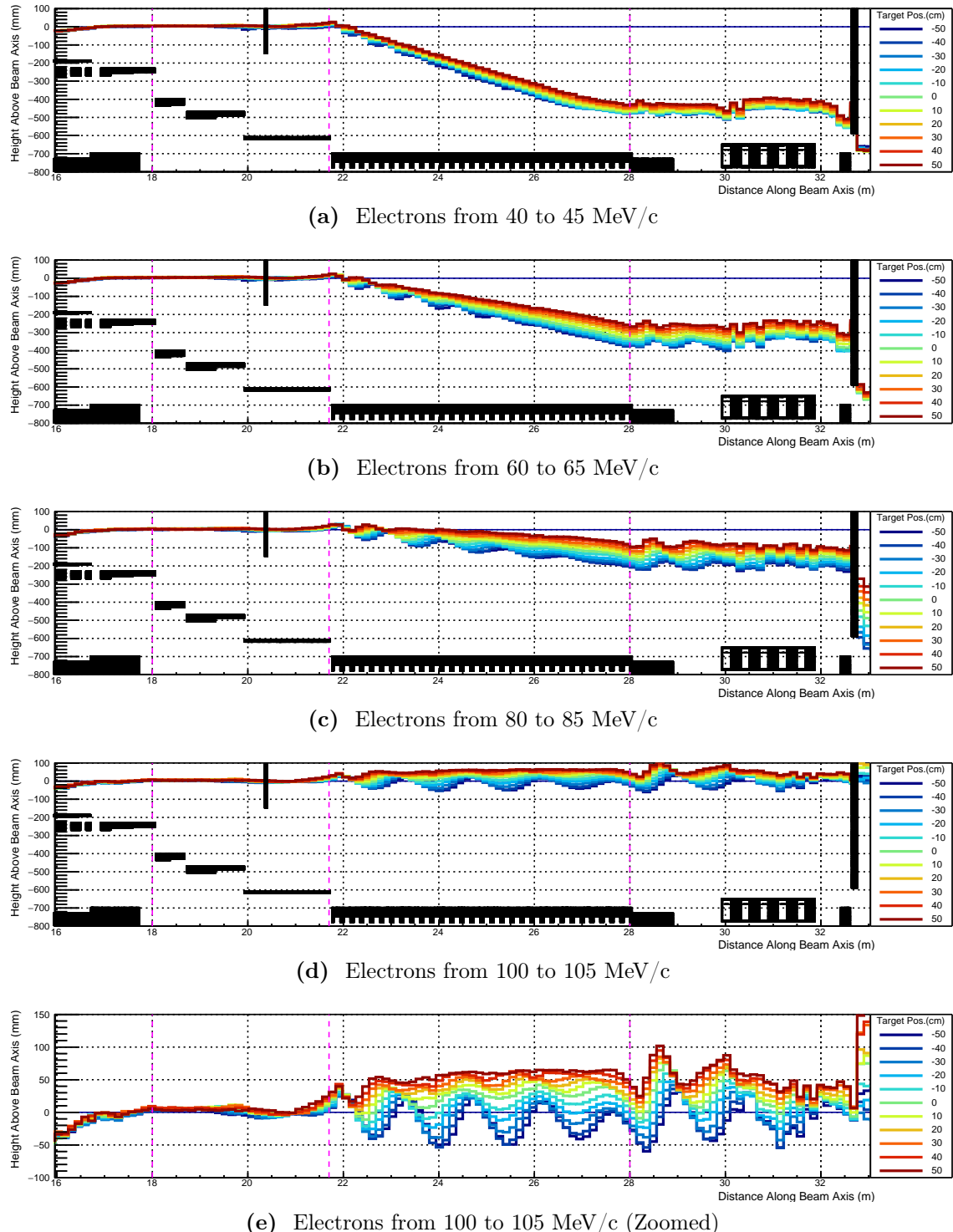


Figure 5.19: The effect of stopping target position on the height of electrons with a fixed momentum as they pass through the Electron Spectrometer. The size of the variation indicates the stability of the dipole tune; the two parameters are clearly correlated. Also striking—particularly in (e)—is the way the dependence on the helical pitch angles is affected by the stopping target position.

5.5.4 Stability of Electron Spectrometer Dipole Tune

Finally the relationship between the stopping target position and the mean height of electrons through the spectrometer is demonstrated in Fig. 5.19. Each plot shows the mean heights for electrons with a given momentum for different stopping target positions and it is clear that there is some correlation between the mean height and the position of the stopping target. For this reason, a more complete optimisation should consider optimising the target position, electron spectrometer dipole, and DIO blocker height simultaneously. Nonetheless the change is not particularly large: about a few centimetres of difference at the end of the spectrometer for signal electrons. This correlation is also likely related to the way the acceptance changes for different target positions when the beam blocker is removed.

The second striking feature from the plots in Fig. 5.19 is the way the mean height acquires a strong sinusoidal component for large target shifts upstream. This suggests that when the target is shifted upstream the electrons passing the entrance to the spectrometer tend to have a particular value for the pitch and phase angles of the trajectories. Several separate mechanisms could produce this effect. Firstly the acceptance around the target itself could acquire a stronger preference for certain pitch and phase angles when the target is moved upstream. Secondly, since the stopping target disks will see more of the muon beam upstream, the muon stopping distribution could become less homogeneous. Whilst electrons are produced isotropically, paths with less target material along them will accept outgoing electrons more readily such that if more muons stop at one side of the target than the other, a dependence on pitch and phase could manifest in the electron acceptance.

5.5.5 Results

Clearly then the stopping target region is a very complicated area; even though this study has focussed on a single parameter—the position of the target itself—many correlations have been observed. This region in the experiment is particularly ripe for further optimisation. Appendix 8 shows some of the first steps that have been made in this direction after the studies described here had been completed.

Unfortunately, at the time this work was carried out an error in the normalisation of these plots lead to the conclusion that the optimal shift was between 0 and 10 cm upstream. Given the complexity of the optimisation in this region, it was decided to

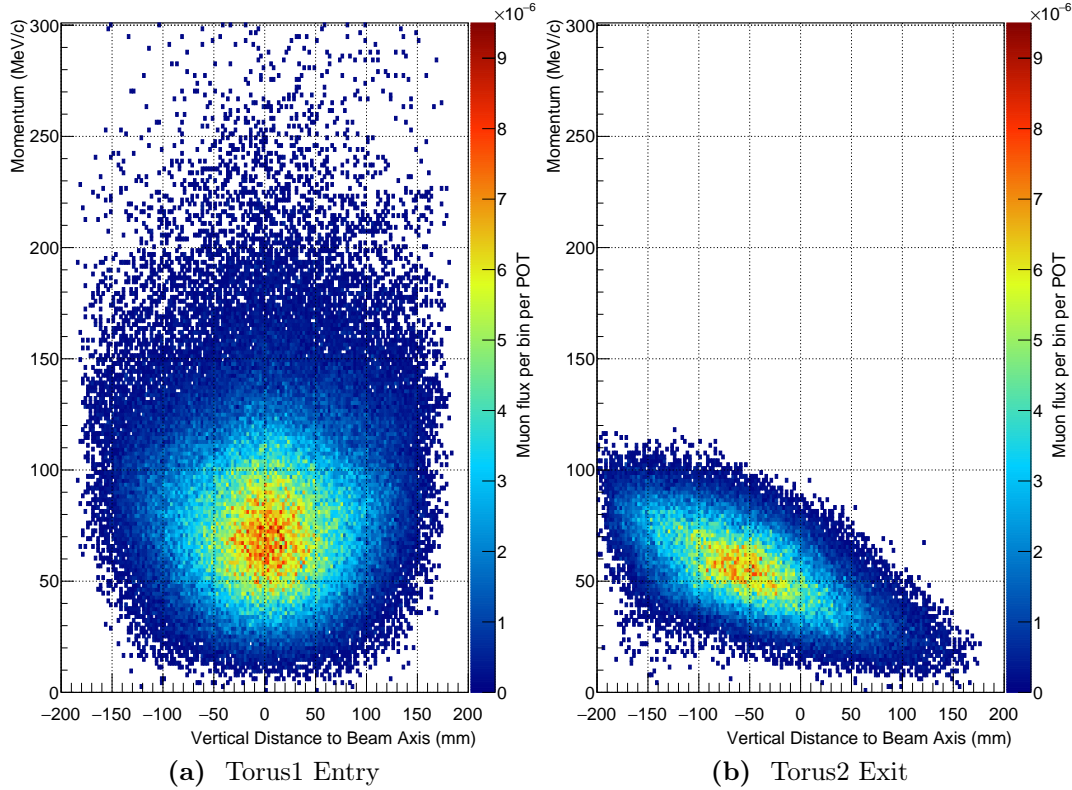


Figure 5.20: Dispersive effect of the 180° bent transport solenoid and dipole field on muons. No collimating material is yet included, so the high-energy muons being removed is due purely to the beam-pipe itself.

keep the stopping target at the nominal location for the subsequent optimisation steps. Having corrected the normalisation of the plots, the conclusion now is that the optimal location is between 10 and 20 cm upstream, so perhaps the target should have been shifted back. However the improvement to the sensitivity would have been small: shifting the target back about 20 cm improves the sensitivity by around 2% compared to the signal acceptance at nominal position.

5.6 Collimators in the Muon Beamline

With the beam line optimised for high signal efficiency, one can look at reducing the background rate by adding collimators into the muon beam line to reduce the flux of high-momentum muons and pions.

Fig. 5.20 shows the dispersive effect of the bent solenoid and dipole field on muons passing through the beamline. Thanks to this dispersion low-momentum muons that can stop in the target and high-momentum muons, which could produce backgrounds, are separated sufficiently for material in the beam pipe to selectively remove the dangerous, high-momentum muons with only a small impact on the muon stopping rate.

5.6.1 Collimator Placement

The plots in Fig. 5.21 give a sense of where best to locate the collimating material. In Fig. 5.21a the paths of all muons along the beamline are shown. Fig. 5.21b then separates out the muons that stop in the target which should be compared to Fig. 5.21c showing the paths of muons that reach the stopping target region with momentum greater than 70 MeV/c — the threshold for a muon to decay to an electron with $p > 100$ MeV/c.

It is interesting to note the apparent asymmetry in the high-momentum muons at the entrance to the Torus1 that can be seen in Fig. 5.21c. However, this is not due to some momentum-dependence in the production target region’s acceptance, but due to the fact that muons in that plot are only included if they are ‘dangerous’ in the region around the stopping target. Even without additional collimators, the beam pipe itself removes high-momentum muons that enter in the lower half of the beamline. The validity of only tagging high-momentum muons around the stopping target region comes from the assumption that the products of high-momentum muons that decay before this region can be reliably removed. It is important then that this assumption be checked, but for this work this is left as a task for the future.

Finally, in Fig. 5.21d the difference between the high-momentum muons and the paths of those that stop is shown. Regions in blue on this plot show where many more high-momentum muons pass than stopping muons; it is in these locations that collimator material will be most effective. This approach could also be improved, since taking the straight difference between the two plots implies equal weighting for stopping muons and high-momentum ones. In reality, whilst a muon tagged as stopping is definitely going to contribute to the signal sensitivity, a high-momentum muon should be weighted by the probability to produce a signal-like electron and the probability that this electron survives to create a background event in the detector. This would make the weighting for the high-momentum muons be a function of the beamline distance itself, which again requires a study into how high-momentum electrons are accepted. However for the purposes of

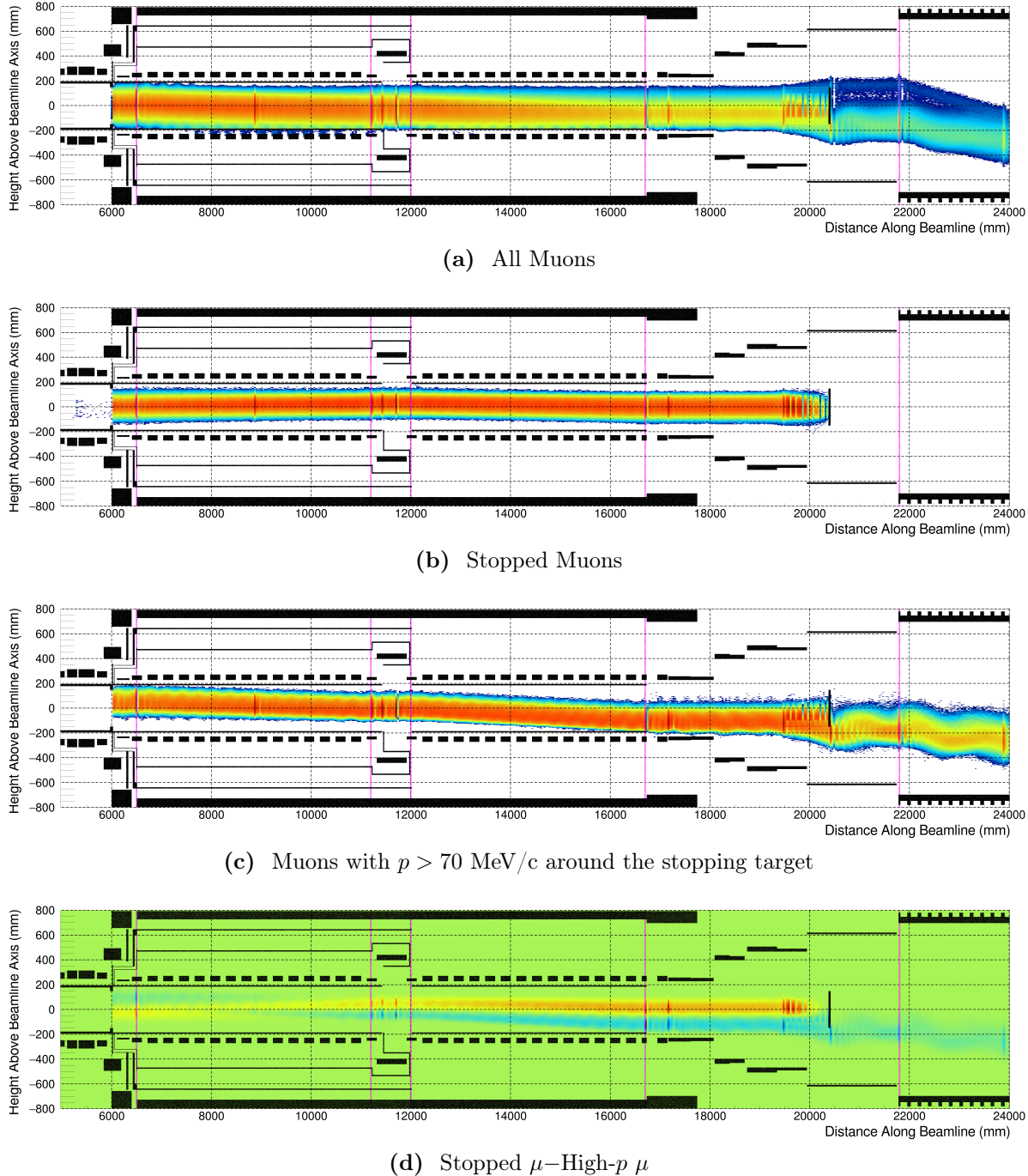


Figure 5.21: The heights of muons as they pass along the beamline. (a) The path of all muons. (b): The paths of muons that stop in the target. (c): The heights of muons with momentum greater than 70 MeV/c when they enter the region around the stopping target. These could potentially decay in flight to give electrons with 100 MeV/c or greater. (d): The difference between plot (b) and plot (c). Regions in dark blue would give the greatest impact in removing high-momentum muons whilst leave the stopping muons untouched. These plots should be compared to those of Fig. 5.26 once collimators have been introduced.

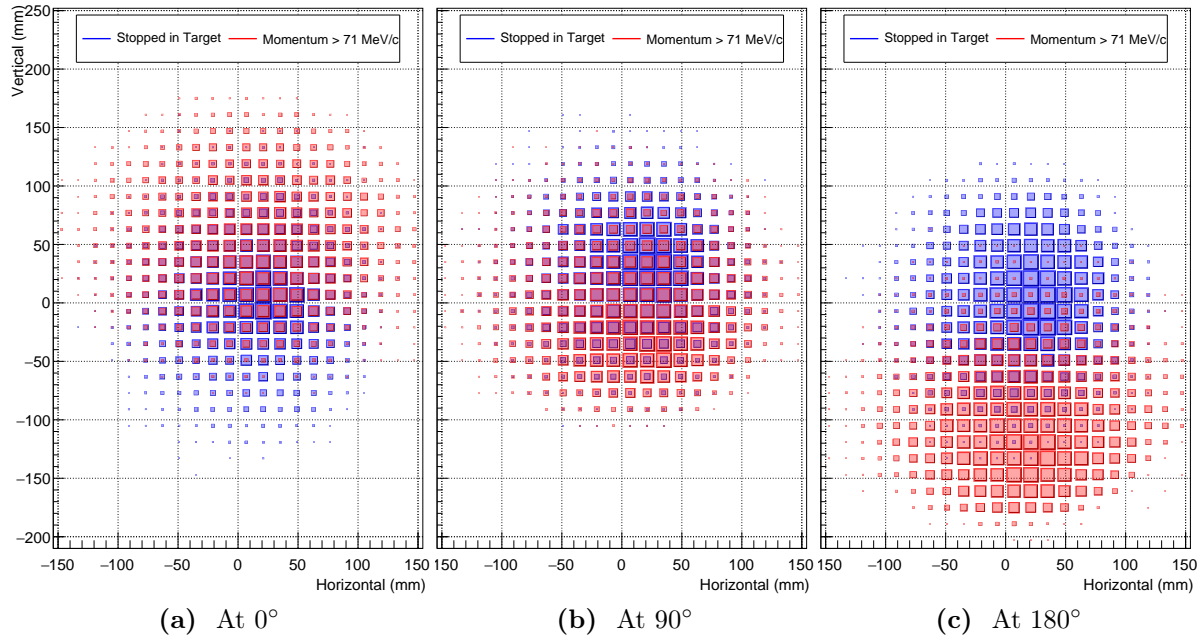


Figure 5.22: The separation between stopping and dangerous muons. The separation is largest at the exit (180°), reasonable at the entrance (0°), and smallest around the mid-point (90°).

obtaining a qualitative sense of where to collimate, the unweighted difference should be sufficient.

Two regions of interest appear: in the upper half of the entrance to Torus1 and the lower half of the exit of Torus2. Collimating at the Torus1 entrance is justified on the basis that high-momentum muons will tend to have larger gyroradii compared to the muons that stop, and that at this point the beam is largely on-axis, having not yet been dispersed. Collimating at the exit of Torus2 is readily understood on the grounds that the high-momentum muons will have all drifted downwards by this point, compared to the low-momentum stopping muons which are kept on-axis by the dipole fields.

These conclusions are backed by the plots shown in Fig. 5.22, which show transverse slices through the beamline at the entrance to Torus1 (0° of bent solenoid), the midpoint between Torus1 and Torus2 (after 90° of bent solenoid), and at the exit of Torus2 (after 180°). From these plots one can also see how in the middle of the bent solenoids (at 90°) the separation between muons that will stop and those that will have momentum greater than or equal to $70 \text{ MeV}/c$ in the stopping target region is weakest, and hence collimators in this location will not be so effective.

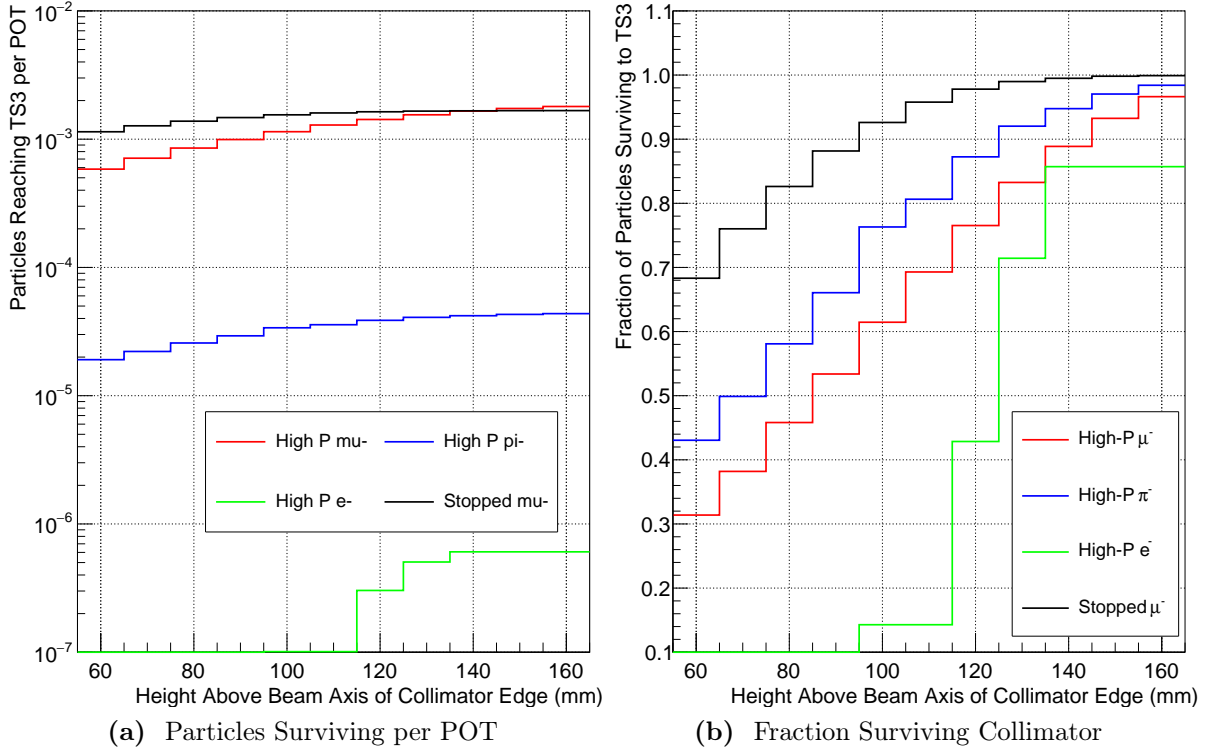


Figure 5.23: The effect of changing the height of the collimator in Torus1 on the particle distributions.

5.6.2 Collimator Height Optimisation

To identify the optimum height for the collimators in a computationally efficient way, events were generated without any collimators included. The full three-dimensional trajectories of all particles, as well as the decay tree, were persisted. This allows for a ‘virtual’ collimator to be used, where particles that enter a defined region and their secondaries are excluded from the downstream plots. Whilst this method allows for many collimator shapes and heights to be tested quickly, it does have limitations. Firstly, the accuracy depends on the trajectory sampling density, which should be made as fine as possible, at the expense of larger data sizes. Secondly, realistic material effects of the collimator cannot be captured, such as the probability a particle is simply scattered rather than stopping completely, or the result of secondary particles produced in the collimator itself.

Fig. 5.23 shows the results of lowering the bottom edge of the collimator material in Torus1. Fig. 5.23a shows the probability per POT that different types of particle (stopped muons and high-momentum electrons, muons, and pions) pass the collimator as

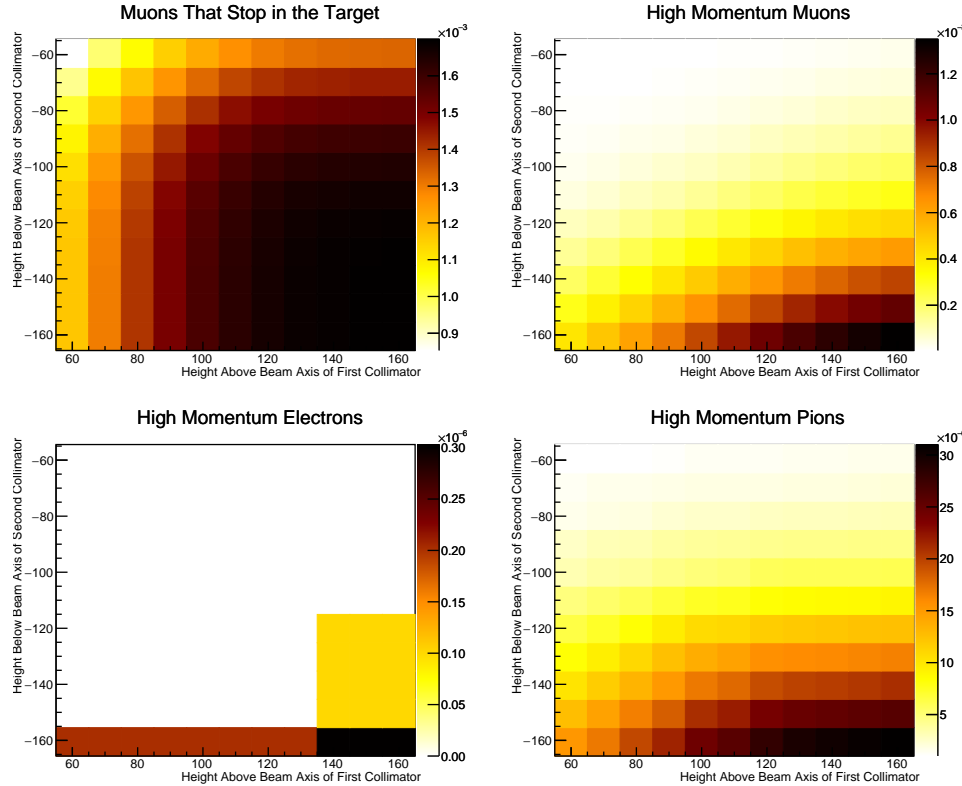


Figure 5.24: The number of particles reaching the end of the Torus2 solenoid relative to the number that enter the Torus1 solenoid (i.e. the survival probability) for different heights of both collimators in Torus1 and Torus2.

a function of the collimator height. On the other hand, Fig. 5.23b shows the same plots but normalised to the total number of each particle type that reaches the collimator in the first place, therefore showing the survival probability along just the collimator region. Based on these plots, for a collimator that starts at 120 mm above the beamline axis, 14% of high-momentum pions are removed, high-momentum muons are suppressed by 24% whilst the muon stopping rate is reduced only by 3%.

For the second collimator at the exit to Torus2, the situation is slightly more complicated since in principle the optimum height could be correlated to the height of the upstream Torus1 collimator. To account for this, the virtual collimator technique was applied for both the Torus1 and Torus2 collimator sections simultaneously. As a result, the 1-dimensional plots of Fig. 5.23 become 2D as can be seen in Fig. 5.24, which is normalised to the particle flux just before the collimator similar to Fig. 5.23b.

Fig. 5.25 represents the stopping and high-momentum plots in a way that is easier to compare the two directly. Each line in that plot is a contour showing a change of

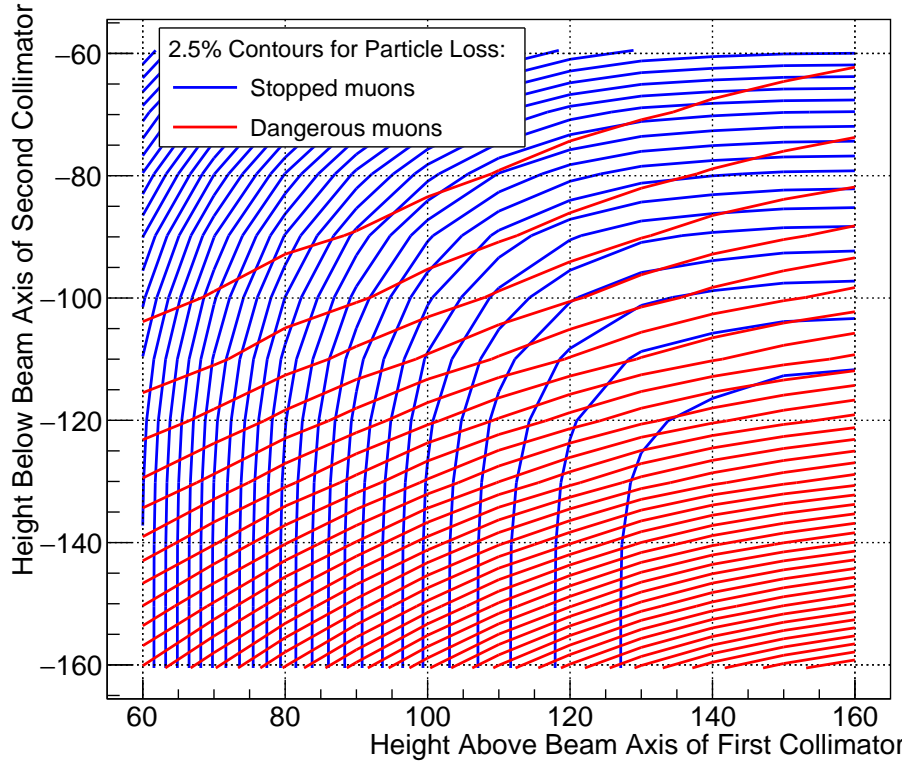


Figure 5.25: Contours showing 2.5 percentage point changes to the stopping (blue) and dangerous (red) muon flux, as a function of the collimator heights. 100% acceptance is found in the bottom right corner.

2.5 percentage points to the yield. Total acceptance, or 100% is in the bottom right corner. From this plot it can be seen that whilst keeping more than 97.5% of the muon stopping rate (the bottom-right most blue contour), the maximum high-momentum muon suppression is achieved when the Torus1 collimator sits about 140 mm above the beam axis, and the Torus2 collimator sits about 120 mm below it. To be precise, at these collimator values the muon stopping rate is kept at 99% of the no-collimator rate, whilst high-momentum pions, muons, and electrons drop to 27.6%, 20.9% and 11% (although this last value is very statistically limited) respectively. At this point the selected values for the collimator heights give conservative background suppressions and tighter values could be chosen. Given that backgrounds from high-momentum muons are suppressed compared to the actual rate of ‘dangerous’ muons by the geometric acceptance of the remaining beamline and the timing and momentum cuts this seems reasonable at this stage although this will of course be investigated in the next chapter.

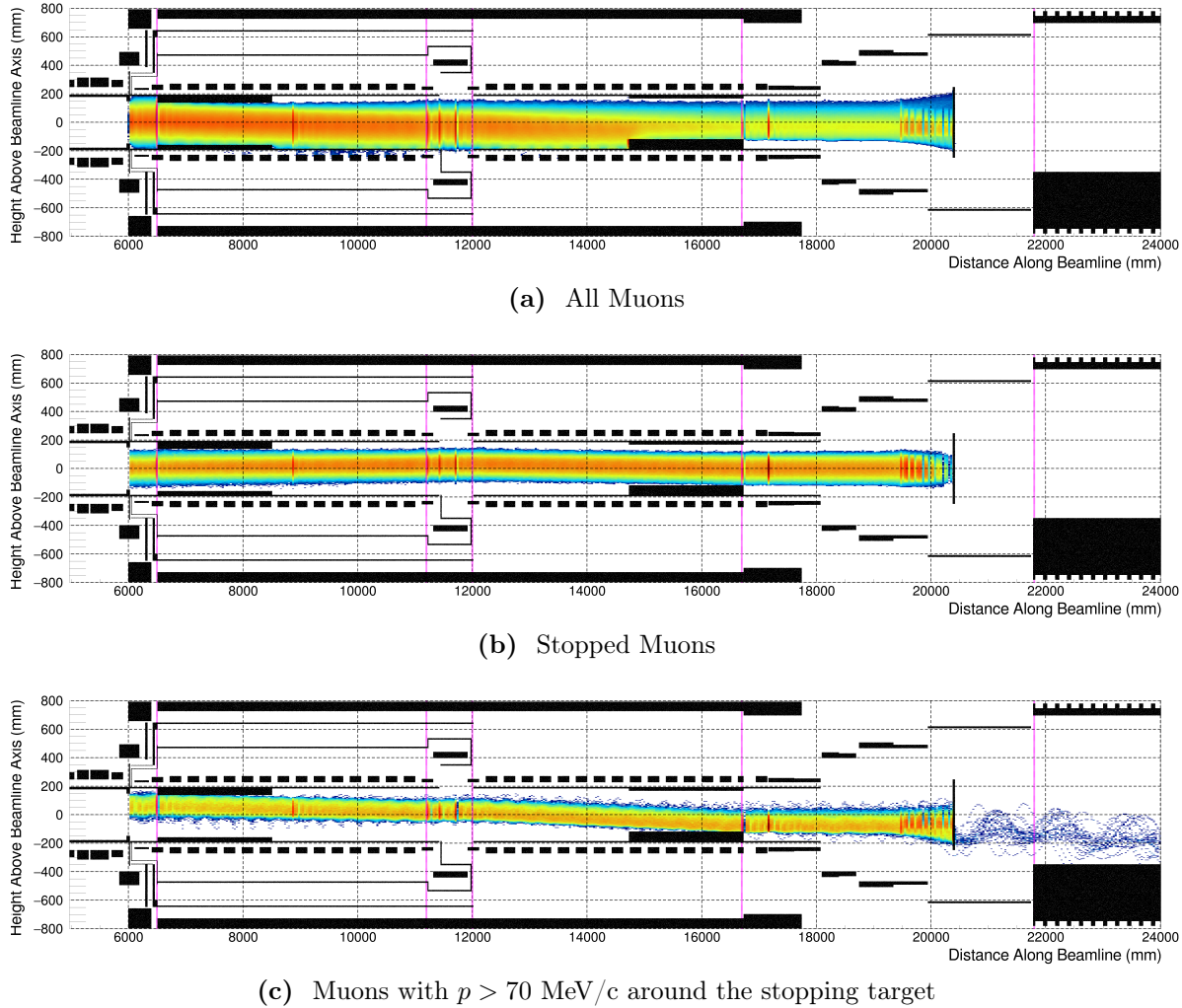


Figure 5.26: The heights of muons as they pass along the beamline. (a) The path of all muons. (b): The paths of muons that stop in the target. (c): The heights of muons with momentum greater than 70 MeV/c when they enter the region around the stopping target. These could potentially decay in flight to give electrons with 100 MeV/c or greater. These plots should be compared to those of Fig. 5.21 before collimators were introduced, where it is clear how well the dangerous muons are being suppressed.

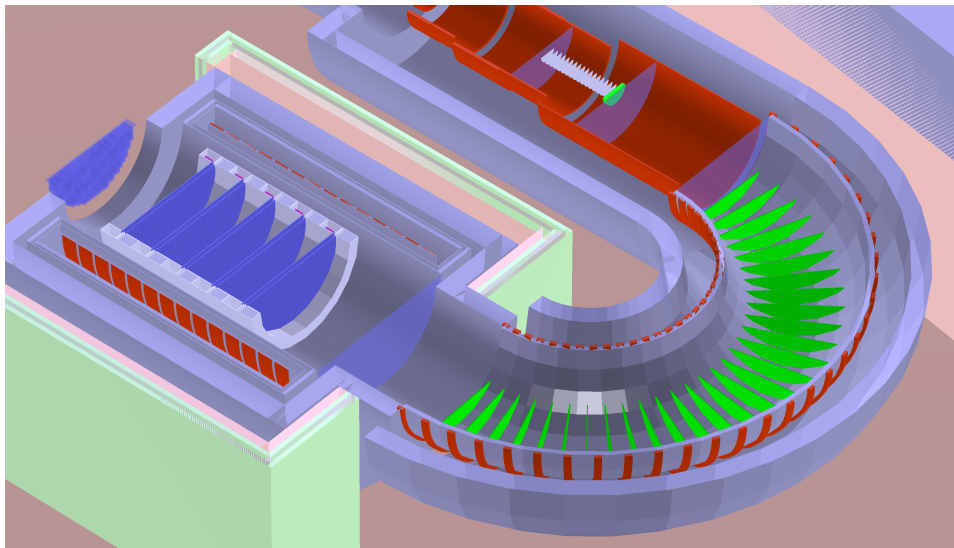


Figure 5.27: Location of the beam blocker and one possible geometry for the DIO blockers, both highlighted in dark green, shown here before optimisation.

Finally, for comparison to the original plots, Fig. 5.26 shows the impact the new collimators have on the muon components of the beam. It is clear how greatly reduced the number of muons passing the stopping target region has now become.

5.7 The Beam and Decay-in-Orbit Blockers

For every muonic atom formed in the stopping target, some 39% will undergo decay-in-orbit (DIO). With about 1.4×10^8 POT per bunch and a muon stopping efficiency of around 1.61×10^{-3} stops per POT, one can expect about 9×10^4 DIO events per bunch. If the detector system were exposed to this number of tracks it would be impossible to resolve any signal electrons. However, above the end-point energy for electrons coming from free muon decay, the DIO spectrum falls extremely quickly, with only around 1% of DIO electrons being produced with more than 59 MeV/c. To this end the electron spectrometer's primary purpose is to disperse away the electrons below 60 MeV/c whilst keep signal electrons on-axis, such that material in the beamline can be tuned to remove the low-energy DIO electrons. The beam and DIO blockers are highlighted in green in Fig. 5.27.

Fig. 5.28 demonstrates the dispersion that appears at the end of the spectrometer with the nominal beam blocker design and no DIO blockers in place. The DIO blockers will be inserted along the bottom of the spectrometer and tuned to scrape away a sufficient

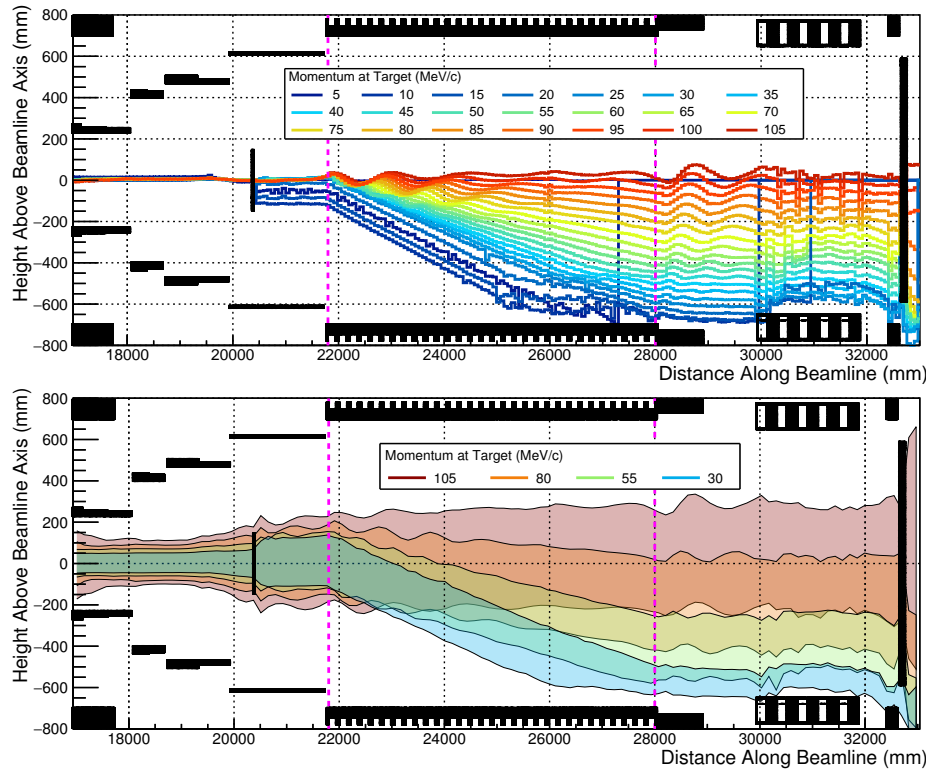


Figure 5.28: Momentum-dependent dispersion of electrons passing through the spectrometer. Top plot: the mean height of different momenta electrons as a function beamline distance, showing how the drift of the centre of gyration is truly proportional to the momentum. Bottom plot: single standard deviation bands for electrons at different momentum, which shows how the envelope for different momenta overlap considerably, reducing the effectiveness of any collimators.

number of DIO electrons, which will tend to travel towards the bottom of the beam pipe. However, whilst the centre of gyration drifts with a well-behaved proportionality in a bent solenoid, the actual separation between signal and DIO electrons is in reality less clear as can be seen by the lower plot in Fig. 5.28.

In addition to the DIO blockers along the spectrometer, the material of the beam blocker immediately after the stopping target also plays a role in suppressing the DIO rate since low-energy electrons remain closer to the beam axis, as can be seen in the lower plot of Fig. 5.28 around the stopping target.

This section therefore describes a simultaneous optimisation of the beam blocker radius and the DIO blocker height. The overall goal is to suppress the DIO rate to less than a single DIO electron per bunch whilst maintain maximal signal acceptance. As for the muon beam collimators, we use the analysis-based collimator approach, where no blocking material is included during simulation. Instead, particle trajectories are

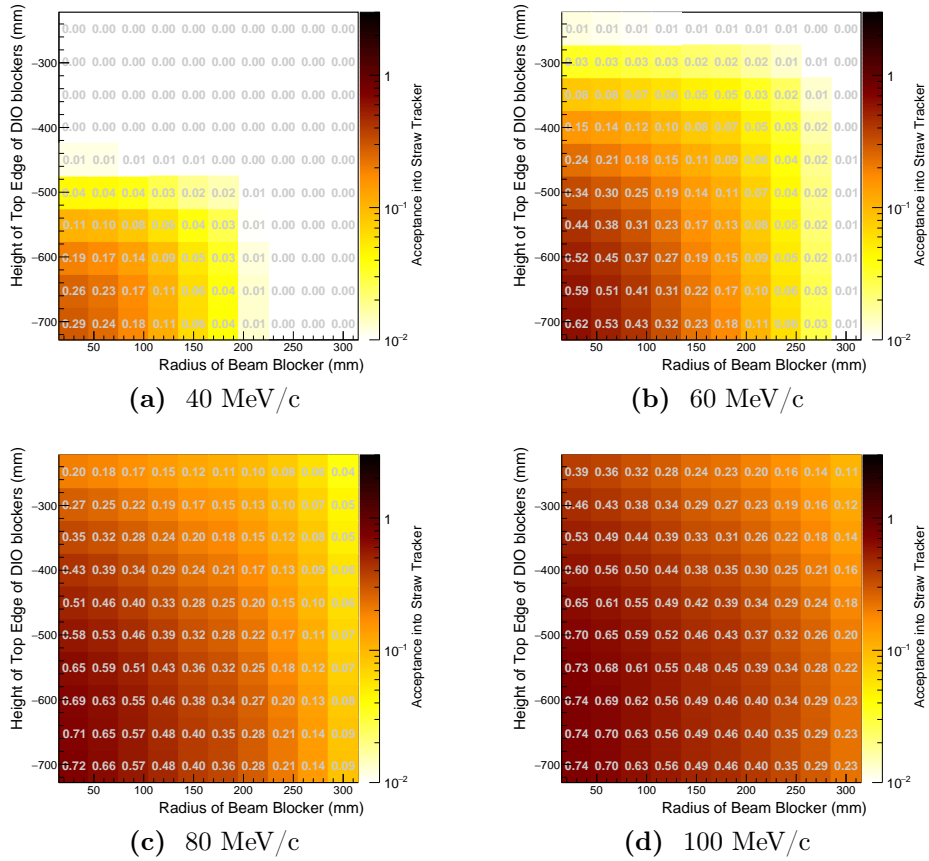


Figure 5.29: Acceptance into the straw tracker for electrons with different momentum at the stopping target as a function of the beam and DIO blocker dimensions. Note the logarithmic scale for the colour bar.

persisted with a high-sampling density such that, during analysis, particles and their secondaries can be ‘killed’ if they enter a region that would contain material of either the DIO or beam blocker.

The results of this study are shown in Fig. 5.29, where the geometric acceptance into the detector is shown for four different electron momenta as a function of the beam blocker radius and DIO blocker height. It is clear that for all values of the blockers’ dimensions, electrons above 100 MeV/c have a much better acceptance.

The mean hit rate per DIO event is shown in Fig. 5.30a. It is formed by, for each combination of DIO and beam blocker dimension, the weighted integral of the acceptance of electrons as a function of momentum with the mean DIO rate in each momentum bin. To compare the hit rate to the acceptance of signal, the ratio between the hit rate and the high-momentum electron acceptance is shown in Fig. 5.30b. It is clear from this

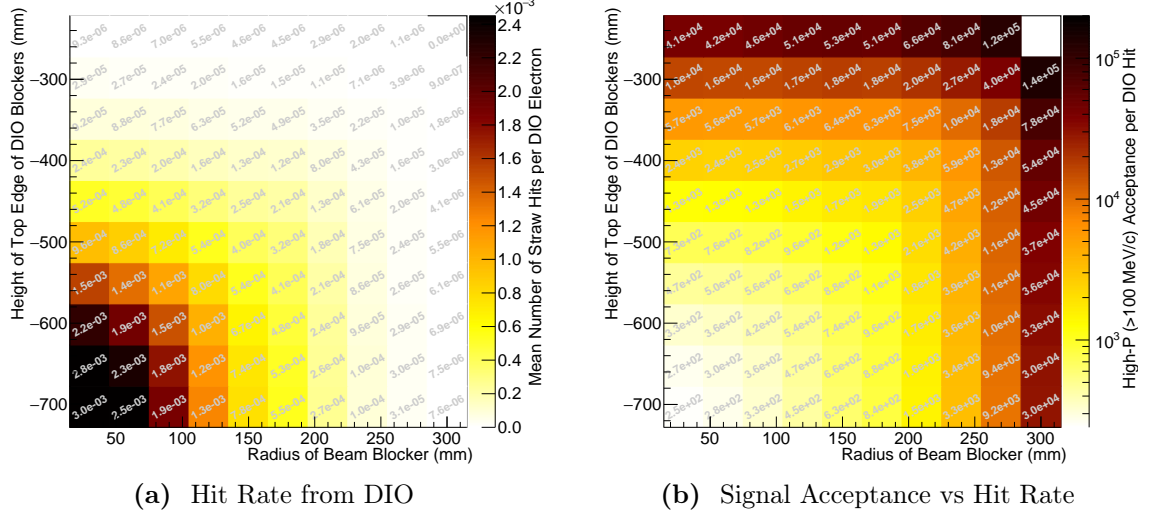


Figure 5.30: (a) Number of straw tracker hits per DIO electron. (b) Ratio between the high-momentum electron ($p > 100$ MeV/c) acceptance to the number of hits per DIO electron. Colour is on a logarithmic scale.

figure how quickly (note the logarithmic colour scale) the DIO hit rate is suppressed by increasing the DIO and beam blocker dimensions compared to the signal acceptance.

With a beam blocker of 24 cm radius and DIO blockers set to 35 cm below the beam axis, the DIO hit rate is about 2.2×10^{-5} per DIO event, or about 2 DIO hits per bunch. For the same blocker dimensions, the geometric signal acceptance is about 0.22%. Given the steep drop-off in hit rate versus signal acceptance around these values a finer scan in this region is an important check for the future. What hit rate in the straw tracker is tolerable is a number for future studies. In Phase-I, the straw tracker is expected to operate with a hit rate around 1 kHz per straw. Phase-II will likely use finer straws, but with the current Phase-I design, some 133 straws occupy a layer, so that a total hit rate into the Straw Tracker of around 200 kHz should be acceptable.

Given the scope for future improvements in the granularity of the Phase-II straw tracker and the sensitivity to the beam and DIO blocker dimensions, the somewhat non-conservative values described above of 24 cm and 35 cm for beam blocker radius and DIO blocker depth below the beam axis are selected here.

| Parameter | Value | Comments |
|-----------------------------------|-----------------------|--|
| Production Target Length | 32 cm | Placed asymmetrically about muon beamline axis |
| Production Target Radius | 1 cm | |
| Torus1 (TS2) Dipole Strength | 0.055 T | same as for Phase-I |
| Torus2 (TS4) Dipole Strength | 0.0275 T | |
| Torus1 Entrance Collimator Height | 14 cm above beam axis | From top of beam pipe downwards |
| Torus2 Exit Collimator Height | 12 cm below beam axis | From bottom of beam pipe upwards |
| Stopping Target Shift | 0 cm | Unchanged from CDR value (2.8 m from centre of final coil in Torus2 to front of target) |
| Electron Spectrometer Dipole | -0.18 T | Negative compared to Torus1 and Torus2 dipole fields |
| Beam Blocker Radius | 24 cm | |
| DIO Blocker Height | 35 cm below beam axis | From bottom of spectrometer upwards |

Table 5.2: Optimised values for the parameters studied in this chapter. Many more parameters remain to be optimised that were considered beyond the scope of the present work.

5.8 Summary of optimised parameters

The complete set of optimised parameters is shown in Table 5.2.

5.9 Future optimisations

The primary goal of this work is to update the previous optimisation from the 2009 CDR and provide a new baseline design. However whilst touching every aspect of the layout of Phase-II, the optimisation developed here is not exhaustive and there is much scope for further work.

The following list is a short summary of some of the areas that could be developed further:

Optimisation criteria In many of these studies only the signal efficiency, or even some proxy, is used to identify the optimal value of the parameter under question. In

reality one ought also to study simultaneously the background rates. These two quantities should be combined into the expected confidence limits given a null or background-only measurement. At the same time other quantities such as cost and run-time will also need considering, although the latter is likely reduced simultaneously with maximising the overall sensitivity.

High-energy electron acceptance vs. beamline distance When tuning the muon beam collimators, the key goal is to remove high-energy particles that can produce high-energy electrons. A particularly useful study would be to evaluate the acceptance to signal-like electrons which originate along the beamline. This should include those electrons which originate with momentum greater than 105 MeV/c but which arrive at the detector with signal-like energies. With this information, it becomes easier to identify how soon along the beamline one must collimate away the high-energy particles which may lead to improvements in the muon stopping rate or the signal acceptance.

Stopping target shape, thickness, and disk spacing This study has focussed only on the position of the stopping target. Clearly the actual shape should be studied as well. In particular, given the dispersion in the muon beam, and the changing solenoidal field strength around the target, a target design that uses disks of varying profile or even thickness has potential to improve the experimental sensitivity.

Correlation between dipole fields and stopping target shape Since the bent solenoids introduce dispersion into the beam and the dipole fields compensate for this, the height and momentum of the muon beam at the stopping target can be controlled to a degree. Whilst in the optimisation of the muon beam dipoles of this thesis the target shape was held fixed, in principle some of the identified correlations might be different if the target design was allowed to vary simultaneously. Such a study would clearly involve an enormous parameter space, so perhaps this is a study that could be best performed with a smarter, machine-learning based approach.

Spectrometer's solenoidal field strength and aperture Since the dispersive effect of a bent solenoid is inversely proportional to the solenoidal field strength, reducing the field in the spectrometer will likely improve the DIO–signal separation, reducing the hit rate. This could, however, also affect the signal acceptance since the trajectories will acquire larger envelopes. Increasing the spectrometer aperture size could compensate this, but then one faces an increase in the cost of the spectrometer and the detector solenoid which would need to be considered.

Chapter 6

COMET Phase-II: Signal Sensitivity

As discussed previously, the signal sensitivity of COMET is a measure of the ability both to produce a signal event and to detect it. The signal efficiency per Proton-on-Target (POT) is therefore the product of the muon stopping rate, the rate of muon capture from the ground state of a muonic atom (the normalisation in the conversion rate), and the total signal acceptance after all analysis cuts and geometric acceptances are considered.

Since signal efficiency describes only the ability to produce and detect signal, this chapter could in principle ignore all possible backgrounds. However in order to tune analysis cuts, one must consider the potential background rates at some level, which must be minimised and controlled. Until the full analysis chain is implemented, we consider only a handful of crude analysis cuts, namely the momentum and timing of electrons. The 2009 Conceptual Design Report (CDR) additionally included cuts on the reconstruction [45] such as track fitting quality, and the ratio between transverse and longitudinal momentum of particles (related to the pitch angle).

6.1 Muon Stopping Rate

Based on a simulation of some 1.1 billion POT, the muon stopping rate of the optimised design was found to be 1.61×10^{-3} per POT. This amounts to 43% of the muons that reach the target itself, a fraction that is determined mostly by the muon momentum distribution and the total amount of target material, as demonstrated by Fig. 6.1 showing the momentum of muons at different points in the beam.

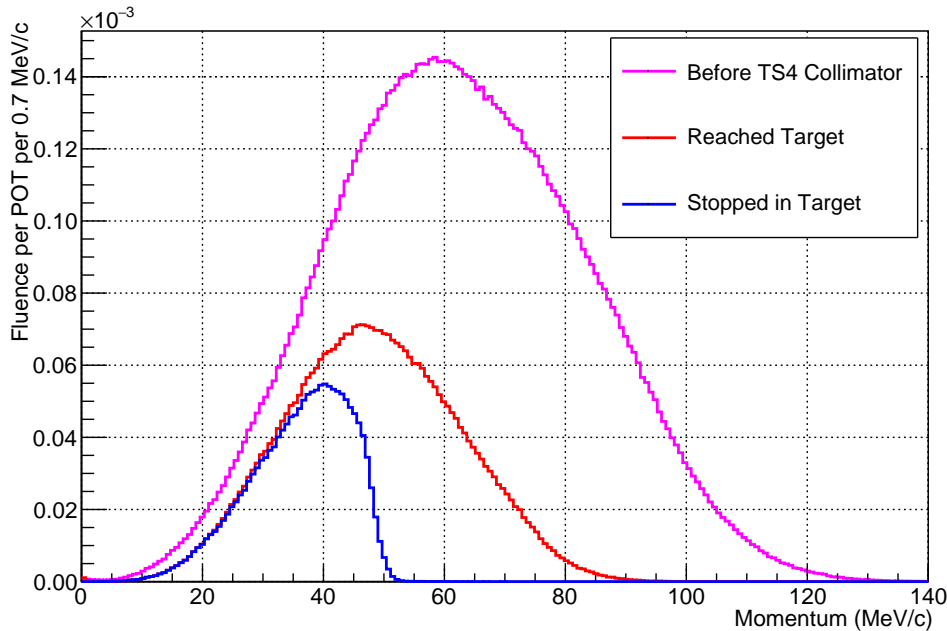


Figure 6.1: The momentum and rates of muons reaching the final beam collimator, the stopping target, and actually stopping in the target. It can be seen how the present target geometry is unable to stop muons of greater than around 50 MeV/c.

Fig. 6.2 shows where muons stop in the target based on this simulation from which it is clear that several asymmetries and correlations exist. For example, the correlation between Z and Y shown in Fig. 6.2c arises due to the dispersion in the muon beam when it arrives at the target. Since high-momentum muons are vertically lower (towards negative Y) in the beam, and since these muons have a larger stopping distance, muons lower down in Y tend to travel further through the target (towards lower values of Z). It is interesting, however, that when the integration is taken over all target disks the distribution in Y demonstrates little asymmetry (Fig. 6.2e). This is most likely due to the fact that the Y-position is controlled by the Torus1 and Torus2 dipole fields which were optimised to maximise the stopping rate, which one might expect to be achieved when the stopping distribution is symmetric.

Given this correlation, there might be a gain in signal sensitivity if there were less material at the top of the target. Since this material is less important for stopping the low-energy muons, removing the extra material might have little impact on the stopping efficiency. On the other hand, it will likely increase signal acceptance since signal electrons will pass through less material.

Whilst the vertical stopping distribution is largely symmetric, a striking asymmetry exists in the horizontal stopping distribution (Fig. 6.2d). The cause of this asymmetry

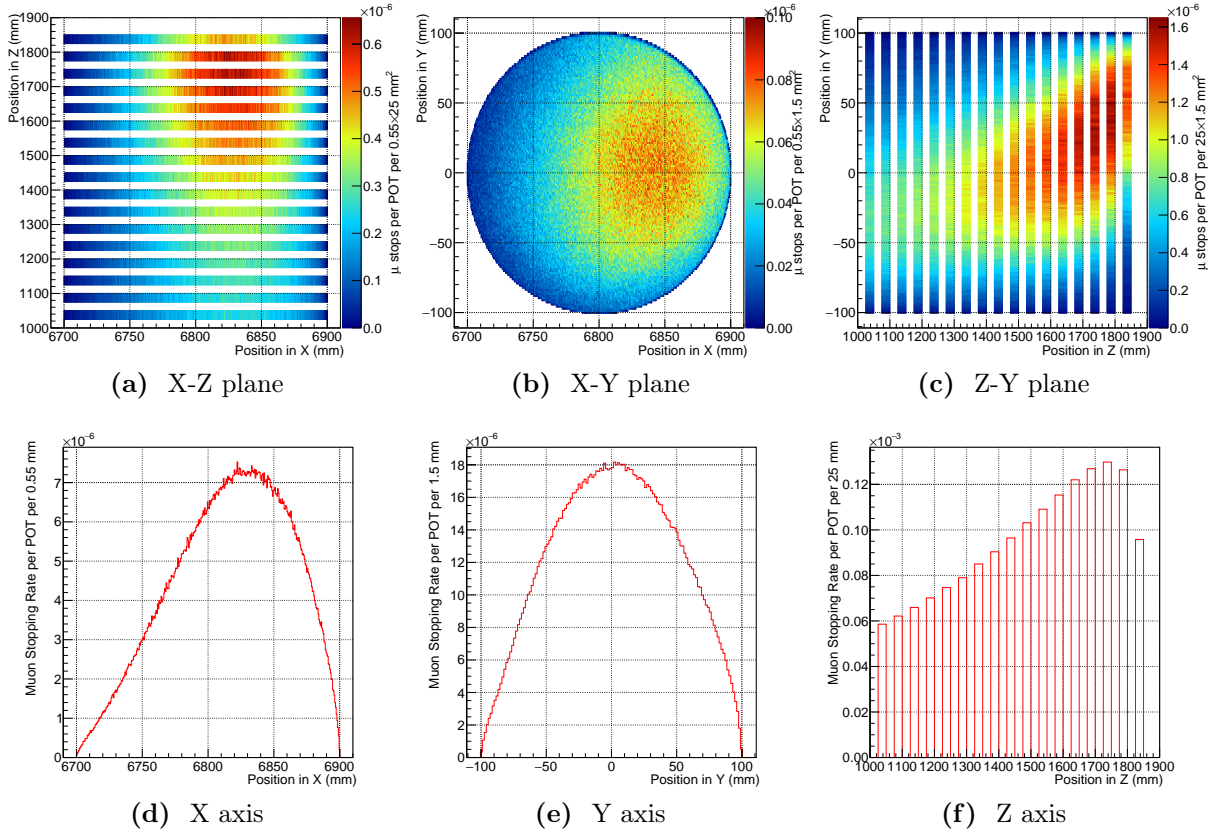


Figure 6.2: Projections of the final position of stopped muons in the stopping target. Axes are from the SimG4 global coordinate system, so that $+X$ points away from the production target, $+Y$ is vertically upwards, and $+Z$ is the direction of the muon beam at the production target. The muon beam in these plots is therefore travelling in the negative- Z direction having passed around through 180° of the bent solenoid.

is unclear at this stage. It could arise from the fact that the production target itself is asymmetric in the horizontal transverse direction, such that more muons and pions are produced to one side of the beam axis. On the other hand, it could also arise from the transportation dynamics of the bent solenoid, dipole field and collimator design. Since this asymmetry could suggest low-energy muons are missing the target on one side, studying the cause of this asymmetry is an important avenue to pursue for further gains in SES! (SES!).

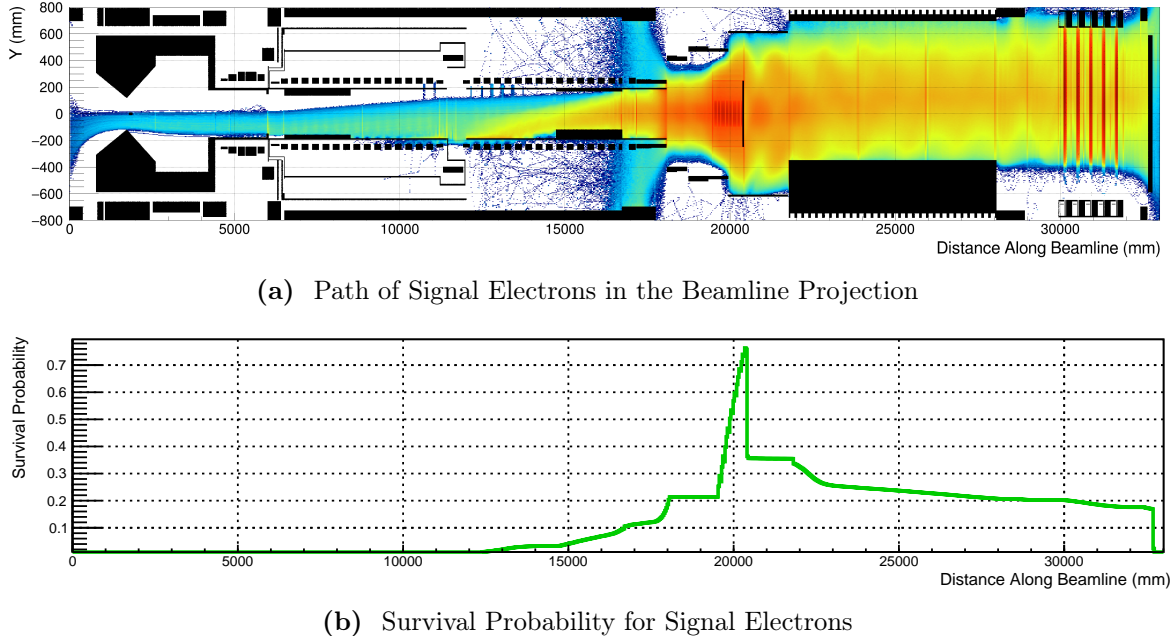


Figure 6.3: Geometric acceptance of signal events. (a) Projection of the trajectories of signal electrons to the surface formed by the beamline axis and the vertical direction. (b) Survival probability of signal electrons as a function of the distance along the beamline axis. The x-axis range is the same in the two plots. From these, it is clear how the acceptance is diminished by the DIO blocker in the spectrometer, although from that point on the rate of signal loss reduces.

6.2 Acceptance of Stopping Target Electrons

Many factors contribute to the signal acceptance; we consider here the geometric acceptance and efficiency of the timing and momentum cuts. Although stopping rate and signal acceptance are often discussed separately, they are in reality coupled through the position and time of the stopped muons. The position impacts on the amount of material the electrons must pass through and, therefore, both their momentum at the detector and their transport through the very inhomogeneous magnetic field of the COMET beamline. Therefore, to study signal acceptance, a realistic muon stopping distribution was first acquired, which was then re-used as the input position and time distribution for signal electrons (although the timing was convolved with the stopped-muon lifetime).

6.2.1 Geometric Acceptance

Fig. 6.3a demonstrates the path of signal electrons injected at the target with a realistic stopping distribution. From this, one can see how the isotropically-directed signal-

electrons are mirrored back to head downstream towards the detector. Fig. 6.3b is a projection of the above plot, normalised to the number of primary signal electrons. As such, it shows the survival probability for electrons as a function of beamline distance.

Based on this and a second analysis that uses the hits in the Straw Tracker directly, the geometric acceptance of the beamline and Straw Tracker is found to be 0.22 per signal electron¹.

6.2.2 Timing Window Efficiency

A time-gated detector window is used to further reduce the background rate. Whether this is implemented in the trigger, in the offline analysis, or at different levels in each one of these is yet to be determined but the impact on signal efficiency will likely be the same.

¹ This is almost exactly the value predicted by the collimator analysis-based approach of 5.7, suggesting that such an approach is truly adequate for this sort of study, despite the concerns mentioned in that section.

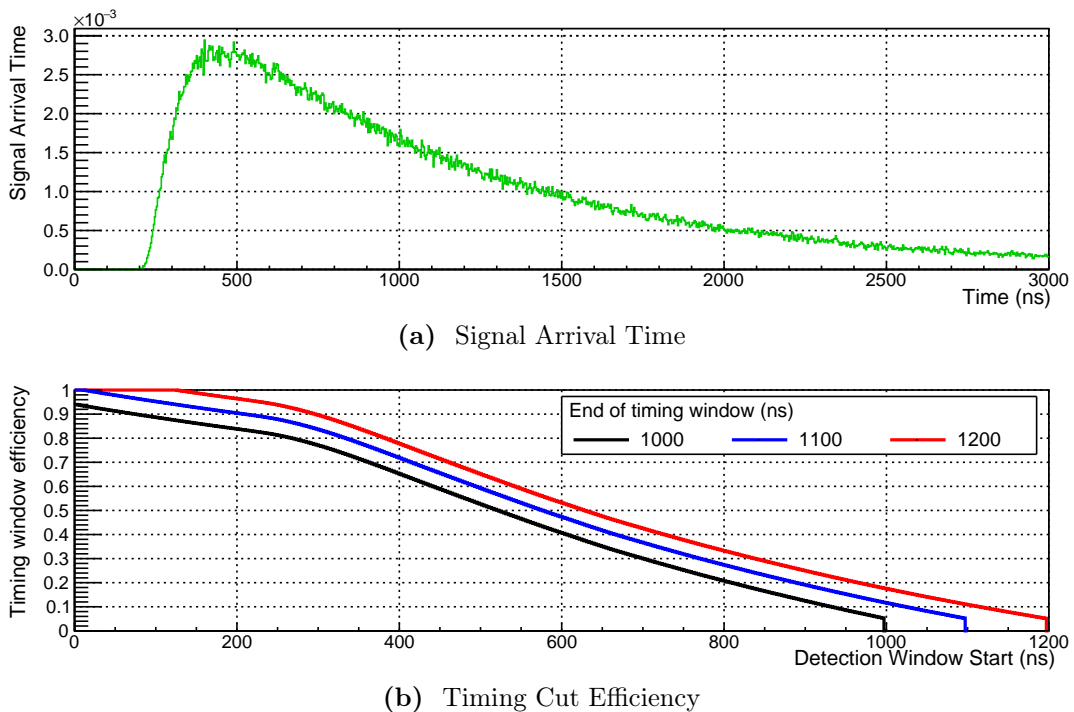


Figure 6.4: Timing of signal electrons. (a) The arrival time of signal electrons at the detector, including the effect of the proton pulse width, particle transportation, and the muon lifetime. (b) the efficiency of the timing window as a function of the switch-on time. Assumes a pulse separation of $1.17 \mu\text{s}$.

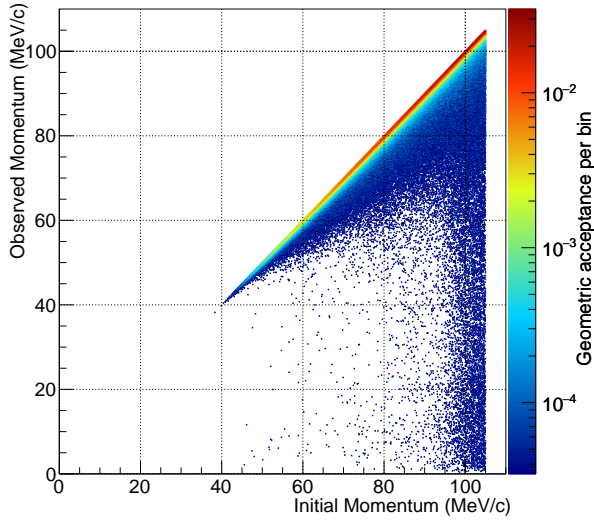


Figure 6.5: The transfer matrix for electrons originating at the target, including the geometric acceptance and energy loss.

Fig. 6.4a shows the arrival time of signal electrons. A subtlety of the gated time window is that since the signal lifetime is large compared to the pulse separation of $1.17 \mu\text{s}$, a signal electron has a reasonable chance of arriving in detector windows later than the first one. Fig. 6.4b shows the signal acceptance as a function of the start time of the detector window for three different stop times. Time in that plot is with respect to the proton pulse's arrival; since it takes about 100 ns before any beam flash hits the detector, it is reasonable that the gated-time detector window be open at the very moment when the proton pulse arrives. This would be the case at the very end of the window that ends at 1200 ns, given that pulses are separated by about 1170 ns.

One must also consider the timing of background processes to pick a valid time window. Motivated primarily by the pion radiative capture background (which will be discussed in completion in section 7.3), a time window of 600 to 1200 ns is selected. The signal efficiency of this timing window is 0.53.

6.2.3 Momentum Cut Efficiency

Between production in the stopping target and detection at the Straw-tube tracker and Electromagnetic Calorimeter (StrECAL), electrons lose energy by scattering, bremsstrahlung and ionisation of material in the electron's path, including the stopping target itself and the detector. Fig. 6.5 shows the momentum transfer function for electrons coming from

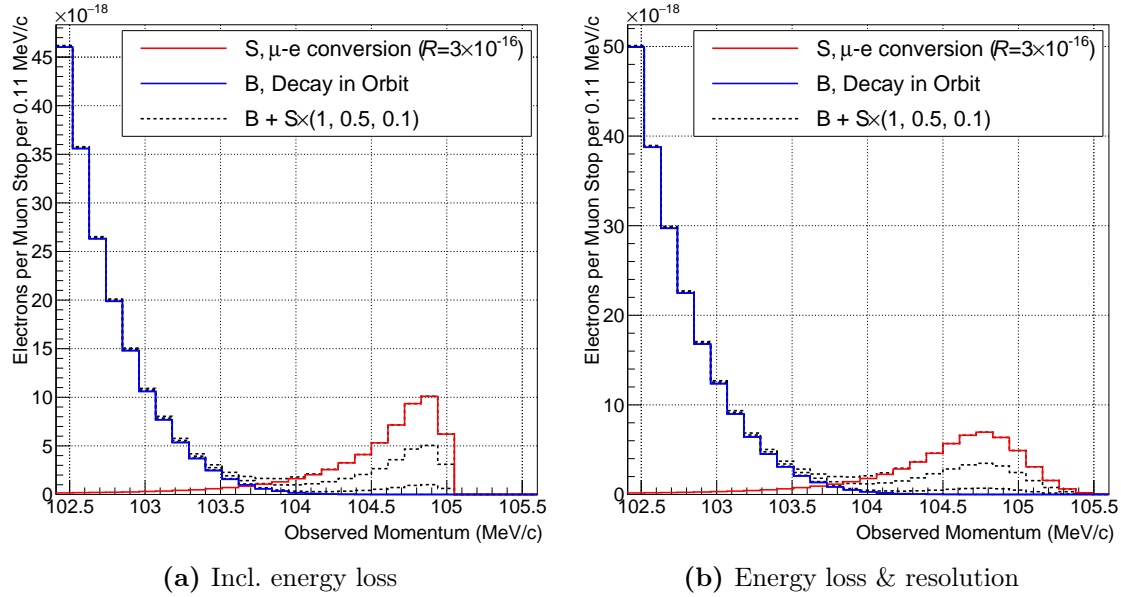


Figure 6.6: The spectrum of electrons coming from DIO and μ -e conversion assuming a conversion rate of $\mathcal{R} = 3 \times 10^{-16}$. Black dashed lines indicate the total electron distribution that would be seen (the sum of S and B) if the signal has the assumed conversion rate of 3×10^{-16} , half that rate, and one tenth that rate. (a) Includes energy losses in the target, beamline, and detector; (b) also includes resolution effects (for a Gaussian resolution function with a standard deviation of $\sigma = 200$ keV/c).

the target and reaching the detector. Each bin represents the probability that an electron is observed at a particular momentum given an initial momentum.

Crucial for signal sensitivity is how this energy loss affects signal electrons compared to DIO electrons. Fig. 6.6a shows the impact this energy loss has close to the signal energy, where it is clear that a low-energy tail is produced from what is an intrinsically monoenergetic signal.

In addition to energy losses in material in the beamline, the resolution of the Straw Tracker and the reconstruction algorithm must be considered. No reconstruction algorithm can ever reproduce the true momentum of a particle with perfect accuracy. A design requirement of the StrECAL has been that it achieves 200 keV/c resolution for 105 MeV/c electrons and indeed work on Phase-I has demonstrated performance better than this. Since, at this time, work on the Phase-II reconstruction has not yet begun and even the Phase-I StrECAL reconstruction requires further development, we approximate the residual function—probability distribution of the difference between reconstructed and true momentum—by a single Gaussian with a standard deviation of 200 keV/c. The

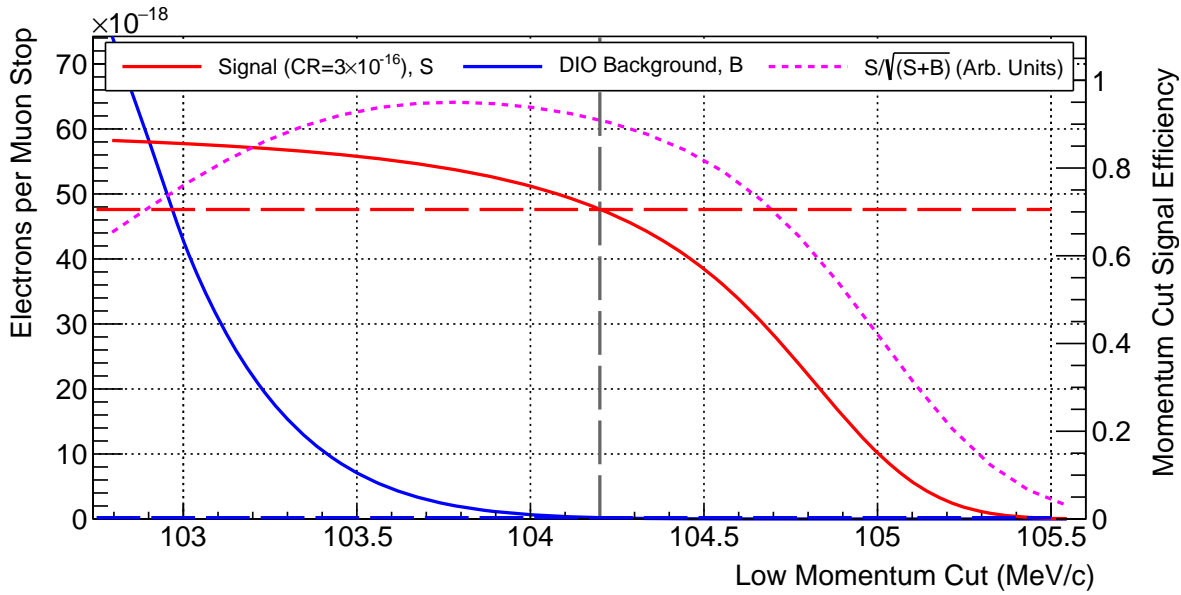


Figure 6.7: Relative signal versus DIO background as a function of the low-momentum cut value assuming a conversion rate of $\mathcal{R} = 3 \times 10^{-16}$ and with a fixed upper threshold of $105.5 \text{ MeV}/c$. The magenta line is the signal over square root of signal plus background for this conversion rate shown as an indicator of the optimum cut value.

impact that such a residual function would have on the observed DIO and μ - e conversion spectra is shown in Fig. 6.6b.

Elaborate analysis techniques might then estimate the number of signal events by simultaneously fitting the above signal and background functions to the measured total spectrum. For the purpose of developing a baseline sensitivity estimate however, we envisage instead a simple analysis procedure which counts the number of events within a momentum window. In that procedure, one would tune the threshold to maximise the signal to background separation, as demonstrated by Fig. 6.7 where the number of events accepted are shown as a function of the low-momentum cut value. Also shown is the function of signal divided by the square root of signal plus background, an indicator of the relative signal to background fluctuations one can expect. Although this function peaks at around $103.68 \text{ MeV}/c$, since this value is only optimal for the demonstration signal conversion of $R = 3 \times 10^{-16}$ and to bring the DIO rate down further (see section 7.1), a low-momentum cut of $104.2 \text{ MeV}/c$ is selected. At this value the signal efficiency of the momentum cut is 0.70. It should be noted, though, that whilst changing the cut value leaves the signal efficiency relatively unchanged, the DIO rate varies dramatically: a shift of the threshold up or down by $0.1 \text{ MeV}/c$ changes the signal acceptance by about 1.5 percentage points, but changes the DIO rate by a factor of 2.

| Overall Acceptance | 2009 CDR [45] | This Study |
|---|---------------|------------|
| Geometric acceptance | 0.20 | 0.22 |
| <i>Solid angle with mirroring</i> | (0.73) | |
| <i>Beam blocker acceptance</i> | (0.57) | |
| <i>Spectrometer acceptance</i> | (0.47) | |
| Timing window efficiency | 0.39 | 0.53 |
| Momentum cut efficiency | 0.72 | 0.70 |
| TDAQ acceptance and efficiency | 0.90 | N/A |
| Reconstruction aspects | 0.78 | N/A |
| <i>Recon. efficiency</i> | (0.88) | |
| <i>Track quality cut efficiency</i> | (0.89) | |
| Additional analysis cuts | 0.81 | N/A |
| <i>Transverse momentum cut efficiency</i> | (0.83) | |
| <i>E/p cut efficiency</i> | (0.99) | |
| <i>Pitch angle cut efficiency</i> | (0.99) | |
| Total acceptance at ‘truth level’ | 0.056 | 0.091 |
| Total (with CDR recon. and TDAQ efficiencies) | 0.039 | 0.057 |

Table 6.1: Numbers that go into estimating the total signal acceptance from this study compared to the previous evaluation in the 2009 CDR. Since this study has not estimated reconstruction issues, we include the previous values in the final estimate on the expectation that with the improvements in reconstruction techniques and with the benefit of Phase-I final reconstruction efficiency will be improved compared to the 2009 CDR values.

6.2.4 Total Signal Acceptance

Table 6.1 gives a summary of the signal acceptance parameters as estimated here and, for comparison, the values from the previous study for the CDR [45]. For the CDR the geometric acceptance had to be factorised into each section of the beamline to reduce the processing power required. The present study, being able to perform this in a single step, should be more reliable for the total geometric acceptance, yet agrees well with the previous estimate.

For reconstruction and Trigger and DAQ efficiencies, we expect the CDR value to be a reliable lower limit and so we re-use these here as a conservative baseline. This is another aspect of this study that can be improved in the future, and indeed thanks to the Phase-I run will not only be finalised within the next year or so but will be tested and

debugged on real data prior to the Phase-II run. Finally, the CDR includes a number of additional analysis cuts, which reduce the sensitivity but were necessary to improve background separation. In this study such cuts are not applied, and so the efficiency of these cuts is not included in the final acceptance calculation.

6.3 Single Signal Event Sensitivity (SES) and Run Time

It remains only to pull all these numbers together into equation (2.4). By expanding N_μ in that equation as the product of the number of protons per second, I_p/e , the muon stopping rate per POT, $R_{\mu/p}$, and the running time, t_{run} , we find the predicted Single-Event Sensitivity (SES) and run time to be related by:

$$\text{S.E.S} \cdot t_{\text{run}} = \frac{1}{(I_p/e)R_{\mu/p}\mathcal{B}_{\text{capture}}A_{\mu \rightarrow e}} = 4.08 \times 10^{-10}, \quad (6.1)$$

where the values for each of these parameters is given in Table 6.2. Accordingly, if the run time were fixed to the value of the CDR, 2.0×10^7 s, an SES of 2.04×10^{-17} would be achievable. Alternatively, the CDR sensitivity, 2.6×10^{-17} , would be achievable in 1.6×10^7 s. In that time, COMET Phase-II would impinge 6.83×10^{20} protons on the production target, resulting in 1.10×10^{18} negative muon stops in the stopping target. As can be seen by Table 6.3, on a year-by-year basis the predicted Phase-II sensitivity is about 3.5 times better than the Mu2e experiment's expectation [42], and about 92 times better than COMET Phase-I.

| | | |
|--------------------------------|-----------------------|--|
| I_p | $7 \mu\text{A}$ | Proton beam current |
| $R_{\mu/p}$ | 1.61×10^{-3} | Muon stopping rate per POT |
| $\mathcal{B}_{\text{capture}}$ | 61% | Branching ratio for muon nuclear capture in Al |
| $A_{\mu \rightarrow e}$ | 5.7 % | Total signal acceptance of Phase-II |

Table 6.2: Parameters that determine the run time and single event sensitivity for COMET Phase-II based on this study.

| | Single event sensitivity | Total POT ($\times 10^{19}$) | Beam time t_{run} (s) | SES in one year of continuous beam |
|--------------------------------|--------------------------|--------------------------------|--------------------------------|------------------------------------|
| COMET Phase-II (this study) | 2.6×10^{-17} | 68.3 | 1.57×10^7 | 1.29×10^{-17} |
| COMET Phase-II (CDR 2009 [45]) | 2.6×10^{-17} | 85 | 2.00×10^7 | 1.65×10^{-17} |
| Mu2e [42] | 2.4×10^{-17} | 36 | 6.00×10^7 | 4.57×10^{-17} |
| COMET Phase-I [44] | 3.0×10^{-15} | 3.2 | 1.26×10^7 | 1.19×10^{-15} |

Table 6.3: Comparison between the run time and single-event sensitivity from this study and from the 2009 CDR, the Phase-I TDR, and the Mu2e experiment’s TDR. The SES in one year of continuous beam is the single-event-sensitivity that can be achieved in 3.15×10^7 seconds of running, assuming no beam shutdown periods.

6.3.1 Fraction of Conversion Events That Excite the Nucleus

In the COMET Phase-I TDR [44], an additional factor, f_{gnd} , is included in the denominator of (6.1). This factor, given with a value of 0.9, covers the fraction of conversion events that do not excite the nucleus in some way (i.e. leave it in its ground state), which will be roughly the same as the fraction of events that can be called ‘coherent’. Whatever the outcome of COMET, whether a signal is observed or not, adapting the final measurement to theoretical predictions will have to include this factor.

However, this factor is not constant and depends on the exact model producing the conversion. It is typically larger than 90%, but can be as low as 57% [76]. Given this model dependence, it has been decided not to include this factor in the above estimate. It must be emphasized, then, that the sensitivity expressed here is the single-event sensitivity for *conversion that leaves the nucleus unexcited*. Theorists and model builders must predict the probability of coherent conversion (and the incoherent probability, if it leaves the nucleus unchanged) that a given New Physics model would produce, and then scale the experiment’s final rate or limit accordingly.

It is interesting to note that models with larger coherent branching ratios favour long-range forces and, therefore, massless propagators. Moreover, if the nucleus is excited, the energy of the electron will be lower than for coherent μ - e conversion. If nuclear resonances exist one might see a spike or kink in the electron spectrum at lower energies. To understand such features, in addition to the excellent experimental momentum resolution, the theoretical uncertainty on the DIO and Radiative Muon Capture (RMC) spectra is, again, especially important.

Chapter 7

COMET Phase-II: Backgrounds

Having optimised and evaluated the signal sensitivity, it is now important to check the expected background rates. Interpreting the final result is only possible if the number of background events has been predicted. The certainty of any observation or the stringency of a final confidence limit is determined by the relative background rate and signal sensitivity; ideally the background rate should be small, well below a single expected event.

The types of background that must be considered for COMET were outlined in 3.2, but in this section they will be evaluated for the optimised experiment design using the improved simulation.

7.1 Muon Decay in Orbit (DIO)

In order to decide the optimal threshold for the momentum cut, it was necessary, in section 6.2.3, to study the rate of decay-in-orbit (DIO) events. With a low-momentum threshold of $104.2 \text{ MeV}/c$, the number of expected DIO events per muon stop is 6.20×10^{-20} . Given the 1.10×10^{18} muon stops that should take place during Phase-II, the total expected number of background events due to DIO is 0.068.

However, it is important to note just how steeply falling the DIO rate is in this region. Fig. 7.1 shows how, given a fixed run time, the number of DIO background events is affected by changing the low-momentum threshold. Changing the momentum threshold also affects the signal acceptance, so that for a fixed run time the SES is also affected. Simultaneously, with more muons stopped the DIO rate will increase for a fixed momentum threshold. Fig. 7.1 was produced using the same DIO and signal

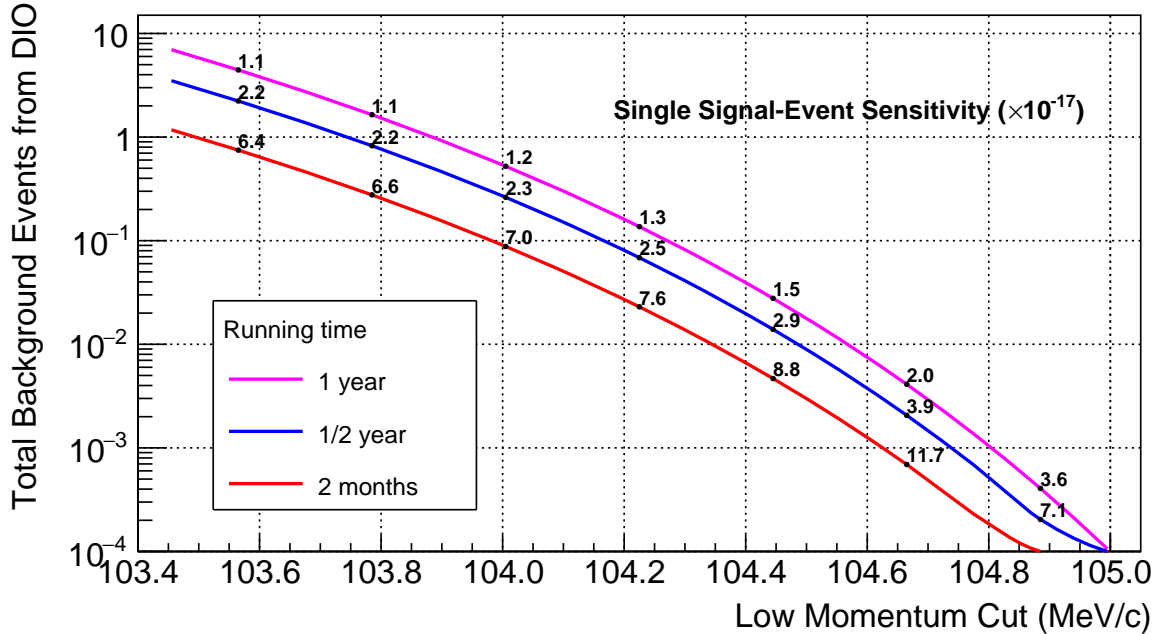


Figure 7.1: The DIO background rate as a function of momentum threshold for different total running times. Given a fixed running time, the total number of stopped muons is also fixed, which in turn sets the signal sensitivity and the DIO background rate. All signal acceptance parameters were held fixed, except for the efficiency of the momentum threshold, which, when combined with the number of stopped muons, determines the SES. The SES is indicated in the number along the lines in units of 1×10^{-17} .

spectra shown in Fig. 6.6b, which included energy losses in the material of the target, beamline, and detector, as well as a 200 keV/c Gaussian resolution function. In addition, all the acceptance parameters of the sensitivity chapter were held fixed, except for the momentum cut efficiency.

The fact that the run-time, signal acceptance, and background rate depend so strongly on the momentum threshold makes the theoretical prediction for the DIO spectrum particularly important. The two most recent calculations of the high-energy tail of the DIO spectrum are shown in Fig. 7.2, as well as the cruder function that fits the whole spectrum range, used in SimG4. The more conservative spectrum from the 2011 paper [34] has been used in this study. However, if one were to use the more recent 2015 spectrum [77], background rates due to DIO would fall to 0.057 events at the same momentum threshold. This would agree with that paper’s statement that the inclusion of radiative corrections suppresses the DIO background by 15% at the end-point.

In total, based on the 2011 DIO spectrum, 3×10^{-18} electrons would be produced per muon stop with momentum greater than 104.2 MeV/c. Therefore, the DIO rejection

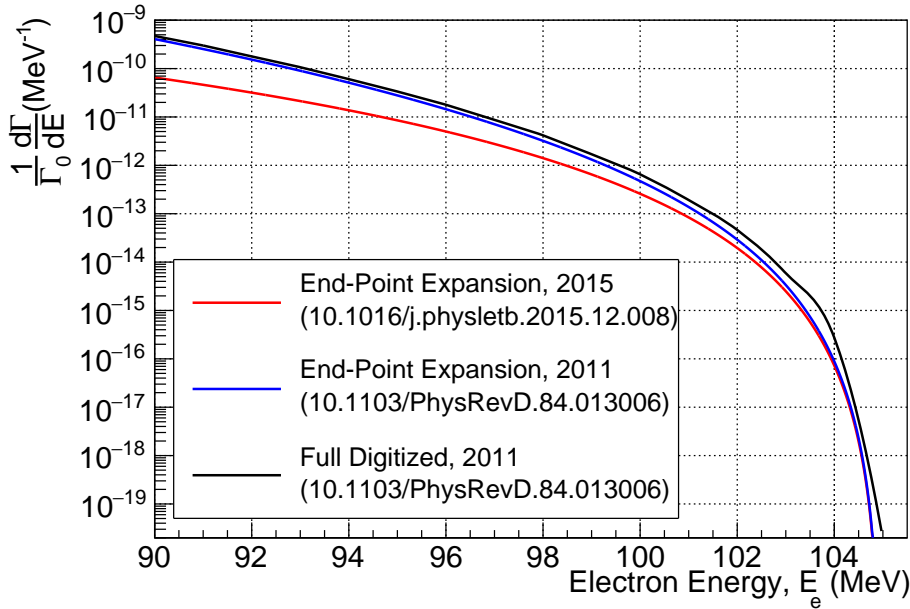


Figure 7.2: Comparison of the various available end-point expansions. The red and blue lines show the parametrisations reported in the literature, whilst the black shows the digitisation of the spectrum used in SimG4. For this study, the more conservative parametrisation from the 2011 Czarnecki paper [34] has been used.

efficiency, including both geometric effects and the threshold on the detected momentum, suppresses the detection of DIO end-point electrons by about 98%.

7.2 Radiative Muon Capture (RMC)

During the process of nuclear muon capture, there is a finite probability of a hard photon being radiated from the muon, nucleus, or the exchanged W -boson. This is known as Radiative Muon Capture (RMC) and is distinguished from radioactive gamma-ray production during nuclear de-excitation or decay of the daughter nucleus. The maximum energy this photon can take, $\max(E_e^{\text{RMC}})$, differs from the μ - e conversion signal and DIO end-point by the minimum energy needed to change the nucleus from $N(A, Z)$ to $N(A, Z - 1)$:

$$\max(E_e^{\text{RMC}}) = (M_\mu - B_{\mu, \text{binding}} - E_{\text{rec}}) - (M_{N_2} + \sum_i M_{h_i} - M_{N_1} - \Delta Z \cdot M_e), \quad (7.1)$$

$$= E_e^{\text{Conversion}} - \Delta M, \quad (7.2)$$

| Reaction | Atomic Mass of Daughter (u) | ΔM (MeV/c ²) | $\max(E_e^{\text{RMC}})$ (MeV/c ²) |
|---|-----------------------------|----------------------------------|--|
| $^{27}\text{Al}(\mu, \gamma\nu)^{27}\text{Mg}$ | 26.984 341 | 3.12 | 101.85 |
| $^{27}\text{Al}(\mu, \gamma\nu 2n)^{26}\text{Mg}$ | 25.982 593 | 9.56 | 95.41 |
| $^{27}\text{Al}(\mu, \gamma\nu 2n)^{25}\text{Mg}$ | 24.985 837 | 20.66 | 84.31 |
| $^{27}\text{Al}(\mu, \gamma\nu p)^{26}\text{Na}$ | 25.992 633 | 18.13 | 87.37 |
| $^{27}\text{Al}(\mu, \gamma\nu np)^{25}\text{Na}$ | 24.989 954 | 23.71 | 81.77 |
| $^{27}\text{Al}(\mu, \gamma\nu d)^{25}\text{Na}$ | 24.989 954 | 21.49 | 84.00 |
| $^{27}\text{Al}(\mu, \gamma\nu \alpha)^{23}\text{Na}$ | 22.994 467 | 15.49 | 91.01 |

Table 7.1: Several potential daughter nuclei of nuclear muon capture in ^{27}Al . The mass of ^{27}Al is 26.98153863 u , and one u is taken as 931.494061 MeV/c² [78]. All masses come from [79].

with M_{N_1} and M_{N_2} the mass of the parent and daughter nuclei respectively, and M_{h_i} the mass of the i -th hadron (proton, neutron, alpha, etc.). The mass of the electron, M_e , must also be included since a free electron must be ejected from the atomic orbitals for every proton removed from the nucleus, equivalent to ΔZ . ΔM is then the total energy lost to changes in the atomic mass¹ of the nuclei and other emitted hadrons.

When an aluminium-27 nucleus captures a muon various daughter nuclei are possible. If no other particles are emitted, as part of direct nucleon capture, the daughter nucleus will be magnesium-27. In general, this could be left in an excited state, but to reach the end-point of the RMC spectrum it will be left in the ground-state configuration. The atomic mass difference between these two nuclei is shown in Table 7.1, where it can be seen that the RMC end-point is separated from the μ - e conversion signal energy by around 3 MeV.

Table 7.2 shows a summary of the experimental data on aluminium, taken from the summary by Gorringe [80]. It is interesting to note that in all experiments to date none of the empirical fits to RMC have suggested an end-point above 90.1 MeV [81, 82, 83]. This is close to the end-point predicted by the various transitions besides $^{27}\text{Al}(\mu, \gamma\nu)^{27}\text{Mg}$.

¹ One has to think of the atomic mass difference, rather than the nuclear mass difference. The distinction is important since consideration of the nuclear masses alone would ignore the effect on the atomic electrons. Under nuclear muon capture (radiative or otherwise), the number of protons in the nucleus is reduced by at least one, and accordingly atomic electrons become unbound. The notation here follows that of the COMET TDR [44] and CDR [45], where the electron mass is absorbed into the value of ΔM (although there it is called Δ_{Z-1}).

| Target | α | $R_\gamma (\times 10^{-5})$ | k_{\max} (MeV) |
|--------------------------------|----------|-----------------------------|------------------|
| <i>Bergbusch et al. (1999)</i> | | | |
| $^{27}_{13}\text{Al}$ | 0.077 | 1.43 ± 0.11 | 90.1 ± 1.8 |
| $^{28}_{14}\text{Si}$ | 0.000 | 2.09 ± 0.20 | 89.4 ± 1.8 |
| <i>Armstrong et al. (1992)</i> | | | |
| $^{27}_{13}\text{Al}$ | 0.077 | 1.43 ± 0.13 | 90.0 ± 2.0 |
| $^{28}_{14}\text{Si}$ | 0.000 | 1.93 ± 0.18 | 92.0 ± 2.0 |
| <i>Döbeli et al. (1986)</i> | | | |
| $^{27}_{13}\text{Al}$ | 0.077 | 1.83 ± 0.26 | 88.8 ± 1.8 |

Table 7.2: Summary of experimental values of the rate of RMC producing photons with energy greater than 57 MeV, R_γ , and the observed end-point, k_{\max} , redacted from [80]. The column labelled ‘ α ’ is the neutron excess for the element, determined by: $\alpha = (A - 2Z)/Z$.

The two most recent of these experiments both measure the branching ratio for RMC producing photons with $E > 57$ MeV to ordinary muon capture to be 1.43×10^{-5} .

To produce a background event in the detector, the high-energy photons produced from RMC must be converted to a high-energy electron. Asymmetric pair production from this photon is one mechanism by which this can occur, although producing the positron at rest is highly suppressed. In addition, around 1 MeV is consumed by the mass of the electron-positron pair. Compton scattering provides another mechanism by which the high-energy photon can convert to a high-energy electron. In the limit where the photon is reflected directly back on itself, the resultant electron has momentum greater than the incoming photon by around $M_e/2$. As such it is Compton scattering which is more of a concern for COMET.

Finally, given the maximum photon energy is below the momentum threshold of 104.2 MeV/c, the electron’s energy needs to be mis-reconstructed by around 2.4 MeV. If the final resolution function were a pure Gaussian with a 200 keV/c width (at signal energies), then mis-reconstruction by such an amount would be an 11σ event, i.e. $P(p_{\text{recon}} - p_{\text{true}} > 2.4 \text{ MeV}/c) = 1.9 \times 10^{-28}$. However, the resolution function is not likely to be a pure Gaussian. On-going studies for reconstruction with the Phase-I StrECAL currently suggest that the tails of the resolution function are much larger than for a pure Gaussian. Although the Phase-I Straw Tracker reconstruction is still being finalised, early studies suggest $P(p_{\text{recon}} - p_{\text{true}} > 2.4 \text{ MeV}/c) = 4.4 \times 10^{-15}$ [84]. Although this is considerably larger than the pure Gaussian, this is based on the most preliminary results of reconstruction algorithms. If need be, cuts on fit quality can be improved over the current Phase-I values; the sensitivity estimate presented here should

be robust against this since it includes the CDR estimate for the signal efficiency of such a cut.

7.2.1 Calculation and Simulation of RMC

Conversion of the RMC photons can take place in any of the material around the target, such as the beam blocker, solenoids, or cryostat. To estimate the acceptance of the electrons produced from this conversion a simulation was performed where RMC photons were input at the stopping target, using the realistic muon stopping distribution obtained previously. Geant4 implements the process of photo-conversion via both of the afore-mentioned methods.

To build a realistic end-point spectrum, the same recipe as used in the Phase-I TDR was applied [44]. The spectrum shape near the end-point is modelled by the equation [85]:

$$\Gamma(\text{RMC}) \propto (1 - 2x + 2x^2)(x)(1 - x)^2, \quad (7.3)$$

where $x = E_\gamma / \max(E_\gamma^{\text{RMC}})$. The largest observed branching ratio for RMC compared to ordinary muon capture— 1.83×10^{-5} —is used to set the normalisation. The relative rate of RMC resulting in photons with energies above 90 MeV is, based on the spectrum in equation (7.3), 7.7×10^{-3} of the experimentally observed rate.

Given the total number of muon stops during Phase-II, the probability of ordinary muon capture, and the relative rates for RMC, one expects some 9.4×10^{10} photons to be produced in the target with energies above 90 MeV. Since this is an intrinsic background, the lifetime of this process will be the same as for signal events. Assuming, therefore, the same timing window acceptance, and applying the same reconstruction and TDAQ efficiencies as for signal, this number is reduced to 3.5×10^{10} .

To check the probability that these photons produce a high-momentum electron in the detector, some 6×10^7 RMC events were generated in the stopping target, with initial photon energies greater than 90 MeV and distributed according to the spectrum in equation (7.3). Fig. 7.3 shows the momentum and rate at which these were detected. Based on this, the fraction of events reaching the detector with momentum larger than 98 MeV/c was 6.2×10^{-7} , whilst above 100 MeV/c only 3.3×10^{-8} electrons per $\text{RMC}|_{p>90}$ event were detected.

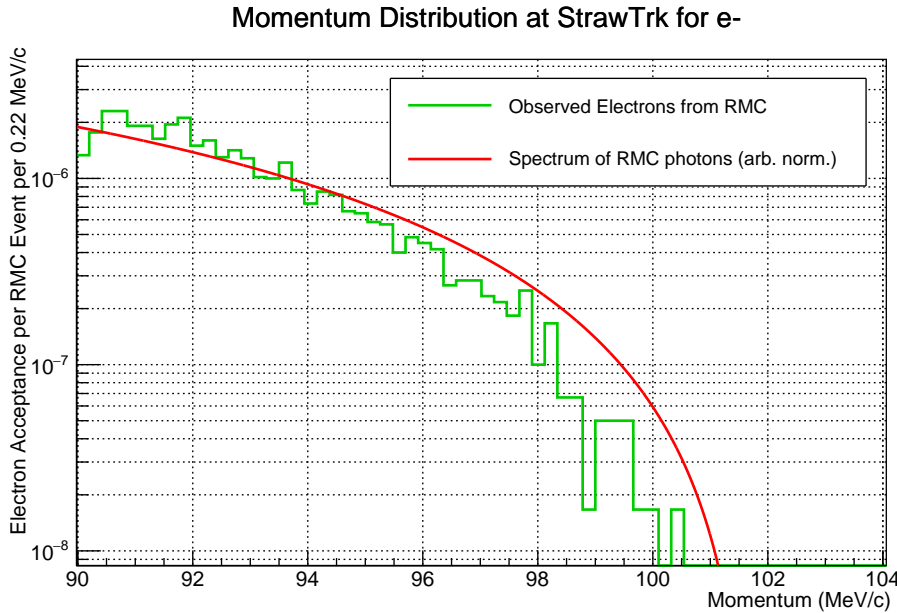


Figure 7.3: Observed electrons from a simulation of 6×10^7 RMC photons. The overlaid spectrum is normalised arbitrarily to fit on the plot.

The total number of electrons arriving with momentum larger than 98 MeV/c, therefore, is 2.2×10^4 . Since the resolution function is somewhat uncertain, this number can be interpreted as setting the limit for the high-momentum mis-reconstruction tail. To have fewer than 0.01 background events produced by RMC, the tails of the resolution distribution should contain fewer than $0.01/2.2 \times 10^4 = 4.5 \times 10^{-7}$ events.

Using the estimate of the resolution function's tail from Phase-I, mentioned above, we predict therefore that Phase-II will produce 3.73×10^{-31} per muon stop or 4.10×10^{-13} during the entire Phase-II run.

7.2.2 Aluminium-26 and RMC

Based on the above energy calculation, the end-point for RMC against ^{26}Al (to ^{26}Mg and with no other particles emitted) would be 108.5 MeV. Clearly such photons would be extremely dangerous to COMET if they are produced.

Aluminium-26 comes in two isomers, one with a half-life of around 6 seconds [86], the other lasting around 700 thousand years [79]. Since Al-26 is unstable its abundance in natural aluminium is low. However, it can be produced by various methods, such as proton and deuteron bombardment of magnesium and sodium, or photo-neutron emission

of the aluminium-27 isotope [87]. With such production mechanisms, it is likely that aluminium-26 will be produced in the COMET stopping target, via the interaction of daughter nuclei of muon capture (which are typically magnesium and sodium) with protons, deuteron, gammas, and neutrons coming from either the beam or as products of muon capture. The exact rate of Al-26 production, however, is a complicated value to estimate and one that unfortunately cannot be estimated here.

One can, however, set an acceptable rate of production if the induced background event rate is to be kept at the level of 0.1 events. Based on the previous simulation of Al-27 RMC, the probability of an electron being detected within 5 MeV of the RMC end-point is 5.6×10^{-18} per nuclear muon capture. With 1.10×10^{18} muon stops during Phase-II, and assuming that the branching ratios for both ordinary and radiative muon capture are the same for Al-26 and Al-27 (61%), then the concentration of Al-26 in the stopping target must be less than 1% (by number density) on average during the entire Phase-II run. The branching ratio for radiative muon capture is, in reality, likely to be slightly more than in Al-27, based on the fact that the neutron excess of a given isotope ($N = A/2 - Z$) seems a better indicator of the branching ratio than atomic number, and that these two numbers appear anti-correlated [80] (the greater the neutron excess, the lower the RMC branching ratio).

Clearly though, there is more work to be done on this, including a better understanding of RMC events coming from Al-26 and of the rate of Al-26 production from muon beams. Data from the AlCap experiment might be able to help with this, however, since the production rate could depend a lot on the exact beam conditions, measuring this on site is important. This should therefore be one of the measurements prioritised at Phase-I.

Finally, if this does produce a sizeable background contribution, one can imagine several techniques to mitigate or reduce the challenge this poses. Provided one can measure the concentration of Al-26 in the stopping target at the end of the run, and ideally at various stages whilst running, then the number of backgrounds can be predicted and possibly subtracted. Additionally, it could be possible to remove the stopping target and replace it with a fresh one such that the Al-26 concentration never rises beyond an unsafe level.

7.3 Radiative Pion Capture (RPC)

When low-energy negative pions are stopped in material they behave similarly to negative muons and form pionic atoms. The probability that the pion is then captured by the nucleus rather than decays in orbit is, however, considerably larger than for a muon. Furthermore, given the extra $30 \text{ MeV}/c^2$ of the pion mass and the lack of an outgoing neutrino, the end-point for Radiative Pion Capture (RPC) by the nucleus is well above the $\mu\text{-}e$ conversion signal energy. As for photons of RMC, the RPC photons can then be converted via Compton scattering or pair production to signal-like electrons. Pion capture could, therefore, be a dangerous source of backgrounds and was one of the dominant sources of background events at SINDRUM-II, along with cosmic sources [40].

Since the pion interacts via the strong force, negative pions capture almost immediately in the nucleus, on the order of picoseconds [88]. The timing of backgrounds caused by pion capture are therefore determined predominantly by the time of pion production, and the delay due to transportation of the pion and signal-like electron. If a background arises from pion capture and the pion was produced in the main muon pulse, then the pion or resultant background electron must have been significantly delayed. Delayed RPC backgrounds are therefore suppressed by the time-gated detector window. If however a background arises because the pion was produced outside of the main proton pulse, due to late-arriving protons (or from antiprotons, but we will treat these separately below), then this background is considered prompt. These prompt RPC background events are, therefore, suppressed by the extinction factor.

The background rate per Proton-on-Target (POT) for prompt and delayed pions is therefore:

$$R_{\text{delayed}} = R_{\pi/p} \mathcal{B}_{\text{RPC}} f_{e,\text{RPC}} A_{\text{time}}, \quad (7.4)$$

$$R_{\text{prompt}} = R_{\pi/p} \mathcal{B}_{\text{RPC}} f_{e,\text{RPC}} \epsilon_{\text{extinction}}, \quad (7.5)$$

where $R_{\pi/p}$ is the pion stopping rate per POT and \mathcal{B}_{RPC} is the branching ratio of RPC for stopped pions. $\epsilon_{\text{extinction}}$ is the extinction factor, whereas A_{time} is the acceptance of the time-gated detector window to electrons coming from delayed RPC. $f_{e,\text{RPC}}$ is the probability that an RPC photon converts to an electron which reaches the detector with signal-like momentum. To a reasonable approximation, this can be factorised as:

$$f_{e,\text{RPC}} = f_{\gamma \rightarrow e^-} A_{\text{geom}} A_{\text{mom}} \quad (7.6)$$

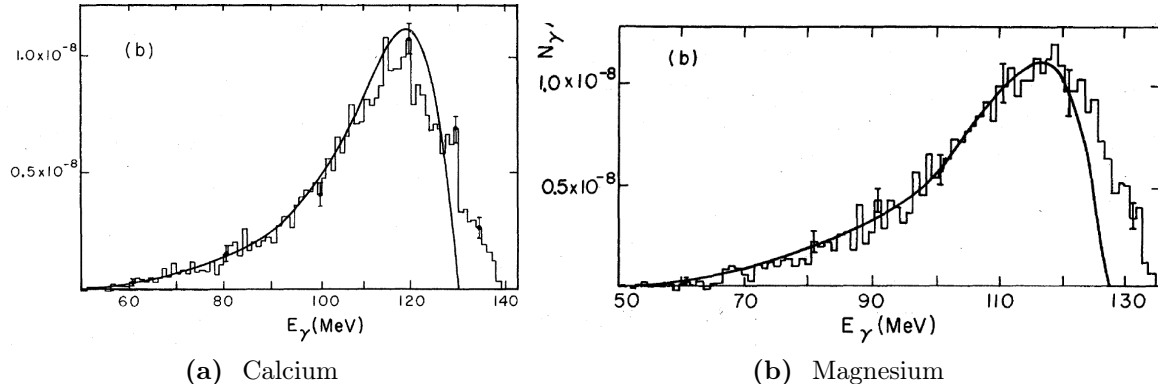


Figure 7.4: Spectrum of photons coming from Radiative Pion Capture (RPC) [89]. The spectrum of magnesium, which is adjacent to aluminium on the periodic table, was used as the basis of these studies.

where $f_{\gamma \rightarrow e^-}$ is the conversion rate of RPC photons to an electron, A_{geom} and A_{mom} are, respectively, the geometric acceptance and momentum cut efficiency for such electrons. However, such a factorisation misses out various correlations, such as where in the experiment the conversion takes place and at what momentum the secondary electron is produced, so that only a single value for $f_{e,\text{RPC}}$ will be reported here.

7.3.1 Photons from Radiative Pion Capture (RPC)

There is a range of experimental and theoretical data on RPC. Fig. 7.4 shows what is perhaps the most useful data currently available: the observed spectrum of photons coming from RPC for magnesium and calcium. Magnesium being adjacent to aluminium on the periodic table, this spectrum is a reasonable proxy for the spectrum of RPC on aluminium. The relative rate for RPC compared to ordinary pion capture is discussed in Amaro et al. [90]. For experimental and theoretical studies of the three isotopes summarised in that paper—carbon, oxygen, and calcium—the measured and predicted branching ratios are all within 1.19% and 2.27%. To be conservative, we take here the branching ratio for RPC on aluminium to be the largest of these at 2.27%.

7.3.2 Pion Stopping Rate

To simulate the pion stopping rate, the pions from the main production simulation were resampled multiple times to build up a large number of pion stops. Fig. 7.5 shows the distribution of pions stopping in the target, in one-dimensional projections to the

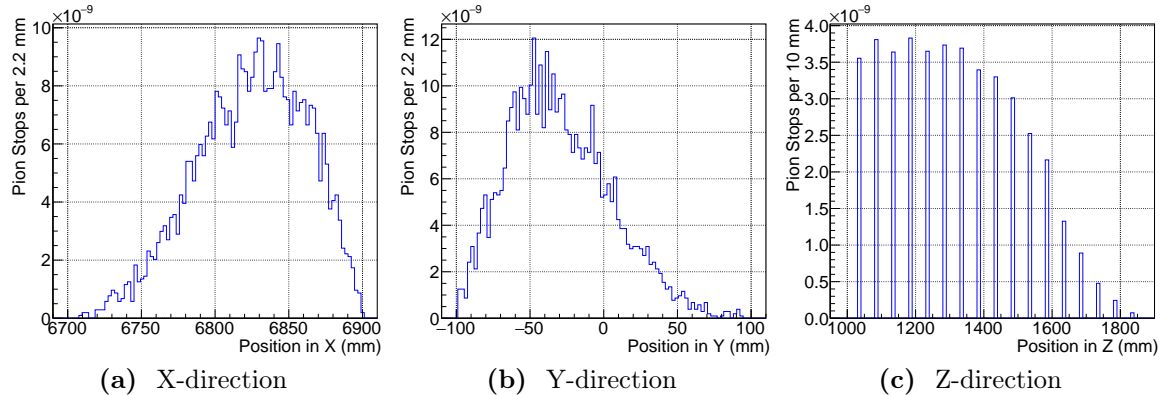


Figure 7.5: Stopping distributions of pions in the target. These distributions have considerably different forms to the muon stopping distributions shown in Fig. 6.2, mostly due to the different momenta of muons and pions.

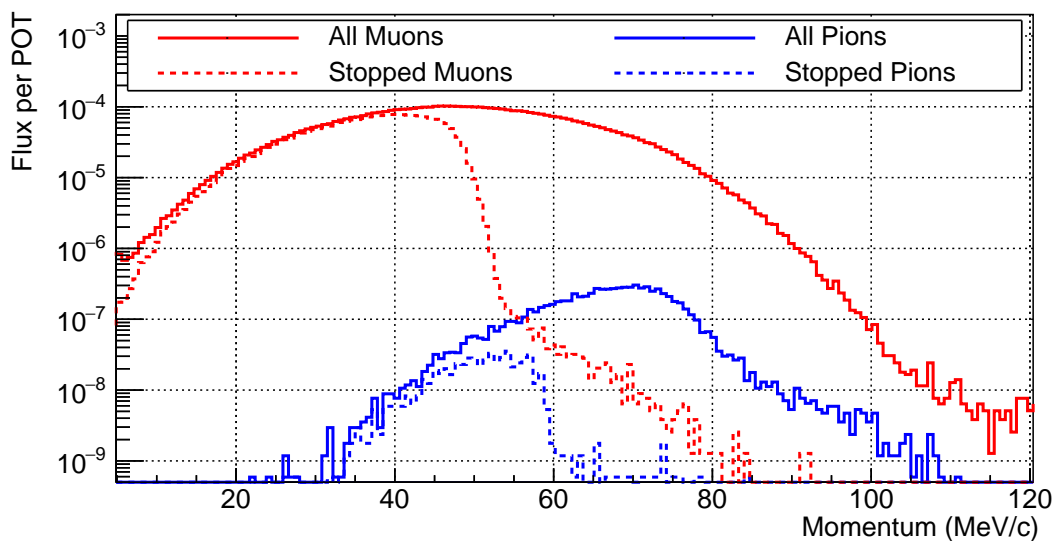


Figure 7.6: The momentum of muons and pions for those that reach the target area and those that actually stop. It is clear how the pion momenta are in general higher, including those that stop, although the maximum stopping momentum for pions is similar to that of muons.

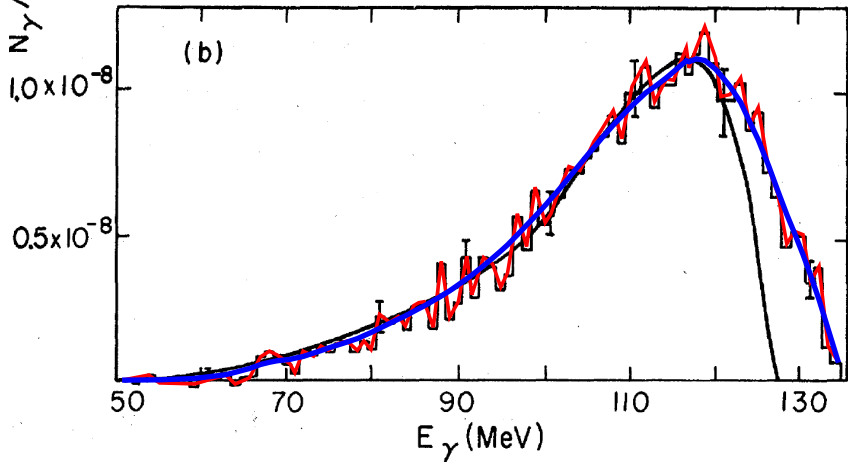


Figure 7.7: Digitised (red) and smoothed (blue) spectrum of RPC from magnesium (see Fig. 7.4b) used as input to the Monte Carlo simulation.

ICEDUST global coordinate system. In that coordinate system, pions arrive from large values of Z at the target, so the pion beam in Fig. 7.5c is going from right to left. By comparison with the plots in Fig. 6.2, pions tend to stop further downstream in the target. This is readily understood by the fact that pions reaching the stopping target tend to have much higher momentum than muons reaching the target, as shown in Fig. 7.6.

In total, the number of pions stopping in the target per POT is $R_{\pi/p} = 4.33 \times 10^{-7}$.

7.3.3 Simulating RPC

Using the realistic pion stopping distribution shown in Fig. 7.5, RPC photons were generated in the target and Geant4 used to convert and track electrons resulting from this process. To model the distribution of photon energies from RPC, the experimentally obtained spectrum from magnesium of ref. [89] was used. To build the model, the raw spectrum was first digitised and then smoothed, using ‘TGraphSmooth::SuperSmooth()’ from the ROOT library [91]. These steps are shown in Fig. 7.7.

Based on a simulation of 4×10^6 RPC photons, the distribution of electrons and positrons reaching the detector was obtained. The timing and momenta of such electrons is shown in Fig. 7.8, where it is clear that although many signal-like electrons are detected, they all arrive well before the gated-time threshold of 600 ns.

The probability of an RPC photon producing an electron that reaches the detector with momentum between 104.2 MeV/c and 105 MeV/c is: $f_{e,RPC} = 1.05 \times 10^{-5}$. To

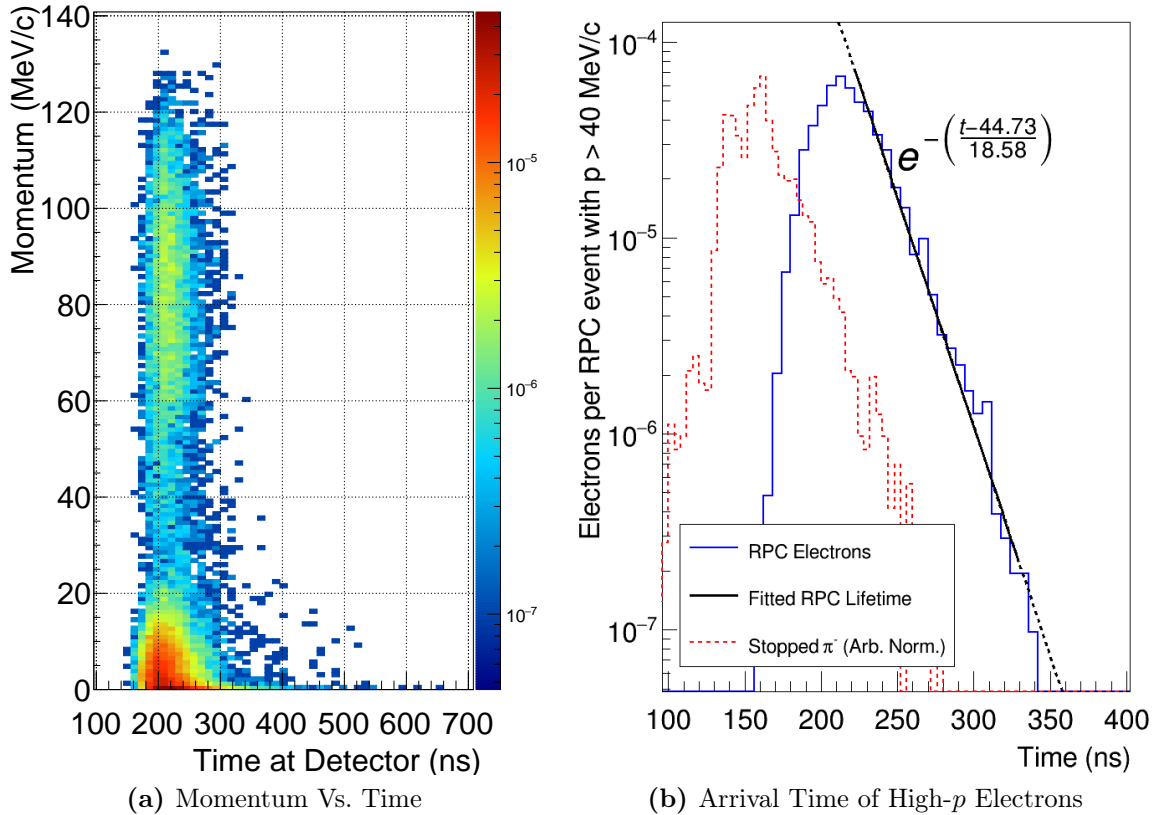


Figure 7.8: Detection of secondaries from RPC photons in the target. Although many high-momentum electrons are detected (a), they are all well before the time-gated detected window (b).

estimate the rate of delayed RPC backgrounds, we also need to know the value of A_{time} . As can be seen in Fig. 7.8a, the timing for electrons originating from RPC photons and detected with momentum greater than 30 MeV/c is independent of the momentum. By fitting the tail of this distribution with a single exponential, as shown in Fig. 7.8b, the lifetime of the high-energy electrons is found to be 18.6 ns, such that with the timing window between 600 and 1200 ns we find the acceptance of the timing window to be: $A_{\text{time}} = 9.50 \times 10^{-15}$.

Table 7.3 summarizes these numbers, from which we find that the rate of backgrounds for delayed RPC is 1.73×10^{-27} per POT, whilst prompt RPC occurs at 1.82×10^{-24} per POT.

| Parameter | Value | Description |
|--------------------------------|------------------------|--|
| $R_{\pi/p}$ | 4.33×10^{-7} | Pion stopping rate per POT |
| \mathcal{B}_{RPC} | 2.27×10^{-2} | Branching ratio of RPC |
| $f_{e,\text{RPC}}$ | 1.05×10^{-5} | Probability of an RPC photon producing signal-like electrons in the detector |
| A_{time} | 9.50×10^{-15} | Acceptance of timing window to secondary electrons from RPC |
| $\epsilon_{\text{extinction}}$ | 1×10^{-11} | Extinction factor |

Table 7.3: Parameters and their values in the determination of the RPC background rate.

7.4 Antiprotons in the Beam

When the primary 8 GeV proton beam interacts with the production target, antiprotons might be produced as a proton–antiproton pair:

$$p + N(A, Z) \rightarrow p + N^*(A, Z) + p + \bar{p}, \quad (7.7)$$

which, given their negative charge, can remain on-axis along the muon beamline if they have momentum around 40 MeV/c. Because their mass is relatively large, at a fixed value of momentum antiprotons travel much more slowly than other particles in the muon beam, causing the beam’s time structure to be smeared for antiprotons and their secondaries. The pulsed beam and time-gated detector window are, therefore, not effective at suppressing backgrounds created by antiprotons in the beam.

The interaction of antiprotons with matter has a strong analogy with muons and negative pions, particularly at low energies, when the antiprotons stop. In matter, antiprotons with energies of a few tens of keV—similar to that of atomic electrons—can become bound in the Coulomb potential of the atom’s nucleus. X-rays emitted in the ensuing electromagnetic cascade are typically not more than a 100 keV [92]. Unlike for muons, the antiproton will only rarely reach the atomic ground state, with interactions with the nucleus becoming dominant before this is possible. Such interactions can take the form of an immediate annihilation or the formation of a composite nucleus where the antiproton becomes bound within the nuclear potential [93, 94]. The binding energy of some of these nuclear levels can reach up to hundreds of MeV, and so in the transition, pions and other hadrons can be readily produced. Eventually the antiproton annihilates

in the nucleus, producing large multiplicities of pions and other mesons. Based on the data in [94], about 1.56 negative pions should be produced for every stopped antiproton.

As such, although antiprotons themselves are not an immediate source of high-energy photons or electrons, they are an additional source of pions, which can produce backgrounds via Radiative Pion Capture (RPC).

7.4.1 Antiproton Production Rate and Spectrum

The literature on antiproton production with 8 GeV protons on a tungsten target and at large angles is somewhat lacking. Accordingly most hadron models are particularly under-constrained when it comes to antiproton production. The QGSP_BERT_HP model used as the basis for SimG4 is, in fact, completely unable to produce antiprotons.

In the COMET TDR [44], the yield of antiprotons per POT is given as 4×10^{-5} , based on the findings of a literature review and simulations undertaken for the MECO experiment [95]. Fig. 7.9 shows the production cross section for antiprotons as a function of incident proton momentum, based on that study.

Simulations of antiprotons for Phase-I have used this information and shown that absorber foils would be needed along the beamline. Since the Phase-II geometry in ICEDUST re-uses most of the implementation for the Production Target Capture and Torus1 sections, the upstream absorbers are also contained in the geometry used to study antiprotons here, although the absorber near 90° is not.

Whilst tungsten targets have not been studied at the relevant angles and proton energies, a set of papers [96, 97] do exist covering antiproton production up to 2 radians for tantalum (which is adjacent to tungsten on the periodic table), copper, aluminium, and beryllium targets and using protons with 10.14 GeV kinetic energy. Between them, these two papers provide the invariant triple-differential cross section as a function of antiproton momentum for production angles of 10, 59, 97 and 119° , defined as:

$$F(p, \theta, \phi) = E \frac{d^3\sigma}{dp^3} = E \frac{d^3\sigma(p, \theta, \phi)}{p^2 dp d\Omega} \quad (7.8)$$

where E and p are the antiproton energy and momentum. The earlier Boyarinov paper actually reports $f = F/A$, where A is the relative atomic mass of the nucleus. To convert the differential invariant cross sections given in the literature (equation (7.8)) into a

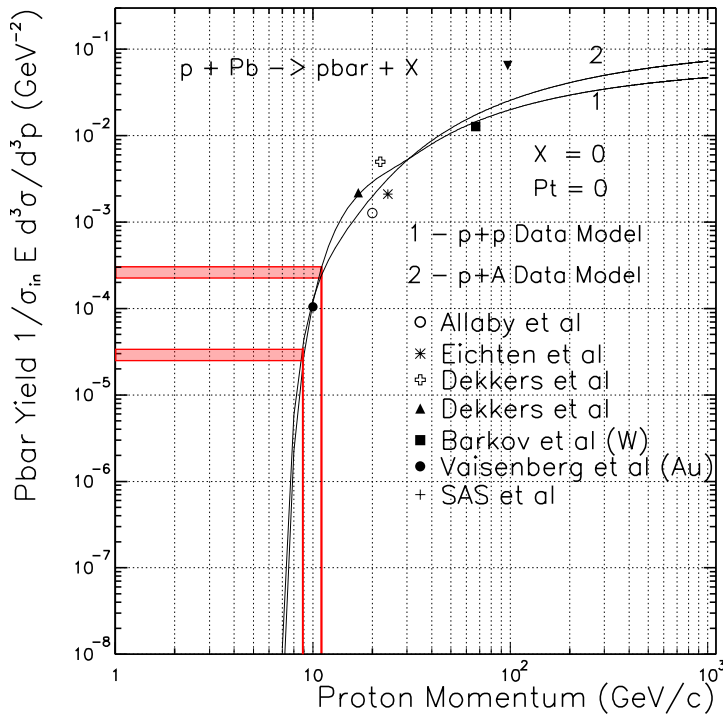


Figure 7.9: Variation in the antiproton production rate as a function of incident proton energy, according to Meco note 24 [95] and used in the COMET TDR [44]. For reference, protons with 8 GeV kinetic energy have 8.89 GeV/c momentum, whilst with 10.14 GeV kinetic energy their momentum is 11.038 GeV/c. The vertical coloured lines have been added to indicate these energies, whilst the horizontal bands show the range of predicted cross sections for the models of proton-nucleon and proton-nucleus interaction.

differential production rate per POT, $d^3R(\theta)/dpd\Omega$, the following formula is used:

$$\frac{d^3R(p, \theta, \phi)}{dp^3} = \frac{F(p, \theta, \phi)}{E} \frac{\rho N_A l}{m_N} \quad (7.9)$$

where ρ is the mass density of the target, 19.25 g/cm³ for Tungsten, m_N the atomic mass, 183.86 g/mol for tungsten, l the length of the target, and N_A is Avogadro's number. Fig. 7.10 shows the data from these papers, after scaling the cross sections for each material to the number of nucleons in tungsten. The data has also been converted to a differential rate of production, given the Phase-II production target dimensions, using equation (7.9). From this data, it is clear that as one moves to larger angles, the spectrum becomes considerably softer whilst the overall rate falls quickly, in much the same way as for pion production.

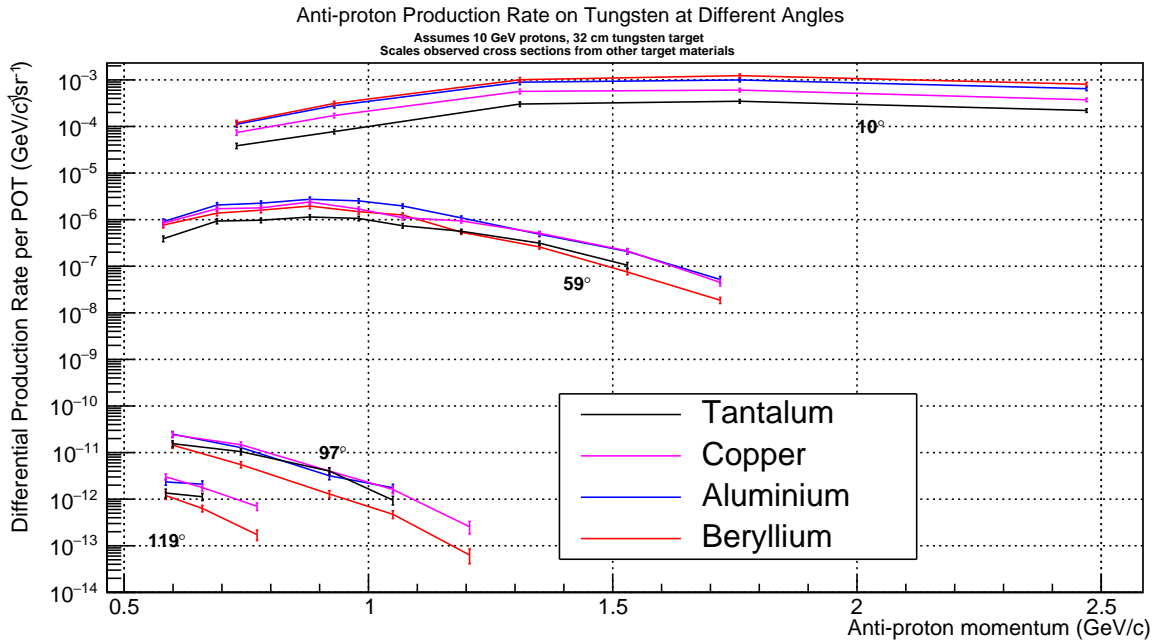


Figure 7.10: Experimental data for antiproton production rates for 10 GeV protons [96, 97]. Each line represents the cross section obtained for the four different target materials covered in those papers, scaled to match the number of nucleons of tungsten and with the additional factors of equation (7.9) included.

7.4.2 Modelling Antiproton Production

To develop the data in the Boyarinov et al. papers into a model for antiproton production, three dependencies must be considered: the incident proton's momentum, the outgoing antiproton's momentum, and the outgoing antiproton's direction with respect to the incident proton.

To account for these dependencies, the cross section was factorised according to the equation:

$$\frac{d^3 R(p, \theta, \phi)}{dp^3} = \xi P(p, \theta_{\min}) \Phi(\theta, \phi), \quad (7.10)$$

where ξ is a scale factor to correct for the different incoming proton energy, $P(p, \theta_{\min})$ models the momentum distribution at a given angle and is normalised to unity (i.e. $\int P(p, \theta_{\min}) dp = 1$), and $\Phi(\theta, \phi)$ encapsulates the dependence on the antiproton's direction. Each of these factors are discussed in-depth below.

Dependence on the Incident Proton's Momentum: ξ

The factor ξ is included in the antiproton production model to account for the difference in proton energy between the available data and the COMET proton beam. It is defined as the ratio of the total production cross sections at the different energies:

$$\xi = \frac{\sigma_{\text{tot}}(E_p = 8 \text{ GeV})}{\sigma_{\text{tot}}(E_p = 10.14 \text{ GeV})} \quad (7.11)$$

The data in the Boyarinov papers was taken using protons with kinetic energies of 10.14 GeV. The threshold for antiproton production against a single, free nucleon is 5.6 GeV; the cross-section increases rapidly above this energy, as indicated in Fig. 7.9. Because of this, COMET has chosen to use an 8 GeV (kinetic energy) beam, and accordingly it is important to scale the antiproton cross sections from the Boyarinov et al. papers to account for this.

Fig. 7.9 suggests that the cross section at 8 GeV is about one order of magnitude smaller than at 10.14 GeV, although the data and models included in that plot are for a lead target as opposed to tungsten.

In a paper by Danielewicz [98], a theoretical calculation is performed to estimate the rate of antiproton production. Equation (4.3) of that paper gives the antiproton production cross section for nucleon-proton interactions as:

$$\sigma_{NN}^{\bar{p}} = C(\sqrt{s} - 4m)^{7/2} \quad (7.12)$$

where \sqrt{s} is the Mandelstam variable for the total invariant incoming energy, and m the mass of a nucleon. C depends on properties of the nucleus and is fixed in that paper using experimental data. Based on this equation, the cross section for antiproton production at 8 GeV should be a factor of 0.12 times that at 10.14 GeV. Since this agrees well with Fig. 7.9, we take $\xi = 0.12$.

Dependence on the Outgoing Antiproton's Momentum: $P(p, \theta_{\min})$

The momentum spectrum of antiprotons at a given angle is captured in the factor $P(p, \theta_{\min})$. We base the shape of this spectrum on the data from the Boyarinov papers.

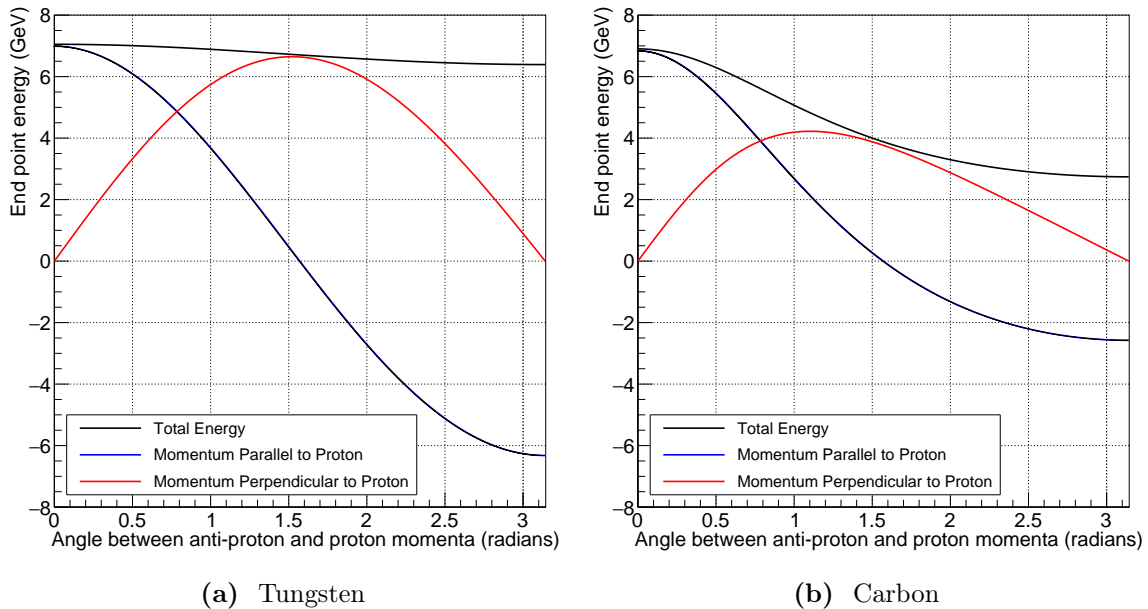


Figure 7.11: The kinematic end-point for antiproton production as a function of the outgoing antiproton direction with respect to the incoming proton in the frame of the target nucleus (the lab frame). The absolute end-point is only achieved when the nucleus and outgoing protons recoils coherently.

In order to complete the data and cover the full range of energies at which antiprotons might be produced, we add two additional points to the experimental data for the maximum and minimum momentum. Including the minimum momentum only adds the constraint that at zero momentum the cross section also be zero. On the other hand, to calculate the maximum momentum, the kinematic end-point was found by considering the entire nucleus and the two outgoing protons to recoil coherently against the antiproton. The value of the end-point kinetic energy and longitudinal and transverse momenta for both tungsten and carbon are shown in Fig. 7.11 using the formulae derived in appendix B. This end-point will be a highly conservative estimate, since in reality not all the nucleus will recoil coherently; the de Broglie wavelength for a proton with 8 GeV kinetic energy is

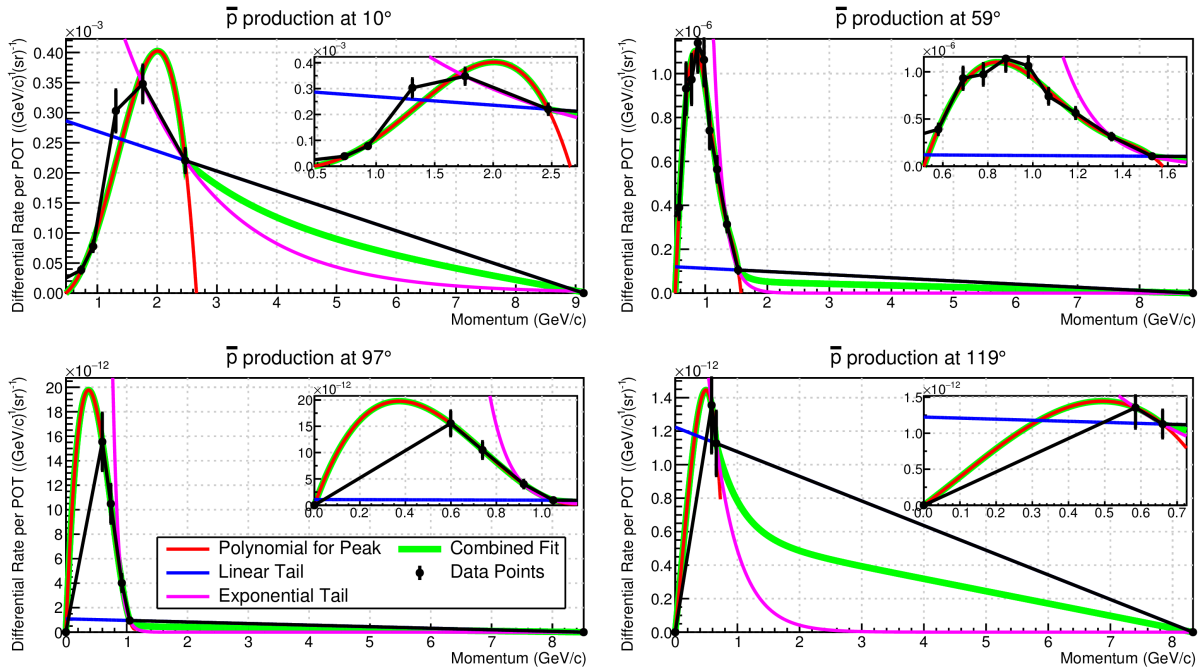


Figure 7.12: Piecewise fitting to experimental data and kinematic end-points. Insets show a zoom around the experimental data points.

about 0.15 fm, compared to the 7 fm or so of a tungsten nucleus². Additionally, achieving this end-point configuration would be highly phase-space suppressed.

With the addition of these two end-points, to interpolate and extrapolate the data, a polynomial of order 4 to 6 (depending on the number of available data points) was used to fit from zero up to the last experimental data-point. For the high-momentum tails of each spectrum, three fits were tried: a straight line fit between the last experimental data-point and the kinematic end-point described above; an exponential fitted to the kinematic end-point and the last two experimental data points; and an average of both of these fits. Fig. 7.12 shows the results of this fitting procedure, where it can be seen that a low-momentum peak is visible and a high-momentum tail well described. Whilst these spectra are likely a poor representation of the true production spectrum, they serve

²Antiproton production from protons in this energy regime was historically referred to as ‘sub-threshold production’, since it is close to the threshold for single nucleon interactions, around 5.6 GeV. The fact antiprotons are observed below this energy is therefore proof that it is not a single, stationary nucleon that interacts with the proton; the nuclear environment as a whole must be considered. Either the nucleons are, themselves, in motion or clusters of bound nucleons are involved. The older literature on this topic in fact refers to a parameter called the ‘cumulative number’ which was related to the number of nucleons that would need to be involved to produce secondary hadrons (e.g. antiprotons or pions) with such outgoing energies, given the incoming proton energy. These sub-threshold secondary particles were themselves sometimes called cumulative particles.

as useful upper bounds which can be used as inputs for the antiproton background rate estimation.

The momentum distribution will, of course, depend on the angle of production relative to the proton beam. With only four production angles available in the experimental data, however, for a given angle, θ , we assign the momentum distribution based on the data at the next smallest production angle, θ_{\min} . Since the spectrum becomes softer at larger values of θ , this will tend to further overestimate the high-energy tail of the momentum distribution. In the case of angles smaller than 10° , given the lack of other data, we fix the shape of the momentum distribution to be the same as that at 10° .

The function $P(p, \theta_{\min})$ is the piecewise function that is fit to the data and kinematic end-points and then normalised so that the integral is one. The overall normalisation is instead absorbed into the angular dependence factor, $\Phi(\theta, \phi)$.

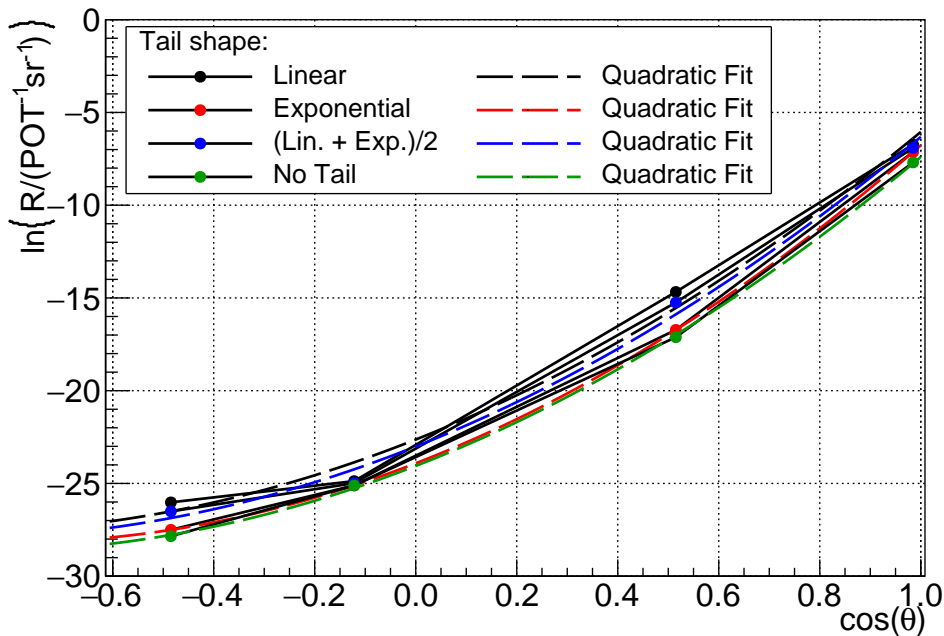


Figure 7.13: The angular dependence of the rate of antiproton emission, integrated over all momenta. The different lines represent the different fits to the high momentum part of the spectrum. The relationship given in [96] would suggest the data here should fit a straight line. The dashed lines represent instead a quadratic fit to these points, which looks like a better fit. For reweighting events the interpolated (straight solid) lines were used to be conservative.

| Region | Data Source | Total \bar{p} per POT in this region | |
|-------------------------------|------------------|--|------------------------|
| | | Linear Tail | Exponential Tail |
| $0 \leq \theta < 59^\circ$ | 10° [97] | 9.13×10^{-5} | 5.26×10^{-5} |
| $59 \leq \theta < 97^\circ$ | 59° [97] | 2.64×10^{-8} | 4.17×10^{-9} |
| $97 \leq \theta < 119^\circ$ | 97° [96] | 3.40×10^{-12} | 1.74×10^{-12} |
| $119 \leq \theta < 180^\circ$ | 119° [96] | 2.58×10^{-12} | 5.71×10^{-13} |

Table 7.4: Angular regions and the source of the data used to build the momentum spectrum for that region. The integrated rate for the two different high-momentum tail descriptions are also given. Note that these values do *not* contain the correction for the different incident proton energies; for the COMET proton beam the antiproton yield is expected to be a factor 0.12 times those given here.

Dependence on the Outgoing Antiproton's Direction: $\Phi(\theta, \phi)$

The function $\Phi(\theta, \phi)$ accounts for the variation of the cross section as the angle between the incoming proton and outgoing antiproton changes. By symmetry, it can be seen that there should be no dependence on ϕ (both the proton beam and target are assumed to be unpolarised).

To estimate the cross section at a given angle, the fitted distributions described in the last section were integrated. The results of these integrations is shown in Fig. 7.13.

Boarinov et al. state [96] that the angular dependence of antiproton production should take the form:

$$\Phi(\theta) = \alpha e^{\beta \cos \theta} \quad (7.13)$$

where α and β are constants.

It is for this reason that the axes of Fig. 7.13 are $\cos \theta$ and $\ln(R)$: if such a function were valid, the points would form a straight line. In fact it seems the variation in these parameters are better described by a quadratic function, although the fitted quadratic functions all reach a minimum for $\cos \theta \neq -1$, which seems unphysical.

However, to keep things conservative, rather than use a linear or quadratic fit to the integrated data, we use the linear interpolation between each adjacent datum to provide the function, $\Phi(\theta, \phi)$. For the same reason, we use the integrated cross sections obtained for the fits that use a linear function for the high-momentum tail.

7.4.3 Simulating Antiproton Backgrounds

To study backgrounds from antiprotons, four separate simulations were performed, one for each of the angular regions described in Table 7.4, with 8×10^7 antiprotons fed in to each simulation. Within each angular region, antiprotons were generated uniformly across the production target, with momenta distributed according to $P(p, \theta_{\min})$. Given how steeply the angular distribution tails off, in order to check the acceptance of antiprotons produced at large angles, events were generated isotropically within the angular region, and then re-weighted during analysis based on $\xi\Phi(\theta, \phi)$, ie. the probability that an antiproton is produced in this direction.

The beamline's acceptance to antiprotons and the secondary pions that they produce are shown in Fig. 7.14. The events in this plot are unweighted by the antiproton angle. From these plots, it is clear that the material at the entrance to the Torus1 solenoid removes a large fraction of the antiprotons—about 99% of the antiprotons produced

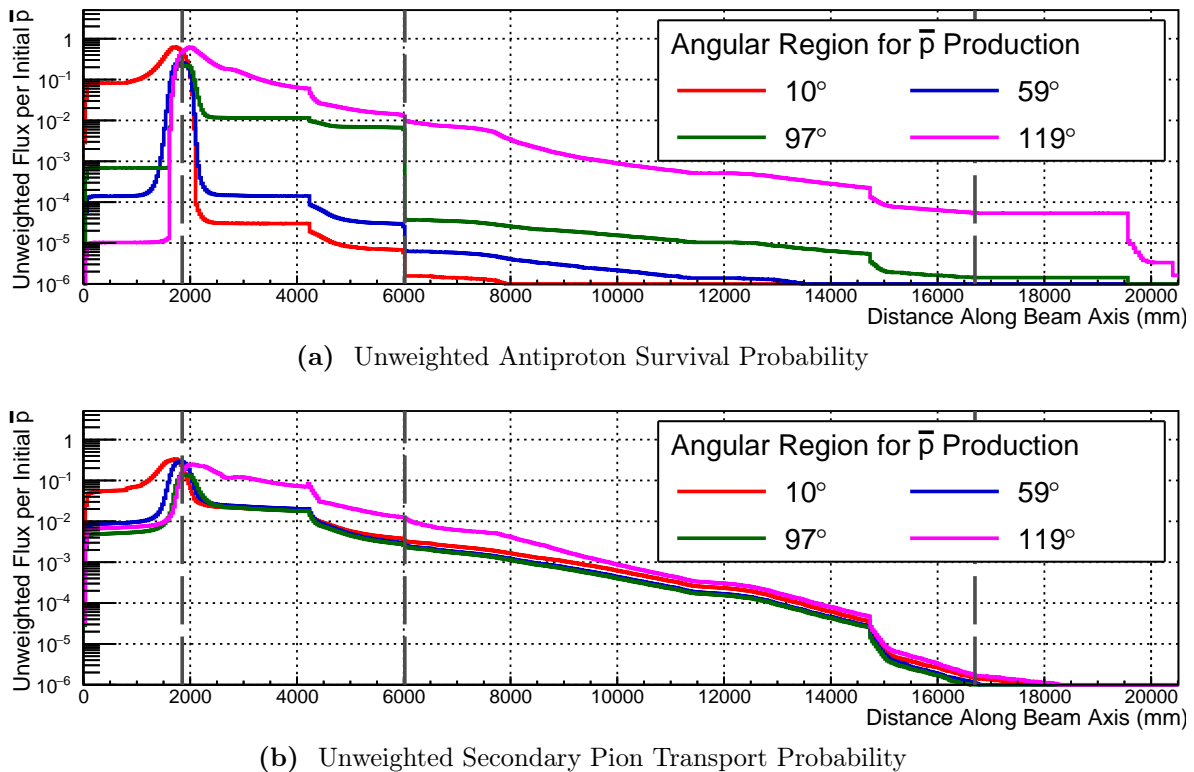


Figure 7.14: The survival probability of antiprotons and secondaries pions per antiproton produced in the target as a function of distance along the beamline. These plots are not weighted by the probability that an antiproton is produced at a particular angle. From left to right the vertical gray lines indicate the production target, Torus1 entrance, and the Torus2 exit.

between 97 and 119°. It can also be seen that the acceptance in the bent solenoids for antiprotons is about two orders of magnitude greater for antiprotons produced at angles greater than 119°, compared to those produced between 97 and 119°.

For pion production and acceptance, however, the unweighted rate for the four angular regions is very similar, particularly towards the end of Torus2. This, and the fact that the transmission probability has a negative gradient for each angular region along the whole beamline, implies that the main source for pions is the interaction of antiprotons in the primary target. Pions produced by antiprotons hitting collimators or the beam-pipe will quickly be removed since they will tend to stay close to this material. If pions were produced at the foil at the entrance to the Torus1 then they would be in the centre of the beam-pipe and have a greater chance of being transported, although this does not seem to be a major source.

Fig. 7.15 shows the trajectories of antiprotons along the beamline, where each trajectory has been weighted according to the antiproton's production direction with respect to the proton beam axis. Similarly, Fig. 7.16 shows the same information but for pions instead. The colour scale and range is the same for each of the four plots in these figures. One can see, then, that although the acceptance per antiproton is considerably larger for larger angle production (119–180°), the production rate is so small that the final probability of observing an antiproton is quite low. As such, it is the antiprotons produced in the forwards direction and scattered backwards by the production target that will dominate the antiproton background rate.

Table 7.5 and Table 7.6 show the number of antiprotons and pions that enter the Torus1 ('Torus1'), reached the final collimator ('Torus2'), and arrived at the target ('Target'). Also shown is the sum over all events with each event weighted by the initial antiproton direction and proton energy scale correction ($\xi \cdot \Phi(\theta, \phi)$), and normalised to the number of antiprotons introduced into the simulation. No antiprotons are seen stopping in the target for the angular region from 0 to 59°. To estimate the stopping rate of antiprotons produced in this direction, the weighted sum for antiprotons just before the collimator was multiplied by the median acceptance of the collimator, $P(\text{Target}|\text{Torus2})$, which occurs for the region from 59 to 97°.

The timing distributions for antiprotons and pions are shown in Fig. 7.17, from where it is clear that timing information from the pulsed proton beam is not meaningful for antiprotons. However, since the majority of secondary pions that are successfully transported to the target originate in the production target, the pulsed beam timing is

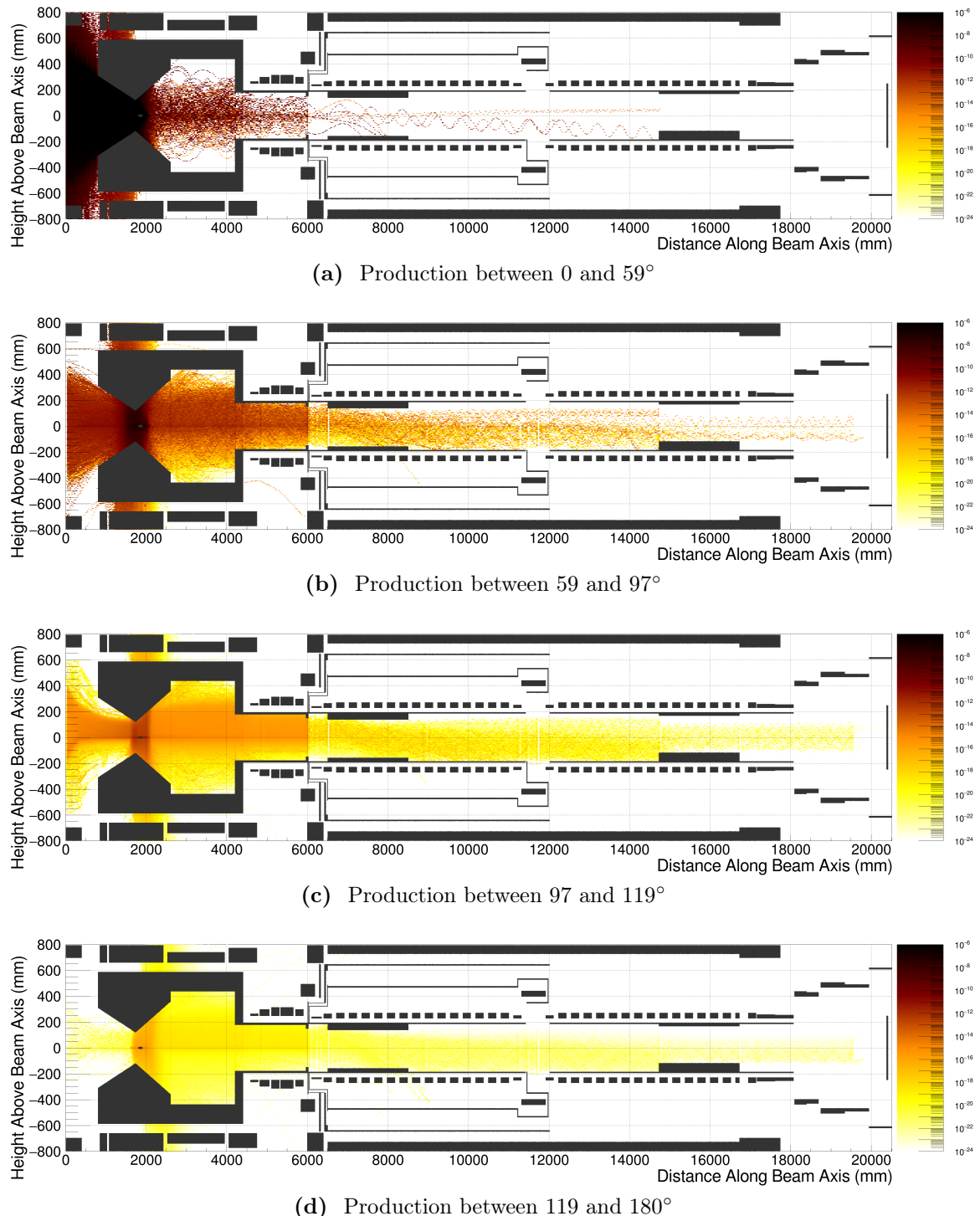


Figure 7.15: The heights of antiprotons passing along the beamline for the four different angular regions of productions. Each antiproton trajectory is weighted by the probability of producing an antiproton at this angle. The colour scale on all these plots is the same.

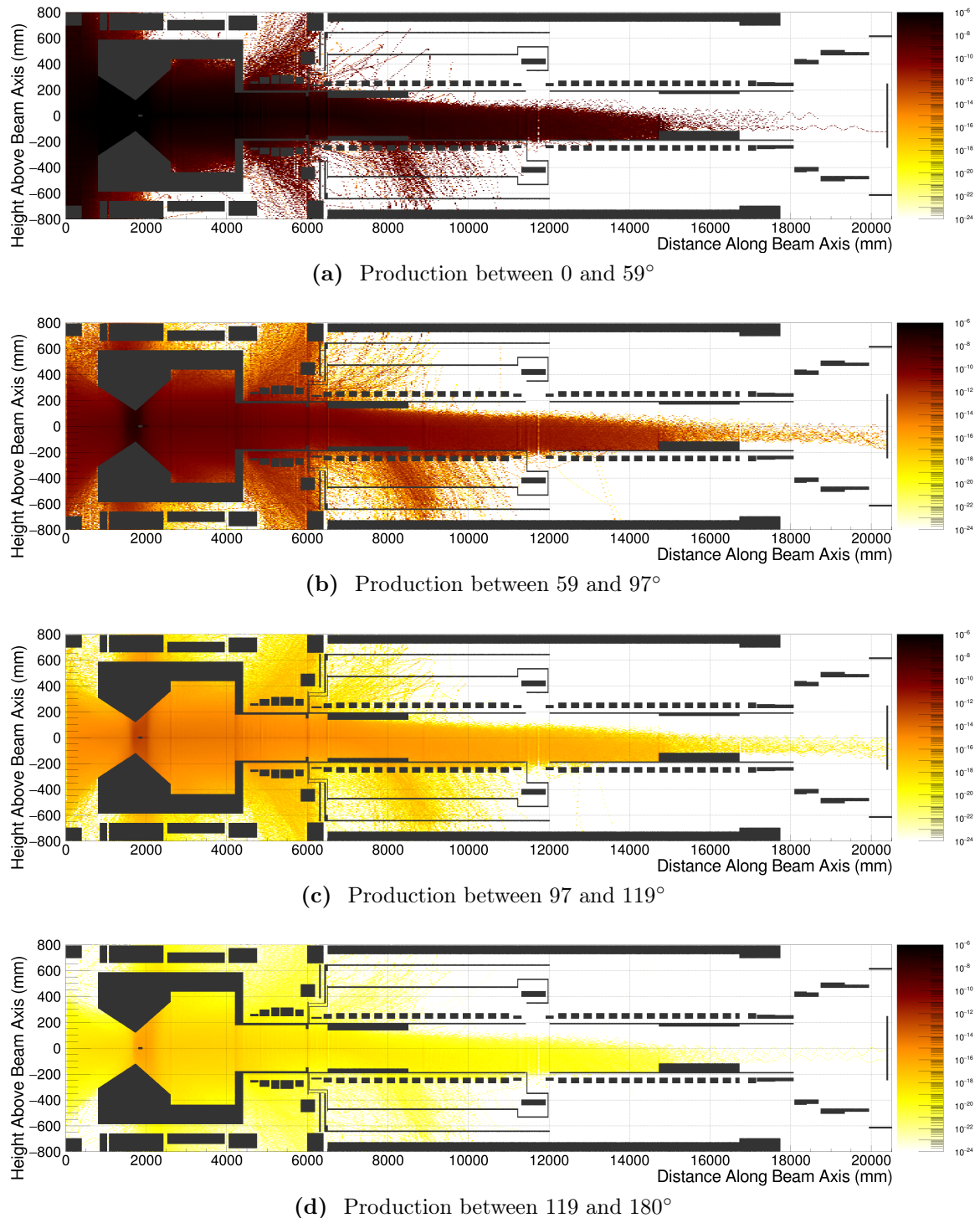


Figure 7.16: The heights of secondary pions passing along the beamline produced from antiprotons in each of the four different angular regions of productions. Each trajectory is weighted by the probability of producing the parent antiproton in its initial direction at the target.

| Rates for \bar{p} Transport | | Angular Region for Antiproton Production | | | |
|----------------------------------|--------|--|-----------------------------|------------------------------|-------------------------------|
| | | $0 \leq \theta < 59^\circ$ | $59 \leq \theta < 97^\circ$ | $97 \leq \theta < 119^\circ$ | $119 \leq \theta < 180^\circ$ |
| Raw Counts | Torus1 | 7 | 270 | 2907 | 278105 |
| | Torus2 | 3 | 58 | 830 | 20787 |
| | Target | 0 | 8 | 114 | 2237 |
| Weighted Mean | Torus1 | 1.68×10^{-10} | 2.04×10^{-13} | 1.32×10^{-17} | 2.72×10^{-20} |
| | Torus2 | 6.16×10^{-12} | 5.77×10^{-14} | 3.97×10^{-18} | 6.23×10^{-21} |
| | Target | $*4.39 \times 10^{-16}$ | 1.39×10^{-15} | 6.20×10^{-20} | 9.29×10^{-22} |
| $P(\text{Target} \text{Torus2})$ | | *0.225 | 0.225 | 0.034 | 0.295 |

Table 7.5: Antiproton stopping rates and fluxes at key points: at the entrance to the bent solenoids (Torus1), just before the final beam collimator (Torus2), and in front of the stopping target (Target). Raw counts are the total number of particles seen in each simulation of 80 million antiprotons. The weighted mean is the average of all particle weights, given by the energy correction factor ξ and the antiproton production angle, $\Phi(\theta, \phi)$. $P(\text{Target}|\text{Torus2})$, gives the survival probability for an antiproton to reach the target, given that it reached the Torus2 collimator. Since no antiprotons were seen stopping for the angular region from 0 to 59° , the value for the final entry in that column—indicated with an asterisk (*)—are obtained by multiplying the antiproton rate expected at the Torus2 collimator with the median collimator acceptance from the other three angular regions.

| Rates for Secondary π^- | | Secondary π^- from Angular Region for Antiproton Production | | | |
|-----------------------------|--------|---|-----------------------------|------------------------------|-------------------------------|
| | | $0 \leq \theta < 59^\circ$ | $59 \leq \theta < 97^\circ$ | $97 \leq \theta < 119^\circ$ | $119 \leq \theta < 180^\circ$ |
| Raw Counts | Torus1 | 16943 | 87230 | 157385 | 222486 |
| | Torus2 | 208 | 1106 | 1995 | 1847 |
| | Target | 1 | 18 | 25 | 30 |
| Weighted Mean | Torus1 | 6.93×10^{-7} | 5.57×10^{-10} | 4.92×10^{-15} | 1.50×10^{-18} |
| | Torus2 | 1.03×10^{-8} | 7.11×10^{-12} | 6.95×10^{-17} | 1.47×10^{-20} |
| | Target | 1.20×10^{-11} | 3.59×10^{-14} | 6.02×10^{-19} | 2.29×10^{-22} |

Table 7.6: Secondary pion fluxes from antiprotons observed at key points along the beamline. See caption to Table 7.5 for a description of the column and row contents.

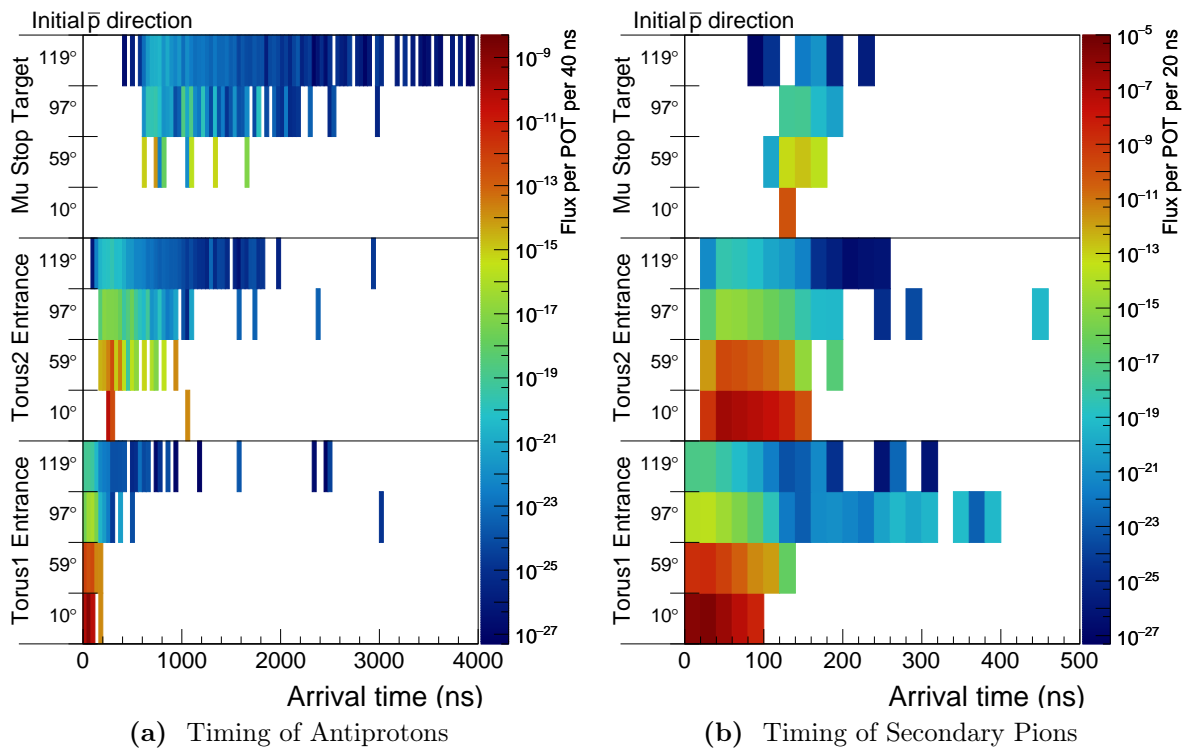


Figure 7.17: The arrival time of antiprotons (a) and pions (b) at various points along the beamline and for the different initial antiproton directions. Note that the x-axis scales are different. Whilst the timing of antiprotons themselves is very delayed, the timing of secondary pions, which are produced predominantly at the production target, is relatively prompt and will be effective at suppressing the induced backgrounds.

a strong way to suppress the backgrounds these can produce via RPC. In fact, given that these pions originate in the production target, the background rate due to RPC of pions directly produced by the proton beam can be reused, including the timing cut. For antiprotons, the rate of RPC backgrounds per pion stop is also used, however the mean number of negative pions produced per antiproton stop is included, as well as the overall efficiency of the timing window, assuming a flat timing distribution. For both pions and antiprotons, the efficiency of the TDAQ and reconstruction are also included, with the same values as for signal electrons. Based on these factors, the numbers in Table 7.5 and Table 7.6 can be converted to background estimates, which are shown in Table 7.7.

The total predicted antiproton rate per POT is therefore 4.34×10^{-22} , which is completely dominated by antiprotons produced in the forward direction but scatter within the production target and are successfully transported to the stopping target. This number is considerably larger than would be desirable for the COMET experiment. It is important, therefore, to remember that this is an especially conservative estimate:

- The kinematic end-point is a large overestimate for the true end-point of the spectrum since the incoming proton will never interact with the entire nucleus.
- The straight-line-fit to the tail, that was used to generate antiprotons in the simulation will produce higher momentum antiprotons than are likely to occur, which changes the penetration depth in material. In addition, the straight-line-fit increases the integrated yield of antiprotons significantly, which impacts on the

| | Stopping Rates | Background Rate per POT | | |
|---------------|-------------------------|-------------------------|------------------------|------------------------|
| | | No Timing | Prompt | Delayed |
| \bar{p} | $0 \leq \theta < 59$ | 4.39×10^{-16} | 2.03×10^{-22} | - |
| | $59 \leq \theta < 97$ | 1.39×10^{-15} | 6.43×10^{-22} | - |
| | $97 \leq \theta < 119$ | 6.20×10^{-20} | 2.87×10^{-26} | - |
| | $119 \leq \theta < 180$ | 9.29×10^{-22} | 4.29×10^{-28} | - |
| π^- | $0 \leq \theta < 59$ | 1.20×10^{-11} | 3.54×10^{-18} | 3.54×10^{-29} |
| | $59 \leq \theta < 97$ | 3.59×10^{-14} | 1.06×10^{-20} | 1.06×10^{-31} |
| | $97 \leq \theta < 119$ | 6.02×10^{-19} | 1.78×10^{-25} | 1.78×10^{-36} |
| | $119 \leq \theta < 180$ | 2.29×10^{-22} | 6.78×10^{-29} | 6.78×10^{-40} |
| Sum (per POT) | | 3.56×10^{-18} | 3.56×10^{-29} | 4.34×10^{-22} |

Table 7.7: Final estimated antiproton-induced background rates. See text for column definitions.

event-by-event weight. For example, for the region from 59–97°, there are up to two orders of magnitude difference on the predicted antiproton yield depending on the high-energy description.

- Antiproton events were generated with a uniform distribution in the production target. Given that the proton beam profile will be close to a double Gaussian, with most of the probability concentrated in the centre of the target, there will typically be more material for the antiprotons to pass through as they leave the target. This will increase the rate of absorption and thus reduce the antiproton rate further.
- The final value assumes that all the negative pions produced from stopping antiprotons are captured by nuclei in the target. In reality, many of these will escape from the target and decay in flight or be stopped and captured elsewhere. The pion multiplicity factor used here is likely an overestimate, therefore.

At the same time, the fact that these results are somewhat statistically limited, given the small number of antiproton stops seen from the forward going antiprotons, one can expect a sizeable uncertainty on this value. In addition, some of the other factors that have been included, such as from the RPC background estimation, also increase the uncertainty since there might be other correlations that such a factorisation cannot include.

On the other hand, the fact that it is scattering from forward produced antiprotons has some advantage, since there is experimental data in the forward region—admittedly with materials other than tungsten or with proton energies other than 8 GeV—that could be used to develop further understanding of this background.

7.4.4 Reducing Antiproton Backgrounds Further

If the background rate due to antiprotons presented here proves correct, then changes to the current beamline design should be implemented to reduce it. There are several options that can be pursued, but each must be checked for its impact on the muon beam intensity.

Firstly, one can simply increase the thickness of the foil at the entrance to the Torus1. In a similar way, one can introduce additional foils along the beamline, such as at the TS3 solenoid in between the Torus1 and Torus2. The downside of both of these methods is that they will be in the path of the muon beam, and since the dE/dx curve for negative

muons below 100 MeV has a negative gradient, this material will likely increase the mean muon momentum (but, of course, decrease the overall intensity).

If material is added, then it would be beneficial if this material were low-Z. This would maximize the ratio of the rate of antiproton loss to the muon loss rate. In fact, a bug in the geometry during initial simulations of antiprotons left air at the exit to the production section. The impact on the muon and pion momentum and acceptance was found to be negligible, but the antiproton acceptance into the Torus1 was zero at the limit of the sample size of the simulations.

It may be possible to identify a region in the beamline close to the production target where a separation occurs between antiprotons and low-energy muons and pions. This would be highly favourable as it would reduce the impact on signal sensitivity, although in the studies performed here such a region has not been apparent. Additionally, material close to the production target would need to be considered from an activation and safety perspective.

Finally, as well as adding material along the beamline, one could consider a slight reduction in the proton beam energy. Even a reduction by 200 MeV would reduce the total antiproton production cross-section by between 40 and 50% based on the methods described above to determine the ξ weighting factor. Reducing the beam power further, by around 500 MeV would reduce the cross section by 75 to 90% of the current estimate, i.e. lower the production rate by about one order of magnitude.

7.5 Direct Beam-Related Backgrounds

Although neither a muon or pion in their rest frame can decay to electrons greater than 55 MeV, if these particles are boosted sufficiently the resulting electron can be produced with signal-like momentum. For muons at 78 MeV/c, Michel electrons can occur at 105 MeV/c if produced in the direction of the muon's momentum (and neglecting muon polarisation). For pions, the threshold for signal-like electrons to be produced during decay is 58 MeV/c, although the branching fraction for this process is helicity suppressed to around 1×10^{-4} .

The bent solenoids and the pulsed beam help to suppress these sorts of backgrounds, whilst the beam blocker, downstream of the target disks, reduces the geometric acceptance. Following the results of chapter 5, the inner radius of the collimator at the exit of Torus2

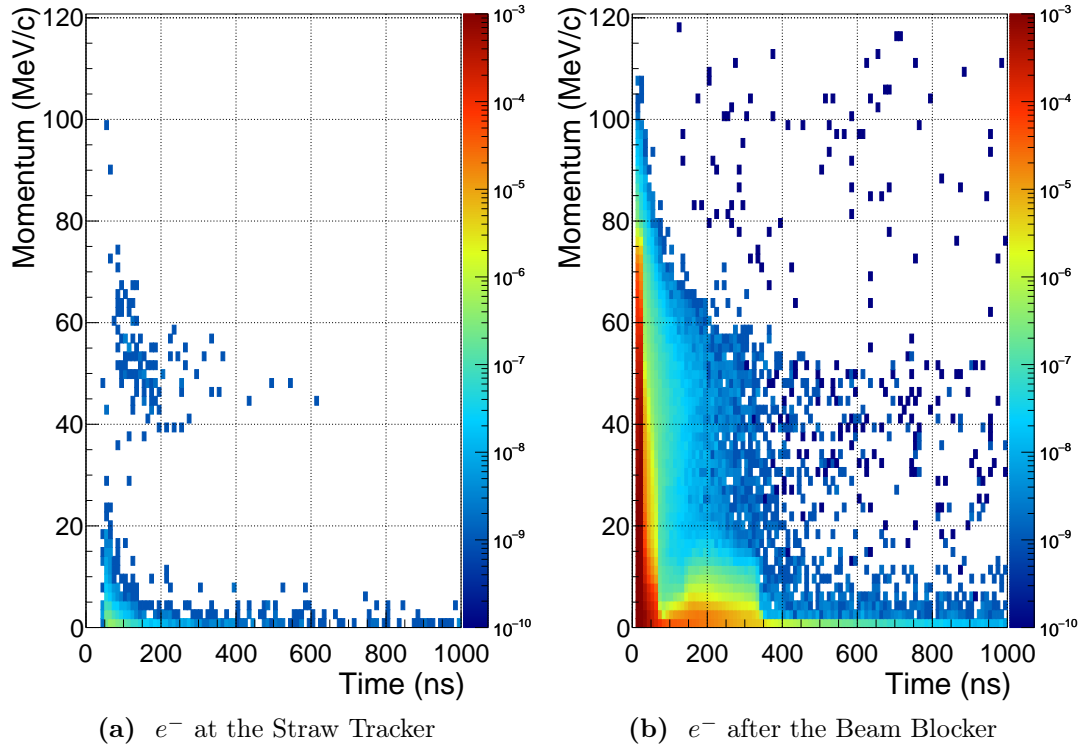


Figure 7.18: The timing and momentum of electrons detected at the straw tracker, (a), and passing a plane immediately after the beam blocker, (b).

is set to 12 cm, whilst the beam blocker has a radius of 25 cm. As the beam passes along the stopping target region, the beam envelope grows due to the reduction in the solenoidal field strength. The radius of the beam blocker, however, is large enough that even with this growth there should be no direct line of sight between the muon beam and the spectrometer. As such, the only way for beam particles to reach the detector are by a hard scatter off the target or beam blocker, or to be produced via decay of another particle close to the target itself.

To check the probability that signal-like electrons are produced in the beam and arrive at the detector in the time window, the output of the large production target simulation was resampled five times, so that around 1.1×10^9 POT events were studied, equivalent to about 8 Phase-II bunches. Fig. 7.18a shows the momentum and timing of electrons at the straw tracker, from which it is clear that no background events were observed within the gated-time detector window. One electron is observed at 98 MeV/c, but this occurs around 100 ns after the proton bunch. This immediately sets a limit on the background rate—less than 1 in 1.4×10^9 per POT.

To be able to understand this background better, it is necessary to apply some extrapolation. Indeed, it will never be feasible to directly simulate the 10^{21} or so POT that would be necessary to deduce the background rate without some extrapolation. To make this extrapolation, we look at the same distribution immediately after the beam blocker. At this point there are far more electrons so it is easier to fit and model the distributions. Fig. 7.18b shows the momentum vs. time plot for electrons immediately after the beam blocker.

The rate of observing delayed, signal-like electrons due to high-energy beam particles is modelled by factorisation of the acceptances:

$$R_{\text{beam}} = A_{\text{geom}} A_{\text{mom}} A_{\text{time}}, \quad (7.14)$$

$$= \left(\frac{N_{\text{obs}}}{N_{\text{POT}}} \right) \left(\frac{\int_{104.2}^{105.5} f(p) dp}{\int_{p_{\text{low}}}^{105.5} f(p) dp} \right) \left(\frac{\int_{600}^{1200} g(t) dt}{\int_{30}^{1200} g(t) dt} \right), \quad (7.15)$$

where A_{geom} , A_{mom} , and A_{time} are geometric acceptance and efficiencies of the momentum and timing thresholds, respectively. N_{obs} is the number of events actually seen at the straw tracker, whilst N_{POT} is the number of simulated POT. In the case of prompt beam electrons, the above equations are the same, except that A_{time} becomes the extinction factor multiplied by the fraction of time spent in the gated-time detection window.

The functions $f(p)$ and $g(t)$ represent the momentum and time projections of electrons after the beam blocker. Their factorisation in this manner is valid due to the lack of strong correlation visible in Fig. 7.18b. It is reasonable to assume that, close to the signal region, the momentum distribution observed immediately after the beam blocker will have the same shape as the momentum distribution at the straw target. Since the acceptance function is essentially flat at the high-energy limit (see 5.5 and 6.2.3), only the normalisation of the spectrum should change, and this we have encapsulated already in the geometric acceptance.

Finally, the timing distribution, $g(t)$, is also taken by fitting the observed electron distribution after the beam blocker. Here, however, one needs to be careful about extrapolating the distribution from after the beam blocker to the straw tracker. The extrapolation must account for two effects: an overall translation of the distribution to later times, and a broadening of the distribution (an increase in the fitted lifetime). Both effects are determined by the time needed for particles at the beam blocker to

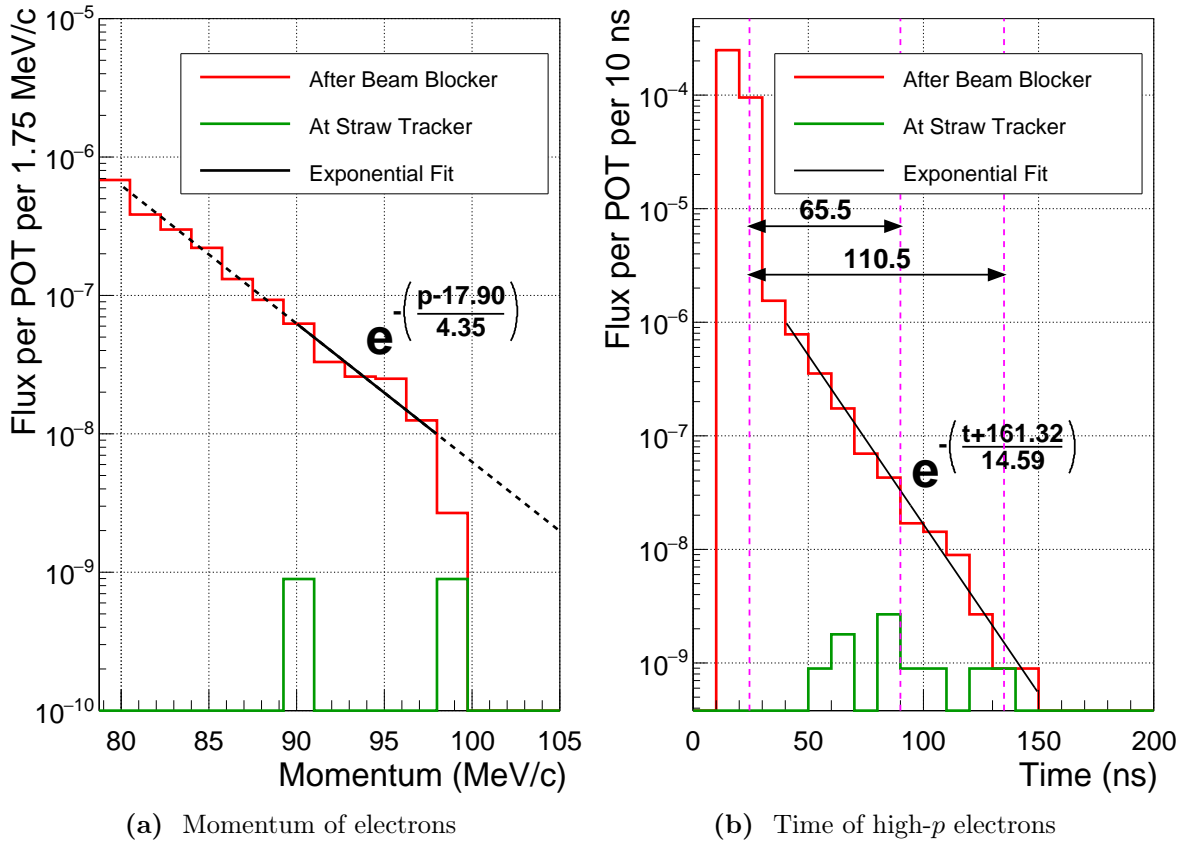


Figure 7.19: Projections of the momentum and arrival time of electrons. (a) shows the momentum for electrons that arrive at any time, whereas (b) only shows the arrival time for electrons with momentum above 65 MeV/c. Magenta lines in (b) indicate the mean arrival time after the beam blocker and the mean and maximum arrival time at the straw tracker. The black line is an exponential fit to the momentum and time of electrons after the beam blocker, with the equation and constants shown next to the fit.

propagate through the spectrometer. With a radius of 2 m, the typical distance travelled along the Spectrometer will be at least about 6 m, and since the electrons are relativistic and travelling at close to the speed of light, transport through the spectrometer can be expected to add about 20 ns. This assumes that the electron's pitch angle is equal to zero so that they follow the beam axis perfectly. With a large pitch angle the distance travelled, and therefore transportation time, will be longer, although since larger pitch angles drift more in the bent solenoids, these particles will tend to be removed more effectively. The effect of broadening on the distribution arises from lower energy electrons moving more slowly, however for the relativistic signal-energy electrons this effect will be negligible.

| Parameter | Value | Description |
|------------------------------------|------------------------|--|
| A_{geom} | 8.93×10^{-9} | Geometric acceptance to high-momentum electrons per POT |
| A_{mom} | 3.13×10^{-5} | Fraction of beam electrons within the signal momentum cuts |
| $A_{\text{time}}^{\text{delayed}}$ | 5.25×10^{-12} | Fraction of beam electrons delayed until the detector window |

Table 7.8: Parameters and their values in the determination of the background rate due to high-energy particles in the beam.

Fig. 7.19 show the momentum and time functions based on the distribution of electrons after the stopping target. The equations for the lines of best fit are also shown, and the region used to fit indicated by the solid black fitted line. The low-momentum threshold for this study, p_{low} , is set to 65 MeV/c, since this removes electrons from DIO of muons along the beamline, which have relatively long life-times but cannot be produced at signal energies. Above this threshold, there are 65 events at the straw tracker, giving a geometric acceptance of 8.93×10^{-9} . For the efficiency of the momentum cut, using the fit to the projection shown in Fig. 7.19a, the ratio of events expected between 104.2 and 105.5 MeV/c compared to the integrated rate from 65 to 105.5 MeV/c is 3.13×10^{-5} . For the timing efficiency, the fit given in Fig. 7.19b is first shifted so that the mean of timing distribution at the beam blocker sits at the time of the latest arriving electron above 65 MeV/c, as indicated by the vertical magenta lines. This amounts to a shift of 110.5 ns, which is about twice as large as if one were to use the mean of the straw tracker electrons. Having applied this shift (which we implement as a shift in the start and stop time for the integration), we find the suppression of electrons due to the time-gated window gives a factor 5.25×10^{-12} .

All of these factors are summarised in Table 7.8. Finally, then, we can pull all these factors together using (7.15), from which we find that the predicted prompt beam-related background rate per POT is 2.80×10^{-24} , whilst the delayed background rate due to beam particles is 1.47×10^{-24} .

Given the extrapolation that has been necessary, this result comes with a large degree of uncertainty. However, in principle this includes all sources of electrons in the beam: high-energy muons, pions, and electrons coming directly from the production target with high energy. This also includes electrons produced from neutron capture, provided the neutron itself originated downstream of the production target section, which were not

included here in order to accelerate the simulation speed. In addition these neutrons should be studied carefully using multiple hadron production models but, as discussed in 7.7.1, these neutrons are left to future studies.

7.6 Cosmic Ray Background

Cosmic rays at sea level consist primarily of positive and negative muons. These are produced when high-energy particles originating in the sun or beyond the solar system strike the upper atmosphere and produce a particle shower. About one muon per square centimetre per minute is expected at sea level, with the average muon energy around 4 GeV [78]. At these energies, not only can such muons readily produce high-momentum electrons, but they are weakly ionising and therefore penetrate material relatively easily.

This makes cosmic muons a potential source of backgrounds, as the high-energy muons can pass through the experiment hall to the beamline whereupon they can produce signal-like electrons. In addition, this background would lack any timing structure. As a result, a Cosmic Ray Veto (CRV) is included in both Phase-I and Phase-II, made with four layers of scintillator bars as the active material. When a cosmic ray passes this, events in the detector can either be tagged, or any trigger on this event vetoed and not read out, such that signal-like electrons produced from cosmic rays should not be included in the analysis.

At the time of writing, the CRV has been optimised and studied for Phase-I [44, 99, 100]. These studies suggest that a miss-rate of fewer than 1 in 10^4 events is achievable. For Phase-II however, given the changes to the experiment geometry, the situation is a little different. Principally, the stopping target in Phase-I is surrounded by the Cylindrical Drift Chamber (CDC), such that cosmic muons must escape detection in both the CRV and CDC, and then decay close to the target. In Phase-II, the stopping target is located well away from the detector, which means cosmic muons can only be vetoed by the CRV. Furthermore, the CRV geometry in Phase-II should cover both the target and the intermediate beamline, in addition to the detector solenoid itself.

Phase-II is expected to run about 1.57×10^7 s as suggested in section 6. During COMET operation, a single accelerator cycle is expected to last 2.48 s, with about 0.7 s for extraction, giving a duty factor of 0.28. In addition, with a time-gated window lasting 600 ns and bunches separated by 1.170 μ s, the overall duty factor drops to about 0.14.

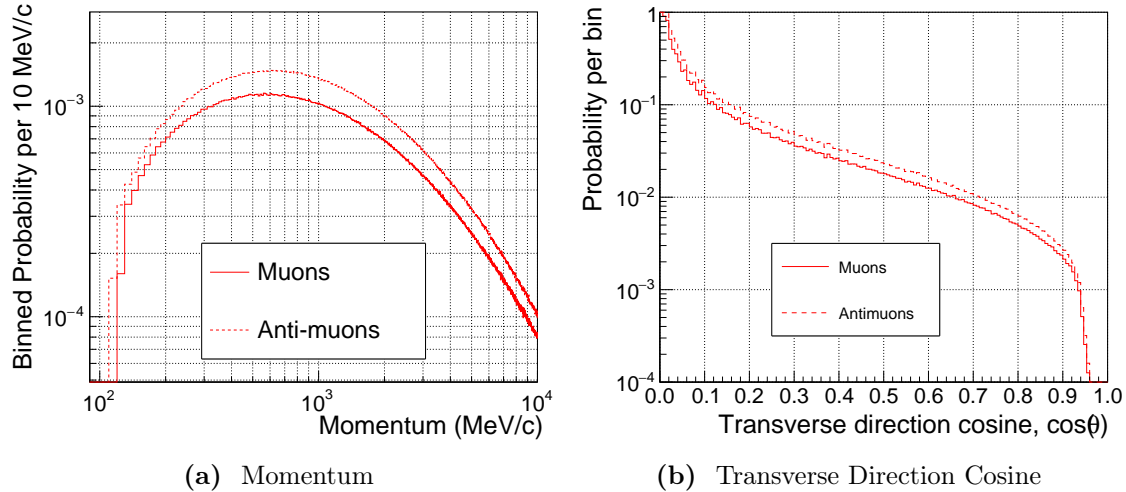


Figure 7.20: Distributions of momenta and the transverse direction for the cosmic muon and antimuon fluxes provided by the ND280 collaboration.

As such, during Phase-II running there are really only about 2.20×10^6 s when a cosmic muon can produce backgrounds. During this time then, 4.8×10^4 cosmic muons should pass through each horizontal square centimetre of the COMET hall. If we assume the miss-rate for the Phase-II will be no worse than for Phase-I, i.e. 1×10^{-4} , then for each square centimetre of the experiment, more than 48 muons should be studied.

7.6.1 Simulating Cosmic Muons

To simulate the cosmic ray background, input muon events were provided by the ND280 experiment [101]. These contained positive and negative muons that had been produced in an air shower simulation using the CORSIKA simulation package [102], for the atmosphere above J-PARC. Fig. 7.20 shows the distributions of momentum and directions that these files contained.

Muons were generated in a horizontal plane directly above the experiment hall (and centred on the origin of the ICEDUST coordinate system, the production target). A 50×50 m 2 square within in this plane was used to generate the events. This immediately adds a limitation to this simulation that very horizontally-moving muons cannot be studied, but it is needed to increase the simulation efficiency. About 1.76×10^8 cosmic events were generated in this way; for the 2500 m 2 region above the experiment where the simulation was started, more than 1.2×10^8 events should be studied, according to the above calculations.

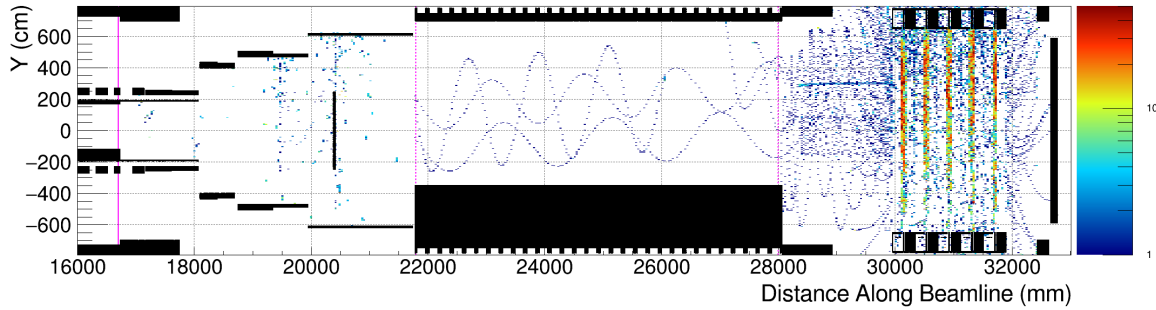


Figure 7.21: Projection onto beamline coordinate system of electrons from cosmic rays with momenta greater than 100 MeV/c, from a simulation of about 170 million cosmic muons. Three tracks can be seen to enter the electron spectrometer and pass along, although their momenta are all above 105 MeV/c as visible from the upwards drift of the trajectories.

Material above the beamline can degrade and stop cosmic muons so it is important this is modelled well. The concrete and iron shielding for the entire experimental hall is implemented, as well as the shielding necessary for the CRV. However, at this stage the geometry in the simulation only has the CRV design intended for Phase-I around the detector solenoid (in its Phase-II position). Since the CRV will need to be extended to include all the way up to the stopping target in Phase-II, there will likely be more shielding material inserted above the beamline.

7.6.2 Results of the Simulated Cosmic Background Rate

The tracks of high-energy electrons that enter the detector region are shown in Fig. 7.21. Fig. 7.22 shows the momentum distribution of observed electrons. There are large fluctuations across the momentum distribution, but this is most likely due to statistical fluctuations rather than truly physical. From 80 to 120 MeV/c, 140 electrons hit at least one layer in the straw tracker, although only 19 of these hit a second plane. The number of background events due to cosmic rays can therefore be estimated as:

$$R_{\text{cosmics}} = R_\mu \frac{n_e^{\text{obs}}}{N_{\text{sim}}} \Delta p (1 - \epsilon_{\text{CRV}}) A_{\text{duty}} A_{\text{timing}} A_{\text{TDAQ,Recon}}, \quad (7.16)$$

where R_μ is the rate of cosmic muons expected through the experiment hall per second, n_e^{obs} is the observed number of events per MeV/c, N_{sim} is the total number of simulated cosmic ray muons, and Δp is the width of momentum thresholds, from 104.2 MeV/c to 105.5 MeV/c. ϵ_{CRV} is the CRV efficiency, such that $(1 - \epsilon_{\text{CRV}})$ is the expected miss-rate.

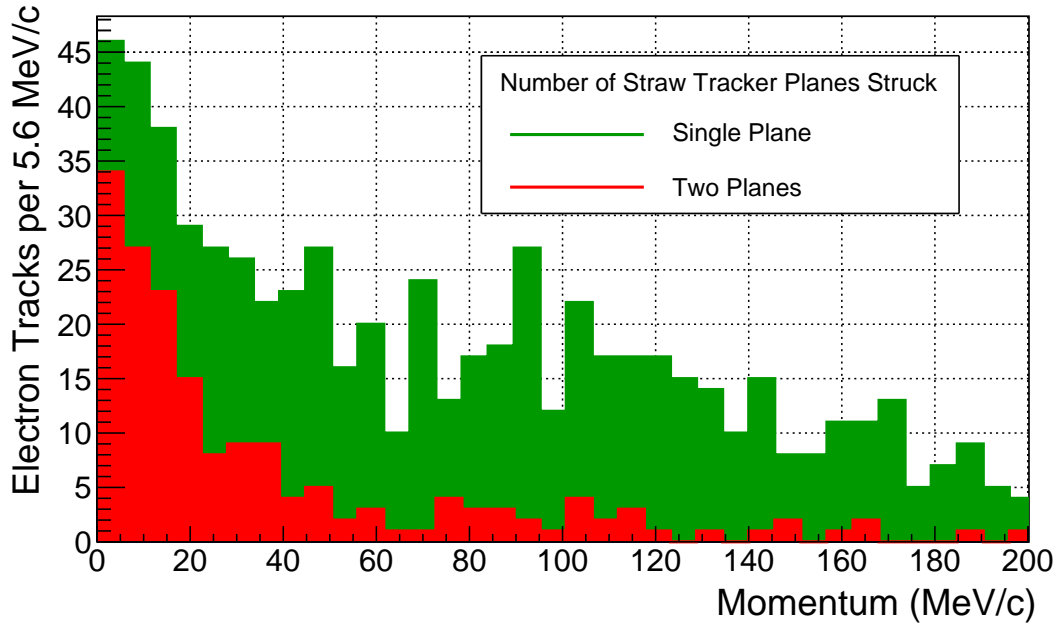


Figure 7.22: Momentum of electrons that hit one and two layers (planes) of the straw tracker. The vertical axis shows the raw number of observed events based on the simulation of 170 million cosmic muons described in the text.

| Parameter | Value | Description |
|-------------------------------|--------------------|---|
| R_μ | 4.17×10^5 | Cosmic ray flux through entire hall per second |
| n_e^{obs} | 0.46 | Observed electrons per MeV/c |
| N_{sim} | 1.76×10^8 | Number of simulated events |
| $(1 - \epsilon_{\text{CRV}})$ | 1×10^{-4} | Miss rate of the CRV |
| A_{duty} | 0.36 | Accelerator duty factor |
| A_{timing} | 0.51 | Fraction of time within gated-time detection window |
| $A_{\text{TDAQ,Recon}}$ | 0.70 | Combined acceptance of TDAQ and Reconstruction |

Table 7.9: Parameters and their values for the determination of the cosmic ray background rate.

The factors A_{duty} , A_{timing} , and $A_{\text{TDAQ,Recon}}$ represent the accelerator duty factor, fraction of time spent during the time-gated detection window, and the combined TDAQ and reconstruction efficiency, respectively. The values for each of these parameters are given in Table 7.9. From this we can estimate that there will be 1.87×10^{-8} backgrounds per second due to cosmic rays.

To reduce the cosmic ray background further, the most important parameter is the CRV efficiency, the complement of which multiplies the entire background rate. Since this background is completely uncorrelated with the beam, the shorter the running time, the lower this background rate will be. If this cannot be reduced further, then it might be necessary to add more material above the beamline or above the experiment hall. Fortunately, rather than depend on simulation for this, Phase-II has the benefit of Phase-I, which will have measured and characterised the cosmic ray flux on the experiment hall floor.

7.7 Summary of Background Rates

Table 7.10 gives an overview of the predicted rates. The overall expected number of background events during Phase-II is 0.662 events, assuming 1.57×10^7 s of run time. This is dominated by the cosmic ray background and events from antiprotons that stop in the target. It is clear, though, that further work must be undertaken on these predictions in the future. In light of the various uncertainties, discussed in more depth below, we have tried to be as conservative as reasonably possible in this estimate; improving the uncertainties would hopefully reduce the estimated number of events.

| Type | Source | Background Rate | | | Total Events | Comment |
|-----------|------------------------|------------------------|------------------------|------------------------|------------------------|---|
| | | per μ^- stop | per POT | per second | | |
| Intrinsic | DIO | 6.20×10^{-20} | 9.92×10^{-23} | 4.31×10^{-9} | 0.068 | Beam includes high-energy electrons from π , μ , and n capture. |
| | RMC | 3.73×10^{-31} | 6.01×10^{-34} | 2.61×10^{-20} | 4.10×10^{-13} | |
| Delayed | RPC | — | 1.73×10^{-27} | 7.51×10^{-14} | 1.18×10^{-6} | Based on conservative interpolation and extrapolation of limited experimental \bar{p} data. |
| | Beam | — | 1.47×10^{-24} | 6.39×10^{-11} | 1.00×10^{-3} | |
| | Stopped \bar{p} | — | 4.34×10^{-22} | 1.89×10^{-8} | 0.296 | |
| Prompt | π^- from \bar{p} | — | 1.95×10^{-30} | 8.49×10^{-17} | 1.33×10^{-9} | Dominated by conservative miss-rate. |
| | RPC | — | 1.82×10^{-24} | 7.91×10^{-11} | 1.24×10^{-3} | |
| | Beam | — | 2.80×10^{-24} | 1.22×10^{-10} | 1.91×10^{-3} | |
| Cosmics | π^- from \bar{p} | — | 3.56×10^{-29} | 1.55×10^{-15} | 2.43×10^{-8} | Dominated by conservative miss-rate. |
| | Total | — | — | 1.87×10^{-8} | 0.294 | |
| | | | 4.22×10^{-8} | 0.662 | | |

Table 7.10: Final predicted background rates and events. The dominant backgrounds are cosmic ray electrons and stopping antiprotons, which are predicted to contribute equally to the final background count. Assumes an extinction factor of 1×10^{-11} , a double-Gaussian momentum resolution with a core resolution of $\sigma = 200$ keV/c and a tail probability of 4.4×10^{-15} that events are misreconstructed with at least an additional 2.4 MeV/c. A momentum window from 104.2 MeV/c to 105.5 MeV/c is used to define the signal region. All other parameters are the same as stated in chapter 6.

7.7.1 Backgrounds Not Considered

Neutrons from the Production Target

Although some of the methods above are different, compared to the Phase-I TDR and Phase-II CDR there is only one source of backgrounds that has not been covered here: the production of high-energy electrons from the capture of neutrons that originate in the production target. These neutrons were killed in order to reach a large number of muons and pions in the simulation, although neutrons produced along the muon beam (from the collimators, stopping target, etc.) have been included with the beam background. Whilst there is a large amount of concrete and iron material in between the production target and the detector, the production target is likely a major source of neutrons in the experiment, and this needs to be studied rigorously using multiple hadron production and neutron transport models.

Such studies have advanced for Phase-I, with the background rate from neutrons estimated to be about 3.1×10^{-29} per POT [44]. With a different experiment layout, production target material, and higher proton beam power, separate studies should be performed for Phase-II. A naïve scaling of this to the Phase-II number of protons on target would suggest that 2.7×10^{-8} events can be expected in Phase-II. Since the detector sits further away from the production target and since there is additional beamline then it is likely that the neutron rate is lower. The change of target material between Phase-I and Phase-II from low to high-Z material will increase the neutron production rate per unit mass of target. However, to compensate for the equivalent reduction in muon yield that this produces, the target in Phase-I will be longer and as such the neutron rate per POT might well be similar.

Detector Performance

It has been implicitly assumed in the preceding work that the StrECAL is able to perfectly distinguish electrons from positrons, muons, and pions. This seems a reasonable assumption given the charge and relativicities of the particles, but it would be important to consider the rate of mis-identification in the event that these particles are able to be transported to the detector. These particles are already suppressed by the long beamline, however, and only muons have been seen to be transported to the detector in the simulations for this thesis.

In a similar vein, the impact of ‘pile-up events’ should be considered. Pile-up occurs when two separate particles enter or strike the same region of a detector in a shorter space of time than the detector can resolve. In the ECAL, pile-up could be an issue for triggering but since the ECAL’s primary purpose in the analysis is to provide a time stamp, this should not be an issue for backgrounds.

Pile-up in the Straw Tracker should be easier to resolve because of the finer granularity of the detector, and the use of multiple hits on multiple straws to reconstruct the trajectory. Instead, it is the occupancy of the Straw Tracker that should be considered. How often is a 105 MeV/c electron found due to the mistaken combination of hits in a high-occupancy event? Machine learning techniques for Phase-I’s Cylindrical Detector (CyDet) have been developed to significantly suppress hits from tracks other than signal electrons [44] and it is likely that a similar approach will be possible in Phase-II. In addition, although the beam power and production target material in Phase-II increase the multiplicity of particles in the beam, the longer beamline may well bring the occupancy down to lower levels than observed in Phase-I.

7.7.2 Impact of Momentum Resolution

The momentum resolution is the key factor in determining the background rates for the intrinsic backgrounds (Radiative Muon Capture (RMC) and decay-in-orbit (DIO)). However, since the distribution of residuals (the resolution function) is not well known for Phase-II, there is a degree of uncertainty over the size of these backgrounds.

To understand how robust these estimates are to changes to the resolution function, a simple parametrisation for the resolution function was used. In this simplified scheme, the probability density for mis-reconstructing an electron’s momentum by a certain amount, is given by the function:

$$P(p_{\text{reco}} - p_{\text{true}}) = P(\Delta p) \propto e^{(\Delta p/\sigma_1)^2} + \kappa e^{(\Delta p/\sigma_2)^2} \quad (7.17)$$

where κ is dimensionless and used to set the relative weight of the second Gaussian, and σ_1 and σ_2 define the widths of the respective Gaussian.

Fig. 7.23 shows the background rates due to DIO and RMC as a function of σ_2 for different values of σ_1 and κ . The current Phase-I results suggest κ to be about 0.08, and σ_1 to be less than 200 keV/c, and so these values are used as baseline estimates. To

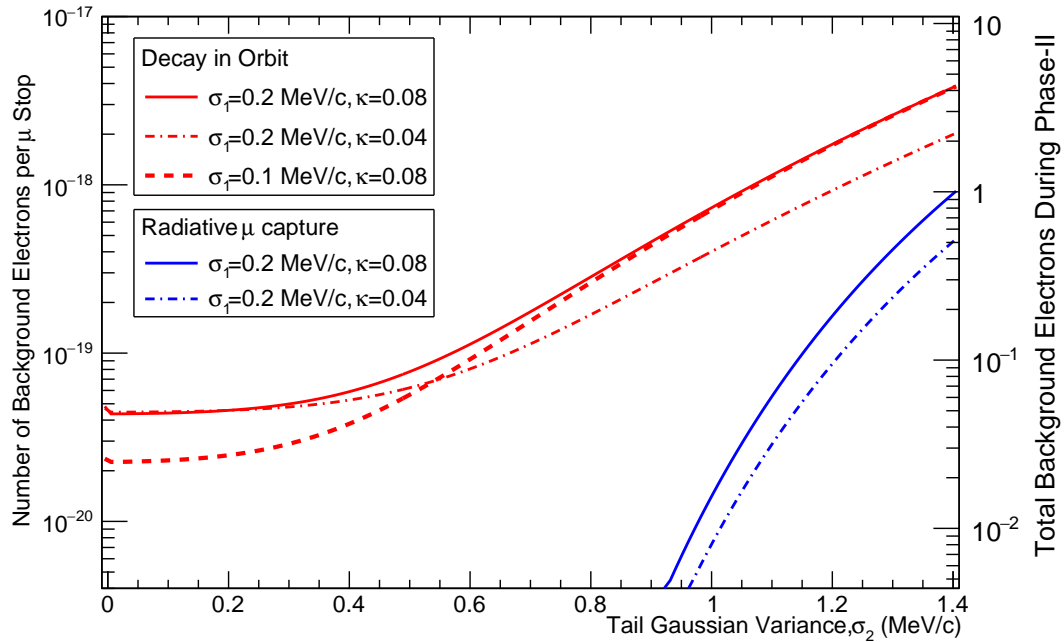


Figure 7.23: Dependence of the intrinsic background rates on σ_2 , the width of the high/low momentum tail in the reconstruction distribution. From this it can be seen that the background rates from DIO will always dominate, compared to RMC.

produce the plot in Fig. 7.23, we fix the momentum thresholds to be 104.2 MeV/c and 105.5 MeV/c, as found from the sensitivity estimates. Over the range of σ_2 values shown in Fig. 7.23, the signal acceptance changes by less than 4.2%, given these momentum thresholds.

From this it is clear that, provided the value of σ_2 is kept below 1 MeV/c, fewer than 0.01 background events would be expected from RMC, whilst the background rate from RMC grows exponentially above this point. However, it is also clear that the rate from DIO electrons will dominate regardless of the resolution. This should not be surprising given that the DIO spectrum reaches up to the μ - e conversion end-point whilst the RMC end-point is separated by some 2.4 MeV/c.

7.7.3 Principal Uncertainties

Whilst it is not possible to make a quantitative estimate of the uncertainty at this time, it is clear that for some backgrounds the uncertainty is large.

Statistical Uncertainty and Use of Extrapolation In many instances the generated sample sizes for these background predictions were too small to directly evaluate

the background rate. In these cases it was necessary to extrapolate from parameters and regions with higher statistical power, such as lower energy parts of a spectrum, earlier in time, or use a more upstream part of the experiment. In addition, it was often necessary to resample particles produced from an earlier stage of the simulation, such as for the muon and pion stopping distributions, or the beam fluxes leaving the production target region. This introduces a different kind of error, which is very difficult to quantify, namely that there will now be some correlation between the events seen downstream. In the future, generating larger Monte Carlo samples using the continually increasing computing power available to the COMET experiment will be important in reducing this uncertainty.

StrECAL Reconstruction and Resolution In the case of DIO and RMC, the two intrinsic sources of background, the main source of uncertainty is in the resolution function. The exact distribution for the residuals after reconstruction is not well known for the Straw-tube tracker and Electromagnetic Calorimeter (StrECAL), especially for Phase-II. In particular, for RMC, the high-energy tail needs to be studied better. It has been assumed that fewer than 4.4×10^{-15} events will be reconstructed with momentum larger by at least 2.4 MeV/c than the true value. This assumption must be confirmed, however.

RPC Spectrum In the case of Radiative Pion Capture (RPC), the dominant uncertainty comes from the spectrum of photons produced during RPC. The study here and in the Phase-I TDR depend entirely on a single set of experiments, which do not cover RPC from aluminium, only on magnesium and calcium. This will be difficult to improve further without additional observations, and it would be useful to study this at Phase-I if possible, perhaps by changing the Torus1's dipole field to improve pion acceptance.

Antiproton Production Given the lack of experimental evidence for antiproton production in the ‘sub-threshold’ energy regime of the backwards direction, there is large uncertainty over the expected rate. Whilst the model developed here was kept conservative, as one of the dominant backgrounds it is important to study this further. A dedicated study comparing multiple different hadron production codes to all the possible experimental datasets (including forward and backward produced antiprotons from the different targets with different proton momentum) could reduce our uncertainty if no new experimental data is forthcoming. Such a study would then be able to extrapolate better for the target material, proton energy, and production direction used in COMET.

In addition to the production rates, there is reasonable uncertainty on the mechanisms by which antiprotons can produce background electrons. Here it has been assumed that the primary mechanism is via pion production, but the rates for such production in aluminium is also not well known. Such an assumption must also be tested.

Phase-I will be able to play a sizeable role in reducing this uncertainty as one of the first experiments to look at antiproton production under the COMET conditions. The fact that the production target will likely be made from graphite in Phase-I as opposed to the tungsten of Phase-II reduces the direct usefulness of such measurements however. On the other hand, given that there is more (although still rather limited) data for graphite will allow Phase-I measurements to better understand the transportation of antiprotons along the COMET beamline. Furthermore, in addition to antiproton measurements during the main Phase-I runs, additional runs are under consideration to specifically study the antiproton background. These could involve changing the production target material is to something other than graphite or changing the beam energy and studying the change in antiproton yields.

Cosmic Ray Veto Geometry and Shielding Without a complete CRV design, it is tough to be confident that the energy loss of cosmic muons is well captured in the Phase-II simulation. In addition, the miss-rate of 1×10^{-4} should be experimentally confirmed and ideally improved.

Again, after Phase-I the uncertainty on this background should be significantly reduced. The muon flux in the experiment hall, at the beamline position will have been measured to a high precision in all directions. Furthermore, since the CRV design will be largely unchanged the miss-rate will be well understood.

RMC on Al-26 RMC on Al-26 was also discussed as a potential concern, since RMC on Al-26 can produce signal-energy photons. However Al-26 has a tiny abundance in natural aluminium, and the rate of production in the COMET muon beam is difficult to predict. This will be measurable at Phase-I, so that by Phase-II, the uncertainty on this process should be much smaller.

Electron Spectrometer Dipole Field The acceptance into the detector is affected by the field of the preceding beamline. For the Electron Spectrometer, the unphysical uniformity and lack of fringe field in the simplistic dipole field map used here may introduce effects that would not be seen in the real experiment.

7.8 Further Studies and Improvements

This chapter has presented a near-comprehensive set of estimates for background sources in Phase-II. It should not, however, be treated as the final set of predictions, but rather as an initial set of studies to be developed further. As well as the previous suggestions regarding uncertainties, the following list suggests additional methods that could be pursued to improve and expand the preceding set of estimates.

Explore techniques for improving the statistical power of limited Monte Carlo data

In addition to the resampling and extrapolation techniques used here, cross checks with various other methods should be explored. Together these would provide an increase in the statistical power of a limited set of simulated data, and provide a validation and uncertainty estimate for one another. Methods such as particle weighting and biasing could also be employed. Additionally, the transmission of each section of the beamline could be studied individually, building a set of multi-dimensional (particle type, momentum, position, etc.) transfer matrices. The total beamline acceptance for a given particle is then the product of these matrices.

Use different hadron production models

Primarily this is needed to cross check the muon and pion yields, and the production target optimisation. This is already well accommodated in ICEDUST, but should be exercised properly.

High-momentum electron acceptance vs. beamline position

Many background estimates would benefit from knowing the downstream acceptance of high-momentum electrons at a given location in the beamline. This could be a multi-dimensional histogram or matrix, and would ideally also contain the acceptance's dependence on the electron direction, and transverse location. With this information, simulations for the cosmic ray backgrounds, photon conversion after RPC and RMC, and beam simulations would only need to know the probability of creating a high-momentum electron at a given location to deduce the resulting background rate. Optimisation studies would also benefit, as mentioned in chapter 5.

The timescale for these studies is fairly varied: whilst Phase-II is several years away still, in some cases the true deadline will be Phase-I. Decisions for the design of Phase-I will impact, in some cases, the design of Phase-II, whilst the run plan for Phase-I will include dedicated studies aimed at reducing key uncertainties of Phase-II. For both of these reasons it is important that there is a continuous effort to maintain and refine the understanding of COMET Phase-II.

Chapter 8

Revisiting the Phase-II Stopping Target Region

Of the various optimisations presented in chapter 5, the stopping target was only optimised for its position, keeping the shape, thickness and size as in the CDR. It was also observed in that chapter that the beam blocker had a large impact on the signal acceptance. To investigate ways in which the sensitivity of Phase-II can be further improved we develop here the idea of a beam blocker-free stopping target design, as well as investigate the impact of changing the target shape.

The overall result of this study suggests an improvement in the signal sensitivity of Phase-II of a factor of 2.5 could be achievable.

8.1 Understanding the Stopping Target Region

One of the challenges when optimising the stopping target is the complexity of the region, and correlations between the various parameters.

The magnetic field around the stopping target, for example, is not a simple solenoidal field. Fig. 8.1 shows the magnitude of the field along the beamline axis in the stopping target region. At the exit of the bent solenoids and for the first straight section immediately downstream, the field is kept close to 3 T. By the entrance of the electron spectrometer, the field on axis is closer to 1 T, although a transverse gradient is introduced from the bent solenoids. The transition from 3 to 1 T happens over 1.5 m across three solenoid sections.

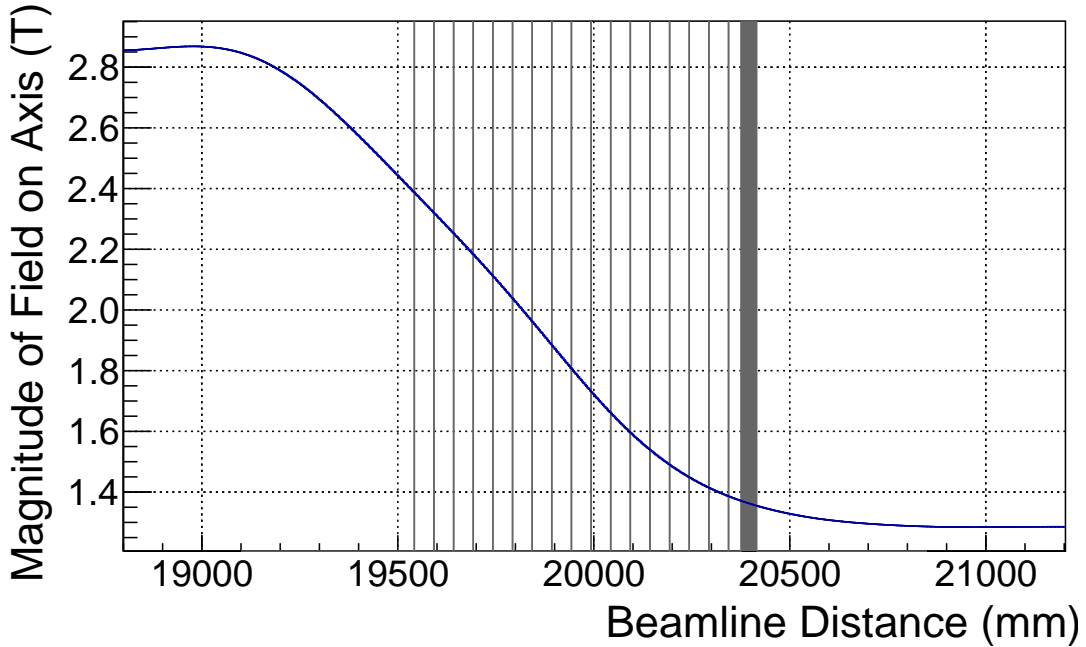


Figure 8.1: The magnitude of the magnetic field around the stopping target. The vertical grey lines indicate the position of the stopping target disks and beam blocker in the target design used in chapter 6. The muon beam arrives from the left, and signal electrons should leave to the right.

The stated purpose of the reduction in field strength is to mirror those signal electrons that are produced in the target heading upstream. This, then, is expected to increase the geometric acceptance of the detector. Magnetic mirroring can be understood in various ways, such as via the adiabatic constants. However, qualitatively and intuitively, since magnetic field lines never end ('there are no magnetic monopoles'), when the field strength is reduced, the field lines spread out. This can be seen as a normal solenoidal field, with a radial component superimposed. Normal gyration around the solenoidal field, therefore, generates a Lorentz force that points back along the direction of the solenoidal field, and reduces the longitudinal velocity of the particle. Thus a particle initially with only transverse momentum in the region of tapering field strength will acquire momentum in the longitudinal direction towards the lower field strength. Similarly a particle initially heading from a low-magnetic field to a high-magnetic field can be mirrored back if the difference in the field is sufficient. The limit for this to occur is given by the condition [103]:

$$\tan^{-1}(\theta) = \left| \frac{v_L}{v_T} \right| < \left(\frac{B_{\max}}{B} - 1 \right)^{1/2}, \quad (8.1)$$

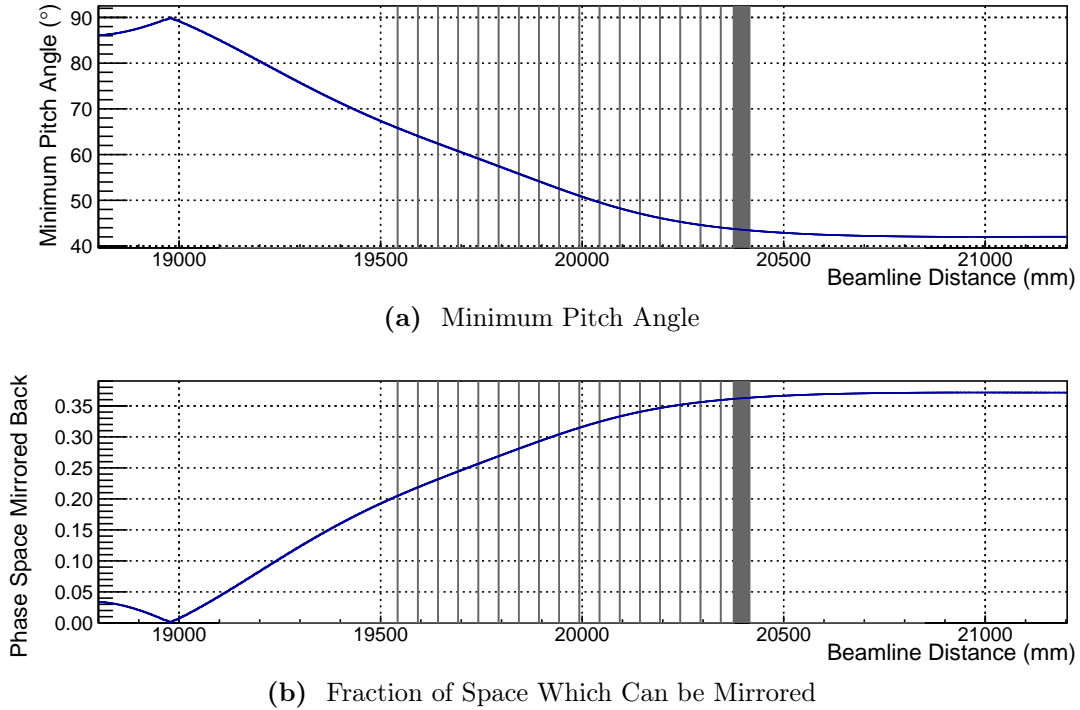


Figure 8.2: The ability for a particle to be mirrored downstream, if it is initially heading upstream at this point. For an electron produced at a given point along the beamline, if its pitch angle is too small it will not be mirrored. The minimum pitch angle is shown in (a). Since electrons are produced isotropically, this minimum pitch angle can be used to define the fraction of phase space that will be mirrored back, (b).

where B_{\max} and B are the maximum field strength and current field strength. v_L and v_T are the longitudinal and transverse velocity of the particle at this point, the ratio of which is the arctangent of the pitch angle, θ , between the particle's velocity and the solenoidal axis.

Given that the maximum field strength occurs at the exit of the Torus2, with a magnitude of $B_{\max} = 2.88$ T, one can calculate the minimum pitch angle an upstream-heading particle must have in order for it to be mirrored back downstream. This is shown in Fig. 8.2a where the minimum pitch angle varies from around 85° to about 43° at the end of Stopping Target Section. Since signal electrons are produced isotropically, this limit can be turned into the fraction of phase space for signal electrons produced at a point along the beamline that will be mirrored back, and this is shown in Fig. 8.2b. This clearly motivates putting the stopping target further downstream in order to maximize the mirroring effect.

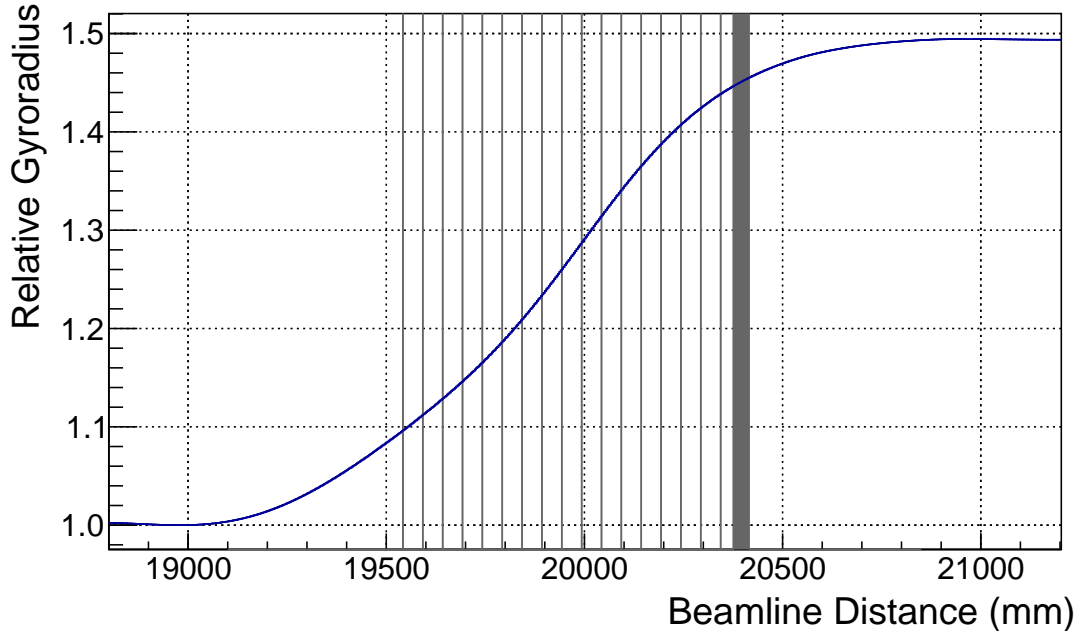


Figure 8.3: As the muon beam progresses along the beamline, the beam envelope varies proportional to the square root of the field strength. The maximum field occurs at the exit of the Torus2 solenoid, with a field strength of about 2.88 T, and this plot shows the relative change in the beam envelope compared to that point.

On the other hand, if the target is located downstream, the muon beam is required to traverse the tapered field. In that case there is another effect, namely the adiabatic growth of the beam envelope, which must be considered. Since particles in the beam follow the field lines, as the field is reduced, the beam profile must grow. This growth is governed by the expression:

$$Ba^2 = \text{const} \quad (8.2)$$

where B is the field strength at a given point, and a the radius of gyration. Thus if the field strength reduced by a factor of 4, for example, the beam envelope can be expected to grow by a factor of 2. The radius of gyration is shown in Fig. 8.3, relative to the radius at the exit of the Torus2, as a function of the distance along the beamline.

The position optimisation of the stopping target shown in chapter 5 kept the target disks at a fixed radius and moved the whole set of target disks (and beam blocker) upstream and downstream. With a fixed radius set of disks, as the target was moved downstream, the fraction of the muon beam expected to hit the target was reduced. This

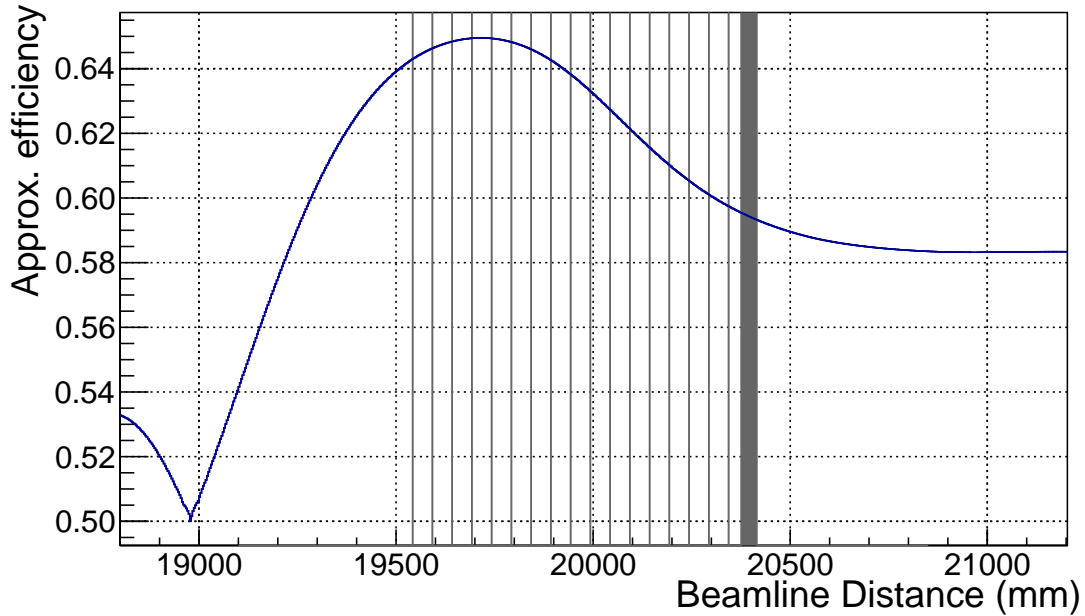


Figure 8.4: The effective signal sensitivity achieved by placing a disk of fixed radius at a given location along the beamline. It suggests an optimal target position slightly upstream of the location found in the optimisation chapter, but the difference is easily explained by simplifications in this model.

favoured putting the stopping target more upstream in order to increase muon stopping rate.

Thus there were two competing effects: move the target downstream and the mirroring of signal events increases, but move the target upstream and the muon stopping rate is increased. These factors can be combined to give a proxy for the expected signal sensitivity for a target disk of fixed radius placed at one point along the beamline. The muon stopping rate will be proportional to the fraction of the beam profile that overlaps with the target. Meanwhile, the fraction of upstream-pointing phase space that would be mirrored downstream, plus the fraction of phase space pointing downstream in the first place (half of it), should be proportional to the signal acceptance. This combination is shown in Fig. 8.4.

Indeed, the maxima of this function, at 19700 mm in beamline coordinates, is very close to the optimal location found during the position scan. This neglects many factors, such as the fact that disks upstream will remove muons from the disks downstream, and that not all electrons that head downstream will be accepted into the detector. Nevertheless, it seems to capture the underlying phenomena that determine the optimal target location.

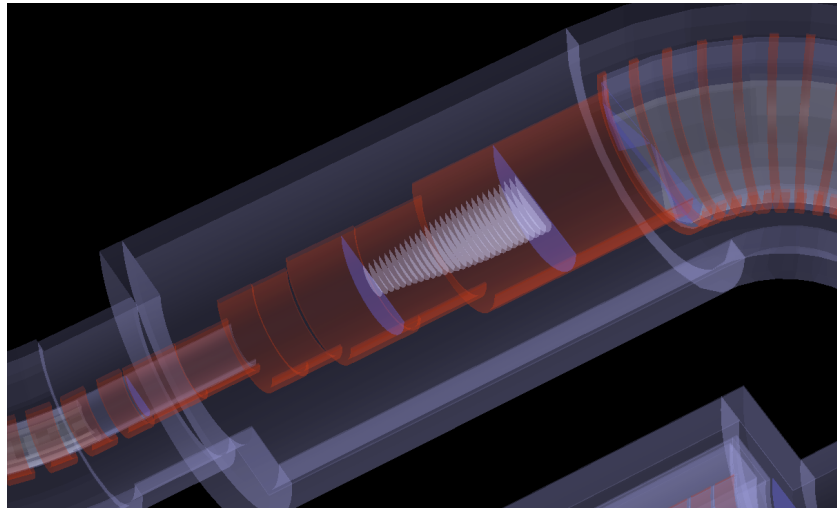


Figure 8.5: The new geometry of the stopping target, with the beam blocker removed. The blue vertical planes are the virtual monitors used in the simulation and not a physical piece of material.

8.2 Improving the Target Design

In order to improve the signal acceptance, and taking into account the previous discussion, we make three key changes to the target design. Firstly we allow the target radius to vary as a function of the beamline distance, thus keeping a constant overlap with the muon beam profile. Secondly we remove the beam blocker, which will hugely increase the acceptance of signal events. Finally, to compensate for the missing beam blocker, and to increase the number of stopped muons, we add more target disks into the target. From Fig. 6.2 in section 6.1 it can be seen that the muon stopping rate per disk has not reached zero by the last disk, which implies more muons could be stopped. In addition, the increasing target radius can be used to remove the line of sight between the Torus2 exit and the electron spectrometer that the beam blocker previously provided to remove beam particles.

Although each of these changes should each be studied carefully, as a proof of principle the design shown in the event display in Fig. 8.5 was tested in a simulation. The disk radii and positions are given in Table 8.1.

To check the sensitivity and stopping rates with this configuration, 75 million POT events were fed in to a simulation that had muon decay-in-orbit (DIO) and nuclear capture disabled, to be able to study the sensitivity in a single simulation.

| Disk Index | Beamline Position (mm) | Relative Gyroradius | Disk Radius in Simulation | Disk Index | Beamline Position (mm) | Relative Gyroradius | Disk Radius in Simulation |
|------------|------------------------|---------------------|---------------------------|------------|------------------------|---------------------|---------------------------|
| 0 | 19 542.0 | 1.098 32 | 144.758 | 18 | 20 443.8 | 1.463 30 | 256.950 |
| 1 | 19 592.1 | 1.114 05 | 148.932 | 19 | 20 493.9 | 1.471 51 | 259.842 |
| 2 | 19 642.2 | 1.130 64 | 153.400 | 20 | 20 544.0 | 1.478 23 | 262.219 |
| 3 | 19 692.3 | 1.148 36 | 158.248 | 21 | 20 594.1 | 1.483 47 | 264.080 |
| 4 | 19 742.4 | 1.167 53 | 163.576 | 22 | 20 644.2 | 1.487 45 | 265.500 |
| 5 | 19 792.5 | 1.188 47 | 169.495 | 23 | 20 694.3 | 1.490 56 | 266.612 |
| 6 | 19 842.6 | 1.211 30 | 176.068 | 24 | 20 744.4 | 1.492 96 | 267.471 |
| 7 | 19 892.7 | 1.236 01 | 183.326 | 25 | 20 794.5 | 1.494 78 | 268.125 |
| 8 | 19 942.8 | 1.262 27 | 191.198 | 26 | 20 844.6 | 1.496 12 | 268.604 |
| 9 | 19 992.9 | 1.289 43 | 199.516 | 27 | 20 894.7 | 1.497 03 | 268.933 |
| 10 | 20 043.0 | 1.316 68 | 208.037 | 28 | 20 944.8 | 1.497 30 | 269.030 |
| 11 | 20 093.1 | 1.343 04 | 216.451 | 29 | 20 994.9 | 1.497 30 | 269.030 |
| 12 | 20 143.2 | 1.367 71 | 224.474 | 30 | 21 045.0 | 1.497 14 | 268.972 |
| 13 | 20 193.3 | 1.390 05 | 231.867 | 31 | 21 095.1 | 1.496 92 | 268.891 |
| 14 | 20 243.4 | 1.409 84 | 238.518 | 32 | 21 145.2 | 1.496 71 | 268.817 |
| 15 | 20 293.5 | 1.426 88 | 244.317 | 33 | 21 195.3 | 1.496 67 | 268.804 |
| 16 | 20 343.6 | 1.441 27 | 249.272 | 34 | 21 245.4 | 1.496 73 | 268.823 |
| 17 | 20 393.7 | 1.453 30 | 253.450 | | | | |

Table 8.1: Parameters of the target disks used in the proof of principle simulation. Since the beamline axis is parallel to the $-z$ direction in the stopping target region, the Z-coordinate can be obtained from the beamline position via: $z = 2164 - (s - 19542)$.

8.2.1 Muon Stopping Rate

From this simulation, the muon stopping rate was found to be 2.8×10^{-3} per POT, and increase of 1.75 times compared to the stopping rate described in chapter 6. The stopping distributions in the target are shown in Fig. 8.6. It can be seen from the projection to the Z-axis that we catch much more of the tail of the distribution. It can also be seen from the YZ projection how there are very few muons stopping in the upper half of the target. This suggests one would really be able to remove this material which would give an additional increase to the signal acceptance.

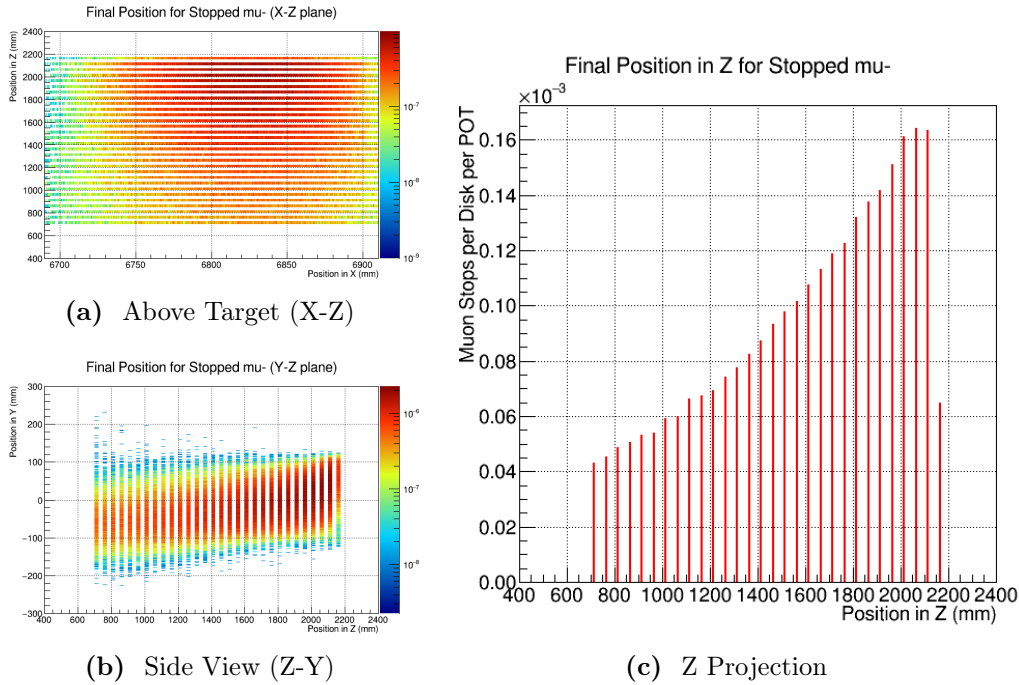


Figure 8.6: Projections of the muon stopping distribution with the improved target design, to be compared to Fig. 6.2. Although the disks are symmetric, it is clear from (b) how there are fewer muon stops in the upper parts of the disks. Removing the material there will improve the signal acceptance further.

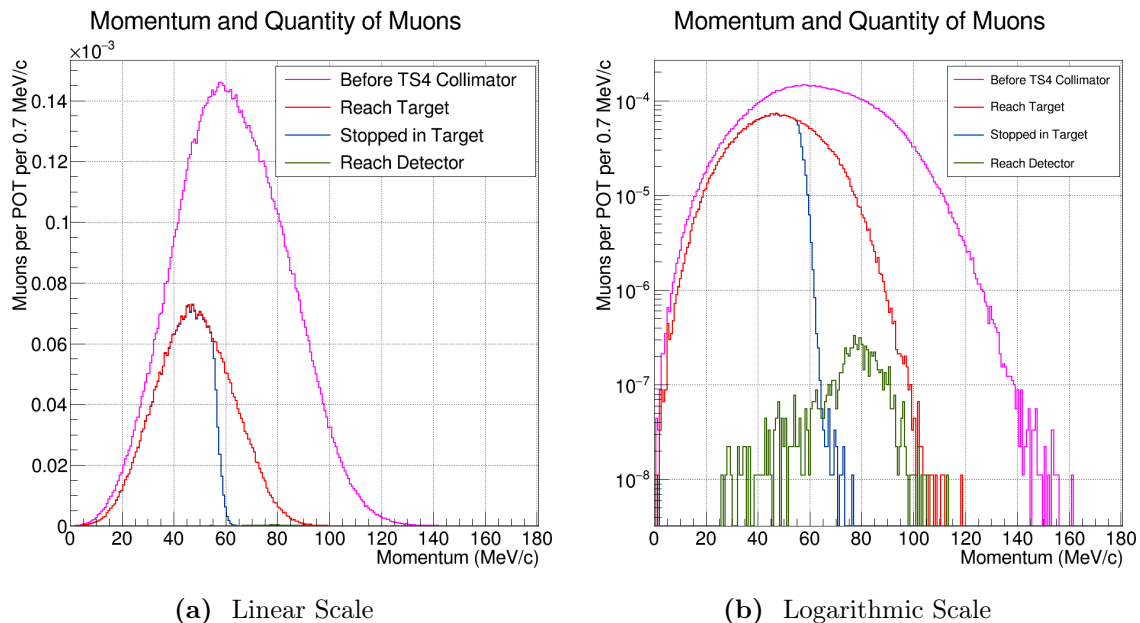


Figure 8.7: The momentum of muons that reach the stopping target and eventually stop. By comparison with Fig. 6.1, the new target design is clearly able to stop much higher momentum muons, although without the beam blocker it is also clear that high energy muons reach the detector.

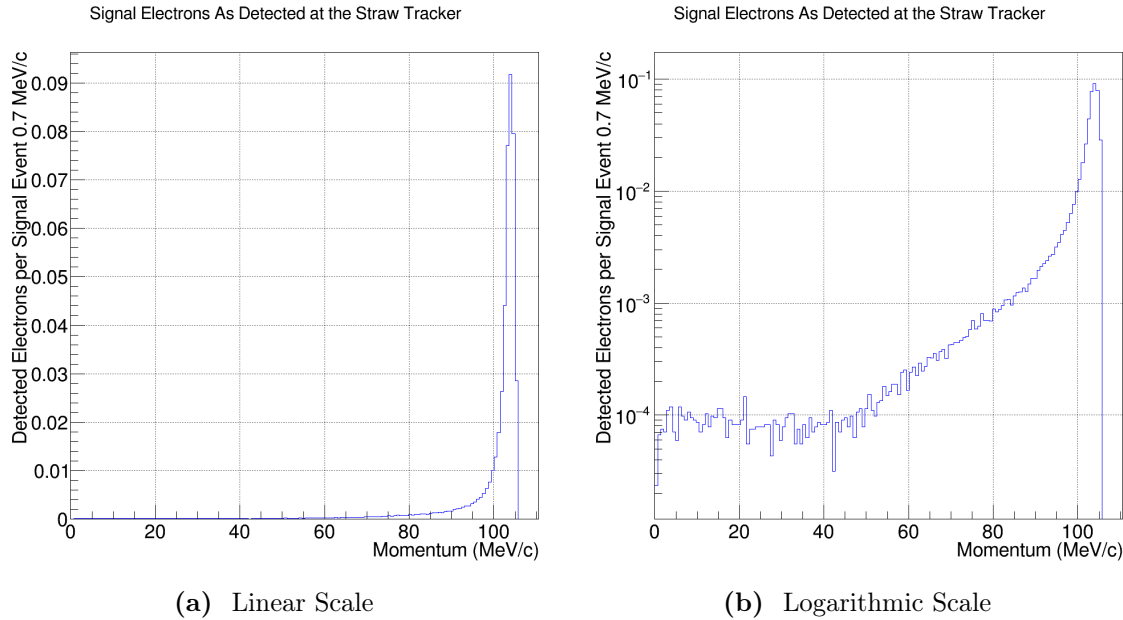


Figure 8.8: The observed momentum distribution and acceptance for signal electrons. Given the extra material, the energy losses in the target are larger than the previous design, although the overall geometric acceptance is significantly increased.

The extra disks and the enlarged radius also mean that the higher energy muons sitting lower down in the beam are more effectively stopped. Being at the bottom of the beam these muons were more likely to miss the old target design, but also penetrated further, requiring more target material to be stopped. This can be seen by comparison of the muon momentum distribution shown in Fig. 8.7 and comparing this with the momenta shown in Fig. 6.1. Whereas before we only stopped muons up to around 50 MeV/c, now muons up to 60 MeV/c are consistently stopped. As a result of all of these changes, the stopping efficiency for muons that reach the target has increased from 43% to about 77%.

Unfortunately, it can also be seen from Fig. 8.7 that some of the high-momentum muons that do not stop in the target reach through to the detector. This means the background rate with the design shown here from beam backgrounds would be significantly larger. However, further optimisations of the target based on this concept might be able to remove these high-momentum muons using additional disks or adjusting the upstream collimators.

8.2.2 Signal Acceptance

Fig. 8.8 shows the detected momentum distribution of electrons. Of the signal events that occur, 48% are detected at the detector, which is the geometric acceptance with this design, and a factor of 2.2 times better than the result in chapter 6. The momentum cut however is less efficient now, accepting only 50% of events, compared to the previous 70%. Overall though, the signal acceptance with this target design is a factor 1.55 times better than the old design.

8.2.3 Summary and Future Improvements

By removing the beam blocker, adding more disks and increasing the disk radius along the beam axis, the muon stopping rate and geometric acceptance increase, although the momentum cut efficiency is decreased. The overall sensitivity can be expected to increase by a factor of 2.5.

Backgrounds from such a design need to be studied, in particular, high-energy electrons and muons in the beam which are no longer removed by the beam blocker, but should be lost in the target. In addition muon DIO might produce more background events with this design — given the poorer momentum resolution and greater signal acceptance — creating a significantly higher hit rate. Other backgrounds like those from antiprotons in the beam, cosmic rays and neutrons will not be changed by the different stopping target. Radiative pion capture will be increased slightly since the pion stopping rate will also likely increase.

In addition to background studies with this design there is further optimisation that can be performed. The most obvious area for improvement is to remove the material at the top part of the target disks, since in this region no muons stop here. In addition one can add more target disks to the lower part to try and catch even more of the high-momentum tail.

The target disk thickness is another parameter that could be studied. In fact, somewhere between these two options is the possibility to use wedge-shaped target disks, that put less material higher up in the beam. If one can control this so that the low-momentum muons stop as far downstream as possible, rather than in the first target disk, as currently occurs, then one can improve both the signal acceptance *and* the momentum resolution.

Chapter 9

Summary

“Phew”

— The author and his readers, upon reaching this point in the thesis

Ever since its discovery, the muon has been instrumental in the development of particle physics’ Standard Model. By studying the muon’s decay, the concept of Lepton Flavour and its conservation were introduced into this theory. And yet, nowadays, we have neutrino oscillations that tell us this concept is flawed. Moreover, a whole host of reasons—some theoretical, others experimental—suggest Charged Lepton Flavour Violation (CLFV) should occur at rates well above those that neutrino oscillations can produce.

Searches for CLFV are a particularly sensitive probe to physics Beyond-the-Standard Model. Of these, it is the channels involving muons that can achieve the greatest sensitivity, and an active field of low-energy, high-intensity neutrinoless-muon decay searches exists around the world. The decays of $\mu^+ \rightarrow e^+\gamma$, $\mu^+ \rightarrow e^+e^-e^+$, and $\mu^-N \rightarrow e^-N$ all have dedicated searches being prepared in Switzerland, the USA, and Japan. Taken together, they offer a highly complimentary set of measurements, able to constrain a large variety of models, and with strong discovery potential.

The COMET experiment will search for the last of these three processes. COherent Muon to Electron Transitions are the neutrinoless decay of a muon in the presence of the Coulomb potential of a nucleus, which is left unchanged by the reaction. The coherent nature of the process increases the sensitivity of the experiment to certain models compared to the other possible decay modes. In addition, the signal—a single

monoenergetic electron of 104.97 MeV/c and with a well defined lifetime—is well separated from most background sources. The current limit on μ - e conversion was set in 2006 by the SINDRUM-II experiment with a 90% C.L. of 7×10^{-13} .

COMET will improve on this in a staged approach, first running in Japanese Fiscal Year (JFY) 2018 and achieving a Single-Event Sensitivity (SES) of 3×10^{-15} —two orders of magnitude better than the current limit. Phase-II will then run at the start of the next decade and push the sensitivity a further two orders of magnitude to 3×10^{-17} . Such improvements are possible thanks to various novel techniques including the use of:

- a high power 8 GeV primary proton beam to maximise the pion yield and suppress antiproton production;
- a 5 T superconducting solenoidal field designed to maximise the capture of backwards-produced pions from the production target;
- a long muon beam transport section formed from bent solenoids, vertical dipole fields and collimators, which produce a high-purity muon beam;
- beam pulsing and a medium-Z target material, which gives a longer muon lifetime than previous experiments, and allows for timing information to suppress most beam-related backgrounds; and
- a large geometric acceptance detector, improved by magnetic mirroring at the stopping target in Phase-II, which has a low material budget and high granularity to ensure better than 200 keV/c resolution.

The novelty of these techniques is the main motivation for the staged approach, since it allows the COMET collaboration to refine its understanding of the experiment before fixing the Phase-II design.

If any observation is to be confirmed as signal, or to achieve the most stringent limits in the event of a null-observation, the background rate must be kept as low as possible. Given that around 10^{21} protons will be used in Phase-II, predicting that such a background rate is achievable requires very efficient and very accurate simulations be available. In addition, the reconstruction software must be able to achieve the necessary resolution and keep the high-energy tails to an absolute minimum. Both of these tasks have been integrated into a common software framework, which also includes calibration and analysis routines. The ICEDUST framework is the COMET experiment’s offline tool-set, and was based on the software of the near-detector for the T2K experiment,

ND280. Three major Monte-Carlo productions have been run using this software, which itself is now used collaboration-wide for various studies. All studies presented in this thesis were performed using the ICEDUST framework.

Given the effort and focus on Phase-I, Phase-II has received less attention, with the last update on performance given in the 2009 CDR. Using the now-mature ICEDUST software, revisiting the Phase-II design has been necessary to validate and improve the past estimates and help inform decisions for Phase-I.

To establish a new baseline for the COMET experiment's Phase-II, a comprehensive set of optimisations were performed. These covered the production target, muon beam transport, stopping target region, and electron spectrometer and detector. These optimisations were described in chapter 5, and summarised in Table 5.2.

Based on these optimisations, the signal acceptance due to the experiment's geometry, momentum resolution, and the signal timing were evaluated. From these acceptances, it was shown that 2.6×10^{-17} would be achievable in 1.57×10^7 seconds of beam. This is 1.3 times better than the Phase-II CDR suggested, as was summarised in Table 6.3.

Since it is equally important to understand the backgrounds that would occur with the updated design and improved simulation, the key set of backgrounds have also been evaluated. The total number of predicted background events is 0.662, dominated by cosmic ray events and antiproton production. Many of the estimates have significant uncertainties, although the quantification of this uncertainty is left for a future study. The uncertainties are partially due to statistical limitations, but also due to uncertainties in the various spectra and rates for secondary particle production. This includes the spectra of photons from Radiative Muon Capture and Radiative Pion Capture, and the distribution of antiprotons produced by protons at the production target. In addition, some uncertainties are due to these aspects of Phase-II not yet being well defined, such as the Cosmic Ray Veto (CRV) miss-rate, and the StrECAL resolution function.

This thesis, therefore, presents a baseline design and set of sensitivity and background estimates for Phase-II of the COMET experiment. It is written with the expectation that future iterations on the design will further reduce both the background rates and their uncertainties, whilst improving the signal efficiency. There are many aspects that could be studied further, or improvements that could be made to the work presented in this thesis, which have been listed at the end of the relevant chapters. A study of the stopping target region, after the main optimisation and background analysis, has already shown that the sensitivity could be further improved by a factor of about 2.5.

List of Acronyms

- BSM** Beyond the Standard Model
- CDC** Cylindrical Drift Chamber
- CDR** Conceptual Design Report
- CERN** Organisation européenne pour la recherche nucléaire
- CLFV** Charged Lepton Flavour Violation
- COM** centre-of-mass
- CRV** Cosmic Ray Veto
- CyDet** Cylindrical Detector
- DIO** decay-in-orbit
- JFY** Japanese Fiscal Year
- J-PARC** the Japanese Proton Accelerator Research Complex
- LFV** Lepton Flavour Violation
- LYSO** Cerium-doped Lutetium Yttrium Oxyorthosilicate
- MR** J-PARC Main Ring
- PID** Particle Identification
- POT** Proton-on-Target
- PMNS** Pontecorvo-Maki-Nakagawa-Sakata
- PSI** The Paul Scherrer Institute
- RCS** J-PARC Rapid Cycling Synchrotron
- RMC** Radiative Muon Capture
- RPC** Radiative Pion Capture
- SES** Single-Event Sensitivity
- SM** Standard Model

StrECAL Straw-tube tracker and Electromagnetic Calorimeter

QCD Quantum Chromodynamics

Bibliography

- [1] H. Yukawa. “On the Interaction of Elementary Particles I”. In: *Proc. Phys. Math. Soc. Jap.* 17 (1935). [Prog. Theor. Phys. Suppl. 1, 1(1935)], pp. 48–57. DOI: 10.1143/PTPS.1.1 (cit. on p. 23).
- [2] E. J. Williams and G. E. Roberts. “Evidence for Transformation of Mesotrons into Electrons [1]”. In: *Nature* 145.3664 (1940). cited By 13, pp. 102–103. URL: <https://www.scopus.com/inward/record.uri?eid=2-s2.0-0009448276&partnerID=40&md5=05a4a0769af62cb1f7e95752e57e8c6c> (cit. on pp. 23, 209).
- [3] Y. Nishina, M. Takeuchi, and T. Ichimiya. “On the Nature of Cosmic-Ray Particles”. In: *Phys. Rev.* 52 (11 1937), pp. 1198–1199. DOI: 10.1103/PhysRev.52.1198. URL: <http://link.aps.org/doi/10.1103/PhysRev.52.1198> (cit. on p. 23).
- [4] S. H. Neddermeyer and C. D. Anderson. “Note on the Nature of Cosmic Ray Particles”. In: *Phys. Rev.* 51 (1937), pp. 884–886. DOI: 10.1103/PhysRev.51.884 (cit. on p. 23).
- [5] J. C. Street and E. C. Stevenson. “New Evidence for the Existence of a Particle of Mass Intermediate Between the Proton and Electron”. In: *Phys. Rev.* 52 (9 1937), pp. 1003–1004. DOI: 10.1103/PhysRev.52.1003. URL: <http://link.aps.org/doi/10.1103/PhysRev.52.1003> (cit. on p. 23).
- [6] B. Pontecorvo. “Nuclear Capture of Mesons and the Meson Decay”. In: *Phys. Rev.* 72 (1947), p. 246. DOI: 10.1103/PhysRev.72.246 (cit. on p. 23).
- [7] E. P. Hincks and B. Pontecorvo. “Search for Gamma-Radiation in the 2.2-Microsecond Meson Decay Process”. In: *Phys. Rev.* 73 (3 1948), pp. 257–258. DOI: 10.1103/PhysRev.73.257. URL: <http://link.aps.org/doi/10.1103/PhysRev.73.257> (cit. on pp. 24, 209).
- [8] G. Danby et al. “Observation of High-Energy Neutrino Reactions and the Existence of Two Kinds of Neutrinos”. In: *Phys. Rev. Lett.* 9 (1 1962), pp. 36–44. DOI: 10.1103/PhysRevLett.9.36. URL: <http://link.aps.org/doi/10.1103/PhysRevLett.9.36> (cit. on p. 25).
- [9] R. Davis Jr., D. S. Harmer, and K. C. Hoffman. “Search for Neutrinos from the Sun”. In: *Phys. Rev. Lett.* 20 (1968), pp. 1205–1209. DOI: 10.1103/PhysRevLett.20.1205 (cit. on p. 26).

- [10] K. Abe et al. “The T2K Experiment”. In: *Nuclear Instruments and Methods in Physics Research Section A: Accelerators, Spectrometers, Detectors and Associated Equipment* 659.1 (2011), pp. 106–135. ISSN: 0168-9002. DOI: 10.1016/j.nima.2011.06.067. URL: <http://www.sciencedirect.com/science/article/pii/S0168900211011910> (cit. on pp. 26, 66, 209).
- [11] D. S. Ayres, P. Stamoulis, et al. *The NOvA Technical Design Report*. 2007. DOI: 10.2172/935497. URL: <http://www.osti.gov/scitech/servlets/purl/935497> (cit. on p. 26).
- [12] R. H. Bernstein and P. S. Cooper. “Charged Lepton Flavor Violation: An Experimenter’s Guide”. In: *Phys. Rept.* 532 (2013), pp. 27–64. DOI: 10.1016/j.physrep.2013.07.002. arXiv: 1307.5787 [hep-ex] (cit. on p. 29).
- [13] D. N. Dinh et al. “The $\mu - e$ Conversion in Nuclei, $\mu \rightarrow e\gamma$, $\mu \rightarrow 3e$ Decays and TeV Scale See-Saw Scenarios of Neutrino Mass Generation”. In: *JHEP* 08 (2012). [Erratum: JHEP09,023(2013)], p. 125. DOI: 10.1007/JHEP09(2013)023, 10.1007/JHEP08(2012)125. arXiv: 1205.4671 [hep-ph] (cit. on p. 30).
- [14] T. Blum et al. “The Muon (g-2) Theory Value: Present and Future”. In: (2013). arXiv: 1311.2198 [hep-ph] (cit. on p. 30).
- [15] H. N. Brown et al. “Precise Measurement of the Positive Muon Anomalous Magnetic Moment”. In: *Phys. Rev. Lett.* 86 (2001), pp. 2227–2231. DOI: 10.1103/PhysRevLett.86.2227. arXiv: hep-ex/0102017 [hep-ex] (cit. on p. 30).
- [16] A. Antognini et al. “Proton Structure from the Measurement of $2S - 2P$ Transition Frequencies of Muonic Hydrogen”. In: *Science* 339 (2013), pp. 417–420. DOI: 10.1126/science.1230016 (cit. on p. 30).
- [17] J. C. Martens and J. P. Ralston. “The Muon Experimental Anomalies Are Explained by a New Interaction Proportional to Charge”. In: (2016). arXiv: 1606.06209 [hep-ph] (cit. on p. 30).
- [18] S. G. Karshenboim, D. McKeen, and M. Pospelov. “Constraints on Muon-specific Dark Forces”. In: *Phys. Rev.* D90.7 (2014). [Addendum: Phys. Rev.D90,no.7,079905(2014)], p. 073004. DOI: 10.1103/PhysRevD.90.073004, 10.1103/PhysRevD.90.079905. arXiv: 1401.6154 [hep-ph] (cit. on p. 30).
- [19] J. Heeck. “Lepton Flavor Violation with Light Vector Bosons”. In: *Phys. Lett.* B758 (2016), pp. 101–105. DOI: 10.1016/j.physletb.2016.05.007. arXiv: 1602.03810 [hep-ph] (cit. on p. 30).
- [20] Roel Aaij et al. “Test of Lepton Universality Using $B^+ \rightarrow K^+\ell^+\ell^-$ Decays”. In: *Phys. Rev. Lett.* 113 (2014), p. 151601. DOI: 10.1103/PhysRevLett.113.151601. arXiv: 1406.6482 [hep-ex] (cit. on p. 30).
- [21] Roel Aaij et al. “Measurement of the Ratio of Branching Fractions $\mathcal{B}(\bar{B}^0 \rightarrow D^{*+}\tau^-\bar{\nu}_\tau)/\mathcal{B}(\bar{B}^0 \rightarrow D^{*+}\mu^-\bar{\nu}_\mu)$ ”. In: *Phys. Rev. Lett.* 115.11 (2015). [Addendum: Phys. Rev. Lett.115,no.15,159901(2015)], p. 111803. DOI: 10.1103/PhysRevLett.115.159901, 10.1103/PhysRevLett.115.111803. arXiv: 1506.08614 [hep-ex] (cit. on p. 30).

- [22] A. Abdesselam et al. “Measurement of the Branching Ratio of $\bar{B}^0 \rightarrow D^{*+}\tau^-\bar{\nu}_\tau$ Relative to $\bar{B}^0 \rightarrow D^{*+}\ell^-\bar{\nu}_\ell$ Decays with a Semileptonic Tagging Method”. In: (2016). arXiv: 1603.06711 [hep-ex] (cit. on p. 30).
- [23] J. P. Lees et al. “Evidence for an Excess of $\bar{B} \rightarrow D^{(*)}\tau^-\bar{\nu}_\tau$ Decays”. In: *Phys. Rev. Lett.* 109 (2012), p. 101802. DOI: 10.1103/PhysRevLett.109.101802. arXiv: 1205.5442 [hep-ex] (cit. on p. 30).
- [24] G. Lafferty. “Pentaquarks and Possible Anomalies at LHCb”. In: *Int. J. Mod. Phys. A* 31.20n21 (2016), p. 1630032. DOI: 10.1142/S0217751X16300325 (cit. on p. 30).
- [25] Vardan Khachatryan et al. “Search for Lepton-Flavour-Violating Decays of the Higgs Boson”. In: *Phys. Lett. B* 749 (2015), pp. 337–362. DOI: 10.1016/j.physletb.2015.07.053. arXiv: 1502.07400 [hep-ex] (cit. on p. 30).
- [26] CMS Collaboration. “Search for Lepton Flavour Violating Decays of the Higgs Boson in the mu-tau Final State at 13 TeV”. In: (2016) (cit. on p. 30).
- [27] S. L. Glashow, D. Guadagnoli, and K. Lane. “Lepton Flavor Violation in B Decays?” In: *Phys. Rev. Lett.* 114 (2015), p. 091801. DOI: 10.1103/PhysRevLett.114.091801. arXiv: 1411.0565 [hep-ph] (cit. on p. 30).
- [28] Deppisch, F. F. and Harz, J. and Hirsch, M. and Huang, W-C. and Päs, H. “Falsifying High-Scale Baryogenesis with Neutrinoless Double Beta Decay and Lepton Flavor Violation”. In: *Phys. Rev. D* 92.3 (2015), p. 036005. DOI: 10.1103/PhysRevD.92.036005. arXiv: 1503.04825 [hep-ph] (cit. on p. 30).
- [29] W. Altmannshofer et al. “Anatomy and Phenomenology of FCNC and CPV Effects in SUSY Theories”. In: *Nuclear Physics B* 830.1–2 (2010), pp. 17–94. ISSN: 0550-3213. DOI: 10.1016/j.nuclphysb.2009.12.019. arXiv: 0909.1333 [hep-ph]. URL: <http://www.sciencedirect.com/science/article/pii/S0550321309006683> (cit. on p. 31).
- [30] The COMET Collaboration. “Experimental Proposal for Phase-1 of the COMET Experiment at J-PARC”. In: (2012) (cit. on p. 32).
- [31] A. de Gouv  a. “(Charged) Lepton Flavor Violation”. In: *Nuclear Physics B - Proceedings Supplements* 188 (2009), pp. 303–308. ISSN: 0920-5632. DOI: 10.1016/j.nuclphysbps.2009.02.071. URL: <http://www.sciencedirect.com/science/article/pii/S0920563209001716> (cit. on p. 32).
- [32] F. J. Hartmann et al. “Measurement of the Muonic X-ray Cascade in Mg, Al, In, Ho, and Au”. In: *Z. Phys. A* 305 (1982), pp. 189–204. DOI: 10.1007/BF01417434 (cit. on pp. 36, 209).
- [33] D. F. Measday and T. J. Stocki. “Comparison of Muon Capture in Light and in Heavy Nuclei”. In: *AIP Conference Proceedings* 947.1 (2007). DOI: 10.1063/1.2813812 (cit. on p. 37).
- [34] A. Czarnecki, X. G. Tormo, and W. J. Marciano. “Muon Decay in Orbit: Spectrum of High-Energy Electrons”. In: *Phys. Rev. D* 84.1 (2011), p. 013006. DOI: 10.1103/PhysRevD.84.013006 (cit. on pp. 38, 81–82, 85, 138–139, 209).

- [35] K. S. Krane et al. “Energetic Charged Particle Spectrum FollowinG Mu-Capture by Nuclei”. In: *Phys. Rev.* C20 (1979), pp. 1873–1877. DOI: 10.1103/PhysRevC.20.1873 (cit. on pp. 40, 209).
- [36] S.E. Sobottka and E.L. Wills. “Energy Spectrum of Charged Particles Emitted Following Muon Capture in Si²⁸”. In: *Phys. Rev. Lett.* 20 (12 1968), pp. 596–598. DOI: 10.1103/PhysRevLett.20.596 (cit. on pp. 40, 209).
- [37] A. Wyttenbach et al. “Probabilities of Muon Induced Nuclear Reactions Involving Charged Particle Emission”. In: *Nucl. Phys.* A294 (1978), pp. 278–292. DOI: 10.1016/0375-9474(78)90218-X (cit. on pp. 40, 209).
- [38] AlCap Collaboration. *Study of Muon Capture For Muon to Electron Conversion Experiments*. http://muon.npl.washington.edu/exp/AlCap/R-13-03.1_BV44.pdf. Accessed: 28-October-2015 (cit. on pp. 40, 82–83, 217).
- [39] N. H. Tran. “A Study of Proton Emission Following Nuclear Muon Capture for the COMET Experiment”. PhD thesis. Osaka U., 2014 (cit. on pp. 40, 55).
- [40] W. H. Bertl et al. “A Search for Muon to Electron Conversion in Muonic Gold”. In: *Eur.Phys.J.* C47 (2006), pp. 337–346. DOI: 10.1140/epjc/s2006-02582-x (cit. on pp. 40–41, 43, 51, 145, 209, 215).
- [41] M. Hebert. “Searching for Muon to Electron Conversion Below the 10⁻¹⁶ Level”. In: *Nucl. Phys.* A721 (2003), pp. 461–464. DOI: 10.1016/S0375-9474(03)01099-6 (cit. on pp. 42, 209).
- [42] L. Bartoszek et al. “Mu2e Technical Design Report”. In: (2014). arXiv: 1501.05241 [physics.ins-det] (cit. on pp. 42, 135–136, 215).
- [43] V. S. Abadzhev et al. “MELC Experiment to Search for the mu⁻ A → e⁻ A Process”. In: (1992) (cit. on p. 41).
- [44] The COMET Collaboration. “COMET Phase-I: Technical Design Report”. In: (2016) (cit. on pp. 45, 54, 58, 62, 98, 136, 140, 142, 151–152, 172, 178–179).
- [45] The COMET Collaboration. “Conceptual Design Report for Experimental Search for Lepton Violating μ^-e^- Conversion at Sensitivity of 10⁻¹⁶ with a Slow-Extracted Bunched Proton Beam (COMET), J-PARC P21”. In: (2009) (cit. on pp. 45, 54, 58, 89, 91, 98, 106, 126, 134, 136, 140).
- [46] R. M. Djilkibaev. *MECO Muon Yield Simulation Using Experimental Data*. MECO Internal Note. 1994 (cit. on pp. 48, 209).
- [47] D. Armutliiski et al. “Hadron Spectra in Hadron - Nucleus Collisions”. In: (1991) (cit. on p. 48).
- [48] S. Agostinelli et al. “Geant4 – A Simulation Toolkit”. In: *NIM in PRS A* 506.3 (2003), pp. 250 –303. ISSN: 0168-9002. DOI: 10.1016/S0168-9002(03)01368-8 (cit. on pp. 52, 70, 80, 91, 221).
- [49] T. Suzuki, D. F. Measday, and J. P. Roalsvig. “Total Nuclear Capture Rates for Negative Muons”. In: *Phys. Rev. C* 35 (6 1987), pp. 2212–2224. DOI: 10.1103/PhysRevC.35.2212. URL: <http://link.aps.org/doi/10.1103/PhysRevC.35.2212> (cit. on pp. 53, 84).

- [50] The COMET Collaboration Software Group. *COMET Software Framework Requirements*. COMET Internal Document. 2013 (cit. on p. 65).
- [51] R. K. Kutschke. “art: A Framework for New, Small Experiments at Fermilab”. In: *Journal of Physics: Conference Series* 331.3 (2011), p. 032019. URL: <http://stacks.iop.org/1742-6596/331/i=3/a=032019> (cit. on p. 65).
- [52] G. Barrand et al. “GAUDI - A Software Architecture and Framework for Building HEP Data Processing Applications”. In: *Comput.Phys.Commun.* 140 (2001), pp. 45–55. DOI: 10.1016/S0010-4655(01)00254-5 (cit. on p. 66).
- [53] *Modular Analysis and Reconstruction for the Linear International Collider (MARLIN)*. URL: <http://ilcsoft.desy.de/marlin> (visited on 09/26/2016) (cit. on p. 66).
- [54] B. Krikler et al. *ICEDUST Conventions*. COMET Internal Document. 2013 (cit. on p. 67).
- [55] The COMET Collaboration Software Group. *Forking from ND280*. COMET Internal Document. 2013. URL: https://gitlab.in2p3.fr/comet/ICEDUST_documentation/tree/master/Forking_from_nd280 (cit. on p. 67).
- [56] C. Hoppner et al. “A Novel Generic Framework for Track Fitting in Complex Detector Systems”. In: *Nucl. Instrum. Meth.* A620 (2010), pp. 518–525. DOI: 10.1016/j.nima.2010.03.136. arXiv: arXiv:0911.1008 [hep-ex] (cit. on p. 68).
- [57] *CMT: Configuration Management Tool*. URL: <http://www.cmtsite.net> (visited on 09/26/2016) (cit. on p. 68).
- [58] *COMET Group on Gitlab*. URL: <https://gitlab.in2p3.fr/comet> (cit. on p. 68).
- [59] *CMake*. URL: <http://www.cmake.org> (visited on 09/26/2016) (cit. on p. 68).
- [60] *MIDAS (Maximum Integration Data Acquisition System)*. URL: <http://midas.psi.ch> (visited on 05/22/2015) (cit. on p. 68).
- [61] H. Iwase, K. Niita, and T. Nakamura. “Development of General-purpose Particle and Heavy Ion Transport Monte Carlo Code”. In: *Journal of Nuclear Science and Technology* 39.11 (2002), pp. 1142–1151. URL: <http://www.scopus.com/inward/record.url?eid=2-s2.0-0036873402&partnerID=40&md5=8e6977510036534b84b34653af66c0ff> (cit. on pp. 70, 80).
- [62] N. V. Mokhov. “The MARS Code System User’s Guide Version 13(95)”. In: (1995) (cit. on pp. 70, 80, 91).
- [63] A. Ferrari et al. “FLUKA: A Multi-Particle Transport Code (Program version 2005)”. In: (2005). CERN-2005-010, SLAC-R-773, INFN-TC-05-11 (cit. on pp. 70, 80).
- [64] R. Brun, A. Gheata, and M. Gheata. “The ROOT Geometry Package”. In: *Nucl. Instrum. Meth.* A502 (2003), pp. 676–680. DOI: 10.1016/S0168-9002(03)00541-2 (cit. on p. 75).

- [65] G4Beamline. “G4Beamline Homepage”. In: (2009). <http://www.muonsinternal.com/muons3/G4beamline>. URL: <http://www.muonsinternal.com/muons3/G4beamline> (cit. on p. 76).
- [66] Cobham Technical Services. URL: <http://operafea.com> (cit. on p. 77).
- [67] A. W. J. Edmonds. “An Estimate of the Hadron Production Uncertainty and a Measurement of the Rate of Proton Emission after Nuclear Muon Capture for the COMET Experiment”. PhD thesis. U. Coll. London, 2015. URL: <http://discovery.ucl.ac.uk/1468926> (cit. on pp. 79–80, 91).
- [68] M. G. Catanesi et al. “The HARP Detector at the CERN PS”. In: *Nucl. Instrum. Meth.* A571 (2007), pp. 527–561. DOI: [10.1016/j.nima.2006.08.132](https://doi.org/10.1016/j.nima.2006.08.132) (cit. on p. 79).
- [69] Y. Yang. “Comparison of Different Hadron Production Models with Available Data”. 2016 (cit. on p. 80).
- [70] B. E. Krikler. *Update on the AlCap Experiment*. 2015 (cit. on p. 82).
- [71] see: http://www.geant4.org/geant4/support/proc_mod_catalog/physics_lists/hadronic/QGSP_BERT.html, checked 21st June ‘16 (cit. on p. 81).
- [72] see: <http://www.geant4.org/geant4/support/physicsLists/referencePL/useCases.shtml> and http://www.geant4.org/geant4/support/proc_mod_catalog/physics_lists/useCases.shtml, checked 21st June ‘16 (cit. on p. 81).
- [73] D. H. Wright and M. H. Kelsey. “The Geant4 Bertini Cascade”. In: *Nucl. Instrum. Meth.* A804 (2015), pp. 175–188. DOI: [10.1016/j.nima.2015.09.058](https://doi.org/10.1016/j.nima.2015.09.058) (cit. on p. 83).
- [74] N. C. Mukhopadhyay. “Nuclear Muon Capture”. In: *Phys. Rept.* 30 (1977), pp. 1–144. DOI: [10.1016/0370-1573\(77\)90073-4](https://doi.org/10.1016/0370-1573(77)90073-4) (cit. on p. 84).
- [75] The COMET Collaboration. “COMET Phase-I: Technical Design Report”. In: (2015). URL: http://www-lib.kek.jp/cgi-bin/kiss_prepri.v8?KN=201524001&OF=8. (cit. on pp. 92, 215).
- [76] T. Siiskonen, J. Suhonen, and T. S. Kosmas. “New Limits for Lepton Flavor Violation from the E Conversion in Al-27”. In: *Phys. Rev.* C60 (1999), p. 062501. DOI: [10.1103/PhysRevC.60.062501](https://doi.org/10.1103/PhysRevC.60.062501) (cit. on p. 136).
- [77] A. Czarnecki et al. “Michel Decay Spectrum for a Muon Bound to a Nucleus”. In: *Phys. Rev.* D90.9 (2014), p. 093002. DOI: [10.1103/PhysRevD.90.093002](https://doi.org/10.1103/PhysRevD.90.093002). arXiv: [1406.3575 \[hep-ph\]](https://arxiv.org/abs/1406.3575) (cit. on pp. 138, 215).
- [78] K. A. Olive and Particle Data Group. “Review of Particle Physics”. In: *Chinese Physics C* 38.9 (2014), p. 090001. URL: <http://stacks.iop.org/1674-1137/38/i=9/a=090001> (cit. on pp. 140, 172).
- [79] G. Audi et al. “The 2003 NUBASE and Atomic Mass Evaluations The Nubase evaluation of nuclear and decay properties”. In: *Nuclear Physics A* 729.1 (2003), pp. 3 –128. ISSN: 0375-9474. DOI: [10.1016/j.nuclphysa.2003.11.001](https://doi.org/10.1016/j.nuclphysa.2003.11.001). URL: <http://www.sciencedirect.com/science/article/pii/S0375947403018074> (cit. on pp. 140, 143).

- [80] T. Gorringe and H. W. Fearing. “Induced Pseudoscalar Coupling of the Proton Weak Interaction”. In: *Rev. Mod. Phys.* 76 (1 2003), pp. 31–91. DOI: 10.1103/RevModPhys.76.31. URL: <http://link.aps.org/doi/10.1103/RevModPhys.76.31> (cit. on pp. 140–141, 144, 209).
- [81] M. Döbeli et al. “Radiative Muon Capture in Nuclei”. In: *Phys. Rev. C* 37 (4 1988), pp. 1633–1646. DOI: 10.1103/PhysRevC.37.1633. URL: <http://link.aps.org/doi/10.1103/PhysRevC.37.1633> (cit. on p. 140).
- [82] D. S. Armstrong et al. “Radiative Muon Capture on Al, Si, Ca, Mo, Sn, and Pb”. In: *Phys. Rev. C* 46 (3 1992), pp. 1094–1107. DOI: 10.1103/PhysRevC.46.1094. URL: <http://link.aps.org/doi/10.1103/PhysRevC.46.1094> (cit. on p. 140).
- [83] P. C. Bergbusch et al. “Radiative Muon Capture on O, Al, Si, Ti, Zr, and Ag”. In: *Phys. Rev. C* 59 (5 1999), pp. 2853–2864. DOI: 10.1103/PhysRevC.59.2853. URL: <http://link.aps.org/doi/10.1103/PhysRevC.59.2853> (cit. on p. 140).
- [84] Private Communication with Yuki Fujii, KEK (cit. on p. 141).
- [85] P. Christillin, M. Rosa-Clot, and S. Servadio. “Radiative Muon Capture in Medium-Heavy Nuclei”. In: *Nuclear Physics A* 345.2 (1980), pp. 331 –366. ISSN: 0375-9474. DOI: 10.1016/0375-9474(80)90344-9. URL: <http://www.sciencedirect.com/science/article/pii/0375947480903449> (cit. on p. 142).
- [86] P. Finlay et al. “High-Precision Half-Life Measurement for the Superallowed β^+ Emitter $^{26}\text{Al}^m$ ”. In: *Phys. Rev. Lett.* 106 (3 2011), p. 032501. DOI: 10.1103/PhysRevLett.106.032501. URL: <http://link.aps.org/doi/10.1103/PhysRevLett.106.032501> (cit. on p. 143).
- [87] M. N. Thompson et al. “The $\text{Al}^{27}(\bar{\nu}, n)\text{Al}^{26}\text{m}$ cross section”. In: *Nuclear Physics* 64.3 (1965), pp. 486 –496. ISSN: 0029-5582. DOI: 10.1016/0029-5582(65)90573-0. URL: <http://www.sciencedirect.com/science/article/pii/0029558265905730> (cit. on p. 144).
- [88] H. D. Engelhardt, C. W. Lewis, and H. Ullrich. “The Absorption of pi- at Rest on Complex Nuclei”. In: *Nucl. Phys.* A258 (1976), pp. 480–512. DOI: 10.1016/0375-9474(76)90486-3 (cit. on p. 145).
- [89] J. A. Bistirlich et al. “Photon Spectra from Radiative Absorption of Pions in Nuclei”. In: *Phys. Rev. C* 5 (1972), pp. 1867–1883. DOI: 10.1103/PhysRevC.5.1867 (cit. on pp. 146, 148, 209).
- [90] J. E. Amaro, A. M. Lallena, and J. Nieves. “Radiative Pion Capture in Nuclei: A Continuum Shell Model Approach”. In: *Nucl. Phys.* A623 (1997), pp. 529–547. DOI: 10.1016/S0375-9474(97)00187-5. arXiv: nucl-th/9704022 [nucl-th] (cit. on p. 146).
- [91] R. Brun and F. Rademakers. “ROOT - An Object Oriented Data Analysis Framework, Proceedings AIHENP’96 Workshop, Lausanne, Sep. 1996,” in: *Nuclear Instruments and Methods in Physics Research Section A* 389 (1997), pp. 81–86. URL: <http://root.cern.ch/> (cit. on p. 148).

- [92] T. Aramaki et al. “A Measurement of Atomic X-ray Yields in Exotic Atoms and Implications for an Antideuteron-based Dark Matter Search”. In: *Astroparticle Physics* 49 (2013), pp. 52–62. ISSN: 0927-6505. DOI: 10.1016/j.astropartphys.2013.08.003. URL: <http://www.sciencedirect.com/science/article/pii/S0927650513001242> (cit. on p. 150).
- [93] C. Y. Wong et al. “Ambiguity in Anti-proton Nucleus Potentials from Anti-protonic Atom Data”. In: *Phys. Rev.* C29 (1984), pp. 574–580. DOI: 10.1103/PhysRevC.29.574 (cit. on p. 150).
- [94] I. N. Mishustin et al. “Antibaryons Bound in Nuclei”. In: *Phys. Rev.* C71 (2005), p. 035201. DOI: 10.1103/PhysRevC.71.035201. arXiv: nucl-th/0404026 [nucl-th] (cit. on pp. 150–151).
- [95] R. M. Djilkibaev. *Antiproton Yields Simulation*. MECO Internal Note. 1995 (cit. on pp. 151–152, 209).
- [96] S. V. Boyarinov et al. “Yields of p, anti-p, pi+-, and K+- Emitted at an Angle of 97-degrees in the Laboratory System from Nuclei Irradiated by 10.14-GeV Protons”. In: *Phys. Atom. Nucl.* 57 (1994). [Yad. Fiz. 57, 1452 (1994)], pp. 1379–1388 (cit. on pp. 151, 153, 157–158).
- [97] Yu. T. Kiselev et al. “Probing of Compact Baryonic Configurations in Nuclei in $A(p, \bar{p})X$ Reactions and Antiproton Formation Length in Nuclear Matter”. In: *Phys. Rev.* C85 (2012), p. 054904. DOI: 10.1103/PhysRevC.85.054904. arXiv: 1204.2669 [nucl-ex] (cit. on pp. 151, 153, 158).
- [98] P. Danielewicz. “Multiparticle Interactions in Backward Proton Production, Sub-threshold Antiproton Production, and Inclusive Electron Scattering from Nuclei”. In: *Phys. Rev. C* 42 (4 1990), pp. 1564–1576. DOI: 10.1103/PhysRevC.42.1564. URL: <http://link.aps.org/doi/10.1103/PhysRevC.42.1564> (cit. on p. 154).
- [99] Krikler. B. *Cosmic Ray Simulation in ICEDUST*. Presented at CM18. 2015. URL: <https://kds.kek.jp/indico/event/20112> (cit. on p. 172).
- [100] Drutskoy. A. *Update of CRV Geometry in ICEDUST*. Presented at CM20. 2016. URL: <https://kds.kek.jp/indico/event/21699> (cit. on p. 172).
- [101] M. A. George. “Calibrating the Electromagnetic Calorimeter of T2K”. PhD thesis. Queen Mary, U. of London (main), 2010. URL: <http://www.t2k.org/docs/thesis/039> (cit. on p. 173).
- [102] D. Heck et al. “Report FZKA 6019.” In: <http://wwwik.fzk.de/corsika/physicsdescription/corsikaphys.html> (1998) (cit. on p. 173).
- [103] J. D. Jackson. *Classical Electrodynamics Third Edition*. Third. Wiley, 1998. ISBN: 047130932X (cit. on p. 185).
- [104] B. E. Krikler. *An Overview of the COMET Experiment and Its Recent Progress*. 2015 (cit. on p. 215).
- [105] R. P. Litchfield. “Status of the AlCap Experiment”. In: *PoS NUFACt2014* (2015), p. 095. arXiv: 1501.04880 [physics.ins-det] (cit. on p. 217).

- [106] T. Adye. “Unfolding Algorithms and Tests Using RooUnfold”. In: *Proceedings of the PHYSTAT 2011 Workshop, CERN, Geneva, Switzerland, January 2011, CERN-2011-006, pp 313-318.* 2011, pp. 313–318. arXiv: 1105.1160 [physics.data-an]. URL: <http://inspirehep.net/record/898599/files/arXiv:1105.1160.pdf> (cit. on p. 221).
- [107] E. Hungerford. *Comments on Proton Emission After Muon Capture.* MECO Internal Note. 1994 (cit. on p. 221).
- [108] A. Blondel et al. “Research Proposal for an Experiment to Search for the Decay $\mu \rightarrow eee$ ”. In: (2013). arXiv: 1301.6113 [physics.ins-det] (cit. on p. 222).

Appendix A

Figure Permissions

| Figure or Table | Source of Work | Copyright Holder | Date of Request | Permission |
|-----------------|----------------|----------------------|-----------------|---|
| Fig. 1.1 | Ref. [2] | ©Nature | 16.2.2017 | Granted via www.copyright.com |
| Fig. 1.2 | Ref. [7] | ©APS | 10.2.2017 | Granted via www.copyright.com |
| Fig. 2.2 | Ref. [32] | ©Springer | 10.2.2017 | Granted via www.copyright.com |
| Fig. 2.3 | Ref. [34] | ©APS | 10.2.2017 | Granted via www.copyright.com |
| Fig. 2.4a | Ref. [35] | ©APS | 10.2.2017 | Granted via www.copyright.com |
| Fig. 2.4b | Ref. [36] | ©APS | 10.2.2017 | Granted via www.copyright.com |
| Fig. 2.4c | Ref. [37] | ©Elsevier | 10.2.2017 | Granted via www.copyright.com |
| Fig. 2.5 | Ref. [40] | ©Springer | 10.2.2017 | Granted via www.copyright.com |
| Fig. 2.6 | Ref. [41] | — | 16.2.2017 | Granted via email from Snowmass2001 organisers (customercare@aps.org) |
| Fig. 3.1 | Ref. [46] | <i>Internal note</i> | 16.2.2017 | Permission granted by author (R. Djilkibaev) by email. |
| Fig. 4.1 | Ref. [10] | ©Elsevier | 12.2.2017 | Granted via www.copyright.com |
| Table 7.2 | Ref. [80] | ©APS | 12.2.2017 | Granted via www.copyright.com |
| Fig. 7.4 | Ref. [89] | ©APS | 12.2.2017 | Granted via www.copyright.com |
| Fig. 7.9 | Ref. [95] | <i>Internal note</i> | 16.2.2017 | Permission granted by author (R. Djilkibaev) by email. |

Appendix B

Kinematic End-point for Antiproton Production

In section 7.4 the background rate due to antiproton production from the proton beam was estimated. To build a complete picture from the available experimental data, the maximum energy for antiprotons produced at a given angle was included in the fit to the data. This appendix provides the derivation for this end-point, which although is a straightforward calculation of relativistic mechanics, is included to help any future studies of antiproton backgrounds.

The end-point is achieved when the incoming proton, and the outgoing nucleus and created proton recoil as a single object against the produced antiproton. In this case, maximum kinetic energy is transferred to the antiproton. This is treated as an increase in the final nucleus' mass equivalent to two proton masses.

In the following derivation, masses, energy and 3-momenta will be denominated by M , E and \mathbf{p} , while ρ will be used for 4-momenta. The subscripts N , p , N' , and \bar{p} will denote respectively the incoming nucleus, incoming proton, outgoing nucleus (with the additional two protons), and outgoing antiproton. Superscripts of L and C indicate whether or not the variable refers to the Lab frame or the centre-of-mass (COM) frame, respectively. Finally, θ is the angle between the momenta of the incoming proton and outgoing antiproton.

B.1 Derivation

In the lab frame, the proton and nucleus 4-momenta are given by:

$$\rho_p^L = (E_p^L, \mathbf{p}_p^L) \quad (\text{B.1})$$

$$\rho_N^L = (E_N^L, \mathbf{p}_N^L) = (M_N, \mathbf{0}) \quad (\text{B.2})$$

To boost to the COM frame, we need only consider the one dimensional Lorentz transform, so the total 4-momentum in the lab frame is related to the COM frame:

$$\begin{pmatrix} E_p^C + E_N^C \\ 0 \end{pmatrix} = \gamma \begin{pmatrix} (E_p^L + M_N) - \beta |\mathbf{p}_p^L| \\ -\beta(E_p + M_N) + |\mathbf{p}_p^L| \end{pmatrix}, \quad (\text{B.3})$$

where γ and β are the boost factor and velocity of the COM frame with respect to the lab frame, related by the equation:

$$\gamma = \frac{1}{\sqrt{1 - \beta^2}} \quad (\text{B.4})$$

From just the result for 3-momentum, one finds that:

$$\beta = \frac{|\mathbf{p}_p^L|}{E_p^L + M_N}, \quad (\text{B.5})$$

which allows the proton's energy in the COM frame to be calculated (and similarly for the nucleus, although this is not needed):

$$E_p^C = \gamma(E_p^L - \beta |\mathbf{p}_p^L|). \quad (\text{B.6})$$

Conservation of 4-momentum requires that:

$$\rho_N + \rho_p = \rho_{N'} + \rho_{\bar{p}}, \quad (\text{B.7})$$

so that taking the square of both sides results in:

$$M_N^2 + M_p^2 + 2(E_p E_N - \mathbf{p}_p \cdot \mathbf{p}_N) = M_{N'}^2 + M_p^2 + 2(E_{\bar{p}} E_{N'} - \mathbf{p}_{\bar{p}} \cdot \mathbf{p}_{N'}). \quad (\text{B.8})$$

In the COM frame the momenta are related by: $\mathbf{p}_p = -\mathbf{p}_N$, and $\mathbf{p}_{\bar{p}} = -\mathbf{p}_{N'}$ (but \mathbf{p}_p is not necessarily parallel to $\mathbf{p}_{\bar{p}}$). In addition, the energy of a particle is related to its momentum and mass by the equation: $E^2 = \mathbf{p}^2 + M^2$. By use of these relations, the above equation reduces to:

$$M_N^2 + 2(E_N^C E_p^C + |\mathbf{p}_p^C|^2) = M_{N'}^2 + 2(E_{N'}^C E_{\bar{p}}^C + |\mathbf{p}_{\bar{p}}^C|^2) \quad (\text{B.9})$$

$$M_N^2 + 2(E_N^C E_p^C + (E_p^C)^2 - M_p^2) = M_{N'}^2 + 2(E_{N'}^C E_{\bar{p}}^C + (E_{\bar{p}}^C)^2 - M_p^2) \quad (\text{B.10})$$

$$M_N^2 + 2E_p^C (E_N^C + E_p^C) = M_{N'}^2 + 2E_{\bar{p}}^C (E_{N'}^C + E_{\bar{p}}^C) \quad (\text{B.11})$$

Now conservation of energy tells us that $E_N + E_p = E_{N'} + E_{\bar{p}}$, and in fact, since we are in the lab frame, this is equal to \sqrt{s} , one of the Lorentz invariant Mandelstram variables. Using this, and the fact that $M_{N'} = M_N + \Delta M = M_N + 2M_p$, reduces the last equation to:

$$E_{\bar{p}}^C = E_p^C - \frac{M_{N'}^2 - M_N^2}{2\sqrt{s}} \quad (\text{B.12})$$

$$= E_p^C - \frac{2M_N \Delta M + \Delta M^2}{2\sqrt{s}} \quad (\text{B.13})$$

$$= E_p^C - \frac{2M_p(M_N + M_p)}{\sqrt{s}} \quad (\text{B.14})$$

Identifying the final term as ΔE , means the 3-momentum of the outgoing antiproton in the COM frame can be written as:

$$(\mathbf{p}_{\bar{p}}^C)^2 = (E_{\bar{p}}^C)^2 - M_p^2 \quad (\text{B.15})$$

$$= (E_p^C)^2 - 2E_p^C \Delta E + \Delta E^2 \quad (\text{B.16})$$

Finally, having found the outgoing 4-momentum in the COM frame, it only remains to boost back to the lab frame. The one subtlety here is that while boosting into the COM frame we did not have to think of the transverse momentum since the COM and all proton and nucleus motions are all parallel, the emitted antiproton can be produced at any angle, with respect to the incoming proton in the COM frame. We must, therefore, use the two-dimensional transform, and so find that the maximum lab frame energy and

momentum of the antiproton is given by:

$$\begin{pmatrix} E_{\bar{p}}^L \\ p_{\bar{p},x}^L \\ p_{\bar{p},z}^L \end{pmatrix} = \gamma \begin{pmatrix} E_{\bar{p}}^C + \beta p_{\bar{p},z}^L \\ p_{\bar{p},x}^L / \gamma \\ p_{\bar{p},z}^L + \beta E_{\bar{p}}^C \end{pmatrix} \quad (\text{B.17})$$

where β has the same value as before, although we have flipped the signs in the boost, and $p_{\bar{p},x}^L$ and $p_{\bar{p},z}^L$ are given by $|\mathbf{p}_{\bar{p}}^L| \sin(\theta_C)$ and $|\mathbf{p}_{\bar{p}}^L| \cos(\theta_C)$, respectively.

Thus we have found the outgoing 4-momentum of the antiproton in the lab frame as a parametric set of equations dependent on the angle between the incoming proton and outgoing antiproton in the COM frame. The relation:

$$\tan(\theta_L) = \frac{p_{\bar{p},x}^L}{p_{\bar{p},z}^L}, \quad (\text{B.18})$$

can be used to produce an additional parametric equation for the antiproton's angle of emission in the lab frame as function of its value in the COM frame.

The full set of relevant variables and factors is summarized below, since the fully expanded result is extremely long and harder to implement into any computer code.

$$\begin{aligned} \gamma &= \frac{1}{\sqrt{1 - \beta^2}}, & \beta &= \frac{|\mathbf{p}_p^L|}{E_p^L + M_N}, & E_p^C &= \gamma(E_p^L - \beta p_p^L), \\ \Delta E &= \frac{2M_p(M_p + M_N)}{\sqrt{s}}, & s &= M_p^2 + M_N^2 + 2M_N E_p^L, \\ E_{\bar{p}}^C &= E_p^C - \Delta E, & |\mathbf{p}_{\bar{p}}^C|^2 &= |\mathbf{p}_p^C|^2 - 2E_p^C \Delta E + (\Delta E)^2, \\ \begin{pmatrix} E_{\bar{p}}^L \\ p_{\bar{p},x}^L \\ p_{\bar{p},z}^L \end{pmatrix} &= \gamma \begin{pmatrix} E_{\bar{p}}^C + \beta |\mathbf{p}_{\bar{p}}^C| \cos(\theta_C) \\ (1/\gamma) |\mathbf{p}_{\bar{p}}^C| \sin(\theta_C) \\ |\mathbf{p}_{\bar{p}}^C| \cos(\theta_C) + \beta E_{\bar{p}}^C \end{pmatrix}, & \tan(\theta_L) &= \frac{p_{\bar{p},x}^C}{p_{\bar{p},z}^C}, \end{aligned}$$

Appendix C

Summary of the AlCap Experiment

The following was originally submitted for the proceedings of NuFact ‘15 and has been published online from the meeting’s home page at: <https://indico.fnal.gov/internalPage.py?pageId=2&confId=8903>. Although peer reviewed, it has not appeared in print, and so I reproduce it here in its entirety.

Abstract

The AlCap experiment studies the emission products following muon capture on an aluminium nucleus. Such a measurement is important in the context of the up-coming muon-to-electron conversion experiments, COMET and Mu2e, which will both use an aluminium stopping target. Despite this, and the potential nuclear and astrophysical implications, the existing range of measurements is incomplete, with the majority of measurements on proton and neutron emissions already some 40 years old.

AlCap first ran in 2013, and will have run twice more by the end of 2015. It is a joint effort by the Mu2e and COMET collaborations.

C.1 Introduction

Both the COMET experiment at J-PARC [75, 104] and the Mu2e experiment at Fermilab [42], aim to improve the search for muon-to-electron conversion by around four orders of magnitude compared to the current limit, set by the SINDRUM-II experiment [40]. Such an increased sensitivity is achieved by the use of a pulsed muon beam and a relatively light stopping target, made of aluminium. Significant background suppression can be achieved since the lifetime of the muon in aluminium is 864 ns, compared to the typical beam flash time of 200 ns. However, this poses an issue for the next generation of μ - e conversion experiments since the stopping of negative muons in aluminium has not been well studied.

In particular, whilst the decay of a muon bound to a nucleus can be relatively well theoretically modelled [77], the nuclear capture of the muon is much harder due to the complexity of the nuclear environment. Captured muons cause emission of various particles, through both prompt and nuclear relaxation mechanisms, which in general can

be written as:

$$\mu + N(A, Z) \rightarrow \nu_\mu + N^*(A, Z - 1) \quad (\text{C.1})$$

$$N^*(A, Z - 1) \rightarrow N(A', Z') + X \quad (\text{C.2})$$

where X is any combination of additional final state particles, such as protons, neutrons, photons, deuterons, alpha particles and so on.

Although producing a 105 MeV electron following muon capture is highly unlikely, the emission of these final state particles causes several additional difficulties in the design and operation of COMET and Mu2e for several reasons. Firstly, neutral particles such as neutrons and photons can cause difficulties for any electronics systems near the detectors. Emitted neutrons can also create fake vetoes in the active Cosmic Ray Veto systems which are based on scintillating bars that a neutron recoil could trigger. If the neutron flux were too high, shielding of the veto system and more radiation-hard electronics might be required. On the other hand, the charged particle emissions will increase the detector occupancy. Since low energy protons are strongly ionising they can blind large parts of the detector to any signal electron. Controlling these particles would require some additional absorbing material between the target and the detector, the downside of this being that any signal electron will also be affected essentially reducing the resolution of the detector. It is important then that the rates and energies of the emitted particles be well understood in order to optimise the designs of the upcoming μ - e conversion experiments.

As a joint collaboration between COMET and Mu2e, AlCap therefore aims to measure:

- the emitted charged particle rates and spectra down to 2.5 MeV with a 5-10 % resolution,
- X-ray and gamma spectra and the relative intensities in the various peaks,
- the neutron spectrum and rate from 1 to 10 MeV.

Work towards these goals has been split between three separate runs, each taking place at the Paul Scherrer Institute (PSI), near Zurich. The first run, Run 2013, took place during the winter of 2013, focussed on charged particle emission but also ran some preliminary neutron measurements. Two runs will have taken place during 2015 with the first, Run 2015a, held in June and focussed primarily on neutral particle emissions (photons and neutrons). Finally, Run 2015b will run during November 2015 and repeat and improve the charged particle measurement from Run 2013.

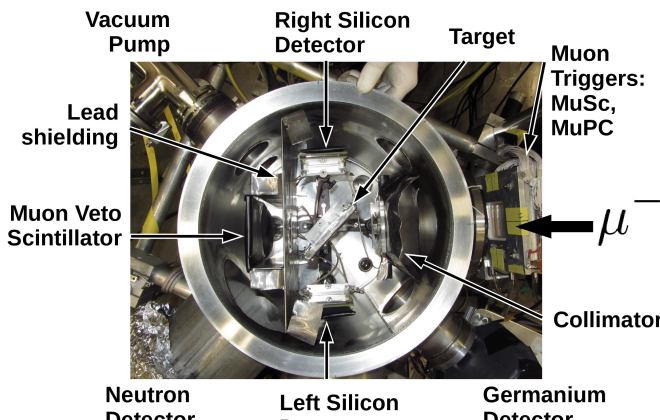
C.2 Run 2013: Charged Particles

The 2013 run dealt primarily with measuring the charged particles emitted following muon capture, and took place from mid-November to the end of the year using the piE1 beamline of the Swiss Muon Source ($S\mu S$) at the Paul Scherrer Institute (PSI). A brief description is provided here whilst more information is provided in [38, 105].

The primary aim for this run was to obtain the emission rates and distributions for low energy protons, deuterons, tritons and alphas particles. To reduce the amount of scattering of the charged capture products both the aluminium target and detector systems were placed in a vacuum and the target size kept to a thickness of less than 1 mm. At such a thickness a beam momentum of around 30 MeV was expected to be roughly optimal to stop all muons in the target. At this energy the muon rate in the piE1 beam was roughly 3-6 kHz, running in a continuous mode.

Fig. C.1 shows the experimental set-up for this run. The muon beam reaches the target by passing through several beam monitors (namely, a scintillator paddle, muSc, and a scintillator paddle with a hole centred on the beam axis, muScA, which together with the muSc defined an on-axis muon entering the chamber, and finally a proportional wire chamber which gave a measurement of the beam profile before the chamber), entering the vacuum chamber through a light-sealed mylar window and passing a lead collimator.

The stopping target was mounted at 45° to the beam to reduce the amount of target material the charged daughter products would have to pass through before reaching the



(a) Setup

| Dataset | Target | Run Time (hrs.) |
|---------------|-----------------------|-----------------|
| Al50 | $50 \mu\text{m}$ Al. | 50 |
| Al100 | $100 \mu\text{m}$ Al. | 17 |
| Si16 | $65 \mu\text{m}$ Si. | 8 |
| SiR2 (Active) | 1.5 mm Si. | 8 |

(b) R13 Datasets

Figure C.1: Experimental set-up and acquired datasets from Run 2013. See text for a full description of the experiment set-up.

two charged particle detectors, which sat to the left and right at 90° with respect to the beam direction at the target position. Behind the stopping target sat another scintillator paddle to veto muons that did not stop in the target. All the remaining surfaces that faced the beam were covered in lead so that secondaries from capture of scattered muons could be removed by a prompt-time cut, since the muon lifetime in lead is only 75 ns.

Each of the two charged particle telescopes consisted of a pair of silicon detectors and a punch-through scintillator paddle. The first of the silicon detectors was only about $65\ \mu\text{m}$ in thickness and divided into 4 quadrants, whilst the second was a single silicon detector of thickness of 1.5 mm. Information on both the particle's identity and energy can be obtained using a coincidence between the thick and thin silicon detectors. Although a vacuum pressure of around $10^{-2}\ \text{Pa}$ would have been sufficient to reduce multiple scattering, to prevent arcing between the quadrants of the thin silicon detector the vacuum was maintained at below $10^{-4}\ \text{Pa}$.

Finally, outside of the vacuum chamber were placed a germanium detector to measure the X-ray and gamma spectrum as well as liquid scintillator neutron detectors.

The 64 or so detector channels were digitised on a mix of custom-built Flash ADCs and CAEN digitizers. All of the silicon detector outputs were passed through both fast and slow analogue filters to provide better time and energy resolution of the individual pulses. Each channel was then operated in a self-trigger mode within a DAQ-active gate that was initiated by the global DAQ system. The DAQ-active gate lasted 112 ms and typically had a dead-time between gates of about 10 ms.

C.2.1 Datasets

Several different datasets were obtained with both silicon and aluminium targets. Fig. C.1b gives a summary of the different datasets obtained in the 2013 run.

Runs dedicated to calibration, background measurements and other cross checks were also performed. These included the use of one of the silicon packages as an active target, which was used both to tune the beam and as a means to cross-check aspects of the analysis.

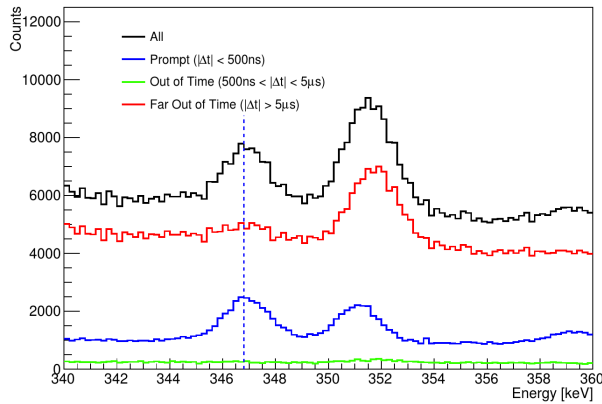


Figure C.2: A close up of the $2p-1s$ transition line at around 347 keV used for the normalisation of stopped muons for the Al100 dataset. The blue solid line shows x-rays coming within 500 ns of muon entering the chamber as determined by the muSc entrance scintillator that was fitted with two Gaussians and a linear background. The second peak at around 352 keV is believed to be a combination of X-rays coming from the radioactive decay chain of lead and thallium.

C.2.2 Preliminary Analysis

Stopped Muon Normalisation

When negative muons come to a stop in a material they become bound to the nucleus. An electromagnetic cascade down to the lowest energy atomic orbital takes place over very short time scales, with the emission of characteristic X-rays corresponding to the transition energy between the muonic atom energy levels. To determine the number of stopped muons during the run, the X-rays from this cascade were observed using the external germanium detector. In particular, the $2p-1s$ line was used, since it has the highest relative intensity and is well separated from any nearby background peaks. A prompt timing cut was made between the germanium detector and the incoming muon scintillator paddle (muSc) to remove accidental backgrounds. The same muon pile-up protection cut was also applied as described below for the charged particle analysis. Fig. C.2 shows the X-ray spectrum from the Al100 dataset around the $2p-1s$ peak. The peak was fitted with a Gaussian plus a linear background and the area under the peak extracted. The detector's acceptance was found using an Eu-152 source and cross checked with a Monte Carlo simulation, and the efficiency at a given energy was obtained by an empirical fit to calibration data. The observed value was scaled by this to give the total number of muons stopped during a run.

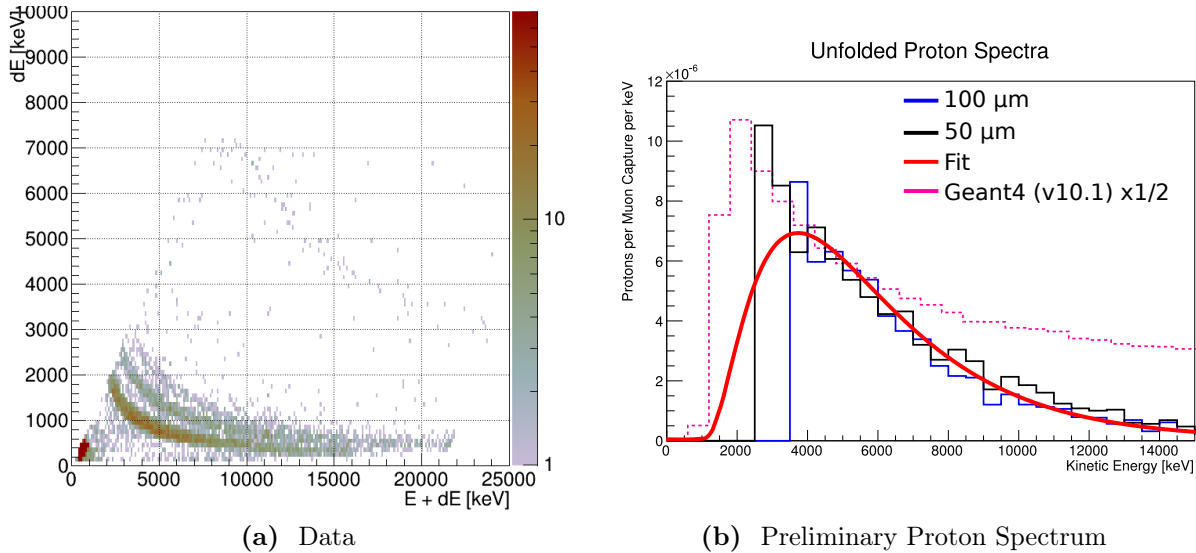


Figure C.3: Charged particle analysis and preliminary results. (a) Bands corresponding to the observation of different particle species at one of the silicon detectors. (b) The preliminary unfolded proton emission spectra from the two aluminium datasets of R2013. Only the range between 3.5 and 10 MeV is considered reliable, since outside of this range the unfolding of the different datasets does not seem stable. The uncertainty on each bin is still under analysis, so no error bars are shown here. Additionally the spectrum produced by standard Geant4 (v10.1) is shown, scaled by a factor 1/2.

Charged Particle Measurement status

For particles stopping in the thick silicon, a coincident hit in the thin allowed for a measurement of both the particle's dE/dx and its total energy. These two values taken together provide for particle identification as shown for simulated data in Fig. C.1a. Variation in the dE/dx due to different angles of incidence was small, given the distance from the target to the detector and was estimated to be around 10%, far less than the separation of the different bands. This set-up allowed for the distinction of protons, deuterons, tritons and alpha particles, over a range of energies from about 2 to 10 MeV. So far only the proton band has been analysed although it is thought that sufficient data was taken to estimate an integrated rate for at least deuteron emission.

The selection criteria for detecting a charged particle used the following cuts: coincidental hits in both thin and thick silicon (to remove accidental backgrounds and noise pulses); coincidence with a Muon-like hit in the muSc (to ensure the particles came from a muon a hit in the muSc must have occurred with 10 μ s and have an amplitude corresponding to the typical energy deposited by a muon); no other muon hit in muSc

within $10 \mu\text{s}$ (removes the mis-identification of protons coming from close-arriving muons, which would complicate the normalisation and timing distributions); time since muSc hit must be greater than 100 ns (removes scattered muons and protons coming from capture in the lead shielding or collimator).

Once a hit is identified as coming from a charged particle emitted after capture in the stopping target, particle identity cuts are applied based on either a geometrical cut on the dE/dx plot or using a probability that the event was from the desired particle, based on a Monte Carlo simulation. Fig. C.3a shows the raw spectrum obtained after applying the above cuts for one of the silicon telescopes.

Preliminary results

Once the raw spectrum has been acquired, to obtain the ‘true’ spectrum following muon capture and account for scattering in the target and the detector’s acceptance, a Bayesian unfolding procedure is applied using the RooUnfold tool-kit [106]. The total response matrix for the combined target-detector system was found using a Monte Carlo simulation based on Geant4 [48]. For protons below around 2.5 MeV the acceptance drops to zero since below this energy they are unable to penetrate the target and thin silicon detector. Above around 4 MeV the response becomes roughly linear.

This procedure has been successfully applied to the aluminium datasets, however, for the active target runs using the silicon detector as the target, the statistics have been too low to perform a successful unfolding and so analysis of those datasets cannot continue. This is unfortunate as it could in principal provide a good cross check of the unfolding process since more information on the distribution at the target is known. This is an area that future runs will address.

Fig. C.3b shows the unfolded spectra where it can be seen that approximate agreement is found from around 3 to 10 MeV between the different $50 \mu\text{m}$ and $100 \mu\text{m}$ aluminium datasets. This region has been fitted with the same function as previously used by the COMET and Mu2e collaborations [107], which is empirically motivated and given by the equation:

$$f(x) = \left(1 - \frac{T_{\text{th}}}{x}\right)^{\alpha} \exp\left(-\frac{x}{T_0}\right), \quad (\text{C.3})$$

where T_{th} is a threshold energy, expected to relate to the Coulomb barrier and Fermi energy of nucleons in the intermediate nucleus, α is a shape parameter that controls the form of the spectrum around the emission threshold, and T_0 should be related to the thermal energy associated with the nucleons in the free-Fermi gas nuclear model.

Based on this fit, the total proton emission rate per muon capture is estimated to be around $3.3 \pm 0.4\%$ although it must be stressed that this is a preliminary value with the final analysis and error assessment still ongoing. At this stage, the leading systematic errors are due to the unfolding process, misalignment in the geometry, uncertainties in the muon stopping distribution and beam profile at the target, and energy calibration of the silicon detectors. Each of these issues will be addressed directly by improvements in the upcoming Run 2015b.

The impacts of this measurement are already being felt for both COMET and Mu2e. Mu2e is re-optimising their proton absorber whilst for COMET Phase-I it has been removed. Furthermore, it is clear that the built-in modelling of muon capture in Geant4 needs improving, since it produces a much harder spectrum with a rate about 7 times to large, as shown by the overlay of the preliminary fitted AlCap spectrum to that from Geant4 in Fig. C.3b.

C.3 Run 2015a: Neutral Particles

Although the 2013 run did include neutron and X-ray detectors, the need for a vacuum chamber and thin target complicated the neutral particle measurement and reduced the final statistics. To improve the situation a two week run dedicated to measuring the neutral particle products without the vacuum chamber and with a thicker stopping target took place in June 2015. This used the piE5 beamline also at PSI, and future home to the Mu3e experiment [108]. With the thicker stopping target, a higher muon beam momentum of about 36 MeV/c could be used which increased the muon rate to about 10 kHz.

C.3.1 Setup

Unlike the charged particle run, no vacuum chamber was needed for the neutral particle measurement. As such, detectors were placed facing a central stopping target directly

which improved acceptance and reduced backgrounds from scattered muons. Neutrons from the muon stopping target were observed by two liquid scintillator neutron detectors, whilst a germanium detector measured the muonic X-rays and gammas. A LYSO array was also included in the set-up to monitor very hard gamma rays from the capture process.

As well as the removal of the vacuum chamber and the thicker target, several other improvements from the 2013 run were included. In particular, better ADCs increased the DAQ stability and a continuous input test pulse has improved the time calibration of signals. Furthermore, the neutron detectors had been calibrated before the run at the Triangle Universities Nuclear Laboratory (TUNL), in North Carolina, USA.

The data taken from Run 2015a is summarised in Table C.1. As well as measuring neutrons and photons from muon capture on aluminium, some time was dedicated to other targets. In particular, titanium, which is an alternative stopping target material for COMET and Mu2e, was studied as well as lead and water to understand potential backgrounds for this measurement.

C.3.2 Activation Study

The current baseline for COMET and Mu2e uses the prompt X-ray spectrum from the electromagnetic cascade of the stopped muon to estimate the number of stopped muons. However, one alternative idea is to look at X-rays coming from decays of the radioactive magnesium isotope Mg-27, left from muon capture. This might suffer fewer backgrounds than the prompt X-ray spectrum and so might be more reliable. To confirm this method a target was activated and monitored with a second germanium detector away from the beam area.

Table C.1: Datasets acquired during R2015a

| Target | Target Thickness (mm) | Approximate Exposure (hours) |
|-----------|--------------------------|---------------------------------|
| Aluminium | 2 | 42 |
| Titanium | 1.1 | 24 |
| Lead | 1.5 | 9 |
| Water | ~ 6 (not uniform) | 4.5 |
| Empty | - | 3 |

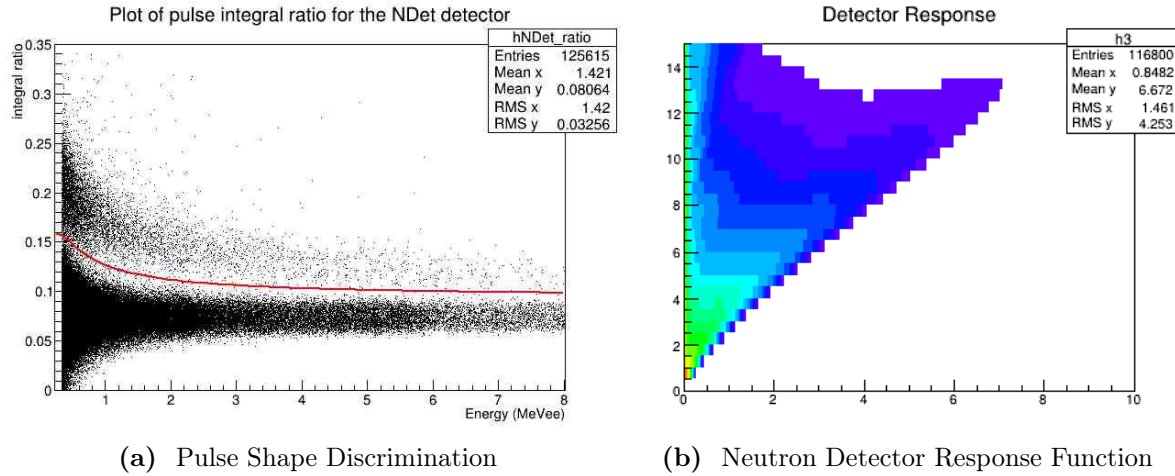


Figure C.4: Progress on analysis of the Neutron detectors. (a) Pulse shape discrimination showing separation between gammas (below red line) and neutrons (above red line) in the neutron detector. (b) The response function for the neutron detector obtained from the TUNL neutron beam.

C.3.3 Analysis

Analysis of this run is in its very first stages, primarily focussed on data quality checks at this time. Nonetheless, the reconstruction of the neutron energy spectrum is moving along.

Firstly, since the liquid scintillator neutron detectors respond to both photons and neutrons, a separation routine must be developed to distinguish the two incoming particles. Pulse Shape Discrimination was used, where the ratio of the integral over an initial portion of the pulse to the integral over the full length indicates the cause of the pulse as a neutron or photon. Since photons in general deposit more energy in the tail of the pulse, the two particles can be separated which can be seen from Fig. C.4a for the aluminium dataset of Run2015a.

Uncovering the neutron spectrum is further complicated by the fact that the observed energy is actually that of a nuclear recoil from a neutron reaching the detector. Unfolding must therefore be performed to recover the real neutron spectrum from the observed energy spectrum, using the response and acceptance of the detectors, based on simulation and calibration runs. The response matrix as a function of input energy can be seen in Fig. C.4b.

Analysis of the other detectors is also under way, with the germanium detector being studied using the techniques developed for the 2013 run. The LYSO array is being studied externally to the AlCap collaboration.

C.4 Run 2015b: Charged Particles

In November of this year, the charged particle measurement will be repeated and refined. In particular, an extra silicon detector with 1.5 mm thickness will be added to the two silicon telescopes which should increase the range for the total energy measurements up to about 25 MeV. To reduce our systematic uncertainties on the muon stopping distribution a scanning beam-monitor device will measure the beam profile at the target position during dedicated runs. Furthermore, a thinner active silicon target will improve the certainty of the stopping depth and distribution as well provide for a more rigorous cross-check of the unfolding procedures.

C.5 Summary

In summary, future μ - e conversion searches need much improved knowledge of the muon capture process in order to predict and protect against the various daughter particles that can be produced. In particular for aluminium, the stopping target of choice for both Mu2e and COMET, the momentum spectrum and rates of both charged and neutral particle emissions must be measured.

The AlCap experiment is a joint effort by COMET and Mu2e to make such a measurement. The first run in 2013 successfully observed the proton spectrum from about 4 to 10 MeV finding the total emission rate to be about 3 % per capture, with a relative uncertainty of about 10 % although analysis is on-going. A second run took place in June 2015 focussed on neutral particles and used a simpler set-up than the 2013 run which had required a vacuum to reduce scattering of the charged particles in air. Thicker stopping targets were used, allowing for higher beam energy and therefore a higher muon rate. Analysis of this data is only in its earliest stages at this time. Nevertheless for the analysis of the neutron spectrum, separation of neutrons from photons has been demonstrated and the detector response function and calibration has been obtained.

Finally, a third run in November 2015 will take place to improve the 2013 results by increasing the statistical sizes, extending the observed energy range and reducing systematic uncertainties.